Journal of Nanomaterials

Recent Advances in Synthesis and Coatings of Nanocomposites

Lead Guest Editor: B. Ramesh
Guest Editors: Ridwan Yahaya and Muhammad P. Jahan

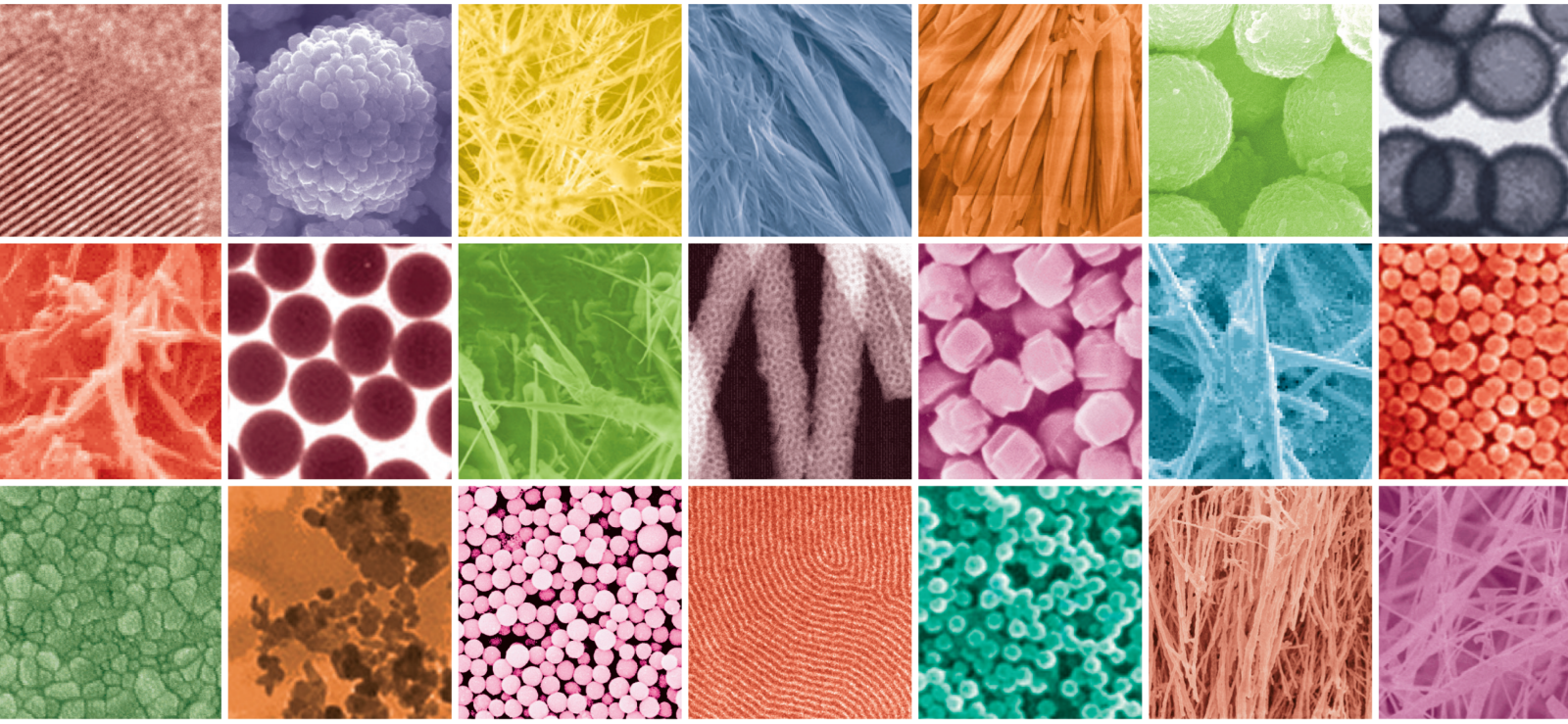

Recent Advances in Synthesis and Coatings of Nanocomposites

Journal of Nanomaterials

Recent Advances in Synthesis and Coatings of Nanocomposites

Lead Guest Editor: B. Ramesh
Guest Editors: Ridwan Yahaya and Muhammad P. Jahan

Contents

Analysis of Spectroscopic, Morphological Characterization and Interaction of Dye Molecules for the Surface Modification of TiB_2 Nanoparticles
S. Mayakannan, R. Rathinam, Rajasekaran Saminathan, R. Deepalakshmi, Mahesh Gopal, J. Justin Maria Hillary, S. Nanthakumar, V. Y. Ganvir, and Pallavi Singh
Research Article (9 pages), Article ID 1033216, Volume 2022 (2022)

Study on Properties of Epoxy Composites Modified by Functional Graphite Oxide and Polyurethane
Yansong Kang, Zenghui Feng, Xinhua Jiang, Lanxuan Liu, Jiafa Tao, Xiwang Huang, Weiwei Wang, and Xiangding Xiao
Research Article (12 pages), Article ID 2302131, Volume 2022 (2022)

Recent Developments in Stimuli Responsive Smart Materials and Applications: An Overview
T. Ramakrishnan, S. Senthil Kumar, Samson Jerold Samuel Chelladurai, S. Gnanasekaran, S. Sivananthan, N. K. Geetha, Ramesh Arthanari, and Gizachew Balcha Assefa
Review Article (7 pages), Article ID 4031059, Volume 2022 (2022)

Synthesis and Food Applications of Resistant Starch-Based Nanoparticles
Fakhar Islam, Muhammad Noman, Muhammad Afzaal, Farhan Saeed, Shabana Ahmad, Muhammad Waqas Zubair, Syeda Mahvish Zahra, Muzzamal Hussain, Huda Ateeq, and Chinaza Godswill Awuchi
Review Article (10 pages), Article ID 8729258, Volume 2022 (2022)

Hindawi
Journal of Nanomaterials
Volume 2023, Article ID 5985188, 10 pages
https://doi.org/10.1155/2023/5985188

Research Article

Analyze the Mechanical Characteristics of Fabricated MMCs on Nanocarbon Influencing with Polymer Composites

N. Vinayaka,[1] Anil Kumar Bodukuri,[2] Ganesh K. Jadhav,[3] N. Padmamalini,[4] Sumit Kumar Pandey,[5] M. Balasubramanian,[6] J. Immanuel Durai Raj,[7] M. Suresh Kumar,[8] and Balkeshwar Singh[9]

[1]*Department of Aeronautical Engineering, Nitte Meenakshi Institute of Technology, Yelahanka, Bengaluru 560064, India*
[2]*Department of Mechanical Engineering, Kakatiya University College of Engineering and Technology, Campus Vidyaranyapuri, Warangal 506009, India*
[3]*Department of Mechanical Engineering, Dr. D.Y. Patil Institute of Engineering, Management and Research, Akurdi, Pimpri-Chinchwad, India*
[4]*Department of Science, St. Joseph's Institute of Technology, Chennai, India*
[5]*Department of Mechanical Engineering, Guru Gobind Singh Educational Society's Technical Campus, Bokaro Steel City, India*
[6]*Department of Mechanical Engineering, University College of Engineering, Ramanathapuram Campus, Pullankudi, Ramanathapuram 623513, India*
[7]*Department of Mechanical Engineering, St. Joseph's Institute of Technology, OMR, Chennai 600119, India*
[8]*Department of Physics, Academy of Maritime Education and Training, Kanathur, Chennai 603112, India*
[9]*Department of Mechanical Design and Manufacturing Engineering, Adama Science and Technology University, Kebele-14, Adama 1888, Ethiopia*

Correspondence should be addressed to Balkeshwar Singh; balkeshwar.singh@astu.edu.et

Received 10 October 2022; Revised 5 December 2022; Accepted 24 April 2023; Published 17 May 2023

Academic Editor: Muhammad P. Jahan

The intention of this research is to recapitulate the two different fillers like E glass fiber and nanocarbon fiber, which were utilized to fabricate the polymer matrix composites by the assistance of epoxy resin. The mechanical compression molding was influenced to produce the polymer-based nanocomposites under consideration of optimal process parameters. There are three different weight fractions E glass fiber (40%, 45%, and 50%), nanocarbon fiber (10%, 15%, and 20%), and epoxy concentrations (30%, 40%, and 50%), respectively, that were used to produce the polymer matrix composites. Those processing parameters were designed by the L9 Taguchi with DOE technique to conduct the mechanical tests like tensile strength and hardness properties. The signal-to-noise ratios were successfully accomplished to identify optimal process parameters for improving the individual responses. The ANOVA and interaction was additional supports to enhance the mechanical properties. The scanning electron microscope was used to examine the fracture surfaces at the tensile fracture specimens with optimal conditions. Moreover, the maximum mechanical characteristics were attained by the increasing of nanocarbon fiber in the processed polymer matrix composites.

1. Introduction

To improve unique characteristics like chemical stability, maximum thermal conductivity, withstand breakdown potency, and better insulation properties which depend on the various applications of packaging-based materials and enhanced electronics-based applications, utilization of nano-based filler materials on the various resins agents was done to produce the polymer nanocomposites. In most of the applications, polymer-based nanocomposites contain better thermal conductivity under the maintenance of 0.5 W/m·k which is less than the limits [1–5].

Maximum utilization of various applications like aerospace, automotive, and biomedical are related to different fields. The nanoreinforcement into the polymer composites fabrication improves the mechanical attributes. In current

applications of composite-related production, thermal conductivity is the most important factor for enhancing the adhesion properties among the base material and nanoreinforcement particles. The addition of nano-based carbon reinforcements enhances the properties of adhesion between the matrix material and nanostrengthening particles [6–7]. The fabricated polymer composites normally contain the special characteristics like simple processing with less cost, less density, better resistance to chemicals, and less thermal conductivity which are related to maximum engineering-based applications, especially in materials. The above-recommended solutions are fulfilled by fiber-based reinforced polymers composites due to the high class of prospective matter that affords the capability to produce the appropriate design of innovative ideas in the trending industries to solve the above-mentioned issues [8–10].

Normally, the fiber-based reinforced polymers had better strength when reinforced into the appropriate reinforcing nanofillers which are embedded in the different polymer-based matrixes. The polymer composite by matrix materials are active in bonding components that support transfer the loading into the fibers for withstand the protecting materials [11–14]. The fabrication of eco life composites are utilized by natural fibers materials like hemp, banana, kenaf, jute, sisal, etc., and the synthetic-based materials are carbon fiber, glass, and Kevlar fiber, etc. Next side of the polymer matrixes, thermos setting, and thermoplastic materials defined by the polymerization process and solving agents are epoxies, vinyl ester, and polyesters which are based on the thermosetting matrixes. These composites achieved the cross-linking mechanism through the polymerization or condensation process. Compared with thermoplastic, thermosetting matrixes have better adhesive properties, excellent mechanical characteristics, and fine impregnation characteristics. The thermosetting processes are estimated by various heat conditions but not under the circumstances of liquefying process; however, it is possible in reheating or solvents. In thermoplastic types, polypropylene, polyvinyl chloride, and polyurethanes are more costly to fabricate and also affect the environment [15–18].

The enhanced mechanical properties are achieved in the fiber-based polymer matrix composites which are based on the polymer matrix and fiber materials. These composites are mostly utilized to establish the duration of the applications, for example, materials structure [19–21]. The fiber-based polymer matrix composites are used in different engineering applications like construction sites, the navy, building sections, aerospace, and automotive. The hybridization enhances the properties of the polymer composites according to previous researchers. Engineering applications are widely developed by hybrid-based polymer composites, but monofiber polymer composites are more complicated to meet the outstanding performance in some special cases [22].

By the influence of nanofiller materials, for composing the fiber-based polymer composites that exhibit the better potential strength is possible by the nitride elements. These nitride elements possess the enhanced mechanical, electrical, and thermal properties when compared with other than nitride based filler materials. Few examples of filler materials are carbon nitride, titanium nitride, silicon nitride, aluminumnitride, titanium nitride, and zirconium nitride and these nitride-based filler elements are normally favored in the fabrication of polymer-based composites to exhibit better wear-resistant and elastic properties, corrosion resistance, magnetic properties, and other electrical attributes [23].

The major important aspect of composite is nanofillers and these nanofilleris are available in the form of fiber, fragment, whiskers, and sheet. Now the nanofillers are a promising method to develop the mechanical properties of the natural fiber-based reinforced polymer composites. Nanofillers produce better properties than base materials due to this composite occupy the smaller region by the larges surfaces [24]. More researchers developed the composites by assured nanomaterials to improve the mechanical attributes and also develop the material properties by the way of electrical, optical, heat resistance, and magnetic characteristics. There two steps single or multiple are involved in composition of the nanocomposites and nanoparticles having a size of 100 nm. The pure epoxy-based resins to produce the composites by the addition of nanofillers have desired characteristics were not achieved due to agglomerated presentation. But the evenly dispersed agglomerated particles achieve the desired properties. The multistep process achieves the better nanocomposites without modifying the melting temperature and processing factors. Figure 1 shows the experimental procedures [25]. From the in depth of literature, nitride-based nano-based fillers are utilized to a great extent to compose better mechanical properties in the presence of polymer-based nanocomposites. Most of the studies are done on various fiber materials and other ceramic-based reinforcements but there is less work that is concentrated on the material of carbon fiber and E glass fiber. Similarly, less work has been done in finding the optimal processing parameter by the S/N ratios. Therefore, in this research, nanobased carbon fiber was selected as nanofillers, and the support of E glass fibers was taken to compose polymer matrix composites by the compression molding process. Then the prepared composites were accounted for measuring the performance of mechanical characteristics with the Taguchi technique.

2. Material and Methods

In this paper, nanobased fillers of carbon fiber and E glass fibers were used to produce the polymer-based nanocomposites having the sizes of each fibers is 70 nm scale for carbon. Owing to this, carbon fiber possess superior density and mechanical properties and are low in cost and simple to purchase. In the various manufacturing and logistical applications, these nanocarbon fillers were broadly used and also used in the automotive, aerospace, and other defense-related applications. And the epoxy resin was selected as the binding material between the base on nanocarbon fillers and the E glass fibers [26].

Initially, the E glass fiber and the nano-based carbon fibers were purchased from the local suppliers having densities 2.05 and 2.60 g/cm^3, respectively. The selected epoxy

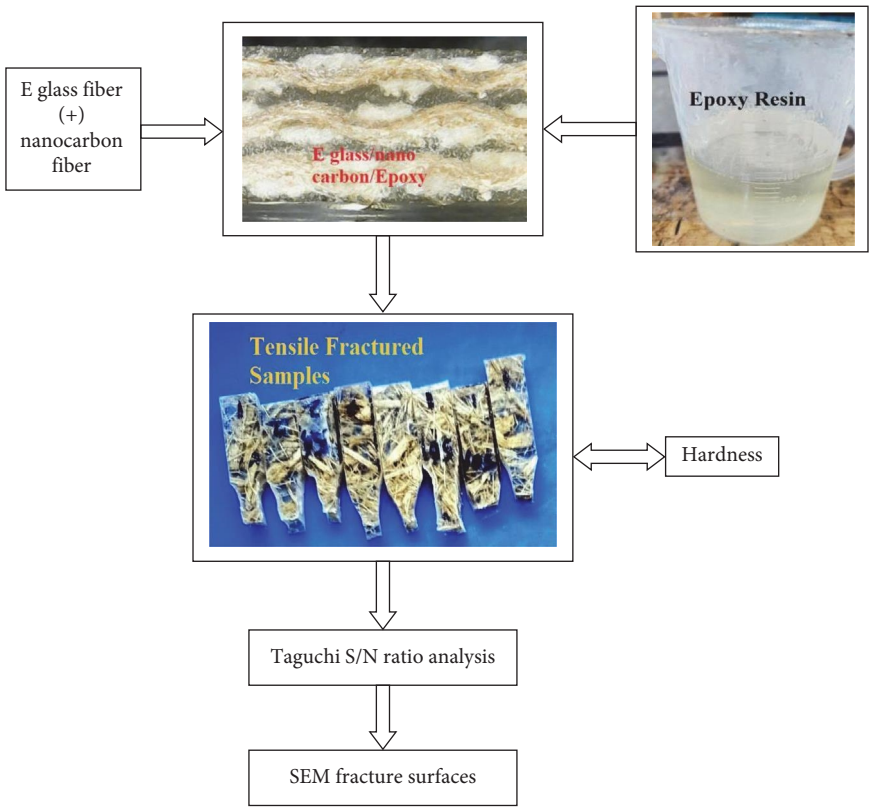

Figure 1: Experimental procedures.

resins had viscosity 10,000 cPS, and the appropriate hardener was the most important factor for merging these nanofillers. By this way, hardener 951 HY was the epoxy material having the cPS range of 17,000. Then these hardeners and epoxy resins were mixed in a ratio of 10 : 1 into the mechanical agitator. Before that, the nanocarbon and E glass fibers were taken as the percentage at different weights, respectively. Before starting the process, the required molding steel plate having the dimensions 300 mm × 280 mm × 6 mm basins was used to produce the polymer composites.

After selecting the materials, base E glass fiber was placed as the primary material in the steel plate with above-mentioned dimensions. Initially, the film is punched with holes was protected on the E glass prepared mat on the steel plate for the desired film-made material. Then the wax was coated on the placed E glass mat for getting quick settling for the curing process. Next, the epoxy resin was concerned for coating over the E glass mat, and subsequently, the first layer of the mat was completed. Then the completed mat was applied by the epoxy to cover the carbon fiber and finally, the second layer was also generated. This process was repeated for three times to make the three layers with 4 mm thickness of specimens. Lastly, the compression molding technique was initiated to produce the successfull components maintaining 150 bar of pressure at a sustained period of 2 hr, and these conditions promoted the final materials having the enhanced surface finishes and desired dimensions. These procedures were followed as per the completion of the stacking process. There are three different weight concentrations E glass fiber (40%, 45%, and 50%), nanocarbon fiber (10%, 15%, and 20%), and epoxy concentrations (30%, 40%, and 50%), respectively were designed by the Taguchi method (Tables 1 and 2).

There was some important factors that were need to fix the cross-linking mechanism to attain better outcomes in the final cured composites part. Therefore, after the removing the laminated form from the mold, the processed composites were approached for hot air process maintaining the oven temperature at 60°C for 2 hr and then cooling process was accomplished for 24 hr at room temperature. The prepared composites were employed to conduct the tensile test under the ASTM D3039 standards with the support of universal testing machine maintaining 100 kN load. After the tensile tests, the hardness test was conducted on the process polymer matrix composites as per the specimen standards of ASTM D785. Different volume fractions of various nanofillers and epoxy resins were designed by the Taguchi method [27].

3. Results and Discussion

3.1. Mechanical Characteristics of E Glass/Nanocarbon Fiber/Epoxy Composites. As per the ASTM specifications of tensile and hardness, all the experiment specimens were prepared. The investigational outcomes like tensile and hardness was extracted from the polymer-based composites. Table 3 shows the polymer outcomes of tensile and hardness values. As shown in Table 3, all the output responses with L9 basis results were improved by the addition of nanocarbon filler

Table 1: Three levels for polymer composites (E glass/nanocarbon/epoxy).

Factors	Input polymer composites	Level of parameters		
1	E glass fiber	40	45	50
2	Nanocarbon fiber	10	15	20
3	Epoxy	30	40	50

Table 2: Taguchi L9 for arranged polymer input factors.

L9	E glass fiber	Nanocarbon fiber	Epoxy
1	40	10	30
2	40	15	40
3	40	20	50
4	45	10	40
5	45	15	50
6	45	20	30
7	50	10	50
8	50	15	30
9	50	20	40

Table 3: Polymer input factors and outputs.

L9	E glass fiber	Nanocarbon fiber	Epoxy	Tensile strength (MPa)	Hardness (HRC)
1	40	10	30	367	60
2	40	15	40	375	58
3	40	20	50	371	63
4	45	10	40	372	59
5	45	15	50	390	62
6	45	20	30	368	65
7	50	10	50	363	57
8	50	15	30	355	55
9	50	20	40	361	79

materials into the E glass fibers by the epoxy-based nanopolymer composites. Especially, the specimen 5 had the maximum tensile strength at the attained parameters of 45 wt% of E glass fiber, 15 wt% of nanocarbon fiber, and 50% of epoxy. The increasing content of nanocarbon fiber and addition of sufficient quantity with 50% epoxy waere the major influencing factors to enhance the tensile strength. Subsequently, the hardness attained maximum effects on the processed polymer matrix composites. The corresponding parameters were 50 wt% of E glass fiber, 20 wt% of nanocarbon fiber, and 40% of epoxy. It is revealed that the maximum content of nanocarbon fiber had a significant role in superior hardness of the polymer matrix composites samples. Figures 2 and 3 shows the individual response analysis of tensile strength and hardness properties on the processed-nanopolymer composites.

As shown in Figure 3, the pie chart analysis of hardness experiments clearly indicated that sample 9 attained the maximum hardness when compared with other sets of polymer composites which were fabricated by E glass fiber, nanocarbon fiber, and epoxy resins. The proper setting which belongs to compression molding factors also has majorly important aspects for enhancing the mechanical characteristics.

3.2. S/N Ratio Analysis on Tensile and Hardness on the Polymer Matrix Composites. Even though the individual responses of polymer matrix composites were concentrated, some individual optimization was definitely influenced to enhance the mechanical characteristics by the upgraded level. Therefore, in this section, signal-to-noise (S/N) ratios were generated for both the individual responses of tensile strength and hardness properties, respectively. As per the instructions of Taguchi and DOE, the S/N ratio was utilized to produce the individual optimization by the supports of ANOVA and interaction plots. Table 4 exhibits the S/N ratios for tensile strength and hardness outcomes. As shown in Table 4, detailed S/N ratios were determined successfully and analyzed by ANOVA. It is understood that the S/N ratio values were attained to maximum as mentioned in the earlier section for individual responses. Now this parameter was validated with interaction plots and ANOVA. Therefore, the linear model regression analysis was implemented to identify the individual responses. Larger the better option was utilized for identifying the individual contribution level. Similarly, the hardness was also attained to the maximum of S/N ratio values as per the larger the better option.

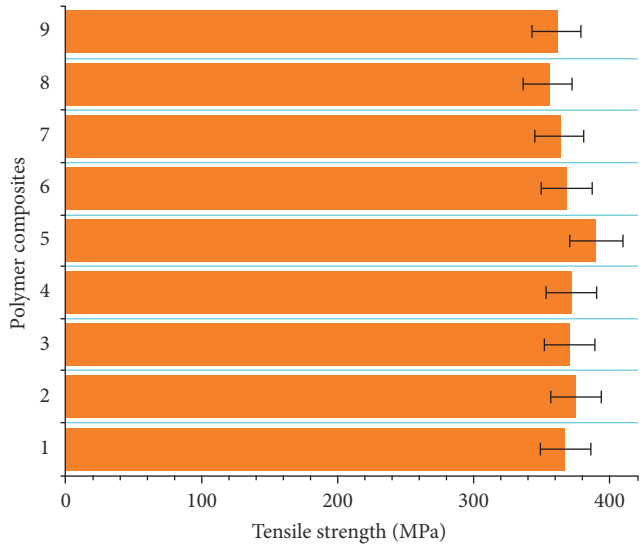

Figure 2: Tensile strength of processed hybrid polymer composite.

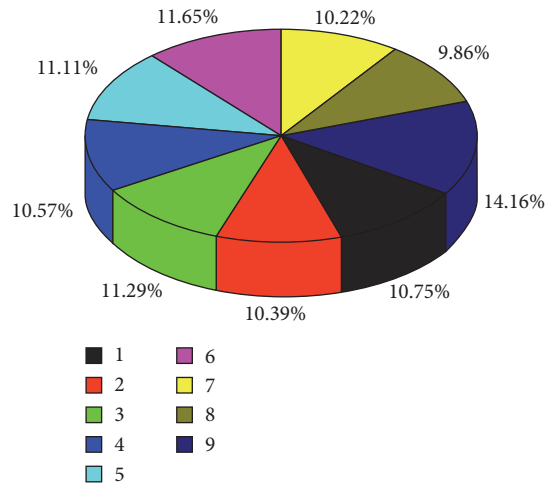

Figure 3: Pie chart analyses for hardness on the E glass/nanocarbon/epoxy composites.

Table 4: S/N ratios for polymer matrix composites with their outputs.

L9	E glass fiber	Nanocarbon fiber	Epoxy	Tensile strength (MPa)	S/N ratios	Hardness (HRC)	S/N ratios
1	40	10	30	367	51.29	60	35.563
2	40	15	40	375	51.48	58	35.268
3	40	20	50	371	51.38	63	35.986
4	45	10	40	372	51.41	59	35.417
5	45	15	50	390	51.82	62	35.847
6	45	20	30	368	51.31	65	36.258
7	50	10	50	363	51.19	57	35.117
8	50	15	30	355	51.00	55	34.807
9	50	20	40	361	51.15	79	37.952

Table 5: ANOVA for input polymer factors with their contribution.

Polymer factors	*df*	SS	MS	*F*	*P*	Percentage
E glass fiber	2	0.24835	0.12417	6.92	0.126	14.8
Nanocarbon fiber	2	0.04109	0.02055	1.15	0.466	55.0
Epoxy	2	0.10477	0.05238	2.92	0.255	30.1
Residual error	2	0.03587	0.01794			0.1
Total	8	0.43009				100

The ANOVA analysis further validated the individual input polymer parameters by the support of P and F values. From these values, the percentage contribution was analyzed properly and the contributed percentage was highly attained with the increase of nanocarbon fibers. The overall contribution was 14.8% of E glass fiber, 55.0 of nanocarbon fiber, and 30.1% of epoxy. The ANOVA for polymer composites input factors with their tensile outcomes performances are exhibited in Table 5. The overall model of R^2 values is 92%.

Table 6 shows the response for S/N ratios of tensile outcomes. As shown in Table 6, each and every rank system was analyzed properly by the influencing of delta order. It is revealed that the maximum rank was accumulated in input factors of E glass fiber that contains the first rank contains the highest point by following the next factors nanocarbon and epoxy occupies the 2 and 3, respectively. Similarly, the interaction graph shows the optimal input factors for polymer composites, shown in Figure 4, which reveals that the optimal polymer input parameters were attained at the range of 45 wt% of E glass fiber, 15 wt% of nanocarbon fiber, and 50 wt% of epoxy.

The ANOVA investigation further confirmed the independent input polymer parameters by the support of P and F significant values. The ANOVA table of hardness and its polymer matrix input factors are displayed in Table 7. As shown in Table 7, the contributed percentage was accomplished by the increasing of nanocarbon fibers. The overall contribution was

Table 6: S/N ratios mean table for tensile with input factors of polymer composites.

Level	E glass fiber	Nanocarbon fiber	Epoxy
1	51.39	51.30	51.20
2	51.52	51.44	51.35
3	51.12	51.28	51.47
Delta	0.40	0.15	0.26
Rank	1	3	2

Table 7: ANOVA for input polymer factors with their contribution.

Polymer input factors	*df*	SS	MS	*F*	*P*	Percentage
E glass fiber	2	0.1937	0.09685	0.10	0.909	46.4
Nanocarbon fiber	2	3.9008	1.95042	2.00	0.333	17.01
Epoxy	2	0.7762	0.38810	0.40	0.715	36.5
Residual error	2	1.9464	0.97322			0.09
Total	8	6.8172				100

Table 8: S/N ratios mean table for hardness with input factors of polymer composites.

Level	E glass fiber	Nanocarbon fiber	Epoxy
1	35.61	35.37	35.54
2	35.84	35.31	36.21
3	35.96	36.73	35.65
Delta	0.35	1.42	0.67
Rank	3	1	2

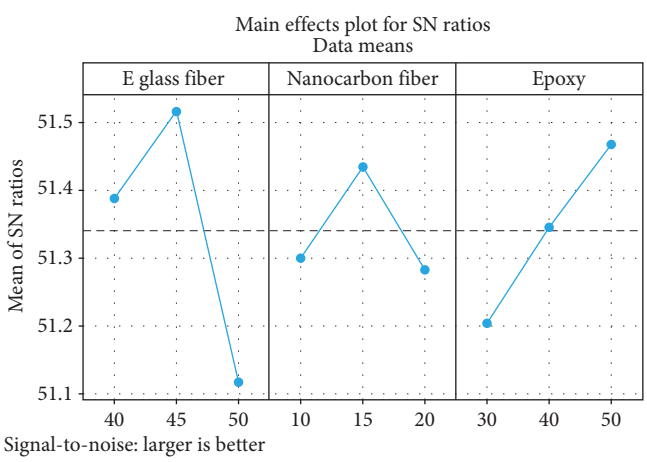

Figure 4: Interaction graph for tensile with input factors.

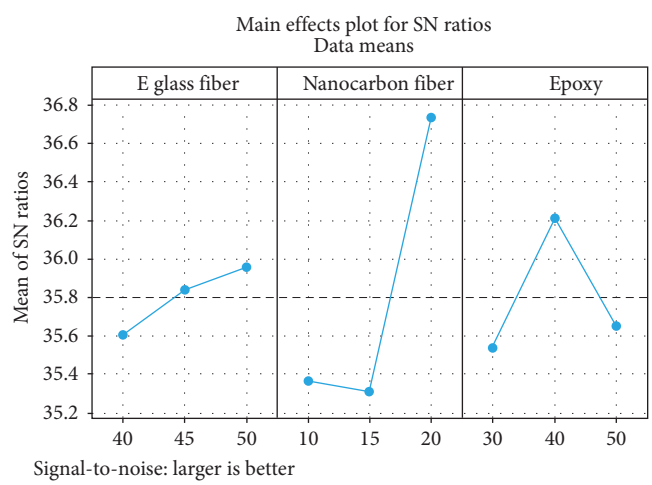

Figure 5: Interaction graph for hardness with input factors.

of 46% of E glass fiber, 17% of nanocarbon fiber, and 36.5% of epoxy. The overall model of R^2 values is 71.45%.

Table 8 exhibits the response for S/N ratios of hardness. As shown in Table 8, each and every rank order combination was measured properly by the influence of delta order. It is understood that the highest rank occurred in the input factors of E glass fiber that contains the first rank; the factors epoxy and nanocarbon attained the ranks 2 and 3, respectively. Similarly, the interaction graph shows the optimal input factors for polymer composites hardness and which are shown in Figure 5. As shown in Figure 5, it was concluded that the optimal polymer input parameters were conquered at the range of 50 wt% of E glass fiber, 20 wt% of nanocarbon fiber, and 40 wt% of epoxy. The main effect plot confirms that the presence of nanocarbon fiber and maximum concentration E glass fiber improves the mechanical properties and the

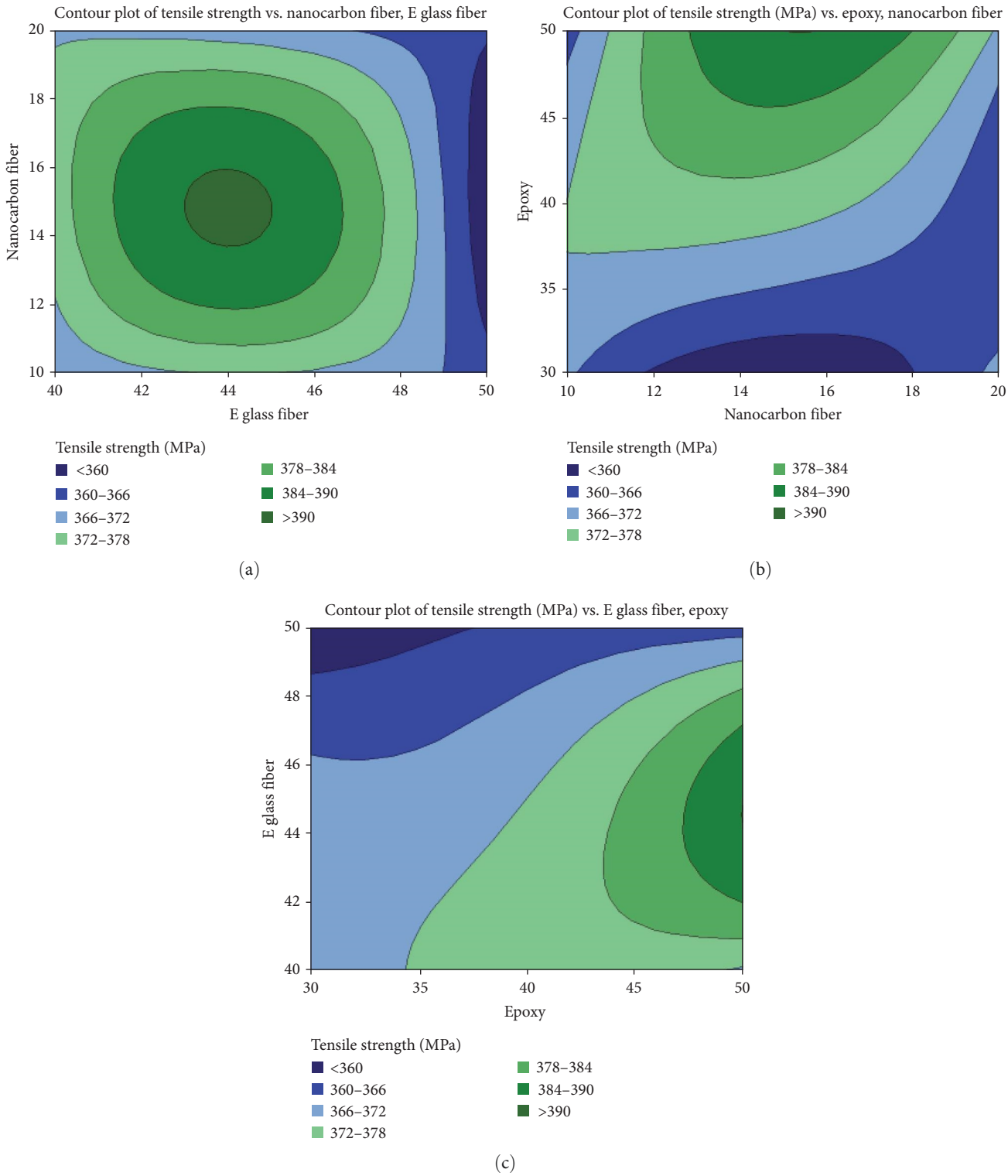

Figure 6: Contours on various input polymer composites of tensile behavior.

S/N ratio which was confirmed by the appearance of rank method as shown in Table 8.

3.3. Contour Investigations on Tensile Strength with Various Input Polymer Composites. Figure 6(a)–6(c) shows various input polymer matrix composites on the attained tensile strength. Figure 6(a) exhibits the E glass and nanocarbon fibers of the obtained tensile strength on the polymer matrix composites. As shown in Figure 6(a), it was implicit that the increasing of carbon nanofiber and E glass fibers improves the ductile strength. Figure 6(b) displays different concentrations of nanocarbon fiber and epoxy of the accomplished

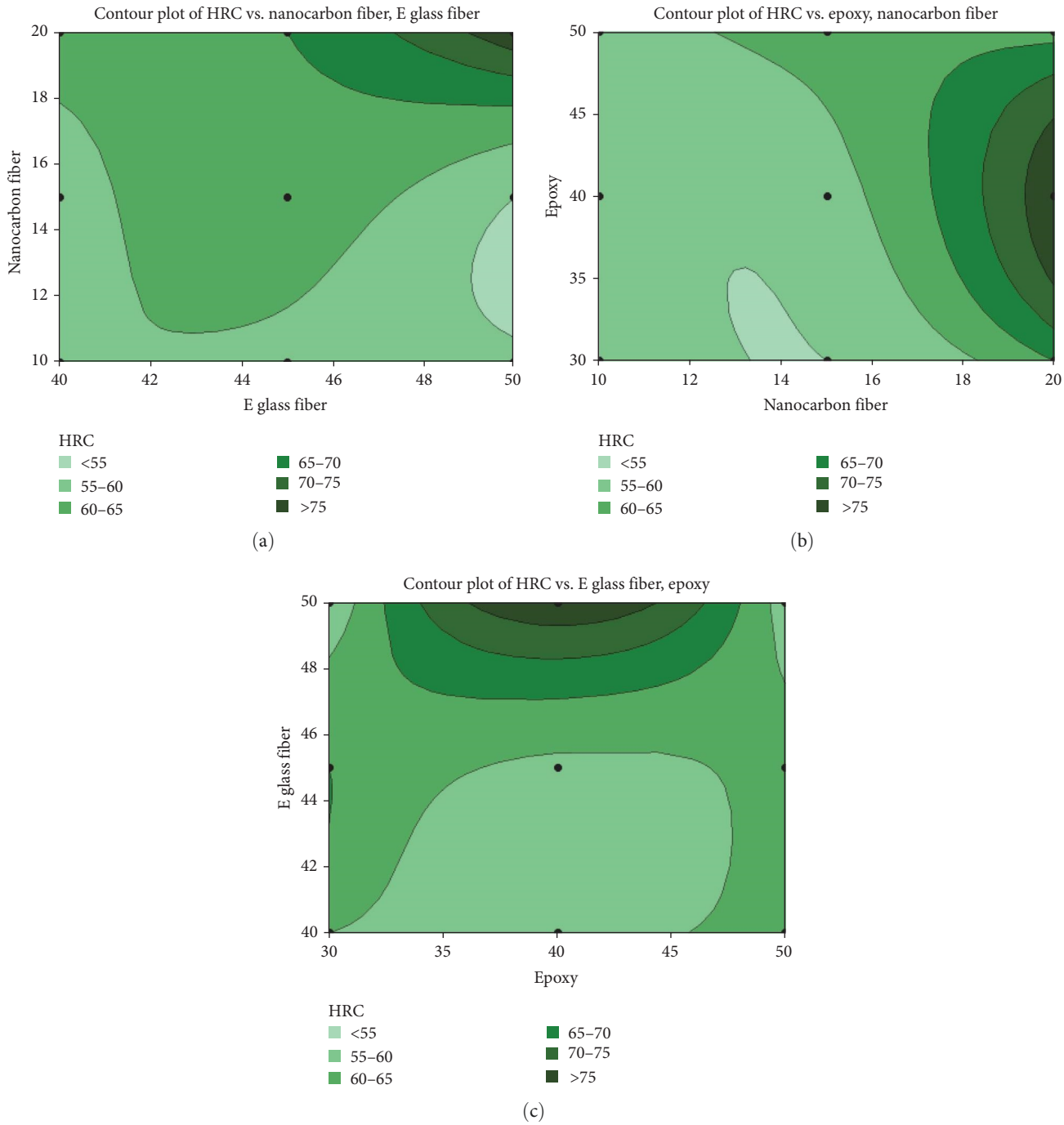

Figure 7: Contours on various input polymer composites of hardness strength.

tensile strength on the processed polymer matrix composites. It is understood that the medium of nanocarbon fiber with low concentration of epoxy produced a better tensile strength. Figure 6(c) shows a different weight percentage of epoxy and E glass fiber on the attained tensile strength of polymer matrix composites. As shown in Figure 6(c), it was revealed that the low content of epoxy and maximum weight percentage of E glass fiber improves the mechanical strength. The maximum concentration of the E glass and nanocarbon fibers improves the interfacial strength and results in developing the grain boundaries to reduce the crack during the processing and tensile test.

3.4. Contour Investigations on Hardness Properties with Various Input Polymer Composites. Figure 7(a)–7(c) shows the various input polymer matrix composites on the produced hardness. Figure 7(a) exhibits the E glass and nanocarbon fibers of the obtained hardness properties on the processed polymer matrix composites. As shown in Figure 7(a), it was implied that the increasing of carbon nanofiber and E glass fibers improves

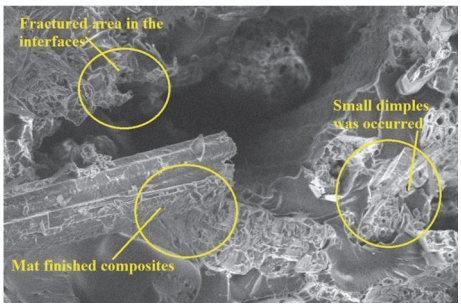

Figure 8: Fracture surfaces on the polymer composites.

the hardness strength. Figure 7(b) displays the various percentages of nanocarbon fiber and epoxy of the obtained hardness properties on the fabricated polymer matrix composites. It is unstated that the maximum nanocarbon fibers with less concentration of epoxy produced better hardness properties. Figure 7(c) shows different weight percentage of epoxy and E glass fiber on the attained hardness strength of polymer matrix composites. As shown in Figure 7(c), it was exposed that the moderate content of epoxy and maximum quantity fraction of E glass fiber improve the hardness strength. From the detailed analysis of contour investigations on the processed polymer composites mechanical characteristics of both the responses were attained. The overall enhanced properties based on the polymer matrix composites were produced effectively by the influence of various working input factors like E glass fiber, nanocarbon fibers, and epoxy resins. The major influencing factor was nanocarbon fibers by increasing the addition from 15% to 20%, less epoxy from 30% to 40%, and E glass fiber 40%–45%, respectively. The processed polymer matrix composites produced better interfacial bonding properties by the influence of nanocarbon fibers.

3.5. Microstructure of Fractured Polymer Matrix Composites at Optimal Condition. Figure 8 shows the fractured region on the polymer matrix composites at the optimal process parameters. That the optimal processing input factors were 45 wt% of E glass fiber, 15 wt% of nanocarbon fiber, and 50 wt% of epoxy. During the ductile fracture, the maximum load was taken between the interfaces of E glass fiber and nanocarbon fiber. This attained structure exposed better interfacial properties which were revealed from the tensile values. The corrected epoxy resins also produces the maximum attained load which migrated from the tensile experiments. Similarly, the maximum hardness was accumulated in these same optimal parameters with slight variation in the epoxy resin concentration [28].

4. Conclusion

From the research result by overall experiment, the modified nanocomposites were achieved effectively by different concentration of input factors like E glass fiber, nanocarbon fibers, and epoxy. During the process, the final mat-finish polymer matrix composites were fabricated under the compression molding process. The maximum concentration of the nanocarbon fiber was the major reason to enhance the mechanical properties. Taguchi was also integrated to generate the individual significant responses by the influence of S/N ratios with linear regression model. The ANOVA composes the maximum utilization of contributed percentage for both mechanical outcomes. The attained optimal parameters with tensile properties were 45 wt% of E glass fiber, 15 wt% of nanocarbon fiber, and 50 wt% of epoxy. Similarly, the hardness achievements are 50 wt% of E glass fiber, 20 wt% of nanocarbon fiber, and 40 wt% of epoxy. The SEM examination successfully revealed the fracture surfaces between the epoxy and the fillers of nanocarbon and E glass fibers.

Data Availability

The data used to support the findings of this study are included within this article.

Conflicts of Interest

The authors declare that they have no conflicts of interest.

References

[1] S. Ahmad, S. Ali, M. Salman, and A. H. Baluch, "A comparative study on the effect of carbon-based and ceramic additives on the properties of fiber reinforced polymer matrix composites for high temperature applications," *Ceramics International*, vol. 47, no. 24, pp. 33956–33971, 2021.

[2] A. Nagaraj, A. Uysal, S. Gururaja, and I. S. Jawahir, "Analysis of surface integrity in drilling carbon fiber reinforced polymer composite material under various cooling/lubricating conditions," *Journal of Manufacturing Processes*, vol. 82, pp. 124–137, 2022.

[3] A. Pariyar, C. S. Perugu, L. S. Toth, and S. V. Kailas, "Microstructure and mechanical behavior of polymer-derived in-situ ceramic reinforced lightweight aluminum matrix composite," *Journal of Alloys and Compounds*, vol. 880, Article ID 160430, 2021.

[4] A. Kasiri and D. Brabazon, "Materials used within polymer matrix composites (PMCs) and PCM production via additive manufacturing," *Encyclopedia of Materials: Composites*, vol. 2, pp. 837–846, 2021.

[5] K. V. Apryatina, E. V. Salomatina, S. S. Sologubov, A. V. Markin, and L. A. Smirnova, "Specific features of thermal properties of polymer composites containing conductive nanoparticles in non-conductive polymer matrices," *Thermochimica Acta*, vol. 705, Article ID 179036, 2021.

[6] S. Das and S. Das, "Properties for polymer, metal and ceramic based composite materials," *Encyclopedia of Materials: Composites*, vol. 2, pp. 815–821, 2021.

[7] P. Jongvivatsakul, C. Thongchom, A. Mathuros et al., "Enhancing bonding behavior between carbon fiber-reinforced polymer plates and concrete using carbon nanotube reinforced epoxy composites," *Case Studies in Construction Materials*, vol. 17, Article ID e01407, 2022.

[8] Z. Abbasi, O. M. Jazani, and M. Sohrabian, "Designing of high-performance epoxy adhesive with recycled polymers and silica nano particles (SNPs) in epoxy/carbon fiber composite-steel bonded joints: mechanical properties, thermal stability and toughening mechanisms," *Journal of the Taiwan Institute of Chemical Engineers*, vol. 123, pp. 310–327, 2021.

[9] M. Monoranu, R. L. Mitchell, K. Kerrigan, J. P. A. Fairclough, and H. Ghadbeigi, "The effect of particle reinforcements on

chip formation and machining induced damage of modified epoxy carbon fibre reinforced polymers (CFRPs)," *Composites Part A: Applied Science and Manufacturing*, vol. 154, Article ID 106793, 2022.

[10] P. Zhang, W. Wang, Y. Lv, K. Wang, and S. Dai, "Effect of polymer coatings on the freezing–thawing and carbonation resistances of nano-SiO2 and polyvinyl alcohol fiber-reinforced cementitious composites," *Journal of Materials Research and Technology*, vol. 21, pp. 69–83, 2022.

[11] V. Carvelli, H. Nishida, T. Fujii, and K. Okubo, "Low velocity impact and CAI of woven carbon fibre reinforced highly polymerized thermoplastic epoxy modified with submicron diameter glass fibres," *Composite Structures*, vol. 236, Article ID 111835, 2020.

[12] D. Zhang, L. Liu, X. Lan, J. Leng, and Y. Liu, "Synchronous deployed design concept triggered by carbon fibre reinforced shape memory polymer composites," *Composite Structures*, vol. 290, Article ID 115513, 2022.

[13] S. Sharma and G. Agrawal, "Biomedical applications of electrospun polymer and carbon fibers," *Encyclopedia of Materials: Plastics and Polymers*, vol. 4, pp. 681–696, 2022.

[14] L. Joseph, P. Sarath Kumar, B. D. S. Deeraj, K. Joseph, K. Jayanarayanan, and K. M. Mini, "Modification of epoxy binder with multi walled carbon nanotubes in hybrid fiber systems used for retrofitting of concrete structures: evaluation of strength characteristics," *Heliyon*, vol. 8, no. 6, Article ID e09609, 2022.

[15] A. Sotiropoulos, S. Koulouridis, A. Masouras, V. Kostopoulos, and H. T. Anastassiu, "Carbon nanotubes films in glass fiber polymer matrix forming structures with high absorption and shielding performance in X-Band," *Composites Part B: Engineering*, vol. 217, Article ID 108896, 2021.

[16] W. Zurowski, J. Zepchlo, A. Krzyzak, E. Gevorkyan, and M. Rucki, "Effect of the quartz powder on the performance of the two layers glass fiber reinforced polymer composite with emulsion binder," *Composite Structures*, vol. 298, Article ID 116024, 2022.

[17] D. Satish Kumar, T. Sathish, S. M. Rangappa, P. Boonyasopon, and S. Siengchin, "Mechanical property analysis of nanocarbon particles/glass fiber reinforced hybrid epoxy composites using RSM," *Composites Communications*, vol. 32, Article ID 101147, 2022.

[18] M. Abu-Okail, N. A. Alsaleh, W. M. Farouk et al., "Effect of dispersion of alumina nanoparticles and graphene nanoplatelets on microstructural and mechanical characteristics of hybrid carbon/glass fibers reinforced polymer composite," *Journal of Materials Research and Technology*, vol. 14, pp. 2624–2637, 2021.

[19] P.-Y. Mechin, V. Keryvin, and J.-C. Grandidier, "Effect of the nano-filler content on the compressive strength of continuous carbon fibre/epoxy matrix composites," *Composites Part B: Engineering*, vol. 224, Article ID 109223, 2021.

[20] N. I. N. Haris, M. Z. Hassan, R. A. Ilyas et al., "Dynamic mechanical properties of natural fiber reinforced hybrid polymer composites: a review," *Journal of Materials Research and Technology*, vol. 19, pp. 167–182, 2022.

[21] T. Mishra, P. Mandal, A. K. Rout, and D. Sahoo, "A state-of-the-art review on potential applications of natural fiber-reinforced polymer composite filled with inorganic nanoparticle," *Composites Part C: Open Access*, vol. 9, Article ID 100298, 2022.

[22] T. Azhary, Kusmono, M. W. Wildan, and Herianto, "Mechanical, morphological, and thermal characteristics of epoxy/glass fiber/cellulose nanofiber hybrid composites," *Polymer Testing*, vol. 110, Article ID 107560, 2022.

[23] Y. Hua, F. Li, N. Hu, and S.-Y. Fu, "Frictional characteristics of graphene oxide-modified continuous glass fiber reinforced epoxy composite," *Composites Science and Technology*, vol. 223, Article ID 109446, 2022.

[24] D. Bellisario, F. Quadrini, L. Iorio et al., "Microscopic testing of carbon fiber laminates with shape memory epoxy interlayer," *Materials Today Communications*, vol. 32, Article ID 103854, 2022.

[25] S. Dehrooyeh, M. Vaseghi, M. Sohrabian, and M. Sameezadeh, "Glass fiber/carbon nanotube/epoxy hybrid composites: achieving superior mechanical properties," *Mechanics of Materials*, vol. 161, Article ID 104025, 2021.

[26] P. Raveendran, S. V. Alagarsamy, C. Chanakyan, M. Meignanamoorthy, M. Ravichandran, and S. Sakthivelu, "A hybrid approach for prediction of machining performances of glass fiber reinforced plastic (Epoxy) composites," *Surface Topography: Metrology and Properties*, vol. 9, no. 3, Article ID 035046, 2021.

[27] C. Chanakyan, S. Sivasankar, M. Meignanamoorthy et al., "Optimization of FSP process parameters on AA5052 employing the S/N ratio and ANOVA method," *Advances in Materials Science and Engineering*, vol. 2021, Article ID 6450251, 15 pages, 2021.

[28] M. Mohammed, R. Rahman, A. M. Mohammed et al., "Surface treatment to improve water repellence and compatibility of natural fiber with polymer matrix: recent advancement," *Polymer Testing*, vol. 115, Article ID 107707, 2022.

Hindawi
Journal of Nanomaterials
Volume 2023, Article ID 8936855, 12 pages
https://doi.org/10.1155/2023/8936855

Research Article

Characterization and Superhydrophobic Anticorrosive Coating of AA-7475/ZrO_2/Polymer Nanocomposites

Anil Kumar Bodukuri,[1] **Aniket Bhanudas Kolekar**,[2] **Rohit Pandey**,[3] **Koli Gajanan Chandrashekhar**,[4] **P. Ram Kumar**,[5] **K. Anandan**,[6] **C. Devanathan**,[7] **Shubhajit Halder**,[8] **and Balkeshwar Singh**[9]

[1]*Department of Mechanical Engineering, Kakatiya University College of Engineering and Technology, Warangal 506009, Telangana, India*
[2]*Department of Mechanical Engineering, Dr. D.Y. Patil Institute of Engineering, Management and Research, Pune 411044, India*
[3]*Department of Mechanical Engineering, Amity University Madhya Pradesh, Maharajpura Dang, Gwalior 474005, MP, India*
[4]*Department of Mechanical Engineering, Sanjeevan Engineering and Technology Institute, Kolhapur 416201, India*
[5]*Department of Chemistry, V.O. Chidambaram College, Tuticorin 628008, India*
[6]*Department of Physics, Academy of Maritime Education and Training (Deemed to be University), Kanathur 603112, India*
[7]*Department of Mechanical Engineering, Rajalakshmi Engineering College, Thandalam, Chennai 602105, India*
[8]*Department of Chemistry, Hislop College, Nagpur 440001, Maharashtra, India*
[9]*Department of Mechanical Design and Manufacturing Engineering, Adama Science and Technology University, Kebele-14, Adama 1888, Ethiopia*

Correspondence should be addressed to Balkeshwar Singh; balkeshwar.singh@astu.edu.et

Received 25 August 2022; Accepted 29 September 2022; Published 10 May 2023

Academic Editor: Ramesh Balasubramanian

An AA-7475 is coated with superhydrophobic (SH) polymer nanocomposites (PNCs), emphasizing the coating's manufacturing, characterization, and anticorrosive qualities. Coating AA-7475 alloy with polyvinyl chloride (PVC), copper stearate (CS), and zirconium oxide (ZrO_2) nanoparticles produces the desired superhydrophobic. Using an X-ray diffractometer, field-emission scanning electron microscopy, Fourier-transform infrared spectrometer, ZrO_2 nanoparticles, CS, and PVC PNCs are analyzed structurally and molecularly. The atomic force microscope picture was analyzed to determine how the surface roughness affected the SH behavior reached by changing the weight percentage of ZrO_2 nanoparticles from 0.6 to 3.0 wt%. PNC-5 with 3.0 wt% ZrO_2 nanoparticles is used as resistance to corrosion coating for AA-7475 due to its water contact angle of 154°. In a 3.5% NaCl solution, uncoated and PNC-5-coated AA-7475 are examined using potentiodynamic polarization and electrochemical spectroscopy. PNC-5 coating reduces AA-7475 corrosion rate from 23.75 to 0.2253 mpy. In this study, we use polarization resistance, corrosion resistance efficiency, double layer capacitance, corrosion current density, and charge transfer resistance to demonstrate that the SH surface air trapping phenomena are responsible for effective corrosion resistance.

1. Introduction

Except for the few noble metals, all other metals oxidize spontaneously in the atmosphere to reach a stable state, making corrosion an inevitable part of their existence [1]. Atmospheric moisture that makes its way to the surfaces of metallic structures promotes the creation of the necessary ions that ultimately lead to the formation of the metal's most stable oxide [2, 3]. Climate change, thermal fluctuation (day and night), environmental pollutants, and corrosive elements like acidic or alkaline compounds all affect the corrosion process [4]. Still, water molecules play the most important role. An oxide layer formed by the spontaneous reaction of aluminum with oxygen and water in the air to produce aluminum oxide can protect the metal against corrosion even in the presence of water [5]. Despite aluminum's inertness in water, its oxide coating quickly deteriorates upon contact with chloride ions [6, 7]. Corrosion of metals occurs when chloride ions penetrate the

oxide layer and catalyze a chemical reaction that forms aluminum chloride and other chemicals [8]. Pits are formed as aluminum chloride dissolves into the water, creating a void that facilitates further corrosion. Alloys of aluminum were used to improve the mechanical and structural qualities [9, 10]. Shipbuilding, coastal equipment, and saltwater desalination are some of the most common applications for the 6xxx Al alloys [11]. For structural applications in the marine industry, AA-7475 alloys are particularly popular. However, aluminum alloys' corrosion resistance is lower than that of pure aluminum [12]. It is necessary to utilize proper coating procedures due to Al-alloy corrosion. Because of its carcinogenic effect on living creatures and high cost, heavy metal chromium should be avoided [13]. Because of this, scientists are searching for more cost-effective and environmentally friendly coating solutions.

Recent years have seen a surge in interest in creating superhydrophobic (SH) coatings among academics. When droplets of water are deposited on SH surfaces, they form a bead-like structure [14, 15]. This is because SH surfaces exhibit assertive water-repellency behavior. A low surface energy material must be deposited onto a substrate with an appropriate roughness to have the SH property [15]. Low surface energy provides hydrophobicity, amplified to a superhydrophobic type by air trapping-induced roughness. Metal corrosion is improved by incorporating a metallic substrate with an SH nature, which does not interact with corroding ions and moisture [16, 17]. Moreover, the air retained on the SH surface prevents the surface from coming into contact with the corrosive chloride ions found in the aqueous medium [18]. Many scientists have worked to build a water-repellent SH coating that can protect metals from corrosion in the chloride-ion-rich maritime atmosphere.

TiO_2 functionalized methyl hydrogen polysiloxane was used by Gao et al. [19] to create SH surfaces on metal by heating the steel first. Corrosion resistance in mild steel is improved by cutting the coating's i_{corr} value from 120.22 to 0.09 A and raising the contact angle with water from 160.7°. To increase the corrosion resistance of the AZ91D alloy, Yin et al. [20] employed thiol-based compounds in a TiO_2/copper/self-assembly approach. To create an SH surface, Yin et al. [21] used a hydrothermal process to coat a dual layer of ZrO_2/SiO_2 over a zinc-based substrate. Using a chemical etching approach, Sharma et al. [22] created SH CuO microneedles to limit the corrosion of copper in the marine atmosphere. By employing the thermal annealing process, Yang et al. [23] produced a water contact angle (WCA)-153° coating with a tilt angle of 5°. Similar to how numerous methods are used in corrosion-resistant manufacturing materials with SH coating, many different approaches have been developed [24]. The methods presented here, however, are not simple enough to be used for SH coating on massive buildings. In addition, the methods used to design SH environments are highly specialized and can only be applied to certain small-scale structures [25]. A nonwettable feature must be imparted to the substrate due to the need to develop an SH mixture that can be applied to large constructions.

2. Materials and Methods

2.1. Required Materials. We developed an SH combination that uses polymer nanocomposite (PNC) strengthened with nanosized ZrO_2 nanoparticles and CS molecules to inhibit aluminum erosion in seawater. It is possible to alter the number of ZrO_2 nanoparticles incorporated in the PNC using PVC resin, a polymer binder. PVC resins are a water-insoluble material with suitable properties, including Young's modulus, shock absorbance, and chemical resistance for a corrosion-resistant coating. The ZrO_2 nanoparticles concentration supplied to the PVC matrix can be adjusted to improve the dried film's surface roughness. The surface energy of the composite is reduced by adding the reduced surface energy substance CS to the PVC matrix. The superhydrophobicity of the chosen polymer is a result of decreased surface energy and factors enhancing roughness. An AA-7475 aluminum alloy is used as a test specimen to determine the SH mixture's corrosion resistance. Ammonium hydroxide, zinc acetate, and copper sulfate are some ingredients that make up this mixture. By creating a coating resistant to corrosion for AA-7475 aluminum alloy, ZrO_2 nanoparticles (which adds roughness) and CS (which lowers surface energy) are mixed into polyvinyl chloride (PVC) binder. We have AA-7475 plates that are 60 mm long, 10 cm wide, and only half a millimeter thick. The surfaces are cleaned using ultrasonication and air dried to prepare the specimens for superhydrophobic (SH) combination.

2.2. Preparation of ZrO_2 Nanoparticles. Using the same easy precipitation method described in our previous research [26], ZrO_2 nanoparticles can be easily made. Simply 50 mL of distilled water was used to dissolve 0.05 M of sodium hydroxide and 0.01 M of Zn acetate. Drop by drop and rapidly agitated at 27°C, the zinc acetate is added to the sodium hydroxide solution until both solutions are neutralized. Zinc hydroxide begins to nucleate and develop, and white precipitate forms during stirring. After centrifuging, filtering, and rinsing with distilled water three times, the residue was dried in a hot air oven for 5 hr at 120°C. After drying, it is calcined for 1 hr at 700°C to produce ZrO_2 nanoparticles, which are then gathered and stored under a vacuum until needed.

2.3. Preparation of CS. The experimental method for preparing copper stearate (CS) is described in the literature [27]. In two different beakers, you'll dissolve 2.49 g of $CuSO_4$ (0.02 M) and 4.98 g of stearic acid (0.03 M) in 62 mm of water and 42 mm of ethanol, respectively. At 60°C for 30 min, while constantly stirring, they are heated in a water bath to combine the liquids. When NH_4OH was added, the mixture's pH raised to 7. After prolonged stirring, a vivid blue precipitate was obtained; this was then systematically washed and filtered using a mixture of distilled water and ethanol at a 1 : 1 ratio. This residue was stored in an airtight container after air-drying.

2.4. Fabrication of Polymer Nanocomposites. ZrO_2 nanoparticles and CS are bound to create SH material using polyvinyl

Table 1: The PVC matrix contains ZrO_2 nanoparticles and CS compositions.

Polymer nanocomposites	ZrO_2 nanoparticles (g)	CS	PVC (g)	THF (mL)
PNC-1 (Sample-1)	0.30	1	0.30	60
PNC-2 (Sample-2)	0.60	1	0.30	60
PNC-3 (Sample-3)	0.90	1	0.30	60
PNC-4 (Sample-4)	1.20	1	0.30	60
PNC-5 (Sample-5)	1.50	1	0.30	60

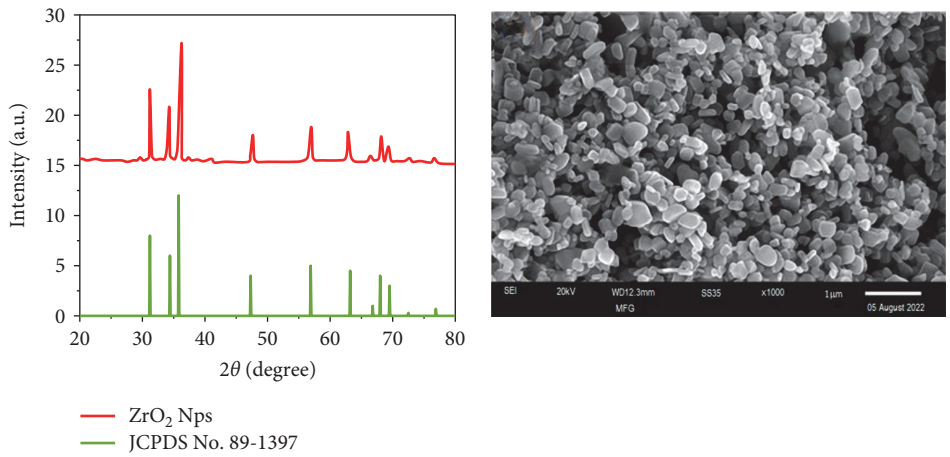

(a) (b)

Figure 1: (a) XRD pattern and (b) FESEM image.

chloride (PVC). THF is first used to dissolve 0.30 g of PVC (0.6 wt%), trailed by adding 1 g of CS (2 wt%), which is agitated while the mixture is stirred. After the mixture is uniform, different amounts of ZrO_2 nanoparticles are added, such as 0.30, 0.60, 0.90, 1.20, and 1.50 g, for weight percentages of 0.6, 1.2, 1.8, 2.4, and 3.0, respectively (Table 1). Sonicating the mixture with a probe-type ultrasonicator produces a homogeneous suspension of ZrO_2 nanoparticles in PVC. Sonication was performed for 30 min, with on-and-off intervals of 30 s each. After sonication, the mixture is degassed in a desiccator at a lower pressure of 0.2 bar for 20 min to reduce the impact on air spaces. After the AA-7475 samples have been ultrasonically cleaned, they are brush coated with the resulting mixture, allowed to air dry for 24 hr, and then kept until further characterization [28, 29].

2.5. Description. This ZrO_2 nanoparticles sample's X-ray diffraction (XRD) pattern was measured using a Siefert XRD with Cu-Kα radiation at a wavelength of $\lambda = 1.5406$ Å and $a = 20°–80°$. The molecular vibrations of PNCs are recorded using an IR spectrometer. Field-emission scanning electron microscopy (FESEM) reveals the ZrO_2 nanoparticles' morphological features. To determine the average roughness of the 3D atomic force microscope (AFM), the XE-70 AFM's topographical line profile analysis is used [30]. After 30 s of immersion in 10 L of water, a goniometer measures the coated surfaces' WCA. Potentiodynamic polarization (PDP) and electrochemical impedance experiments in a 3.5% NaCl solution were used to evaluate the SH coating produced by CH instruments for corrosion resistance.

3. Results and Discussion

It is necessary to increase the surface roughness of PNC by using wet, chemically produced ZrO_2. It depicts the XRD structure of the ZrO_2 nanoparticles produced in the range of 20°–80° in Figure 1(a). There are well-defined crystallization patterns in the $2\theta = 31.7488°$, 34.4094°, 36.2346°, 47.5557°, 56.5974°, 62.8460°, 66.4176°, 67.9315°, 69.0682°, 72.5721°, and 77.0375° peaks in the XRD spectrum. Peaks (100, 002, 101, 102, 110, 103) are good match for JCPDS No. 89-1397 (Figure 1(a)). A tetrahedral hexagonal wurtzite phase of ZrO_2 nanoparticles features Zn^{2+} ringed by four O_2 molecules. For the ZrO_2 nanoparticles were created, Scherer's formula [31] was used to calculate the average crystallite size.

$$D = 0.9\lambda/(\text{FWHM} \times \cos\theta). \quad (1)$$

The FWHM is the whole breadth at half-maximal of the deflected peak, and θ is the XRD angle. ZrO_2 nanoparticles have a crystallite size of 40 nm, according to the formula above. ZrO_2 nanoparticles defects are to blame for the deviation from the conventional values of 3.253 Å, 5.213 Å, and 47.77 3 $Å^3$ for the lattice parameters a to c, and volume of the

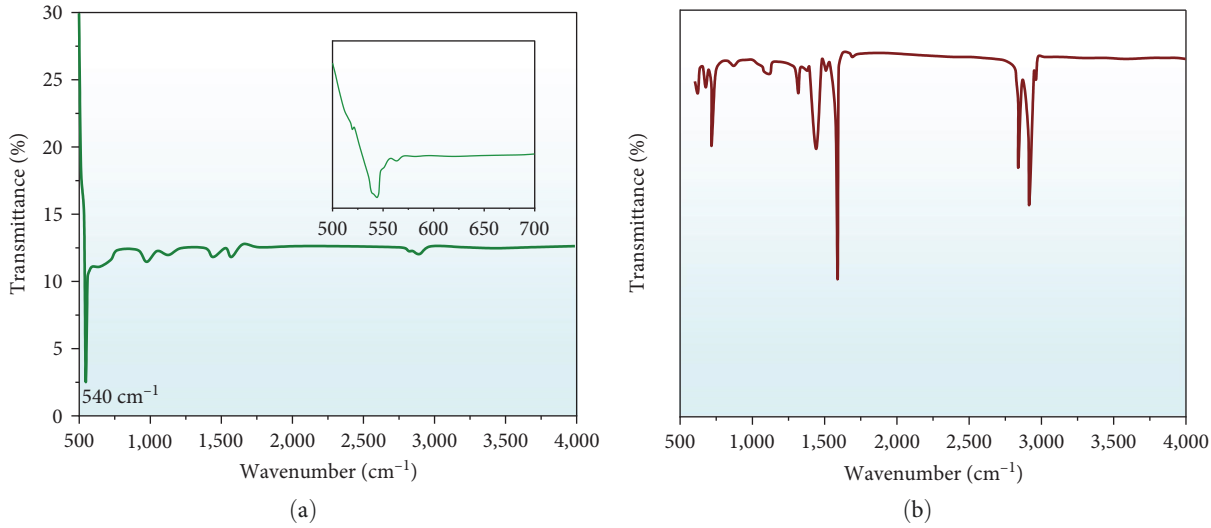

Figure 2: (a) Fourier-transform infrared spectrum of ZrO_2 nanoparticles and (b) CS.

ZrO_2, which are 3.24915 Å, 5.20673 Å, and 47.6031 3 Å^3 correspondingly.

ZrO_2 nanoparticles secondary electron FESEM image as shown in Figure 1(b). The ZrO_2 nanoparticles structures depicted in the figure range in size from 100 to 200 nm and are polydispersed. The ZrO_2 nanoparticles have a highly crystalline character, confirming the results of XRD.

Figure 2(a) shows the Fourier-transform infrared spectra of ZrO_2 nanoparticles produced between 500 and 4,000 cm^{-1}. ZrO_2 vibrational has highest at 540 cm^{-1} in extended-spectrum shown in Figure 2(a). Copper precursor ions easily react with $CH_3(CH_2)16COO^-$ ions in stearic acid during the CS synthesis in the occurrence of ethanol, resulting in Cu $(CH_3(CH_2)16COO)_2$ molecules. An illustrated in Figure 2(b), which depicts the characteristic molecular vibrational patterns of each of its elements. Stearic acid's distinctive stretching frequency (1,512–1,520 cm^{-1}) has vanished from Figure 2(b). The carboxylate group produced by the interaction of stearic acid with the metal precursor resulted in a strong signal at 1,762 cm^{-1}. The aliphatic C–H stretching frequencies of the CS molecule are 2,846 and 2,910 cm^{-1}, respectively. Vibrations in the 1,441 and 717 cm^{-1} range for C–C and C–H show bending and asymmetric stretching.

ZrO_2 nanoparticles of 0.6, 1.2, 1.8, 2.4, and 3.0 are distributed with 2.4 wt% copper stearate and various weight percentages of ZrO_2 nanoparticles (PNC-1 to PNC-5) in THF at a concentration of 0.6 wt%. The spectrum of PNC in the region of 500–4,000 cm^{-1} is shown in Figure 3 (right). The distinctive ZrO_2, CS, and PVC bands were seen in all spectra. The peak of the Zn–O vibrations can be located at 520 cm^{-1}, and its intensity increases as ZrO_2 nanoparticles wt% increases. Spectral peaks in the 500–1,500 cm^{-1} range suggest the presence of PVC. All of the PVC stretching processes are attributed to the peaks at 1,306 cm^{-1} (–CH scissoring of PVC), 1,433, 2,856 cm^{-1}, and CH asymmetric stretching of polyvinyl chloride.

With this research, we hope to create an AA-7475 corrosion-resistant coating with a superhydrophobic characteristic. Roughening components and low surface energy are

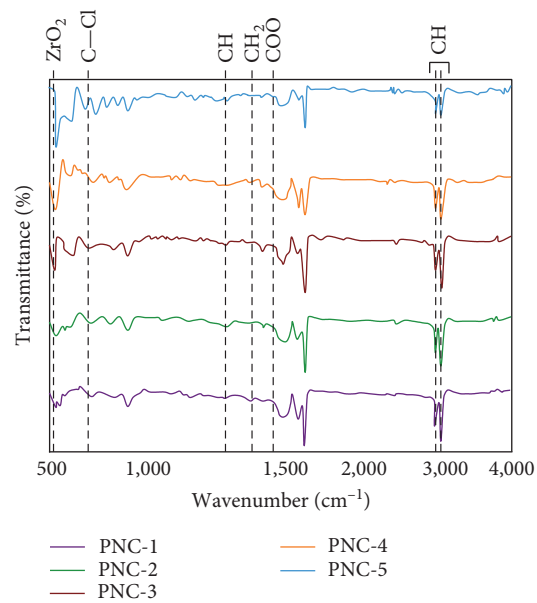

Figure 3: Fourier-transform infrared spectrum of polynanocomposites: (a) Sample-1, (b) Sample-2, (c) Sample-3, (d) Sample-4, and (e) Sample-5.

combined to form a superhydrophobic surface with a WCA of more than 150° PVC binder in THF solvent blended with roughening components. WCA of coating, which is made of ZrO_2 nanoparticles and CS in PVC, has been improved by using this material. The bigger the number of ZrO_2 nanoparticles in the coating, the greater the WCA. Line profile analysis is a valuable technique in the software used to interpret pictures to evaluate the coating surface roughness. Using a WCA, the surface roughness (Ra) of the PNC-1 was determined to be 12.74 nm at an angle WCA of 124°, as indicated in Figure 4(a). ZrO_2 nanoparticles wt% is increased from 0.6 to 1.2, although the WCA only increases by 128° (Figure 4(b)). WCA is not significantly improved because the difference in Ra is just

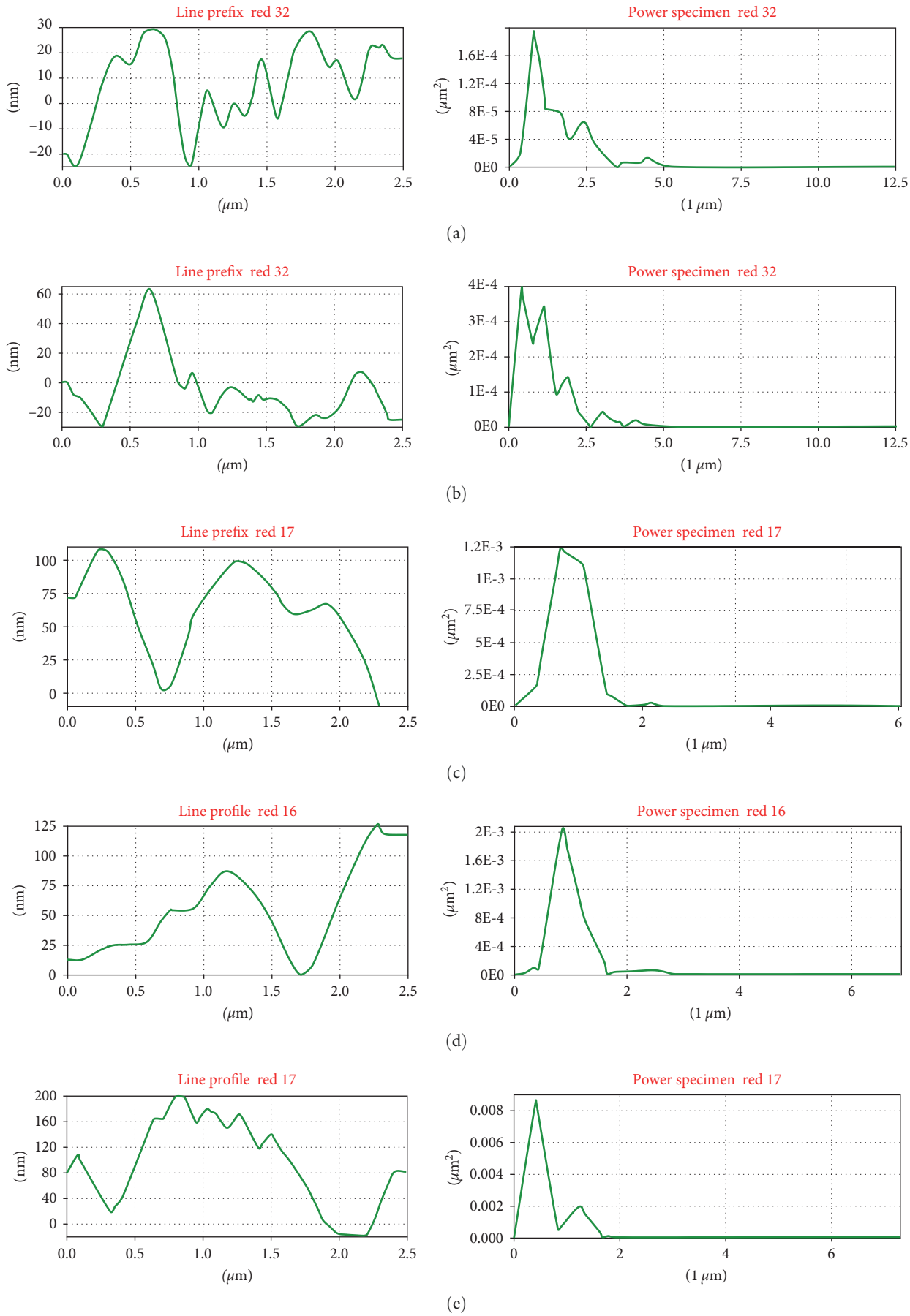

Figure 4: Line profile analysis of polymer nanocomposites: (a) Sample-1, (b) Sample-2, (c) Sample-3, (d) Sample-4, and (e) Sample-5.

Table 2: Mean roughness and WCA of polymer nanocomposites.

Polymer nanocomposites	ZrO_2 nanoparticles (wt%)	Avg. roughness (nm)	WCA (°)
PNC-1 (Sample-1)	0.6	11.82	125
PNC-2 (Sample-2)	1.2	15.36	126
PNC-3 (Sample-3)	1.8	25.81	134
PNC-4 (Sample-4)	2.4	29.96	136
PNC-5 (Sample-5)	3.0	60.52	154

WCA, water contact angle.

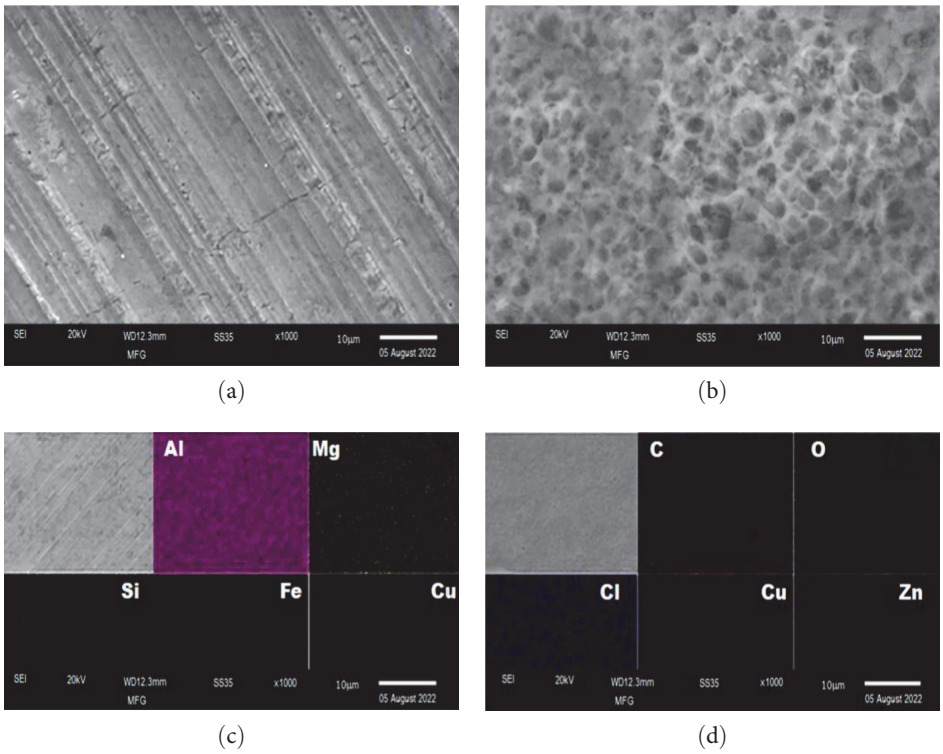

Figure 5: (a, b) SEM and (c, d) EDX mapping images of bare and PNC-5-coated AA-7475.

16.47 nm. With ZrO_2 nanoparticles content rising to 1.8 and 2.4 wt%, the roughness value rises to 26.72 and 30.90 nm in PNC-3 and PNC-4 accordingly (Figures 4(c) and 4(d)). Ra values have increased. However, WCA does not reach superhydrophobic (about 150°) levels despite this. It turns out that the Ra value is double for PNC-4 when 3.0 wt% of ZrO_2 nanoparticles (PNC-5) is added. This PNC-5 coating is classified as SH because of its 154° WCA on such a roughened surface.

These results indicate a strong correlation between roughness and SH activity, forming comparable nanoscale pillars [32]. Due to its hierarchical structure, air molecules are trapped between valleys and peaks of the PNC covering [33]. The Cassie–Baxter model is a good fit for these SH surface phenomena.

$$\cos\theta_{CB} = f_{ls}\ \cos\theta_0 - f_{lv}, \tag{2}$$

where θ_{CB} is the WCA of PNCs, θ_0 is Young's angle of contact, f_{ls} and f_{lv} divides the projected area by the contact region between liquid and solid and liquid and vapor. Surface roughness is a crucial aspect that contributes to creating SH surfaces in the current scenario. As a result, Peng et al. [34] is substituted into the equation,

$$\cos\theta_{CB} = r_f f\ \cos\theta_0 - f - 1, \tag{3}$$

where r_f is the surface roughness, and f is the percentage of a solid surface covered by water. There are varied ZrO_2 nanoparticle concentration percentages in Table 2 for PNC-1 to 5.

PNC-5-coated AA-7475 exhibits a WCA of 154°, indicating that it has a superhydrophobic coating, as may be deduced from Table 2. When it comes to corrosion protection, the PNC coated with AA-7475 alloy serves this purpose.

Images of AA-7475 coated with PNC-5, as shown in Figures 5(c) and 5(b). Figure 5(a) depicts the AA-7475 surface morphology without any holes. Porous structures are formed on the surface of PNC-5 when it is applied. The ZrO_2 nanoparticles induce the coating's roughness, and the porous structure may have been formed due to the coating's presence of CS [31, 35]. The porous structure of the coating's

Table 3: Details of corrosion parameters obtained from potentiodynamic polarization studies.

Sample	Corrosion potential E_{corr} (V)	Pitting corrosion potential E_{pit} (V)	Corrosion current density i_{corr} (A)	Protective efficiency (%)	Corrosion rate v_{corr} (mpy)
Bare AA-7475	−1.260	−0.676	5.536×10^{-5}	–	2.376×10^{1}
PNC-5-coated AA-7475	−0.397		5.362×10^{-7}	99.06	2.252×10^{1}

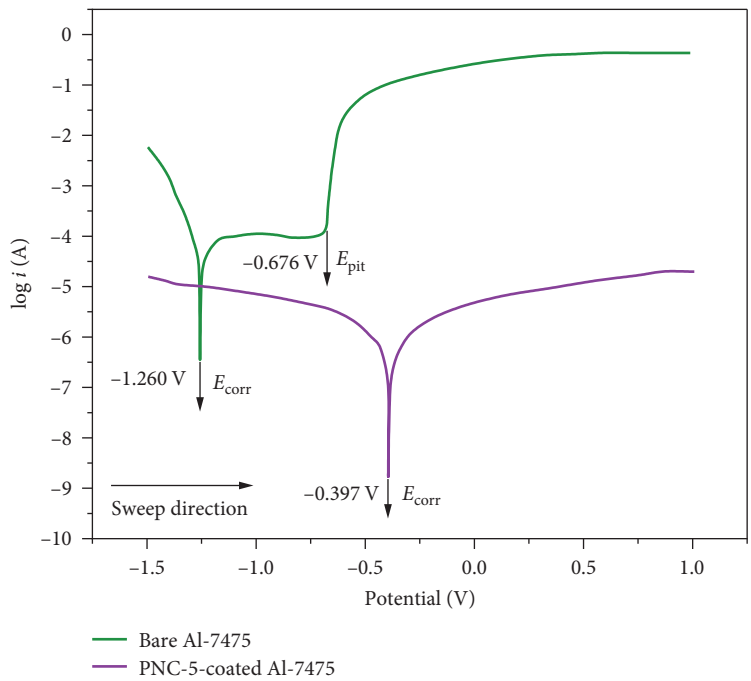

Figure 6: Potentio-dynamic polarization studies of (a) bare and (b) PNC-5-coated AA-7475.

surface may be responsible for the greater WCA. Figures 5(c) and 5(d) show the EDX mapping of the AA-7475 coated with PNC-5 and naked samples. ZrO_2 and CS were found to be present. Elemental maps of AA-7475 show a high concentration (>99%) of Al, although there are also trace amounts of Mg and Si and Fe, and Cu, as well as other elements. The alloying ingredients in AA-7475 are thought to be responsible for the trace element presence [36]. PVC matrix constituents C, O, and Cl can be seen on the surface of AA-7475 coated with PNC-5 (Figure 5(d)). For this reason, trace amounts of zinc, copper, and other metals can be found in the completed product. Since Zn and Cu atoms are uniformly distributed across the PNC-5 surface, this supports the presence of ZrO_2 nanoparticles and CS.

The corrosion resistance of superhydrophobic PNC-5 coated and uncoated Aluminum-7475 specimens are studied using PDP and electrochemical impedance spectroscopy (EIS) investigations. The cathode uses the electrons released by the oxidation reaction on the working electrode's surface to perform the reduction. The following is a list of aluminum corrosion reactions:

$$Al \longrightarrow Al^{3+} + 3e^{-}, \quad (4)$$

$$O_2 + 2H_2O + 4e^{-} \longrightarrow 4OH^{-}, \quad (5)$$

$$Al^{3+} + 3OH^{-} \longrightarrow Al(OH)_3, \quad (6)$$

$$2Al(OH)_3 + \text{in air} \longrightarrow Al_2O_3 \cdot 3H_2O. \quad (7)$$

Anode Al atoms consume the hydroxide ions produced on the cathode, resulting in aluminum hydroxide, which is then transformed into an aluminum oxide coating by the anode. A barrier between hydroxides and our substrates can prevent the formation of oxide layers. A layer of SH material is applied to the AA-7475 to shield the substrate from direct contact with the electrolyte [37]. The resulting specimen is used as a counter and a reference electrode because platinum and Ag/silver chloride are both acceptable electrode materials [38, 39]. All tests are conducted with a marine-like electrolyte solution of 3.5% NaCl. Samples are stabilized in 3.5% sodium chloride for an hour before electrochemical tests are conducted and the open circuit potential is determined.

Aluminum-7475 (ASTM standard) was bare and coated with PNC-5 at a scan rate of 0.1667 mV/s to estimate corrosion potential (E_{corr}), corrosion current density (i_{corr}), polarization resistance (R_p), (i'_{corr}) corrosion current density of AA-7475 and other electrochemical parameters. These samples' corrosion behavior may be estimated and summarized in Table 3 using anodic and cathodic polarization curves, which are shown in Figure 6. PNC-5 was shown to reduce the corrosion resistance of AA-7475 from 5.536×10^{-5} A to

Table 4: Resistance data in the linear polarization direction.

Specimen	Slope at anode b_a	Slope at cathode b_c	Corrosive current density i_{corr} (A)	Polarized resistance R_p ($\Omega\cdot cm^2$)
Bare AA-7575	2.370	11.341	5.538×10^{-5}	14.135×10^3
PNC-5-coated AA-7475	5.031	5.524	5.253×10^{-7}	20.682×10^5

5.253×10^{-7} A, based on the data in Table 3. When aluminum-7475 was stacked on top of PNC-5, the E_{corr} voltage dropped from −1.260 to −0.397 V after coated, with a positive shift of 0.863 V. The superhydrophobic surface produced with PNC-5 effectively shields the metallic surface from corrosion, preventing electrolytes from penetrating toward working electrodes, as seen by the decrease in i_{corr} and increased E_{corr} values. AA-7475 surfaces are protected from erosion by limiting hydroxide generation. To assess the PNC-5 coating's level of protection, apply the following formula to estimate P_i:

$$P_i(\%) = [1 - (i_{corr}/i'corr)] \times 100. \quad (8)$$

Samples coated with PNC-5 had a P_i that is 99.05% corrosion-resistant. Corrosion rates (mpy) of AA-7475 coated and uncoated can be determined using the formula [29].

$$v_{corr} = \frac{i_{corr} K E_w}{\rho A}, \quad (9)$$

where E_w is the metal's equivalent weight to be tested for corrosion rate, K is a constant that measures 1.288×10^{-5}, ρ is a representation of metal density, and A, which metal surfaces in a PDP sample were immersed in the conductive electrolyte during the test. AA-7475 corrosion rate is 23.75 mpy, but PNC-5-layered AA-7475 is 0.2253 mpy, which is 100 times less corrosion-resistant.

In this case, the pitting corrosion is responsible for the appearance of the hump at −0.675 V, which can be seen in a typical PDP pattern on bare Al. The damaged aluminum reacts with the electrolyte at higher anodic ranges, forming aluminum salts and a pit in the specimen. "Pitting potential" refers to that point in developing a pit where further development is possible (Epit). During exposure to high Cl concentrations, localized corrosion creates microscopic holes in the aluminum surface, leading to pitting [40]. A small region acts as an anode for the heavy corrosion that produces small pits, influencing pitting corrosion. The start, metastable development, and stable, autocatalytic growth stages of pit formation are described by Chang et al. [41]. To avoid pitting, an appropriate coating must be applied to the areas that are susceptible to pitting, according to their findings. The breakdown of aluminum in a chloride-rich atmosphere causes pitting corrosion.

$$Al = Al^{3+} + 3e^-, \quad (10)$$

$$Al^{3+} + 4Cl^- = AlCl_4^-. \quad (11)$$

Figure 5 demonstrates that the naked AA-7475 is pitting corroded at a potential of −0.676 V. However, the sample does not reveal any peak matching to Epit when coated with superhydrophobic material, i.e., PNC-5. When an AA-7475 surface is coated with a PNC-5 electrolyte solution and cannot migrate into the interior, anodic and cathodic islands are prevented from forming. 3.5% NaCl solution did not produce pits when PNC-5 was applied as the protective coating.

For the bare and coated AA-7475, the polarization resistance (R_p) was calculated using an equation based on Stern–Geary [42].

$$R_p = \frac{B}{i_{corr}}, \quad (12)$$

$$B = \frac{b_a b_c}{2.3(b_a + b_c)}, \quad (13)$$

where b_a and b_c slopes of the anodic and cathodic conductors. Table 4 contains the values of R_p and various other factors. The results reveal that coating PNC-5 over AA-7475 enhances b_a while decreasing b_c, demonstrating that corrosion slowed in the coated specimens. As a result, the coated sample has a higher R_p ($21.682 \times 10^3\,\Omega\cdot cm^2$) than the bare AA-7475 ($15.135 \times 103\,\Omega\cdot cm^2$). It has been determined that the SH coating on the PNC-5 provides adequate corrosion protection in a maritime environment based on PDP data.

EIS analysis can determine electron transfer mechanisms between the working electrolyte and the electrode. Recordings of PNC-5 coated aluminum-7475 in 3.5% sodium chloride solutions were plotted in Figure 7 from 0.01 to 100,000 Hz. The R_{ct} of the specimens is measured using a capacitive loop at high frequencies. As demonstrated in Table 5, the coated specimen has an R_{ct} value of $2.598\,\Omega\cdot cm^{-2}$, which is significantly greater than the untreated sample R_{ct} value of $51.29\,\Omega\cdot cm^{-2}$.

As displayed in Figure 7(c), bode charts of magnitude and phase angle can be seen in both naked and PNC-5-coated samples. The PNC-5-coated sample demonstrated a higher impedance than the bare AA-7475 in all frequency bands. For bare AA-7475, plotting the phase angle shows only one-time constant of roughly ∼50 Hz, owing to the oxide coating produced on the Al surface. The maximum frequency (∼1,000,000 Hz) can increase by increasing the time constant of PNC-5-coated AA-7475. The AA-7475 surface has been protected from corrosion by the PNC-5 coating, which has altered the time constant significantly. For evaluating electrochemical parameters through curve fitting, we can use the EEC model for the Nyquist plot (Figure 7(d)). Table 5 shows the calculated values for the circuit parameters, which indicate solution resistance, resistance to charge transfer two-layer capacitance, and the Warburg factor. While AA-7475 with no PNC-5 coating has an R_s of just $2.974\,\Omega$, the PNC-5-coated AA-7475 has an R_s of $7.187\,\Omega$

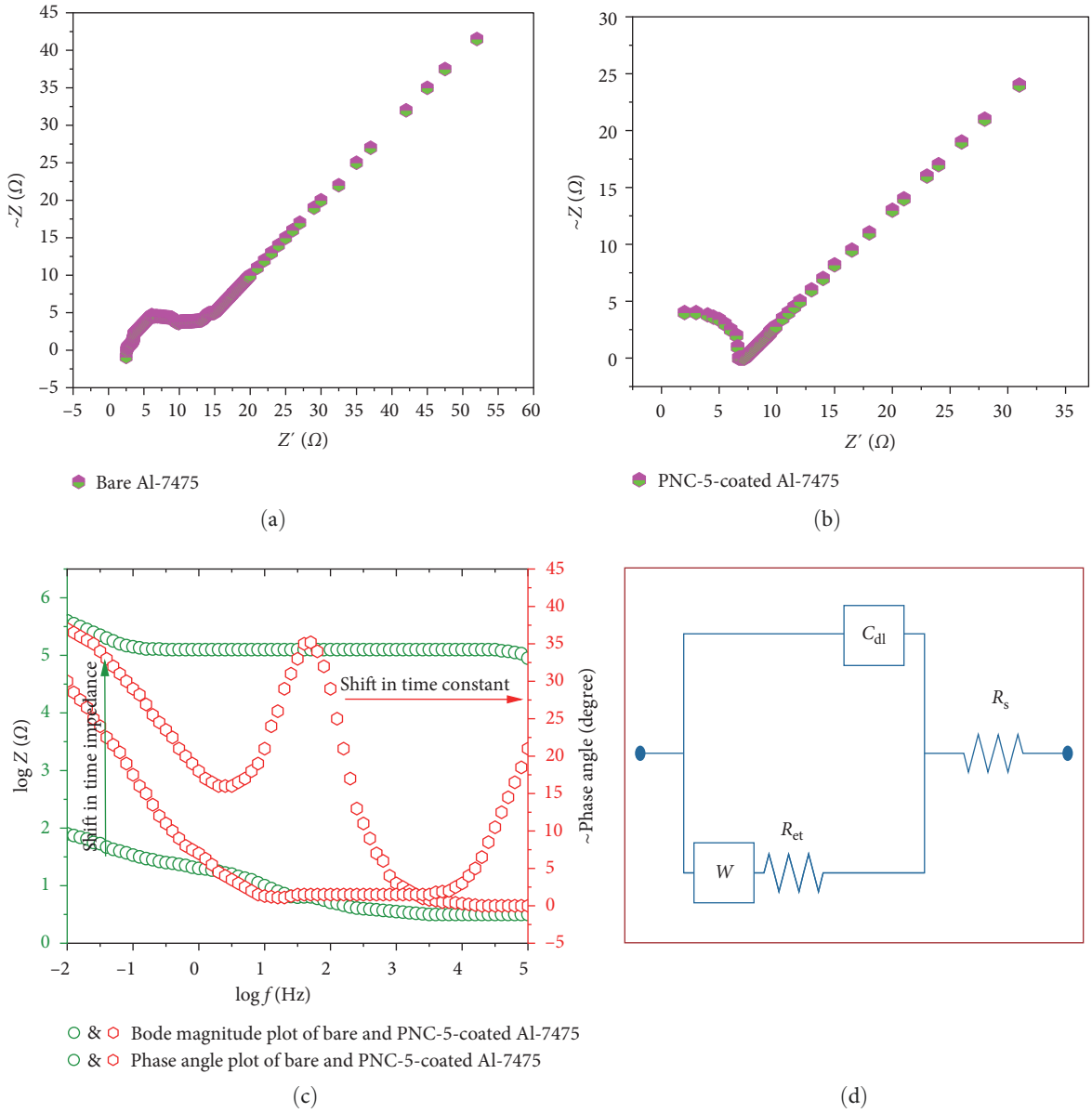

Figure 7: (a) Nyquist plot for bare AA-7475, (b) polymer nanocomposites-5 coating with AA-7475 (c) magnitude plot and phase angle (d) equivalent circuit.

Table 5: Equivalent circuit data.

Specimen	R_s (Ω)	R_{et} ($\Omega\cdot cm^2$)	C_{dl} ($F\cdot cm^2$)	W
Bare AA-7475	2.974	51.79	7.05×10^{-4}	6.290×10^{-2}
PNC-5-coated AA-7475	7.187×10^{4}	2.598×10^{5}	3.932×10^{-11}	1.748×10^{-5}

by the same order of magnitude. An increase in R_s has been attributed to an air-trapping phenomenon that successfully repels the electrolyte from PNC-5-coated samples because of their SH composition. This indicates that the PNC-5-coated AA-7475 is an excellent conductor of electricity between metallic surfaces and electrolytes because it has the highest C_{dl}, compared to bare aluminum [43]. It also shows that the creation of compound W successfully limits the flow of electrons in an electrochemical circuit. According to these data, corrosion of AA-7475 is prevented by PNC-5's SH surface.

Figure 8(a)–8(d) shows before and after PDP measures on AA-7475 coated with PNC-5 and bare AA-7475 using scanning electron microscopy (SEM). According to the SEM picture in Figure 8(a), the AA-7475 surface is completely noncorrosive

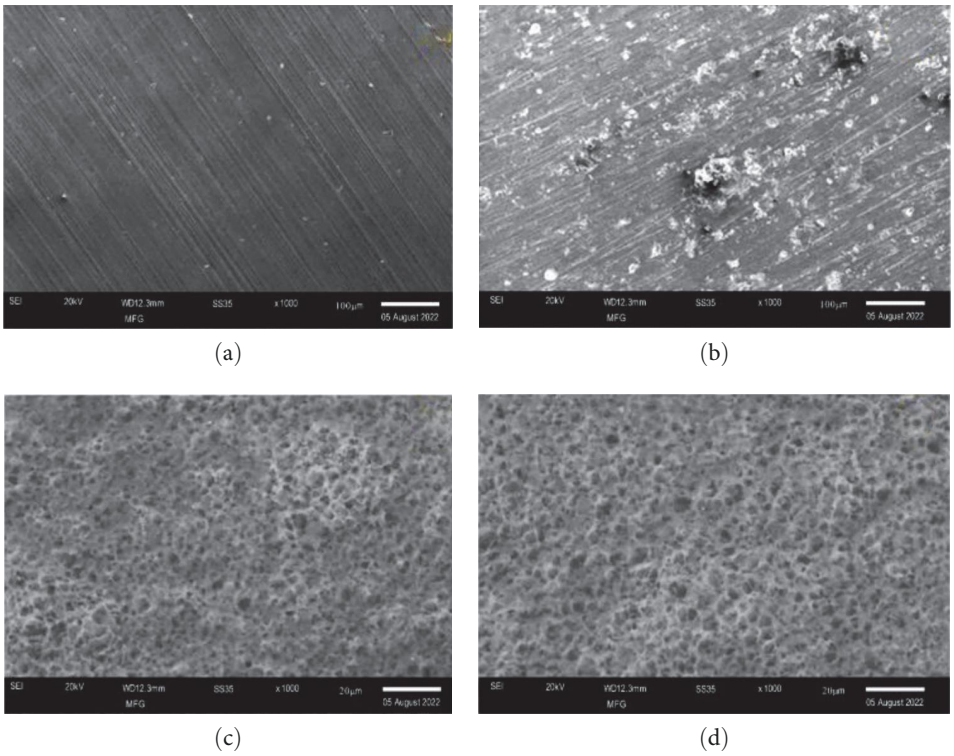

Figure 8: SEM image of bare and PNC-5-coated AA-7475 before (a, c) and after (b, d) potentiodynamic polarization studies.

(Figure 8(a)). However, after PDP examinations, the surface is eroded, with pits forming on all of its surfaces, confirming the conclusions of the PDP graph. No cracks or delaminations were found on the AA-7475 coated with PNC-5 compared to AA-7475 untreated as a control. An unbroken and undamaged PNC-5 shows that the underlying AA-7475 (Figures 8(a) and 8(d)) has been completely protected.

An X-cut tape testing, performed by ASTM D 3359-96.4 cm X-cut on a layer of the angle at 30°, is used to determine the observance of the PNC-5 coating. The X-cut region is covered with adhesive tape and left for 60 s. During the 60 s, an adhesive tape is applied and left in place on the X-cut area. During the first 60 s of peeling, the peeling angle should be close to 180°. The coating is classified as 5 A denotes the absence of peeling, and 0 A denotes the removal of coating from the substrate. Using a screw gauge, the coating thickness is determined to be 160 μm.

4. Conclusion

(i) To create a superhydrophobic polymer, nanocomposite PVC, copper stearate, and ZrO_2 are mixed in the right proportions. Changing the weight percentage of ZrO_2 nanoparticles to 0.6, 1.2, 1.8, 2.4, and 3.0 wt% allows researchers to investigate the impact of average roughness on SH behavior.

(ii) According to the WCA data, the PNC (PNC-5) included in the 3.0 wt% ZrO_2 nanoparticles exhibits SH character. The average roughness of the coating has been found to significantly impact the SH surface from the line profile analysis of the AFM picture. After brush coating, an AA-7475 substrate with the SH PNC-5 combination, electrochemical workstations assess corrosion resistance in a 3.5% NaCl.

(iii) As a result of these findings, the PNC-5-coated A1-7475 has a higher $E_{corr} = 0.397$ V, the lowest $i_{corr} = 5.513 \times 10^{-7}$ A, the smallest V_{corr} is 0.2254 mpy, and a higher $R_p = 21.682 \times 10^5\ \Omega\cdot cm^2$ than bare AA-7475 ($E_{corr} = -1.260$ V, $i_{corr} = 5.513 \times 10^{-5}$ A, $v_{corr} = 23.76$ mpy, and $R_p = 21.682 \times 10^5\ \Omega\cdot cm^2$. Because of the nanocomposite's SH property, pitting corrosion in PNC-5 high corrosion-resistant performance on AA-7475 alloy is greatly reduced.

Data Availability

The data used to support the findings of this study are included within the article.

Conflicts of Interest

The authors declare that they have no conflicts of interest.

References

[1] X. Cao, X. Sun, S. Xiao, G. Cai, X. Zhang, and Z. Dong, "Preparation and anti-wearing and anticorrosion properties of 3D superhydrophobic coating based on poly-benzoxazine," *Acta Materiae Compositae Sinica*, vol. 39, no. 2, pp. 617–627, 2022.

[2] A. S. Sarkın, N. Ekren, and Ş. Sağlam, "A review of anti-reflection and self-cleaning coatings on photovoltaic panels," *Solar Energy*, vol. 199, pp. 63–73, 2020.

[3] J. Kujawa, "From nanoscale modification to separation—the role of substrate and modifiers in the transport properties of ceramic membranes in membrane distillation," *Journal of Membrane Science*, vol. 580, pp. 296–306, 2019.

[4] X. Yu, L. An, J. Yang, S.-T. Tu, and J. Yan, "CO_2 capture using a superhydrophobic ceramic membrane contactor," *Journal of Membrane Science*, vol. 496, pp. 1–12, 2015.

[5] M. Tuominen, H. Teisala, J. Haapanen et al., "Adjustable wetting of liquid flame spray (LFS) TiO_2-nanoparticle coated board: batch-type versus roll-to-roll stimulation methods," *Nordic Pulp & Paper Research Journal*, vol. 29, no. 2, pp. 271–279, 2014.

[6] E. Nyankson, H. Agbe, G. K. S. Takyi, Y. D. Bensah, and D. K. Sarkar, "Recent advances in nanostructured superhydrophobic surfaces: fabrication and long-term durability challenges," *Current Opinion in Chemical Engineering*, vol. 36, Article ID 100790, 2022.

[7] A. Jagtap, P. G. Wagle, E. Jagtiani, and A. P. More, "Layered double hydroxides (LDHs) for coating applications," *Journal of Coatings Technology and Research*, vol. 19, pp. 1009–1032, 2022.

[8] Y. Cheng, X. Zuo, X. Yuan et al., "Preparation of fluorine silicon copolymer superhydrophobic anticorrosive coating on copper aluminium composite by one step spraying," *Materials Letters*, vol. 304, Article ID 130496, 2021.

[9] H. Zheng, Z. Li, L. Liu, F. Meng, Y. Cui, and F. Wang, "Superhydrophobic composite coatings in bacterial culture media: durable antibacterial activity and enhanced corrosion resistance," *Composites Communications*, vol. 27, Article ID 100857, 2021.

[10] W. Wang, "Preparation of new polymer nanocomposites and analysis of their superhydrophobic properties," *IOP Conference Series: Earth and Environmental Science*, vol. 714, Article ID 032072, 2021.

[11] M. S. Selim, S. A. El-Safty, M. A. Abbas, and M. A. Shenashen, "Facile design of graphene oxide-ZnO nanorod-based ternary nanocomposite as a superhydrophobic and corrosion-barrier coating," *Colloids and Surfaces A: Physicochemical and Engineering Aspects*, vol. 611, Article ID 125793, 2021.

[12] T. Ning, W. Xu, and S. Lu, "Fabrication of superhydrophobic surfaces on zinc substrates and their application as effective corrosion barriers," *Applied Surface Science*, vol. 258, no. 4, pp. 1359–1365, 2011.

[13] C. H. Lee, J. Drelich, and Y. K. Yap, "Superhydrophobicity of boron nitride nanotubes grown on silicon substrates," *Langmuir*, vol. 25, no. 9, pp. 4853–4860, 2009.

[14] R. B. Jeen Robert, G. S. Hikku, K. Jeyasubramanian, J. Jacobjose, and R. Malkiya Rasalin Prince, "ZnO nanoparticles impregnated polymer composite as superhydrophobic anticorrosive coating for Aluminium-6061 alloy," *Materials Research Express*, vol. 6, no. 7, Article ID 075705, 2019.

[15] A. Barhoum, J. Jeevanandam, and M. K. Danquah, *Fundamentals of Bionanomaterials*, Elsevier, 2022.

[16] C. C. Ong, R. Jose, and M. S. M. Saheed, "Atomic defects of graphene-carbon nanotubes impact on surface wettability," *Applied Surface Science*, vol. 567, Article ID 150803, 2021.

[17] S. G. V. Kumar, P. Prabhakar, R. K. Sen, N. Uppal, M. A. Khan, and A. K. Srivastava, "Development of superhydrophobic cotton fabric using zinc oxide nanoflower/polydimethylsiloxane (PDMS) nanocomposite coatings," *Textile & Leather Review*, vol. 4, no. 4, pp. 253–266, 2021.

[18] S. Ghosh, B. Nitin, S. Remanan et al., "A multifunctional smart textile derived from merino wool/nylon polymer nanocomposites as next generation microwave absorber and soft touch sensor," *ACS Applied Materials & Interfaces*, vol. 12, no. 15, pp. 17988–18001, 2020.

[19] F. Gao, J. Mu, Z. Bi, S. Wang, and Z. Li, "Recent advances of polyaniline composites in anticorrosive coatings: a review," *Progress in Organic Coatings*, vol. 151, Article ID 106071, 2021.

[20] B. Yin, T. Xu, D. Hou et al., "Superhydrophobic anticorrosive coating for concrete through in-situ bionic induction and gradient mineralization," *Construction and Building Materials*, vol. 257, Article ID 119510, 2020.

[21] X. Yin, P. Mu, Q. Wang, and J. Li, "Superhydrophobic ZIF-8-based dual-layer coating for enhanced corrosion protection of Mg alloy," *ACS Applied Materials & Interfaces*, vol. 12, no. 31, pp. 35453–35463, 2020.

[22] V. Sharma, V. Sharma, M. S. Goyat et al., "Recent progress in nano-oxides and CNTs based corrosion resistant superhydrophobic coatings: a critical review," *Progress in Organic Coatings*, vol. 140, Article ID 105512, 2020.

[23] Z. Yang, X. Liu, and Y. Tian, "A contrastive investigation on anticorrosive performance of laser-induced super-hydrophobic and oil-infused slippery coatings," *Progress in Organic Coatings*, vol. 138, Article ID 105313, 2020.

[24] S. Ibrahim and M. Sultan, "Superhydrophobic coating polymer/silica nanocomposites: part I synthesis and characterization as eco-friendly coating," *Silicon*, vol. 12, pp. 805–811, 2020.

[25] Y. K. Hefni, "Hydrophobic zinc oxide nanocomposites for consolidation and protection of quartzite sculptures: a case study," *Journal of Nano Research*, vol. 63, pp. 64–75, 2020.

[26] C. Anitha, S. Syed Azim, S. Arunkumar, and S. Mayavan, "One pot fabrication of superhydrophobic anticorrosive coating without fluoro compounds and inhibitive pigments," *Progress in Organic Coatings*, vol. 125, pp. 137–145, 2018.

[27] R. Ramachandran and M. Nosonovsky, "Coupling of surface energy with electric potential makes superhydrophobic surfaces corrosion-resistant," *Physical Chemistry Chemical Physics*, vol. 17, no. 38, pp. 24988–24997, 2015.

[28] W. F. Huang, Y. L. Xiao, Z. J. Huang et al., "Super-hydrophobic polyaniline-TiO_2 hierarchical nanocomposite as anticorrosion coating," *Materials Letters*, vol. 258, Article ID 126822, 2020.

[29] E. Cho, S. H. Kim, M. Kim, J.-S. Park, and S.-J. Lee, "Superhydrophobic and antimicrobial properties of Ag-PPFC nanocomposite thin films fabricated using a ternary carbon nanotube-Ag-PTFE composite sputtering target," *Surface and Coatings Technology*, vol. 370, pp. 18–23, 2019.

[30] I. Sulym, A. Kubiak, K. Jankowska et al., "Superhydrophobic MWCNTs/PDMS-nanocomposite materials: Preparation and characterization," *Physicochemical Problems of Mineral Processing*, vol. 55, no. 6, pp. 1394–1400, 2019.

[31] K.-C. Chang and J.-M. Yeh, "Electroactive polymer-based anticorrosive coatings," in *Intelligent Coatings for Corrosion Control*, pp. 557–583, Butterworth-Heinemann, 2015.

[32] M. Akhavan, I. Hejazi, J. Seyfi et al., "Investigating the effect of surface composition and morphology on oil/water separation efficiency of sponges coated with polymer nanocomposites," *Polymer Composites*, vol. 40, no. S1, pp. e431–e439, 2019.

[33] T. Zhai, Q. Zheng, Z. Cai, L.-S. Turng, H. Xia, and S. Gong, "Poly (vinyl alcohol)/cellulose nanofibril hybrid aerogels with an aligned microtubular porous structure and their composites with

polydimethylsiloxane," *ACS Applied Materials & Interfaces*, vol. 7, no. 13, pp. 7436–7444, 2015.

[34] C.-W. Peng, K.-C. Chang, C.-J. Weng et al., "UV-curable nanocasting technique to prepare bio-mimetic superhydrophobic non-fluorinated polymeric surfaces for advanced anticorrosive coatings," *Polymer Chemistry*, vol. 4, no. 4, pp. 926–932, 2013.

[35] H. Chang, K. Tu, X. Wang, and J. Liu, "Facile preparation of stable superhydrophobic coatings on wood surfaces using silica-polymer nanocomposites," *BioResources*, vol. 10, no. 2, pp. 2585–2596, 2015.

[36] I. S. Bayer, "Smart polymer nanocomposite water and oil repellent coatings for aluminum," in *Handbook of Smart Coatings for Materials Protection*, pp. 510–529, Woodhead Publishing, 2014.

[37] S. Nagappan, S. S. Park, and C.-S. Ha, "Recent advances in superhydrophobic nanomaterials and nanoscale systems," *Journal of Nanoscience and Nanotechnology*, vol. 14, no. 2, pp. 1441–1462, 2014.

[38] C. P. Wong, "Recent advances on nanomaterials for advanced packaging applications," in *2012 7th IEEE International Conference on Nano/Micro Engineered and Molecular Systems (NEMS)*, p. 1, IEEE, 2012.

[39] A. Milionis, D. Fragouli, I. Bayer, G. C. Anyfantis, R. Cingolani, and A. Athanassiou, "Magnetically induced drop movement on nano rough micropatterned nanocomposites," in *Technical Proceedings of the 2011 NSTI Nanotechnology Conference and Expo*, vol. 1, pp. 592–595, NSTI-Nanotech, 2011.

[40] Y. Li, R. Zhang, L. Zhu et al., "Nano materials and composites for electronic and photo packaging," in *2009 9th IEEE Conference on Nanotechnology*, pp. 1–3, IEEE NANO, 2009.

[41] C.-H. Chang, M.-H. Hsu, C.-J. Weng et al., "3D-bioprinting approach to fabricate superhydrophobic epoxy/organophilic clay as an advanced anticorrosive coating with the synergistic effect of superhydrophobicity and gas barrier properties," *Journal of Materials Chemistry A*, vol. 1, no. 44, pp. 13869–13877, 2013.

[42] C.-J. Weng, C.-W. Peng, C.-H. Chang, Y.-H. Chang, and J.-M. Yeh, "Corrosion resistance conferred by superhydrophobic fluorinated polyacrylate–silica composite coatings on cold-rolled steel," *Journal of Applied Polymer Science*, vol. 126, no. S2, pp. e48–e55, 2012.

[43] Y. Li, Y. Sun, L. Zhu et al., "Nanocomposite for advanced packaging of microelectronics," in *2006 International Conference on Electronic Materials and Packaging*, pp. 1–16, IEEE, 2006.

Hindawi
Journal of Nanomaterials
Volume 2023, Article ID 7267093, 11 pages
https://doi.org/10.1155/2023/7267093

Research Article

Investigation of Mechanical Behavior and Surface Characteristics of Cold Spray Metallized B_4C/AA7075 Composites Coated by AZ64 Alloy through Plasma Electrolytic Oxidation

Selvakumaran Thunaipragasam,[1] Aniket Bhanudas Kolekar,[2] Koli Gajanan Chandrashekhar,[3] Rohit Pandey,[4] Mohammad Shahid,[5] K. Rajesh,[6] P. Ragupathi,[7] Asheesh Kumar,[8] and Balkeshwar Singh[9]

[1]*Department of Aerospace Engineering, SRM Institute of Science and Technology, Kattankulathur 603203, Chennai, India*
[2]*Department of Mechanical Engineering, Dr. D Y Patil Institute of Engineering Management and Research, Pune 411044, India*
[3]*Department of Mechanical Engineering, Sanjeevan Engineering and Technology Institute, Kolhapur 416201, India*
[4]*Department of Mechanical Engineering, Amity University Madhya Pradesh, Maharajpura Dang, Gwalior 474005, Madhya Pradesh, India*
[5]*Department of Electrical Engineering, Galgotias College of Engineering and Technology, Greater Noida, Uttar Pradesh, India*
[6]*Department of Physics, Academy of Maritime Education and Training (Deemed to be University), 135, East Coast Road, Kanathur 603112, India*
[7]*Department of Mechanical Engineering, Karpagam Academy of Higher Education (Deemed to be University), Pollachi Main Road, Eachanari, Coimbatore 641021, India*
[8]*Department of Mechanical Engineering, Mahatma Gandhi Institute of Technology, Hyderabad, India*
[9]*Department of Mechanical Design and Manufacturing Engineering, Adama Science and Technology University, Kebele-14, Adama 1888, Ethiopia*

Correspondence should be addressed to Balkeshwar Singh; balkeshwar.singh@astu.edu.et

Received 17 August 2022; Accepted 20 September 2022; Published 20 April 2023

Academic Editor: Ramesh Balasubramanian

Metallized cold-spray coatings were employed to make B_4C/AA7075 and aluminum + plasma electrolytic oxidation (PEO) duplex coatings on AZ64. In addition, the phase structure, mechanical characteristics, wear, and PEO ceramic coatings examine the corrosion resistance. According to the findings, the PEO ceramic coating comprises α-aluminum oxide and γ-aluminum oxide, with some remnants of B_4C still being preserved. PEO ceramic coatings outperformed their corresponding CS counterparts regarding mechanical characteristics and wear resistance. For example, the PEO-B_4C coating achieved a hardness of 13.8 GPa and an elastic modulus of 185.5 GPa, which were 21.0% and 23.5%, respectively, more significant than the comparable values for the coating with CS. The PEO-B_4C coating was 58% and 15.7% less abrasive than the equivalent CS coating due to its lower wear rate of 4.84×10^{-5} mm^3/Nm and relatively lower of 0.64. The density of corrosion current in the PEO-treated B_4C-AA7075 coating (3.735×10^6 A/cm^2) is similar to the corrosion current density in the untreated CS coatings. Finally, compared to untreated CS B_4C-AA7075, the coating's mechanical characteristics and wear resistance are considerably enhanced by the PEO treatment.

1. Introduction

Roughening components and low surface energy are combined to form an SH surface with a water contact angle (WCA) of more than 150° when PVC binder in THF solvent is mixed with roughening components (referred to as "superhydrophobic") [1]. Since AZ91 alloys are not very hard, corrosion resistant, and wear resistant, they are used in high-stress technical applications [2, 3]. Material characteristics improve by employing a wide variety of surface engineering techniques. It is called CS, and it is a new way to alter textures [4–6]. While still in solid, CS particles

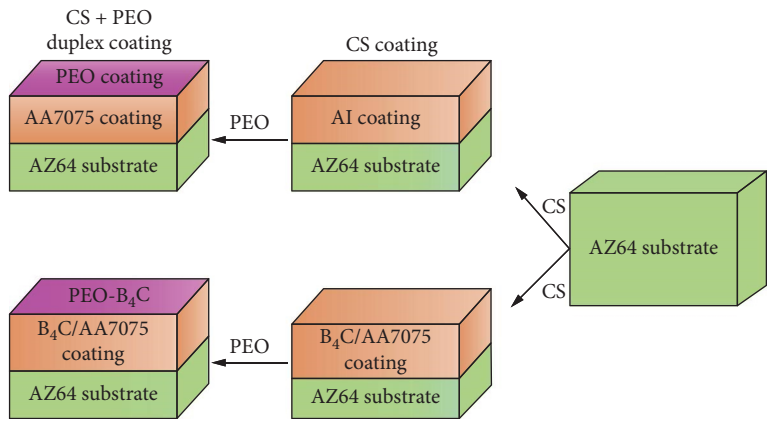

Figure 1: Al + PEO and B_4C-AA7075 + PEO duplex coating preparation schemes.

deposit on the substrate with significant kinetic energy. This technique is better than conventional thermal spray methods due to its comparatively "cool" working gas temperature [7]. Therefore, high-temperature exposures such as those seen in ovens and microwaves can be avoided, along with the resulting oxidation, melting, phase changes, etc. [8]. Many alloys analyze with CS deposits for surface protection, including Al, Al_2O_3-Al, ND-Al, and B_4C-AA7075 [9]. The CS coating's resistance to wear and corrosion is not up to par with the rigorous requirements of the many applications and environmental circumstances [10].

The plasma electrolytic oxidation (PEO) deposition method results in a ceramic sheathing that dramatically increases the wear and hardness of softer and more malleable metals, including aluminum, magnesium, Ti, and their alloys [11]. The Al_2O_3 oxide converting layer produced by the PEO method significantly enhances the resistance to wear and corrosion of aluminum and related alloys, as demonstrated by many studies [12–14]. As a result of these findings, a hybrid CS + PEO dual coating technique is to develop a hard metallurgically supporting ceramics surface. PEO technology turns the metallic coating into a ceramic coating after it applies to the substrate with CS [15]. Using a CS and PEO method, coated AZ31 alloy with an aluminum-based PEO layer [16]. The aluminum-based PEO coating improved wear resistance by 87% compared to an Al coating and had corrosion resistance on par with pure aluminum [17–19]. Analyses were performed on the two CS + PEO dual coatings to determine their microstructure, mechanical characteristics, phase composition, wear, corrosion, and abrasion resistance [20, 21]. Duplex coating, generally protected by magnesium and its coatings, particularly Al_2O_3, showed superior resistance to wear and corrosion (an improvement of 61% on the order of magnitude for each property). A duplex coating provides hybrid, unique, and efficient surface protection for alloys used in demanding situations by fusing the CS and PEO processes [22]. However, there is a lack of literature on this hybrid process. The CS B_4C-AA7075 and aluminum coatings applied on AZ64 were employed as seed surfaces and subjected to PEO treatment to create the corresponding duplex coatings [23–25]. Microstructure, mechanical characteristics, and phase composition of two CS + PEO duplex coatings were analyzed, as their resistance to wear, corrosion, and abrasion [26, 27]. The two duplex coatings outperform conventional CS coatings in protecting AZ64 alloy substrates. It must be noted that the first and only paper to describe the use of PEO treatment to produce an additional layer of protection on top of an existing CSP coating (CS B_4C-AA7075).

In this research, metallized cold-spray coatings were used to produce the composite structures of boron carbide with AA7075 and PEO with aluminum coatings on the AZ64 magnesium alloy. The mechanical behavior, phase structure, and wear and PEO ceramic coatings were used to examine the corrosive resistance.

2. Experimental Procedure

Pure Al powder (D50 = 34 μm) and B_4C-AA7075 composite (D50 = 37 μm) as CS's powder raw materials. As a percentage of the total mass, B_4C made up 1% of the composite powder, and its average particle size ranged from 10 to 50 nm. The SST-P CGDS system applies coatings of CS. The spray angle, pressure, and temperature were set to 90° at 1.7 MPa and 350°C, using nitrogen as the gas phase. Methods for preparing CS coatings (such as Al coating and B_4C-AA7075 coating) are explained in greater depth elsewhere. PEO coating refers to a coating made from PEO-treated Al, and PEO-B_4C coating refers to a coating made from PEO and B_4C on AA7075 (the substrate/seed material). A 15 kW pulse power source was used to run the PEO machinery. For 10 min, the samples were subjected to a PEO treatment with a continuous 0.6 A/0.3 A positive/negative current [28].

The wavelength of the yield was 2,000 Hz, and the duty ratio was 8 g of $NaAlO_2$ per liter of potassium hydroxide, 2 g of sodium ethylenediaminetetraacetic acid per liter, and 2 g of sodium ($Na_3C_6H_5O_{7.2}$) in water in the electrolyte. Figure 1 shows how Al + PEO and B_4C-AA7075 + PEO duplex coatings are created. Using a Miniflex 600 XRD with copper-Kα radiation ($\lambda = 1.5420$) at 41 kV and 16 mA, it also determined the phase compositions of the materials.

The coating's hardness and elasticity evaluate by a battery of nanomechanical properties (UNHT + MCT + MST). A Berkovich diamond indenter applies a force that gradually increases to 10 mN in 30 s during the nanoindentation test. Then, the burden slowly carried down to zero. The corrosion

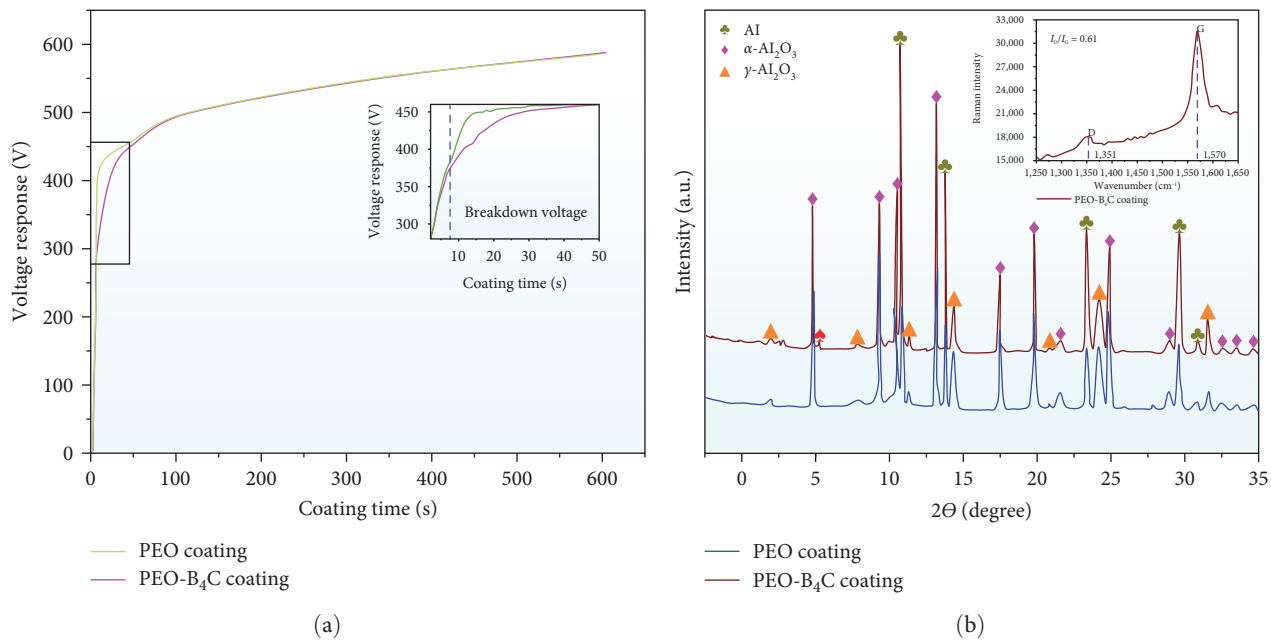

Figure 2: (a) Time–voltage response and (b) XRD pattern.

process testing (ASTM G59-97) was performed at room temperature in a 3.6 wt% NaCl utilizing the CHI600C electrochemical workstation. The sample is the working electrode in a constant potential setup that includes a platinum reference plate and an additional platinum plate. After 30 min in the solution, the open circuit voltage potential was steady enough to conclude the sample. During the polarization scan, the input potential was scanned from −600 to +1,600 mV OCP at a rate of 1 mV/s. Two duplexes' coatings focus on the slide-wearing test (ASTM G99-17) utilizing a test for wear and friction using a ball-disk HT-1000 device at room temperature [29]. The counterbody was a 6 mm Al_2O_3 ball. Test conditions included a load of 2 N applied in a circular motion along a 3 mm radius wear track. It slided the coatings at 300 rpm for 20 min. It determined the volumetric wear rate after measuring the cross-sectional zone with a 3D digital microscope and describing the wear track's morphology.

3. Results

3.1. Phase Composition of the Microstructure. PEO ceramic coating development using the time–voltage response curve is shown in Figure 2(a). Early on in PEO treatment, the effect of the Al_2O_3 coating was demonstrated by a sudden rise in the voltage response [30]. Microdischarge happened when the voltage response was close to the drain current (seen in the inset of Figure 2(a)), slowing the voltage reaction increase and leading to stable saturation voltage. With its high thermal and electrical conductivity, B_4C reduces the breakdown voltage in a B_4C-AA7075 matrix from ∼301 to ∼262 V. As a result, the B_4C-AA7075 coating reached the breakdown voltage much faster during the PEO process than the pure Al coating. Figure 2(b) shows the PEO and PEO-B_4C coatings' on X-ray diffraction (XRD) patterns. Both α-aluminum oxide and γ-aluminum oxide form aluminum oxide in all PEO ceramic coatings. There were also traces of Al and B_4C peaks in the diffraction patterns. It is possible that the carbon peak created from the B_4C-AA7075 coating beneath the PEO-B_4C one, considering how deeply the X-rays penetrate the PEO-B_4C coating. Raman spectroscopy confirmed the presence of graphitic C ($I_D/I_G = 0.61$) in the PEO-B_4C layer (shown as an inset in Figure 2(b)).

It indicates that the PEO procedure has a negligible effect on the B_4Cs stability. The B_4C from the PEO-B_4C coating was, thus, successfully retained in the B_4C-AA7075 coating. Figures 3(a) and 3(d) show the micrographs of cross sections of aluminum + PEO and B_4C-AA7075 + PEO duplex coatings. PEO ceramic coatings make solid, gap-free contact with their substrates. Figures 3(a) and 3(d) show the measured thickness of 315 and 313 m for the Al + PEO and B_4C-AA7075 + PEO duplex coatings. On average, PEO-B_4C coatings were 25 m thicker than PEO coatings (18vs. 5 μm).

The PEO-B_4C coating took longer to mature because of its smaller drain current than AA7075 (Figure 2(a)). Therefore, PEO-B_4C coating was significantly more robust than PEO coating. Cross-sectional analysis reveals that the PEO-B_4C coating consists of two distinct layers [31]. The surface was pocked with pores and fractures, while the interior was considerably thicker. Figure 3(b)–3(e) depicts the surface morphology of PEO and PEO-B_4C coatings. The PEO ceramic coatings had the same rough texture, fractures, and pancake-like porosity lamellar structure. The lamellar pores provided vents for the molten Al_2O_3. An apparent volcanic structure formed around the pores as the Al_2O_3 solidified [32]. The PEO-B_4C coating has higher and finer volcanic peaks than the PEO coating. During PEO, B_4C raised the pressure and temperature locally within the discharge channel [33].

As molten Al_2O_3 poured out of the composite coating's discharge channel, more coating vanished. The EDS scan

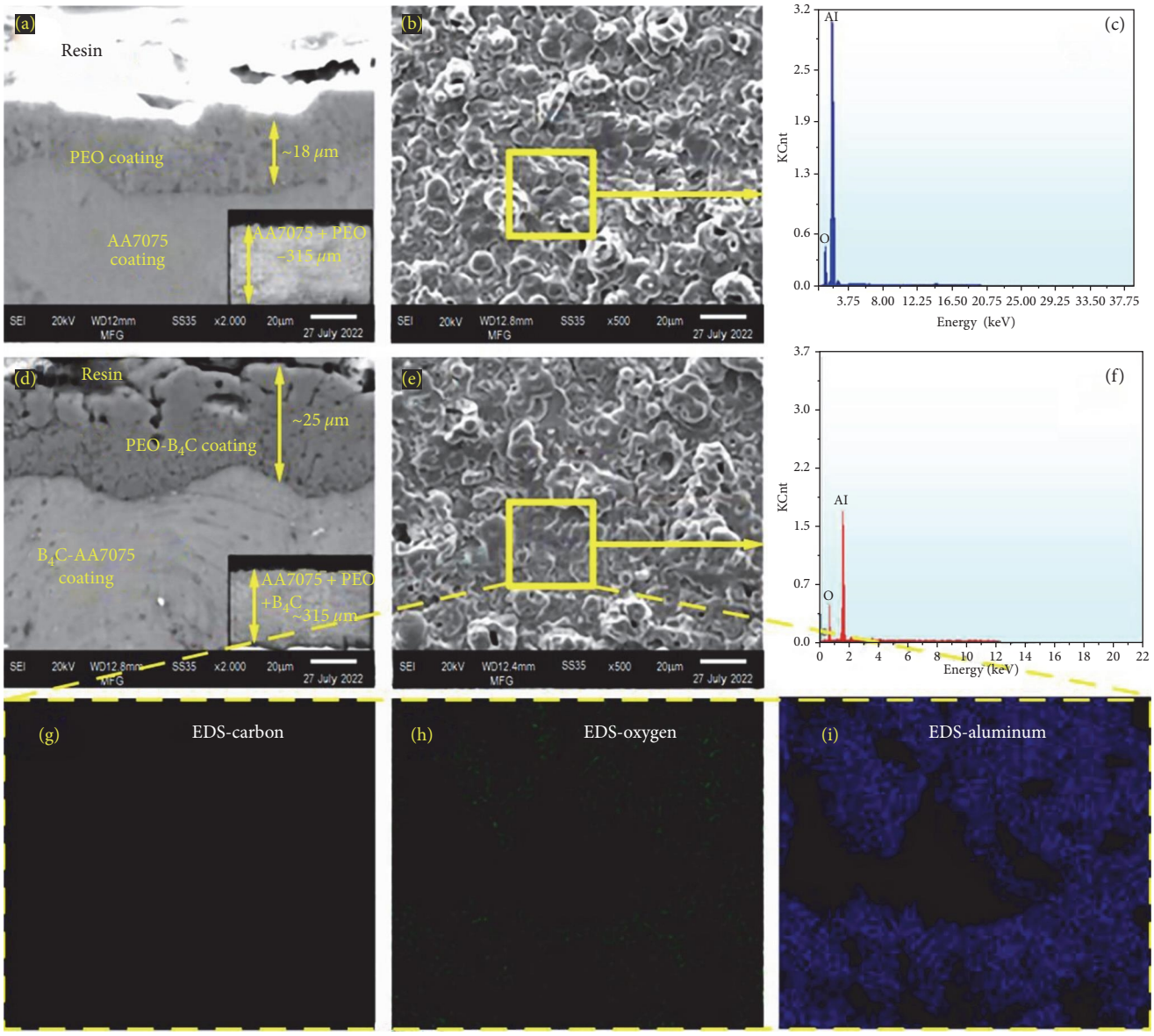

FIGURE 3: SEM images (a, d) cross section, (b, e) surface characteristics, and EDS of (c) PEO coating, (f) PEO-B_4C duplex coating, (g) EDS-carbon, (h) EDS-oxygen, and (i) EDS-aluminum dispersal, as shown in Figure 3(e).

revealed carbon uniformly dispersed throughout the PEO-B_4C coating (Figures 3(c) and 3(f)). C, O, and Al EDS plots are shown in Figure 3 (an expanded portion of Figure 3(e)–3(i)). The EDS scan has revealed carbon dispersed uniformly throughout. It emphasized that the PEO ceramic coating, not CS coating, is the source of the O in the sample. Carbon has a relatively similar distribution pattern to that of O and Al. The element-free zone in EDS maps results from spatial inhomogeneity in the sampling area. It noted that the PEO ceramic coating, not the CS layer, is the source of O in the sample.

3.2. Test Results on Surface Roughness. Figure 4 depicts the R_a value of PEO coating materials. It discovered that PEO-B_4C coating had a rougher surface than PEO coating. The PEO process causes the B_4C-AA7075 coating to produce more molten Al_2O_3, which helps to form crater-like forms on the coating's surface. Consequently, PEO-B_4C coating had a rougher texture than PEO coating. The scanning electron microscopy (SEM) pictures and roughness test results support this (Figures 3(b) and 3(e)).

3.3. Mechanical Characteristics. To evaluate the nanomechanical characteristics of cold-sprayed metallized and PEO ceramic coatings, researchers ran identical tests on all samples, removing factors such as loading and unloading rate and load. The B4C-AA7075 composite material's mechanical characteristics are evaluated using low nanoindentation stress. PEO ceramic coating thickness was also down, making it unsuitable for heavy weights. Accordingly, the nanoindentation tests were

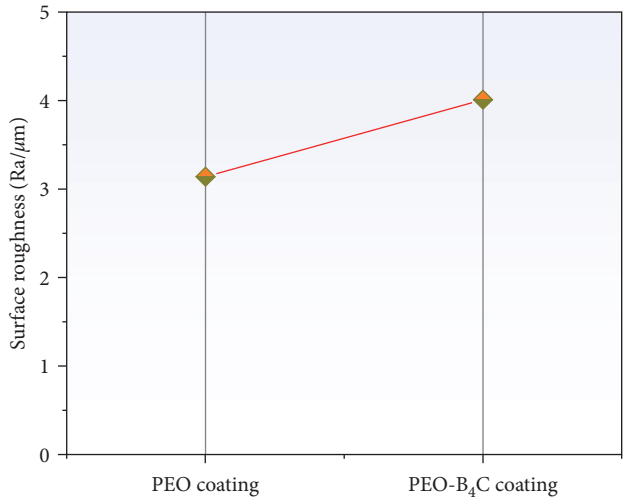

Figure 4: Surface roughness.

conducted with a notional load of 10 mN on AA7075 substrates coated with CS or PEO ceramics, displacement–load curve, nanohardness, and flexion modulus, as shown in Figure 5.

The PEO-B_4C coating improved the material's properties by 23.5% in hardness (13.8 GPa) and 21.6% in elastic modulus (185.4 GPa) compared to the PEO coating. As expected, PEO treatment significantly enhanced the CS coating's mechanical characteristics. Furthermore, the mechanical properties were significantly affected by the PEO-treated B_4C-AA7075 coating as opposed to the PEO-treated AA7075 coating.

3.4. Wear Resistance. Figure 6(a) shows the dry sliding wear rates and coefficient of frictions (COFs) for a PEO ceramics coating on an AZ64 alloy substrate with a CS coating. Figure 6(a) shows that PEO ceramic coatings have slightly lower COF than their CS counterparts. The COF of PEO ceramic coatings increased in the early stages. After a brief rise in the second phase, the COF remained relatively stable. Compared to PEO, the COF of the PEO-B_4C coating is lesser (0.66 and 0.78). In addition, its COF shows lower steady-state variability. The PEO ceramic coating considerably reduced the wear rate compared to a similar CS layer. The PEO-B_4C coating significantly reduced the wear rate to 4.84×10^5 mm^3/Nm compared to the PEO coating. PEO treatment substantially enhances the CS coating's resistance to wear.

3.5. Corrosion Resistance. The optical constant of refraction (OCR) and PDP curves of PEO, as well as PEO-B_4C coatings, are shown in Figure 7. Figure 7(a) shows that after initially falling, the OCR value of PEO coating stabilized at 0.669 V. In contrast, the OCP shift on PEO-B_4C coating was more involved. This process consists of two phases. During the first step, OCP is reduced slowly, starting at −0.56 V to a lesser, more enduring of −0.71 V. A minimum of 1.040 V will be the optical constant of refraction, indicating that the electrolyte has penetrated and settled on both sides of the internal barrier/external porosity layer contact at the end of level II.

The electrolyte presumably diffuses through the barrier layer before coating with CS B_4C-AA7075. Moreover, the SEM pictures showed that the OCP becomes stable once the composite coating saturates with electrolytes (Figures 3(a) and 3(d)). The porosity and dense barrier layers have two separate corrosion phases in PEO-B_4C coatings. Because of the PEO coating's tight molecular structure, the corrosive solution is either on its surface or within its pores (not through the PEO coating). As a result, its susceptibility to corrode is reduced (OCP is higher) compared to PEO-B_4C coating. Protective characteristics of PEO coatings evaluated in a 3.6% NaCl solution using the potent-dynamic polarized technique, as shown in Figure 7(b). Potential for corrosion (E_{corr}) and density of current (I_{corr}) for a CS coating on an AZ64 substrate are shown in Table 1. Corrosion current density condensed below the AZ64 substrate (1.127×10^4 A/cm^2) by covering the sample. The results prove that CS and PEO coatings significantly improve the substrate's resistance to corrosion. Furthermore, PEO coating had superior corrosion current density (1.703×10^8 A/cm^2) and corrosion potential (0.47 V) than the aluminum coating. According to these results, PEO treatment dramatically enhances the CS aluminum coating's resistance to corrosion.

Comparatively, the PEO-B_4C coating's possibility for corrosion and current density of 1.127 V and 3.735×10^6 A/cm^2, respectively, align with the B_4C-AA7075 coating (0.940 V and 2.031×10^6 A/cm^2, respectively) that not treated with PEO. Accordingly, the PEO-B_4C coating offers the same level of corrosion protection as the B_4C-AA7075 layer. The corrosion resistance of a B_4C-AA7075 layer is unaffected by the PEO treatment.

4. Discussion

4.1. Coating Mechanical Properties of Plasma Electrolyte Oxidation. Nanoindentation demonstrates that PEO ceramic coatings have superior mechanical properties to cold-spray metallized coatings [34]. Metal coating on aluminum-based substrates can be transformed into ceramic Al_2O_3 layers by PEO treatment [35]. Al_2O_3 cermet significantly greater hardness and elasticity than Al and its composites. As a result, it is not surprising that PEO ceramic coatings are over CS coats in terms of hardness and flexural modulus. The PEO-B_4C coating has an elastic modulus of 23.5% points higher and is 21% points tougher than the PEO layer. It may have occurred because of the induction of B_4Cs in the matrix, which has high mechanical characteristics. As mentioned in the prior report, CS B_4C-AA7075 coating has superior mechanical qualities to the CS Al coating. Increased hardness of the B_4C-AA7075 coating is the result of reinforcing the B_4C in these coatings. In addition, the tensile properties of the B_4C-AA7075 coating enhance by the high modulus B_4C. In conclusion, the mechanical properties of a B_4C coating on Al_2O_3 ceramic improved with PEO treatment compared to those on a B_4C coating on AA7075 ceramic.

4.2. Dry Wear Behavior. Compared to a CS coating, the CS + PEO duplex coating showed more excellent resistance to wear in a series of wear tests. The PEO process increases the coating's durability by adding an oxide coating to the CS coat; this is why, the duplex coating is much more durable [36]. The B_4C-AA7075 sample treated with PEO exhibited

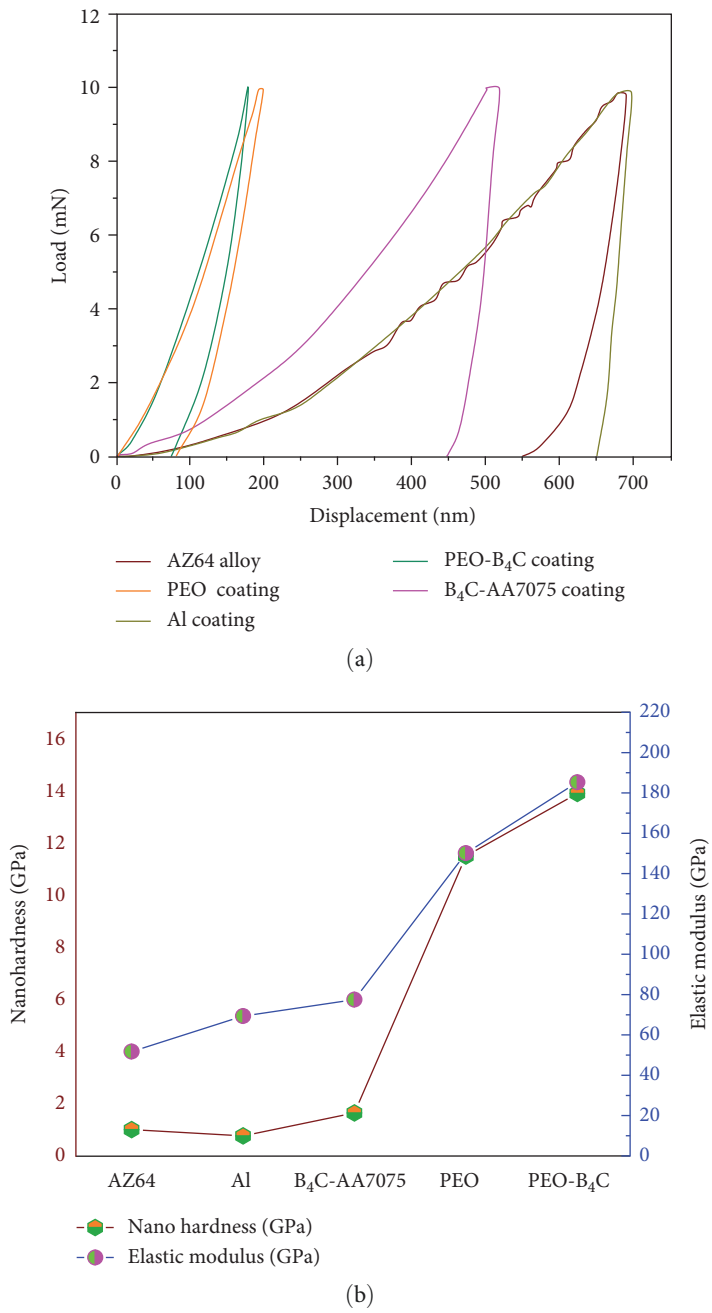

Figure 5: (a) Displacement curvature based on loads and (b) comparison of nanohardness and elastic modulus.

more excellent wear resistance than the Al sample treated with PEO. Figures 8(a) and 8(b) show a profile of the worn path in cross section for the PEO and PEO-B_4C coatings.

The PEO-B_4C coating is thinner than the PEO coating in terms of the wear track [37]. Figures 8(a) and 8(b) show a wear track formed by a PEO ceramic layer. The PEO-B_4C coating has a smaller wear track than the PEO coating. Tribological testing showed that the PEO-B_4C coating drastically reduced material removal and boosted resistance to wear [38]. In most cases, a coating made of Al_2O_3 will have a high resistance to wear because of the strong relationship between these two factors. Improved wear resistance increases the material's hardness. B_4C testing of PEO nanohardness revealed a value of 13.8 GPa, significantly higher than PEO coating (11.6 GPa). As a result, the PEO-B_4C coating offers excellent durability. The oxide layer of PEO-B_4C coating contained carbon elements (including B_4C or other types of amorphous carbon), which may serve as nanolubricants [39].

Carbon components that lubricate themselves, such as B_4C, can reduce wear volumetric loss and friction coefficient [40]. Many other elements influence and enhance the wear resistance of PEO-B_4C coatings. Due to the random

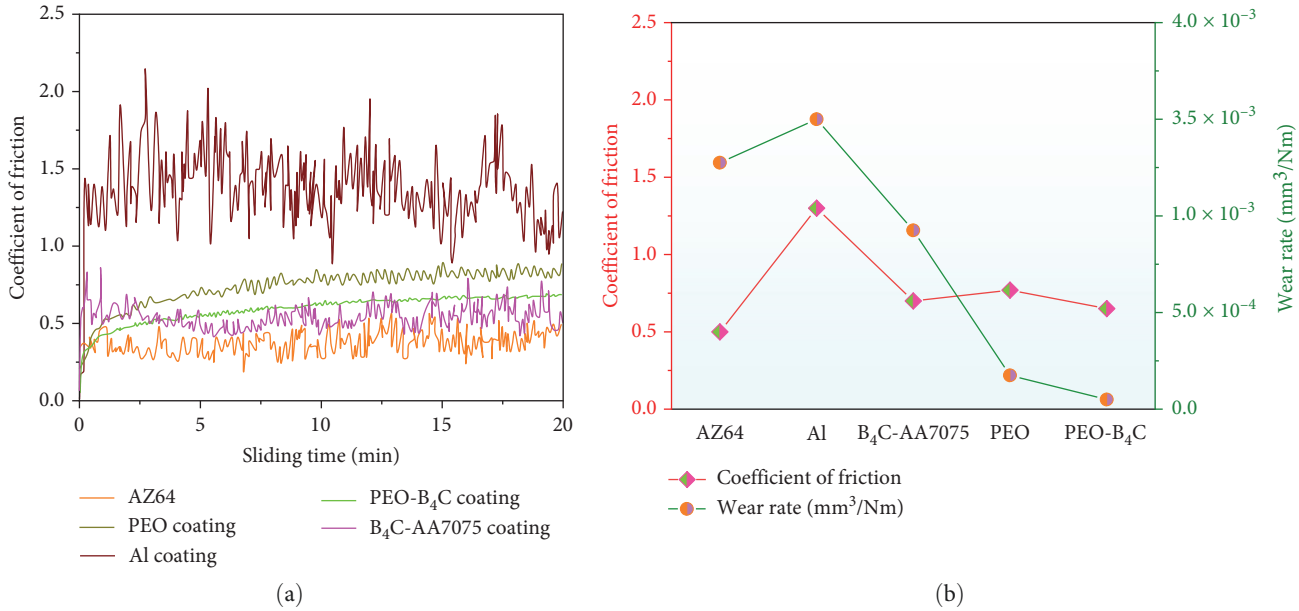

Figure 6: (a) Sliding time and friction coefficient and (b) friction coefficient and wear rate.

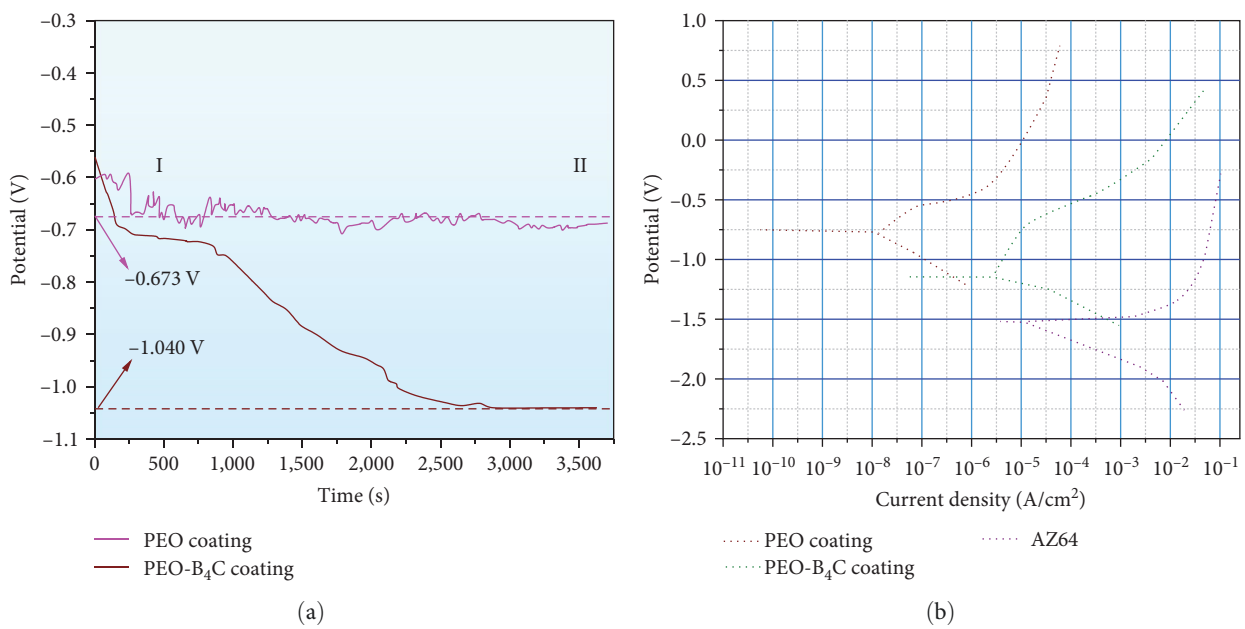

Figure 7: (a) Time responses on OCP and (b) potential vs. current density observed in 3.6 wt% NaCl solution.

distribution of microcracks in the PEO ceramic coatings, the wear tracks displayed a flaky morphology (Figures 8(c) and 8(d)). This conclusion indicates that the PEO ceramic layer wore away due to fatigue. Fatigue cracks in PEO-B_4C were more extensive than those in PEO covering. Fractures propagate in the direction of defects (pores, holes, microcracks) caused by sliding wear. However, the thick PEO-B_4C coating's porous top layer made the microcracks on the wear track more noticeable than they would have been in a PEO coating.

Table 1: Comparison of corrosion potential (E_{corr}) and current density (I_{corr}).

Examples	E_{corr} (V)	I_{corr} (A/cm^2)
Plasma electrolytic oxidation coating	−0.755	1.703×10^{-8}
Plasma electrolytic oxidation-B_4C coated	−1.127	3.735×10^{-6}
AA7075 coated	−1.225	4.660×10^{-6}
B_4C-AA7075 coated	0.940	2.031×10^{-5}
AZ64	−1.514	1.127×10^{-4}

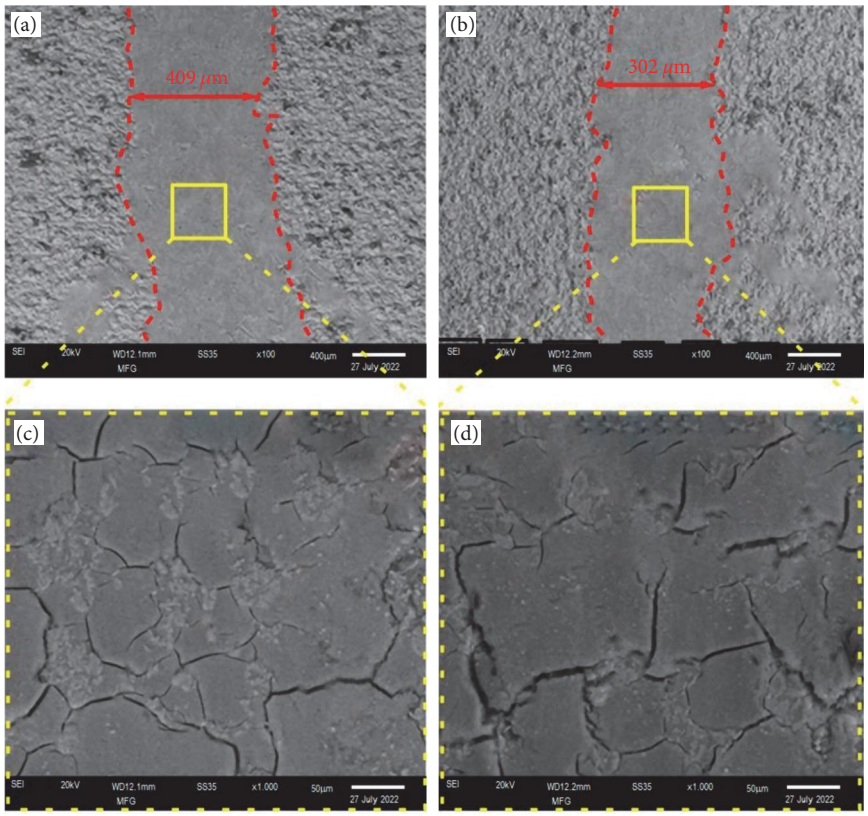

Figure 8: (a, b) SEM images and (c, d) high magnification morphology of PEO with B_4C coating.

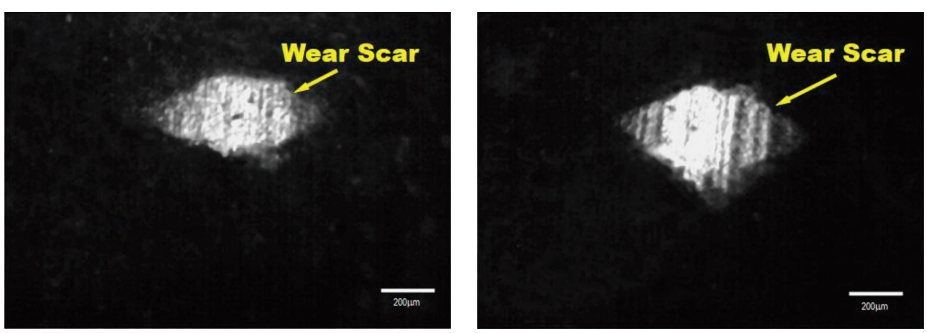

(a) (b)

Figure 9: Optical images of (a) plasma electrolyte oxidation coating and (b) plasma electrolyte oxidation + B_4C coating of the Al_2O_3 ball paired.

The PEO-B_4C coating's wear resistance is approximately a magnitude more than that of the PEO coating because of the B_4Cs self-lubricating impact [41]. Figure 9 shows an optical image showing the PEO and PEO-B_4C coatings' interaction with the Al_2O_3 spherical counterbody, where wear marks on the surface of PEO, the ceramic-coated Al_2O_3 ball. Even though the PEO ceramic coating is highly durable, the Al_2O_3 ball counterbody affects wear during the sliding process. Wear scars on the PEO-B_4C-coated Al_2O_3 ball was more noticeable than those on the PEO-coated Al_2O_3 ball. Stress wearing of the Al_2O_3 by the B_4C PEO layer's reduction in the contact area between the ball and the bearing. The COF of the PEO-B_4C coating was much smaller than that PEO layer. The homogeneous distribution of carbon components like B_4C in the PEO-B_4C coating is responsible for its better wear resistance; these elements lessen the resistance to sliding between the ceramic covering and the Al_2O_3 ball counterbodies.

4.3. Electrochemical Corrosion Analysis. The density in the aluminum coating dropped by two orders of magnitude after being treated with PEO, as shown by electrochemical corrosion testing [42]. However, the PEO treatment did not noticeably alter the B_4C-Al coating's resistance to corrosion. Coatings made of PEO were practical barriers between substrates and corrosive solutions. Its corrosion resistance

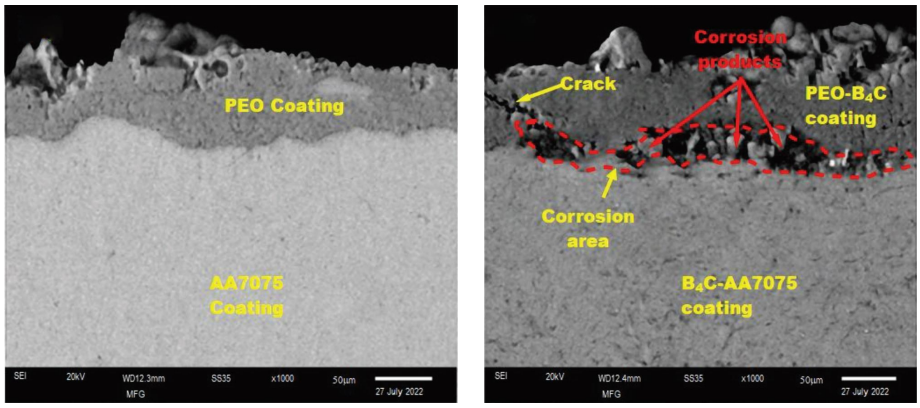

(a) (b)

Figure 10: (a) AA7075 + PEO and (b) B_4C-AA7075 + PEO cross-sectional SEM images of duplex coatings after electrochemical corrosion.

enhances by preventing corrosive media from penetrating the coating [43]. However, the substrate corroded because the electrolyte penetrated the interface through fissures and holes in PEO ceramic covering, creating channels for corrosion. Corroded specimens of aluminum+ PEO and B_4C-AA7075 + PEO twin coatings exhibit in the cross-sectional SEM image, as shown in Figures 10(a) and 10(b).

A massive corroded region is visible under the PEO-B_4C coating, as seen in Figure 10. Corrosion solution entered via fracture in PEO ceramic coating (arrow in Figure 10(b)), corroding B_4C-AA7075 coating. Instead, a cross section of PEO covering showed minimal fissures and pores [37]. As a result, the Al coating protects from corrosion. The PEO ceramic layer developed on the CS aluminum coating sample was denser and smoother than the PEO ceramic coating developed on CS B_4C-AA7075 coating specimens. It enabled more channels for the electrolyte to infiltrate through corrosion to the PEO-B_4C coating. The B_4C-AA7075 coating's corrosion resistance is not drastically altered by the PEO treatment. PEO treatment on an Al substrate creates PEO-B_4C and PEO coatings. A PEO ceramic coat applied to an Al substrate was shown to be less effective at preventing corrosion in the presence of B_4C. To further enhance its corrosion resistance, PEO-B_4C coating could benefit from the application of sealing methods.

5. Conclusion

Successful duplex coatings on AZ64 alloy using the CS technique combined with PEO, including B_4C-AA7075 + PEO and AA7075 + PEO. Mechanical characteristics, wearing, and resistance to corrosion of CS+PEO duplex coatings compared to the cold-spray metallized coatings. The results of this study indicate the following:

(1) Depending on the cold-spray coating's composition, the PEO ceramic coatings included α-Al_2O_3, γ-Al_2O_3, and a trace quantity of the B_4C. The PEO-B_4C coating also had a uniform distribution of carbon.

(2) Hardness and elastic modulus improved upon the PEO-B_4C coating compared to their CS counterparts. PEO-B_4C coatings were thicker (~25 μm) than standard PEO coatings (~18 μm). It results in more significant results for hardness (13.8 GPa) and elastic modulus (185.4 GPa) for the PEO-B_4C coating (21% and 23.5% higher).

(3) Compared to the wear rates of PEO and B_4C-AA7075 coatings, PEO-B_4C coating was significantly more durable, with a rate of only 4.84×10^5 mm^3/Nm. The Al_2O_3 layer is complex, and the B_4C acts as a natural lubricant. Not only that, it also has remarkable antifriction qualities.

(4) The PEO raises aluminum coating corrosion resistivity by lowering the current density in the coating by two magnitudes. By an outcome of these defects in the B_4C-AA7075 coating, the PEO treatment did tiny to enhance the material's resistance to corrosion.

(5) The resulting duplex coating comprises CS with the PEO technique. It has superior mechanical, wear, and corrosion characteristics equated to the independent cold-spray metallized coating. This resilient that the hybrid CS-PEO method is effective in surface engineering.

Data Availability

The data used to support the findings of this study are included within the article.

Conflicts of Interest

The authors declare that they have no conflicts of interest.

References

[1] H. Soliman, M. K. Ahmed, and R. Elbadewy, "Enhanced corrosion resistance of plasma electrolytic oxidation coatings prepared on Mg alloy ZX using nano-Al_2O_3 and NaF incorporated electrolyte," *Surface Engineering*, vol. 37, no. 2, pp. 246–252, 2021.

[2] D. Han, J. Zhang, Y. Lian, P. Ji, W. Xu, and G. Tang, "Control of ZM5 alloy ignition via PEO/aluminum phosphate

composite coating," *Surface and Coatings Technology*, vol. 436, Article ID 128309, 2022.

[3] I. A. Rastegaev and A. V. Polunin, "Regularities and features of acoustic emission under plasma electrolytic oxidation of wrought Al-Mg alloy," *Journal of Physics: Conference Series*, vol. 2144, Article ID 012020, 2021.

[4] P. Długosz, A. Garbacz-Klempka, J. Piwowońska, P. Darłak, and M. Młynarczyk, "Plasma coatings on aluminium–silicon alloy surfaces," *Archives of Foundry Engineering*, vol. 21, no. 3, pp. 96–101, 2021.

[5] J. Dou, J. Wang, H. Li, Y. Lu, H. Yu, and C. Chen, "Enhanced corrosion resistance of magnesium alloy by plasma electrolytic oxidation plus hydrothermal treatment," *Surface and Coatings Technology*, vol. 424, Article ID 127662, 2021.

[6] Y. Lv, C. Zhang, Y. Zhang, Q. Wang, X. Zhang, and Z. Dong, "Microstructure and corrosion resistance of plasma electrolytic oxidized recycled Mg alloy," *Acta Metallurgica Sinica (English Letters)*, vol. 35, pp. 961–974, 2022.

[7] S. Jin, X. Ma, R. Wu et al., "Effect of carbonate additive on the microstructure and corrosion resistance of plasma electrolytic oxidation coating on Mg-9Li-3Al alloy," *International Journal of Minerals, Metallurgy and Materials*, vol. 29, pp. 1453–1463, 2022.

[8] T. C. Senocak, T. A. Yilmaz, H. F. Budak et al., "Influence of sodium pentaborate ($B_5H_{10}NaO_{13}$) additive in plasma electrolytic oxidation process on WE43 magnesium alloys," *Materials Today Communications*, vol. 30, Article ID 103157, 2022.

[9] S. N. Grigoriev, I. O. Kondratsky, B. L. Krit et al., "Protective and thermophysical characteristics of plasma-electrolytic coatings on the ultralight magnesium alloy," *Journal of Engineering Materials and Technology*, vol. 144, no. 2, Article ID 021006, 2022.

[10] J. Wang, F. Peng, X. Wu et al., "Biocompatibility and bone regeneration of PEO/Mg-Al LDH-coated pure Mg: an *in vitro* and *in vivo* study," *Science China Materials*, vol. 64, pp. 460–473, 2021.

[11] R. R. Solís, Ö. Dinc, G. Fang, M. N. Nadagouda, and D. D. Dionysiou, "Activation of inorganic peroxides with magnetic graphene for the removal of antibiotics from wastewater," *Environmental Science: Nano*, vol. 8, no. 4, pp. 960–977, 2021.

[12] M. Ahmadi and F. Ghanbari, "Organic dye degradation through peroxymonosulfate catalyzed by reusable graphite felt/ferriferrous oxide: mechanism and identification of intermediates," *Materials Research Bulletin*, vol. 111, pp. 43–52, 2019.

[13] I. M. Patil, C. P. Jijil, M. Lokanathan, A. Swami, and B. Kakade, "Mechanical activation in reduced graphite oxide/boron nitride nanocomposite electrocatalysts for significant improvement in dioxygen reduction," *Sustainable Energy & Fuels*, vol. 2, no. 1, pp. 252–261, 2018.

[14] Y. Chen, K. Cui, M. Cui et al., "Insight into the degradation of tetracycline hydrochloride by non-radical-dominated peroxymonosulfate activation with hollow shell–core Co@NC: role of cobalt species," *Separation and Purification Technology*, vol. 289, Article ID 120662, 2022.

[15] L. Dong, Y. Li, X. Chen, D. Zhang, and Y. Guan, "ZIF-67 loaded on Fe_3O_4–MnO_2 as efficient peroxymonosulfate activator for rapid degradation of carbamazepine," *Advanced Materials Interfaces*, vol. 8, no. 11, Article ID 2100178, 2021.

[16] Y. Gerasymchuk, A. Wędzyńska, and W. Stręk, "Liquid "syngas" based on supercritical water and graphite oxide/TiO_2 composite as catalyst for CO_2 to organic conversion," *Catalysis Letters*, vol. 152, pp. 2840–2851, 2022.

[17] K. Zhang, D. Sun, C. Ma, G. Wang, X. Dong, and X. Zhang, "Activation of peroxymonosulfate by $CoFe_2O_4$ loaded on metal–organic framework for the degradation of organic dye," *Chemosphere*, vol. 241, Article ID 125021, 2020.

[18] H. Wang, Y. Xue, B. Zhu et al., "CeO_2 nanowires stretch-embedded in reduced graphite oxide nanocomposite support for Pt nanoparticles as potential electrocatalyst for methanol oxidation reaction," *International Journal of Hydrogen Energy*, vol. 42, no. 32, pp. 20549–20559, 2017.

[19] J. J. Rueda-Márquez, J. Moreno-Andrés, A. Rey et al., "Post-treatment of real municipal wastewater effluents by means of granular activated carbon (GAC) based catalytic processes: a focus on abatement of pharmaceutically active compounds," *Water Research*, vol. 192, Article ID 116833, 2021.

[20] Q. Meng, K. Wang, Y. Tang et al., "Facile synthesis of porous flower-like Co_3O_4-SiO_2 composite for catalytic decoloration of rhodamine B," *ChemistrySelect*, vol. 2, no. 32, pp. 10442–10448, 2017.

[21] X. Xu, Y. Li, G. Zhang, F. Yang, and P. He, "NiO-$NiFe_2O_4$-rGO magnetic nanomaterials for activated peroxymonosulfate degradation of rhodamine B," *Water*, vol. 11, no. 2, Article ID 384, 2019.

[22] X. Zhao, Q.-D. An, S.-F. Bo et al., "Highly efficient dynamic degradation of methylene blue on hierarchical nitrogen/cobalt-co-doped carbonaceous beads with diffusion promoting nanostructures," *ChemNanoMat*, vol. 5, no. 6, pp. 802–813, 2019.

[23] X. Qin, P. Shi, H. Liu et al., "Magnetic M_xO_y@N-C as heterogeneous catalysts for the catalytic oxidation of aniline solution with sulfate radicals," *Journal of Nanoparticle Research*, vol. 19, Article ID 225, 2017.

[24] M. Kohantorabi, G. Moussavi, S. Mohammadi, P. Oulego, and S. Giannakis, "Photocatalytic activation of peroxymonosulfate (PMS) by novel mesoporous Ag/ZnO@$NiFe_2O_4$ nanorods, inducing radical-mediated acetaminophen degradation under UVA irradiation," *Chemosphere*, vol. 277, Article ID 130271, 2021.

[25] X. Li, Q. Zou, Y. Wei et al., "Graphite assisted room-temperature synthesis of structurally defected OMS-2 nanorods for peroxymonosulfate activation," *Applied Surface Science*, vol. 497, Article ID 143770, 2019.

[26] S. Fadaei, M. Noorisepehr, H. Pourzamani et al., "Heterogeneous activation of peroxymonosulfate with Fe_3O_4 magnetic nanoparticles for degradation of Reactive Black 5: batch and column study," *Journal of Environmental Chemical Engineering*, vol. 9, no. 4, Article ID 105414, 2021.

[27] T. Zeng, S. Li, J. Hua et al., "Synergistically enhancing Fenton-like degradation of organics by *in situ* transformation from Fe_3O_4 microspheres to mesoporous Fe, N-dual doped carbon," *Science of The Total Environment*, vol. 645, pp. 550–559, 2018.

[28] G. Rotella and D. Umbrello, "Numerical simulation of surface modification in dry and cryogenic machining of AA7075 alloy," *Procedia CIRP*, vol. 13, pp. 327–332, 2014.

[29] G. Rotella, L. Settineri, D. Umbrello, O. W. Dillon Jr., and I. S. Jawahir, "Finite element modeling of microstructural changes in turning of *AA7075-T651* alloy and validation," *Proceedings of NAMRI/SME*, vol. 40, pp. 481–490, 2012.

[30] "2nd International conference on sustainable energy resources, materials and technologies, ISERMAT 2019," *Materials Science Forum*, vol. 979, Article ID 196, 2020.

[31] S. Pan, T. Saso, N. Yu et al., "New study on tribological performance of AA7075-TiB_2 nanocomposites," *Tribology International*, vol. 152, Article ID 106565, 2020.

[32] V. M. Posuvailo, V. V. Kulyk, Z. A. Duriagina, I. V. Koval'chuck, M. M. Student, and B. D. Vasyliv, "The effect of electrolyte composition on the plasma electrolyte oxidation and phase composition of oxide ceramic coatings formed on 2024 aluminium alloy," *Archives of Materials Science and Engineering*, vol. 105, no. 2, pp. 49–55, 2020.

[33] Z. Shahri, S. R. Allahkaram, R. Soltani, and H. Jafari, "Study on corrosion behavior of nano-structured coatings developed on biodegradable as cast Mg–Zn–Ca alloy by plasma electrolyte oxidation," *Surface and Coatings Technology*, vol. 347, pp. 225–234, 2018.

[34] K. Qian, W. Li, X. Lu et al., "Effect of phosphate-based sealing treatment on the corrosion performance of a PEO coated AZ91D Mg alloy," *Journal of Magnesium and Alloys*, vol. 8, no. 4, pp. 1328–1340, 2020.

[35] G. A. Mengesha, J. P. Chu, B.-S. Lou, and J.-W. Lee, "Effects of processing parameters on the corrosion performance of plasma electrolytic oxidation grown oxide on commercially pure aluminum," *Metals*, vol. 10, no. 3, Article ID 394, 2020.

[36] P. Vishwakarma, S. Soni, and P. M. Mishra, "Effect of reinforcement and volume fraction on mechanical behaviour of AA7075/B_4C/fly-ash MMCp," *International Journal of Engineering and Advanced Technology*, vol. 8, no. 4, pp. 1503–1510, 2019.

[37] J. Veerasundaram, K. Kani, R. Nallumuthu, and M. Thangaraj, "Experimental and theoretical investigation of extrusion load for AA6063/SiC extruded composite billet," *Proceedings of the Institution of Mechanical Engineers, Part E: Journal of Process Mechanical Engineering*, 2022.

[38] S. Ebrahimi, A. Bordbar-Khiabani, and B. Yarmand, "Immobilization of rGO/ZnO hybrid composites on the Zn substrate for enhanced photocatalytic activity and corrosion stability," *Journal of Alloys and Compounds*, vol. 845, Article ID 156219, 2020.

[39] E. Nikoomanzari, A. Fattah-alhosseini, M. R. P. Alamoti, and M. K. Keshavarz, "Effect of ZrO_2 nanoparticles addition to PEO coatings on Ti–6Al–4V substrate: microstructural analysis, corrosion behavior and antibacterial effect of coatings in Hank's physiological solution," *Ceramics International*, vol. 46, no. 9, pp. 13114–13124, 2020.

[40] D. S. Chandra Mouli and R. Umamaheswara Rao, "Optimization of friction stir process parameters for micro-hardness and wear characteristics of silicon carbide-reinforced Al-7075 surface composite," *Transactions of the Indian Institute of Metals*, vol. 74, pp. 3135–3143, 2021.

[41] C. P. Luo, J. Liu, and H. Liu, "Effects of Al/Zn ratio on the microstructure and strengthening of Mg-Al-Zn alloys," *Materials Science Forum*, vol. 488-489, pp. 205–210, 2005.

[42] S. Vijay Ananth, R. Srimurugan, V. Jayaseelan, A. Geethan, and J. Francis Xavier, "Experimental investigation on superplastic forming behavior of AA 6063/SiCp using stir casting," *AIP Conference Proceedings*, vol. 2283, no. 1, Article ID 020118, 2020.

[43] V. Jayaseelan, S. Vijayananth, J. Francis Xavier, S. Ajith Arul Daniel, N. M. Kumar, and X. X. Jiang, "Experimental investigation on bi-axial superplastic forming characteristics of AA6063/SiCp with various percentages of SiCp under various temperatures and pressures," *Results in Physics*, vol. 15, Article ID 102624, 2019.

Hindawi
Journal of Nanomaterials
Volume 2023, Article ID 3657314, 11 pages
https://doi.org/10.1155/2023/3657314

Research Article

Analytical and Neural Network Analysis on Flux-Coated Aluminium Alloy by Activated TIG Welding with Synthesized Nanocomposites

V. L. Raja,[1] A. M. Senthil Kumar,[2] K. Shantha Kumari,[3] R. Bharanidharan,[4] P. Ezhilarasi,[5] S. Rajeshkannan,[5] T. M. Nithya,[6] and S. Venkatesh Kumar[7]

[1]*Department of Mechanical Engineering, Loyola Institute of Technology, Palanchur, Chennai 600123, Tamil Nadu, India*
[2]*School of Computer Science and Engineering, Vellore Institute of Technology, Chennai 600127, Tamil Nadu, India*
[3]*Department of Data Science and Business Systems, School of Computing, SRM Institute of Science and Technology, Chennai 603203, Tamil Nadu, India*
[4]*Department of Electrical and Electronics Engineering, Karpagam Academy of Higher Education, Coimbatore 641021, Tamil Nadu, India*
[5]*Department of Electronics and Communication Engineering, St. Joseph's College of Engineering, OMR, Chennai 600119, Tamil Nadu, India*
[6]*Department of Computer Science and Engineering, K. Ramakrishnan College of Engineering, Trichy 621112, Tamil Nadu, India*
[7]*Department of Mechanical Engineering, College of Engineering and Technology, Mettu University, P.O. Box: 318, Mettu, Ethiopia*

Correspondence should be addressed to S. Venkatesh Kumar; s.venkateshkumar@meu.edu.et

Received 27 August 2022; Revised 11 December 2022; Accepted 25 January 2023; Published 20 February 2023

Academic Editor: Ridwan Yahaya

This research focused to synthesize the material by the tungsten inert gas (TIG) welding process with support of appropriate flux coating material. Therefore the required amount of flux coating material was utilized to enhance the mechanical properties of the specified localized welded regions. Hence, this study concentrated to select the nano-SiO_2 flux particles that were employed for TIG process. This activated TIG welding composes the flux-coated welding on the base metal of AA5083-H111, as this material was highly reactive with SiO_2 by the presence of magnesium precipitates and well synthesized after the welding. The post- and preheat treatment process was achieved before and after welding. The selection of activated TIG process parameters composed of strengthened weld specimens along with constant parameters like electrode tip angle and flow rate, respectively. Initially, the process parameters were designed by the statistical analysis of Box Behnken method with support of regression formulation to determine the optimal solution. The maximum tensile strength was attained at the welding process parameters of welding speed (100 mm/min), voltage (13 V), and current (125 amps). The higher hardness was achieved at the process parameters of welding speed (80 mm/min), voltage (12 V), and current (125 amps), respectively. Finally, the neural network approach was utilized to verify the predicted responses of tensile and microhardness properties. The interaction plots, mean plots, and 3D scatter plots were influenced to enhance the process parameters. In this research, mechanical properties were enhanced by the flux-coated SiO_2 and the analytical method also advances the optimal parameters.

1. Introduction

Over the years, various categories of welding have been utilized in various sectors of the industries [1]. But since welded joints could not properly accommodate with thermoplastic condition, the entire welding operations totally collapsed [2]. Different categories of welding are used in various mechanical industries [3]. Especially, tungsten inert gas (TIG) welding is used highly in these industries [4]. The TIG welding generates heat with ultimate support of electric arc with consumable tungsten electrodes to join various metals together [5]. TIG welding was initiated in 1942 by the scientist Russel; many researchers developed welding into the aluminum-based magnesium alloy [6]. Formerly, this type of material joint

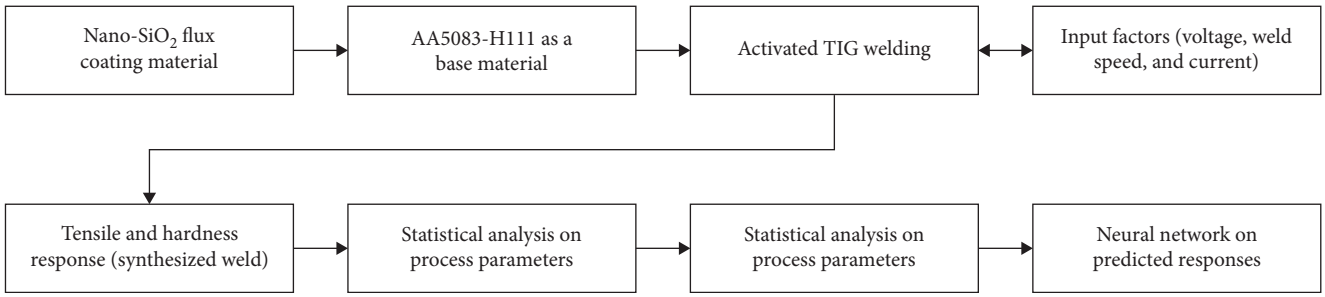

Figure 1: A-TIG-coated process layout.

was difficult to weld during the TIG process [7]. Nonferrous and ferrous materials are frequently joined together by TIG process [8].

At the same time, TIG welding was used where there were requirements to fulfill the quality and serious situations [9]. It has protected the weld pool by shielding gas, and this welding is easy to carry in any position, and fine soft welding was carried out. TIG welding works under the activated flux or without flux based on the applications. Meanwhile activated-flux-TIG welding is used where thicker welding is needed. This welding was used in various applications like, pipe, plate, casted plate or pipe, ship building, and aerospace sectors. Some of the minor limitations are accomplished in the TIG welding process [10].

During the single bead of weld on higher thickness materials, joint was not properly attained. Similarly, the edge preparation enhancements need more filler materials to pack the welds and the cost of operation was also high [11]. Plates exceeding 3 mm thickness needed more than one pass of TIG welding then only the joint efficiency was highly accomplished [12]. To improve the maximum thickness, the component should meet the necessity of lesser welding speed and multipass method and then will blend together [13]. After the completion of the process, additional cost was needed to clean the edges and maximum time was consumed to attain the full process [14]. Pavan et al. [15] presented the bead on plate TIG process with aiding of activated flux to stainless steel material. The design of experiments was used to measure the optimization of process parameters. Finally, the maximum density of welded specimens were achieved at bead on plate processed 316L stain less steel. Babbar et al. [16] investigated that the activated TIG welding on the multi-based flux materials were influenced on the stainless material. In this study, tensile strength and depths of penetrations were analyzed in detail. The current, voltage, and flow rates were highly utilized to enhance the process parameters. Moreover, most of the specimens achieved better mechanical characteristics in the welded joints. Sakthivel et al. [17] studied the activated TIG process on the 316L stainless steel material with maximum temperature at 923 K. The mechanical properties, like creep strength, were achieved at high on the welded area. At the same time cavitations also reduced. The characterization of the welded region provides better intermetallic phases. Muzamil et al. [18] synthesized the nanocarbon tubes, and titanium oxide flux-coated materials were incorporated on the AA6061 aluminium alloy. Addition of flux on AA6061 enhances its mechanical properties. Similarly, weld depths, distortions, and weld seams were analyzed on the welded region of AA6061. Vora and Badheka [19] presented the activated TIG on the steel with the utilization of ferritic material. The postweld treatment was achieved on all the welded samples for improving the mechanical properties. The flux-treated samples achieved better enhanced properties than the unprocessed materials. Above literature clearly define various activated TIG processes on various materials. But AA5083-H111 with nano-SiO_2 flux treating was not achieved fully. So this research concentrates to focus AA5083-H111 with constant weight fraction of nano-SiO_2-synthesized samples which were composed by the A-TIG welding. Wu et al. [20] investigated the TIG welded on the titanium alloy and analyzed the mechanical properties by various influence of frequency. The mechanical properties were improved by increasing the frequencies. At the same time, statistical and neural network combination was approached on the TIG-welded samples to analyze the optimal process parameters. Figure 1 shows the graphical layout for present investigation.

2. Material and Methods

In this TIG welding process, AA5083-H111 aluminium–magnesium alloy was utilized to conduct the joining process. Before the initiation of TIG process, base material could be engaged for heat treatment process. The two stages of preweld actions, that is, 850°C kept at 20 hr and 750°C kept at 18 hr were carried out on the selected base material. The uniform dispersion of strengthening particles was successfully carried out, and the required dimensions of the base plate were machined to 150 mm × 50 mm × 6 mm size from the purchased materials. Then 45° notch with V type was designed on the above dimension plate to fill the flux material. The nano-SiO_2 flux was coated on the selected base metal with support of carbinol mixing to attain regularity that looks like a paint material. Then the help of paint brush was taken to fulfill the 45° V notch gap.

The welding parameters are the most important aspect to attain complete welding. The welding parameters are welding speed (80–100 mm/min), voltage (12–14 V), and current (120–130 amps), respectively. These parameters composed better joints as stated by different researchers [21]. The butt joint configuration was completed through this TIG welding process with flux-coated material along the center portion of the base material. The 10 mg nano-SiO_2 flux was coated on

Table 1: Box Behnken-based design of welding parameters.

Std. order	Weld order	Pt. categories	Blocks	Welding speed (mm/min)	Voltage (V)	Current (amp)
14	1	0	1	90	13	125
10	2	2	1	90	14	120
2	3	2	1	100	12	125
3	4	2	1	80	14	125
13	5	0	1	90	13	125
7	6	2	1	80	13	130
5	7	2	1	80	13	120
9	8	2	1	90	12	120
4	9	2	1	100	14	125
8	10	2	1	100	13	130
6	11	2	1	100	13	120
11	12	2	1	90	12	130
12	13	2	1	90	14	130
15	14	0	1	90	13	125
1	15	2	1	80	12	125

the base material then the weld was produced or synthesized on the weldment region [21]. During the activated TIG welding process, 65° tip angle with 3% thorium-mixed electrode was used and flow rate of 13 L/min was maintained. During the postwelding process, temperature of 690°C was kept at 20 hr time period for all the specimens to mitigate the internal stresses [22]. Then the welded synthesized specimens were employed to conduct the mechanical testing and characterization examinations. After the postweld heat treatment process, all the welded samples were entered into the nondestructive tests for analyzing the defect-free surfaces. All the mechanical performances were conducted as per the ASTM system [23]. During the mechanical tests, tensile was prepared as per ASTM of E-09 and hardness was prepared as per the ASTM of E-384, respectively.

Prior to A-TIG welding on AA 5083-H111 base material, the process parameters are designed by the statistical method of response surface methodology. From the response method, Box Behnken technique was assigned the parameter levels with supporting of Minitab software [24]. Among the various optimization methods like grey relational, central composite design, desirability, and TOPSIS approach, Box Behnken method provides a better optimal solution by the increase of maximum necessity trial runs than the general factorial method. Overall 15 weld runs were accommodated to produce the butt weld on the base material of AA5083-H111. The design table of processing parameters is presented in Table 1.

3. Results and Discussion

After the postweld heat treatment was conducted, weld specimens were accounted into tensile and hardness strength experiment to analyze the mechanical potency of welded samples. As per the design of Box Behnken method, the entire weld runs were completed with activated flux-coated TIG welding. As per the ASTM systems of E-09 subcategories, tensile specimens were prepared. Similarly, hardness specimens were prepared and the standard dimension and the measurement values were taken on the nugget surface region by Vicker's hardness testing machine [25]. The entire weld specimens achieved better tensile properties and enhanced hardness strength than the as-cast raw base material. The base metal properties are 220 MPa and 74 Hv, respectively. Table 2 shows the overall mechanical properties of welded specimens. As per the recommendations of Box Behnken design, all 15 welded specimens were engaged to carry out the mechanical testing. The entire welded specimens achieved better mechanical propertied when compared with base material. Figures 2 and 3 shows the tensile properties' and hardness strength's graphical representations. Those figures were plotted by the origin tools implementing the 5% error plots on the tensile and hardness bars. From Figure 2, it is understood that the sample 14 attained the maximum tensile properties when compared with other set of flux-coated samples. The 14th sample's parameters were 90 mm/min, 13 V, and 125 amps with respect to welding speed, voltage, and current. The nano-SiO_2 flux-coated sample was fully synthesized on the base material. Due to the presence of nano-SiO_2 the tensile properties and hardness strength enhances. At the same time, aluminum–magnesium alloy with nano-SiO_2 was synthesized during the single pass of the activated TIG welding technique.

The hardness portion of welded specimens achieved fine strength due to the presence of nano-SiO_2 flux material. Similarly, heat-affected zone strength was significantly less when compared with flux-coated zones due to the synthesized nanosilicon oxide particles dispersed uniformly on the AA5083-H111. At the same time, V notch groove successfully packed the nano-SiO_2 particles by the activated TIG welding process. Moderate welding speed and voltage with increment of welding current improves the weld strength, and evenly dispersed silicon oxide flux causes enhancement in the hardness properties in the weld zone.

Table 2: Mechanical properties of TIG-activated-flux-coated welded samples.

Weld order	Welding speed (mm/min)	Voltage (V)	Current (amp)	Tensile	Hardness
1	90	13	125	245	81
2	90	14	120	254	85
3	100	12	125	261	84
4	80	14	125	258	89
5	90	13	125	265	91
6	80	13	130	238	88
7	80	13	120	263	86
8	90	12	120	241	92
9	100	14	125	256	83
10	100	13	130	274	79
11	100	13	120	267	82
12	90	12	130	258	85
13	90	14	130	261	81
14	90	13	125	280	91
15	80	12	125	249	90

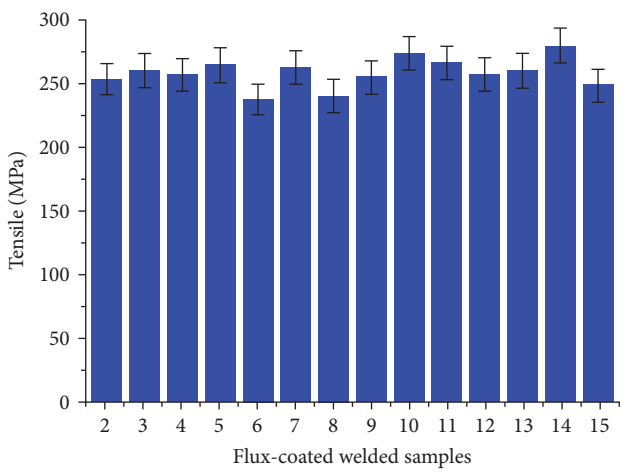

Figure 2: Tensile properties on the nano-SiO_2-flux-coated specimens.

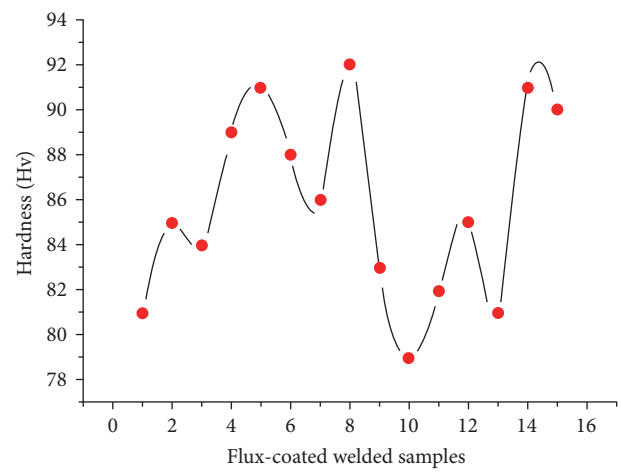

Figure 3: Hardness on the nano-SiO_2-flux-coated specimens.

3.1. Statistical Analysis of Activated TIG Welding Process Parameters. In this research, TIG-welded processing parameters were engaged into the statistical performance for improving the welding characteristics with respected outcomes. Therefore, response surface methodology was an appropriate technique to implement the welding characteristics. From the RSM method, Box Behnken method was used to analyze the processing parameters with effect various plots like histogram plots, Pareto charts, interaction plots, and main effect plos. These plots were used to enhance the outcomes with standardized effects. Regression equations create the model effectively with uncoded units for tensile response. The following equation shows the regression equation of tensile strength.

$$\begin{aligned}\text{Tensile strength} = {} & -2158 - 14.5 \text{ welding speed} + 283 \text{ voltage} + 18.9 \text{ current} \\ & -0.0017 \text{ welding speed} \times \text{welding speed} - 7.17 \text{ voltage} \times \text{voltage} \\ & -0.107 \text{ current} \times \text{current } 0.350 \text{ welding speed} \times \text{voltage} + 0.160 \text{ welding speed} \times \text{current} \\ & -0.50 \text{ voltage} \times \text{current}.\end{aligned} \tag{1}$$

The coded coefficients were incorporated with various input factors with the P and T values. In this method weight was assigned to the input parameters in the range of <0.5. Therefore, this P value reaches the required positions, particularly the combinations of welding speed (0.260), current (0.302), and voltage and current (0.368). The coded coefficients of A-TIG process parameters were presented in Table 3. Similarly, Figure 4 exhibits the Pareto chart for

Table 3: Coded coefficients of flux-coated welded response by A-TIG.

Term	Coef	SE coef	T-value	P-value	VIF
Constant	263.33	8.03	32.79	0.001	
Welding speed	6.25	4.92	1.27	0.260	1.00
Voltage	2.50	4.92	0.51	0.633	1.00
Current	0.75	4.92	0.15	0.885	1.00
Welding speed × welding speed	−0.17	7.24	−0.02	0.983	1.01
Voltage × voltage	−7.17	7.24	−0.99	0.368	1.01
Current × current	−2.67	7.24	−0.37	0.728	1.01
Welding speed × voltage	−3.50	6.96	−0.50	0.636	1.00
Welding speed × current	8.00	6.96	1.15	0.302	1.00
Voltage × current	−2.50	6.96	−0.36	0.734	1.00

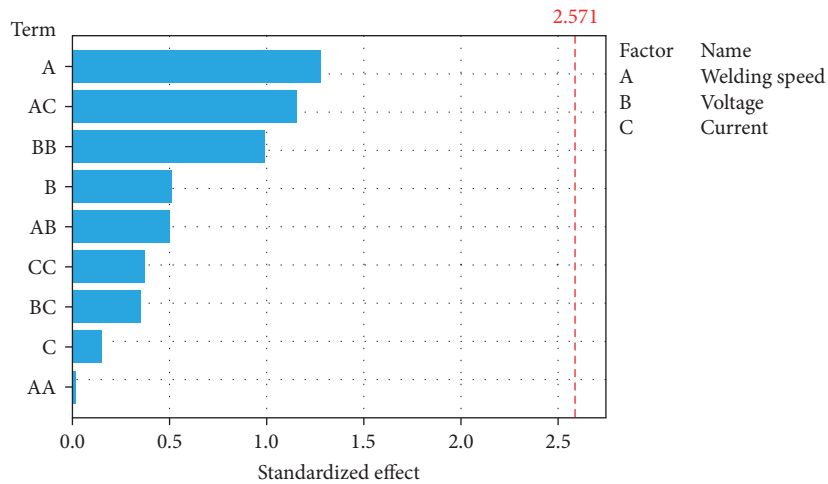

Figure 4: Standardized effect of Pareto chart for tensile strength.

tensile outcomes with normalized effects. From Figure 4, welding speed individual factor attained most level than other combinations of process parameters. The significant level was achieved in lesser level standardized effects of 1.5 limits. The ANOVA analysis was required to identify the significant level with various errors systems and the significant level was improved along with some processing parameters as discussed in the coefficients section. ANOVA creates significant factors for improving the characteristics of process parameters. Most of the parameters accomplished better significance. Table 4 displays the ANOVA for tensile outcomes with the input factors.

Regression equations build the model successfully with uncoded units for hardness response. The following equation displays the regression formulation for hardness strength.

$$\begin{aligned}\text{Hardness strength} = {} & -1379 + 5.66 \text{ welding speed} - 31.2 \text{ voltage} + 23.3 \text{ current} \\ & - 0.0158 \text{ welding speed} \times \text{welding speed} + 0.42 \text{ voltage} \times \text{voltage} \\ & - 0.0933 \text{ current} \times \text{current} + 0.000 \text{ welding speed} \times \text{voltage} \\ & - 0.0250 \text{ welding speed} \times \text{current} + 0.150 \text{ voltage} \times \text{current}.\end{aligned} \tag{2}$$

The coded coefficients of hardness response were incorporated with a choice of activated TIG factors with the P and T values. In this technique, weight basis was allotted to the input activated-TIG process parameters in the range (<0.5). Consequently, this P value performs the required ranking especially, the amalgamation of voltage (0.327), current (0.362), current × current (0.338), and welding speed and current (0.580) arrangements. The coded coefficients of A-TIG process parameters for hardness are shown in Table 5. Similarly, Figure 5 displays the Pareto chart for hardness outcome with standardized effects. From Figure 6, welding speed individual factor was accomplished most significant level than

Table 4: ANOVA for tensile output with their activated coated TIG parameters.

Basis	*df*	Adj. SS	Adj. MS	*F*-value	*P*-value
Model	9	904.33	100.481	0.52	0.815
Linear	3	367.00	122.333	0.63	0.625
Welding speed	1	312.50	312.500	1.61	0.260
Voltage	1	50.00	50.000	0.26	0.633
Current	1	4.50	4.500	0.02	0.885
Square	3	207.33	69.111	0.36	0.787
Welding speed × welding speed	1	0.10	0.103	0.00	0.983
Voltage × voltage	1	189.64	189.641	0.98	0.368
Current × current	1	26.26	26.256	0.14	0.728
Two-way interaction	3	330.00	110.000	0.57	0.660
Welding speed × voltage	1	49.00	49.000	0.25	0.636
Welding speed × current	1	256.00	256.000	1.32	0.302
Voltage × current	1	25.00	25.000	0.13	0.734
Error	5	967.67	193.533		
Lack-of-fit	3	351.00	117.000	0.38	0.782
Pure error	2	616.67	308.333		
Total	14	1,872.00			

Table 5: Coded coefficients for hardness response with various A-TIG process parameters.

Term	Coef	SE coef	*T*-value	*P*-value
Constant	87.67	2.44	35.91	0.001
Welding speed	−3.13	1.50	−2.09	0.091
Voltage	−1.62	1.50	−1.09	0.327
Current	−1.50	1.50	−1.00	0.362
Welding speed × welding speed	−1.58	2.20	−0.72	0.504
Voltage × voltage	0.42	2.20	0.19	0.857
Current × current	−2.33	2.20	−1.06	0.338
Welding speed × voltage	0.00	2.11	0.00	1.000
Welding speed × current	−1.25	2.11	−0.59	0.580
Voltage × current	0.75	2.11	0.35	0.737

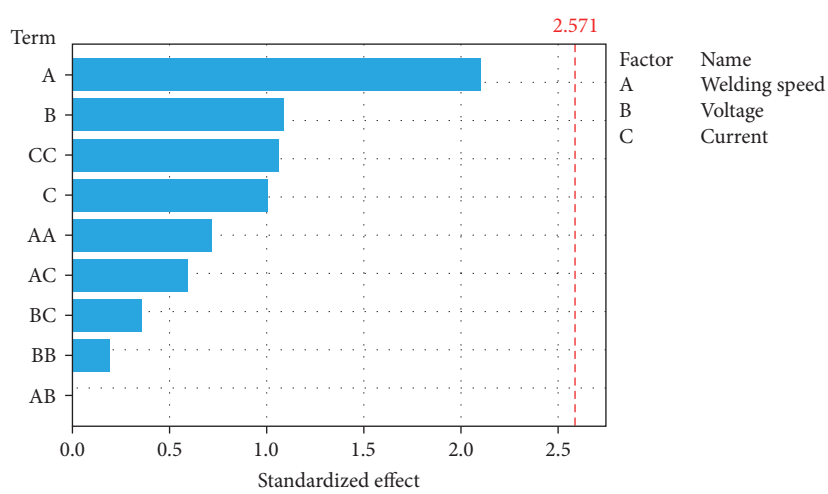

Figure 5: Standardized effect of Pareto chart for hardness strength.

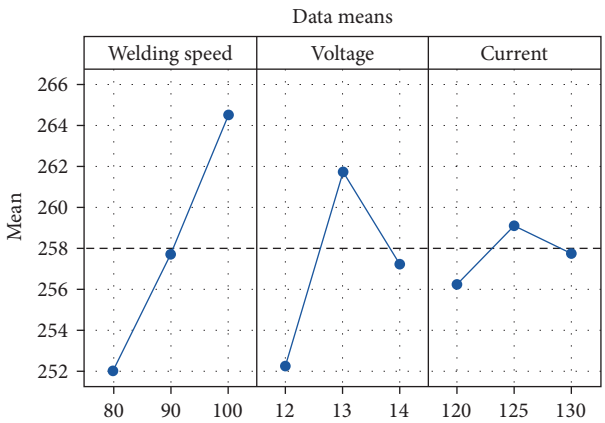

Figure 6: Main effect plot for tensile outcome with A-TIG-coated process samples.

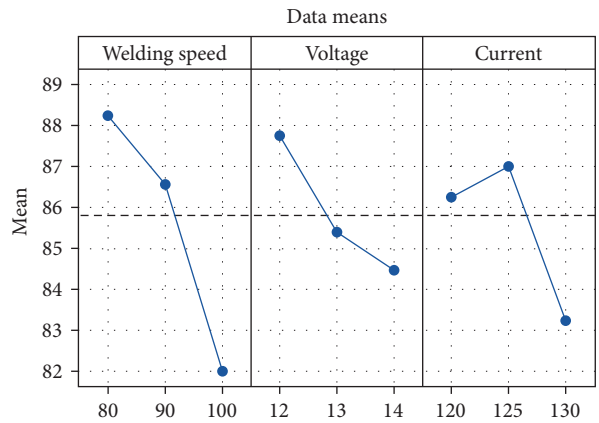

Figure 7: Main effect plot for hardness impact with A-TIG-coated process samples.

Table 6: ANOVA for hardness with their activated coated TIG parameters.

Source	*df*	Adj. SS	Adj. MS	*F*-value	*P*-value
Model	9	154.983	17.2204	0.96	0.549
Linear	3	117.250	39.0833	2.19	0.208
Welding speed	1	78.125	78.1250	4.37	0.091
Voltage	1	21.125	21.1250	1.18	0.327
Current	1	18.000	18.0000	1.01	0.362
Square	3	29.233	9.7444	0.54	0.673
Welding speed × welding speed	1	9.256	9.2564	0.52	0.504
Voltage × voltage	1	0.641	0.6410	0.04	0.857
Current × current	1	20.103	20.1026	1.12	0.338
2-way interaction	3	8.500	2.8333	0.16	0.920
Welding speed × voltage	1	0.000	0.0000	0.00	1.000
Welding speed × current	1	6.250	6.2500	0.35	0.580
Voltage × current	1	2.250	2.2500	0.13	0.737
Error	5	89.417	17.8833		
Lack-of-fit	3	22.750	7.5833	0.23	0.872
Pure error	2	66.667	33.3333		
Total	14	244.400			

the other combinations of A-TIG process parameters. The significant level was achieved in lesser level standardized effects of 2.0 limits.

The ANOVA was mandatory to recognize the noteworthy level with various errors system and the considerable level was enhanced along with some A-TIG processing parameters as conferred in the coefficients section. ANOVA produces significant factors for advancing the uniqueness of A-TIG process parameters. Most of the parameters proficient better significance. Table 6 shows the ANOVA for hardness outcomes with activated flux-coated TIG process input factors.

After the conclusion of ANOVA for both the responses tensile and hardness, further optimal values should be engaged to mean effect plots for enhancing the input parameters with combinational effects. Figure 6 displays the mean effect plot for tensile response with various A-TIG-coated process parameters. From these parameters, welding speed (100 mm/min), voltage (13 V), and current (125 amps) influenced the response to the next level so these parameters were optimal than the other TIG parameters.

Figure 7 exhibits the mean effect plot for hardness response with different A-TIG-coated process parameters. From these parameters, welding speed (80 mm/min), voltage (12 V), and current (125 amps) influenced the response to the next level so these parameters were optimal than the other TIG parameters. Compared with those mean effect plots both the processed parameters were attained efficiently, especially the current parameters on activated-nano-SiO_2 sample procures common factors for both the outcomes. During the TIG welding process, presence of nano-SiO_2 provides much adequate oxide levels in the welded region to remove the moisture gases and enhance the welded strength.

After mean effect plots, interaction effects were discussed in this part for the combinational arrangements for entire TIG process parameters to compose better joints among the AA5083-H111 specimens. Therefore, Figures 8 and 9 show

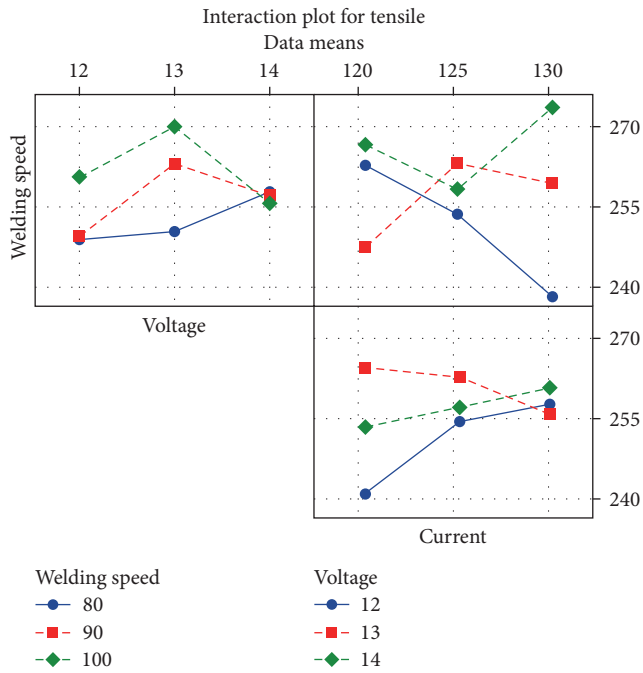

Figure 8: Interaction effect for tensile with A-TIG process on flux-coated welded AA5083.

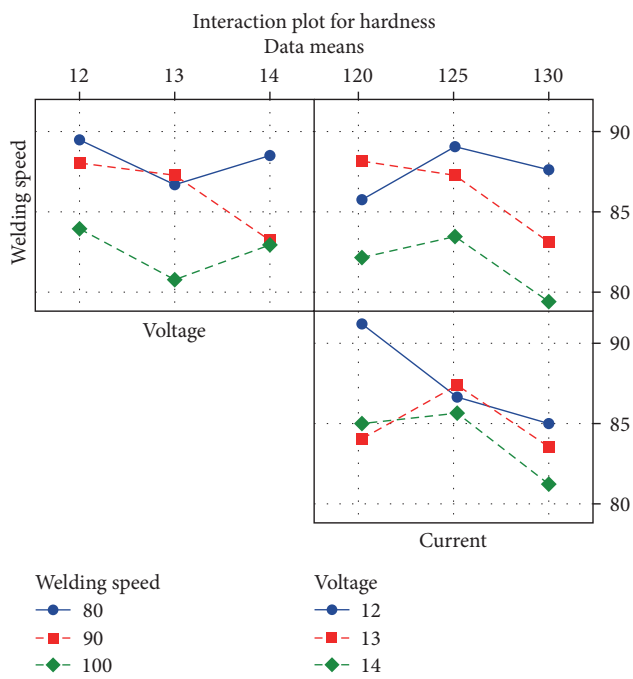

Figure 9: Interaction effect for hardness with A-TIG process on flux-coated welded AA5083.

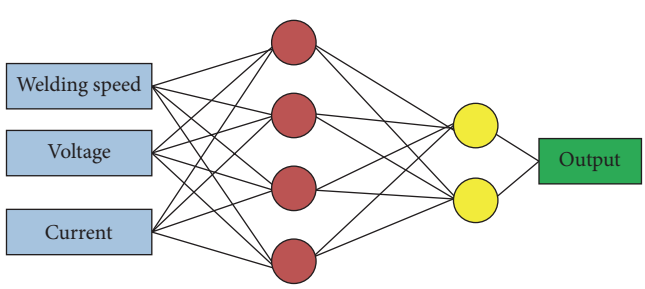

Figure 10: Neural network model for output responses with flux-coated welded AA5083.

Table 7: Predicted ANN for both coated welded outputs.

Weld order	Welding speed (mm/min)	Voltage (V)	Current (amp)	Tensile	ANN tensile	Hardness	ANN hardness
1	90	13	125	245	244.52	81	80.25
2	90	14	120	254	253.25	85	54.12
3	100	12	125	261	259.15	84	83.56
4	80	14	125	258	258.69	89	89.35
5	90	13	125	265	266.12	91	91.87
6	80	13	130	238	239.01	88	87.84
7	80	13	120	263	263.98	86	85.89
8	90	12	120	241	241.58	92	92.16
9	100	14	125	256	255.14	83	84.15
10	100	13	130	274	273.15	79	79.56
11	100	13	120	267	266.59	82	82.64
12	90	12	130	258	258.12	85	85.97
13	90	14	130	261	260.16	81	81.37
14	90	13	125	280	278.56	91	91.65
15	80	12	125	249	249.13	90	91.08

ANN, artificial neural network.

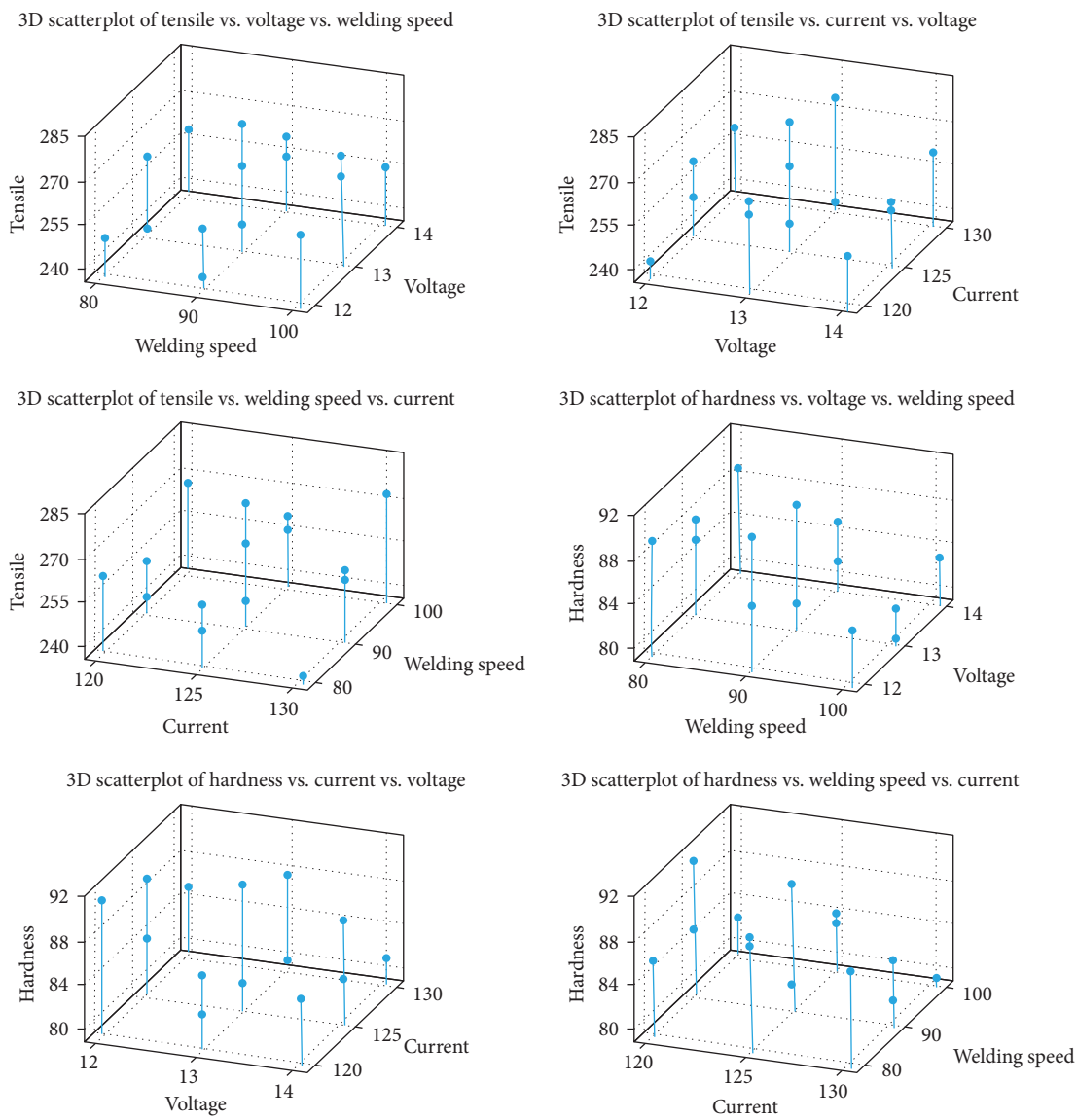

Figure 11: 3D scatter plot of output responses with activated TIG-flux-coated welded AA5083.

the interaction plots for tensile and hardness properties, respectively.

4. Neural Network Model for Predicting the Mechanical Responses

Neural network method was used to resolve the issues in more complicated responses. Therefore, neural network technique was created using the predicted values with appropriate weight basis process. Initially, the models were interconnected with various elements of training data with manipulation of weighted values. The real structure of neural network model was displayed in Figure 10. These networks values were bonded in proper way for each and every input factor that could lead to enhance the specified output responses. And the total sum of square responses were formed among the actual TIG-coated responses and predicted responses. Various researchers conducted numerous problems in the field of neural network method. In this research, Weka 3.8 software was utilized to compose the predicted response with selected A-TIG process parameters. In this technique, rate of learning, thrust, and hidden layers were the target and trial methods to maximize the coefficient of interrelations and to minimize the root mean square with error analysis. From the multilayer model with observation category, the predicted and investigational outputs were analyzed and are presented in Table 7. Table 7 predicts that artificial neural network (ANN) of output responses were enhanced effectively than the other investigational outcomes. Similarly, the 3D scatter plot also measured with experimental and predicted outcomes which fully relates with A-TIG-coated welded samples. Figure 11 shows the 3D scatter plot for output responses with various A-TIG-coated welded samples.

5. Conclusion

(1) The AA5083 and flux-coated nano-SiO_2 was synthesized successfully by the activated TIG welding process.

(2) The influence of nano-SiO_2 improves the welding strength with appropriate TIG process parameters.

(3) Process parameters were successfully optimized by Box–Behnken statistical method with the RSM technique.

(4) The output responses like tensile and hardness properties were enhanced effectively on the welded AA5083-H111.

(5) Due to the presence of nano-SiO_2 flux-coated optimum parameters, the optimal solution highly attains on sample 14 with a welding speed of 90 mm/min, voltage of 13 V, and current of 125 amps.

(6) Similarly, the regression analysis was utilized to analyze the parameters. Then the interaction plots and mean effects plots were successfully developed to improve the performances of process parameters.

(7) The ANOVA proves that the welding speed is the most influencing parameter than the other TIG welding parameters. The corresponding F value (0.09) of welding speed is less than other parameter values.

(8) Finally, the neural network approaches were influenced to observe the actual and predictable outcomes with support of 3D scatter plot.

(9) In the analysis of ANN, most of the outputs were improved by the predicted values and these process parameters were also validated with the ANOVA technique.

(10) The different particles categories like TiO_2, B4C, and chromium-based ceramic particles could be utilized in the upcoming research work.

Data Availability

The data used to support the findings of this study are included in the article. Should further data or information be required, these are available from the corresponding author upon request.

Conflicts of Interest

The authors declare that they have no conflicts of interest.

References

[1] D. Ren, Y. Jiang, X. Hu et al., "Investigation of tensile and high cycle fatigue failure behavior on a TIG welded titanium alloy," *Intermetallics*, vol. 132, Article ID 107115, 2021.

[2] A. Merneedi, L. Natrayan, S. Kaliappan et al., "Experimental investigation on mechanical properties of carbon nanotube-reinforced epoxy composites for automobile application," *Journal of Nanomaterials*, vol. 2021, Article ID 4937059, 7 pages, 2021.

[3] C. Meng, J. Yang, Z. Zhang et al., "Effect of laser bionic treatment on the microstructure and mechanical properties of TIG welded AZ31B magnesium alloy joints," *Materials Science and Engineering: A*, vol. 839, Article ID 142864, 2022.

[4] H. Rana, V. Badheka, P. Patel, V. Patel, W. Li, and J. Andersson, "Augmentation of weld penetration by flux assisted TIG welding and its distinct variants for oxygen free copper," *Journal of Materials Research and Technology*, vol. 10, pp. 138–151, 2021.

[5] L. Natrayan and M. S. Kumar, "Influence of silicon carbide on tribological behaviour of AA2024/Al_2O_3/SiC/Gr hybrid metal matrix squeeze cast composite using Taguchi technique," *Materials Research Express*, vol. 6, no. 12, Article ID 1265f9, 2019.

[6] V. Bhanu, A. Gupta, and C. Pandey, "Role of A-TIG process in joining of martensitic and austenitic steels for ultra-supercritical power plants—a state of the art review," *Nuclear Engineering and Technology*, vol. 54, no. 8, pp. 2755–2770, 2022.

[7] A. B. Zala, N. I. Jamnapara, C. S. Sasmal, S. Sam, and M. Ranjan, "Study of microstructure & mechanical properties of TIG welded aluminized 9Cr-1Mo steel," *Fusion Engineering and Design*, vol. 176, Article ID 113038, 2022.

[8] S. Yogeshwaran, R. Prabhu, L. Natrayan, and R. Murugan, "Mechanical properties of leaf ashes reinforced aluminum alloy

metal matrix composites," *International Journal of Applied Engineering Research*, vol. 10, no. 13, pp. 11048–11052, 2015.

[9] C. Meng, Z. Zhang, J. Yang, W. Zhuang, and H. Shi, "Effect of laser bionic treatment on fatigue crack growth behavior of TIG welded AZ31B magnesium alloy joint," *Materials Letters*, vol. 320, Article ID 132334, 2022.

[10] M. S. Kumar, L. Natrayan, R. D. Hemanth, K. Annamalai, and E. Karthick, "Experimental investigations on mechanical and microstructural properties of Al_2O_3/SiC reinforced hybrid metal matrix composite," *IOP Conference Series: Materials Science and Engineering*, vol. 402, Article ID 012123, 2018.

[11] A. K. Unni and M. Vasudevan, "Numerical modelling of fluid flow and weld penetration in activated TIG welding," *Materials Today: Proceedings*, vol. 27, Part 3, pp. 2768–2773, 2020.

[12] P. Sharma and D. K. Dwivedi, "Improving the strength-ductility synergy and impact toughness of dissimilar martensitic–austenitic steel joints by A-TIG welding with wire feed," *Materials Letters*, vol. 285, Article ID 129063, 2021.

[13] K.-H. Tseng and C.-Y. Hsu, "Performance of activated TIG process in austenitic stainless steel welds," *Journal of Materials Processing Technology*, vol. 211, no. 3, pp. 503–512, 2011.

[14] S. Chai, S. Zhong, Q. Yang et al., "Transformation of laves phases and its effect on the mechanical properties of TIG welded Mg–Al–Ca–Mn alloys," *Journal of Materials Science & Technology*, vol. 120, pp. 108–117, 2022.

[15] A. R. Pavan, N. Chandrasekar, B. Arivazhagan, S. Kumar, and M. Vasudevan, "Study of arc characteristics using varying shielding gas and optimization of activated-TIG welding technique for thick AISI 316L(N) plates," *CIRP Journal of Manufacturing Science and Technology*, vol. 35, pp. 675–690, 2021.

[16] A. Babbar, A. Kumar, V. Jain, and D. Gupta, "Enhancement of activated tungsten inert gas (A-TIG) welding using multi-component TiO_2–SiO_2–Al_2O_3 hybrid flux," *Measurement*, vol. 148, Article ID 106912, 2019.

[17] T. Sakthivel, M. Vasudevan, K. Laha et al., "Comparison of creep rupture behaviour of type 316L(N) austenitic stainless steel joints welded by TIG and activated TIG welding processes," *Materials Science and Engineering: A*, vol. 528, no. 22-23, pp. 6971–6980, 2011.

[18] M. Muzamil, J. Wu, M. Akhtar, V. Patel, A. Majeed, and J. Yang, "Multicomponent enabled MWCNTs-TiO_2 nano-activating flux for controlling the geometrical behavior of modified TIG welding joint process," *Diamond and Related Materials*, vol. 97, Article ID 107442, 2019.

[19] J. J. Vora and V. J. Badheka, "Experimental investigation on microstructure and mechanical properties of activated TIG welded reduced activation ferritic/martensitic steel joints," *Journal of Manufacturing Processes*, vol. 25, pp. 85–93, 2017.

[20] J. Wu, Z. Wang, S. Lin et al., "Effect of fast-frequency pulsed waveforms on the microstructure and mechanical properties of Ti–6Al–4V alloy welded by FFP-TIG," *Journal of Materials Research and Technology*, vol. 20, pp. 516–531, 2022.

[21] L. Natrayan, R. Anand, and S. Santhosh Kumar, "Optimization of process parameters in TIG welding of AISI 4140 stainless steel using Taguchi technique," *Materials Today: Proceedings*, vol. 37, Part 2, pp. 1550–1553, 2021.

[22] J. Zhang, Y. Huang, D. Fan et al., "Microstructure and performances of dissimilar joints between 12Cr2Mo1R steel and 06Cr18Ni11Ti austenitic stainless steel joined by AA-TIG welding," *Journal of Manufacturing Processes*, vol. 60, pp. 96–106, 2020.

[23] A. Baghel, C. Sharma, S. Rathee, and M. Srivastava, "Activated flux TIG welding of dissimilar SS202 and SS304 alloys: effect of oxide and chloride fluxes on microstructure and mechanical properties of joints," *Materials Today: Proceedings*, vol. 47, Part 19, pp. 7189–7195, 2021.

[24] G. Qin, C. Feng, and H. Ma, "Suppression mechanism of weld appearance defects in tandem TIG welding by numerical modeling," *Journal of Materials Research and Technology*, vol. 14, pp. 160–173, 2021.

[25] B. Qin, F.-C. Yin, C.-Z. Zeng, J.-C. Xie, and J. Shen, "Microstructure and mechanical properties of TIG/A-TIG welded AZ61/ZK60 magnesium alloy joints," *Transactions of Nonferrous Metals Society of China*, vol. 29, no. 9, pp. 1864–1872, 2019.

Hindawi
Journal of Nanomaterials
Volume 2023, Article ID 6453166, 9 pages
https://doi.org/10.1155/2023/6453166

Research Article

Tribological Behavior on Stir-Casted Metal Matrix Composites of Al8011 and Nano Boron Carbide Particles

N. Vinayaka,[1] K. G. Jaya Christiyan,[2] Sarange Shreepad,[3] S. N. Padhi,[4] Sunil G. Dambhare,[5] Ranjit kumar Puse,[6] K. Gayathri,[7] Aniket Bhanudas Kolekar,[5] and S. Nagarajan[8]

[1]*Department of Aeronautical Engineering, Nitte Meenakshi Institute of Technology, Yelahanka, Bengaluru 560064, India*
[2]*Department of Mechanical Engineering, M S Ramaiah Institute of Technology, Bengaluru 560022, India*
[3]*Department of Mechanical Engineering, Ajeenkya D Y Patil School of Engineering, Lohegaon, Pune, India*
[4]*Department of Mechanical Engineering, Koneru Lakshmaiah Education Foundation, Vaddeswaram, Andhra Pradesh, India*
[5]*Department of Mechanical Engineering, Dr D Y Patil Institute of Engineering Management and Research, Akurdi, Pune 411044, India*
[6]*Department of Physical Science Chemistry, Rabindranath Tagore University, Bhopal, Madhya Pradesh, India*
[7]*Department of Physics, Academy of Maritime Education and Training, Kanathur, Chennai 603112, India*
[8]*Department of Mechanical Engineering, College of Engineering and Technology, Mettu University, Mettu, Ethiopia*

Correspondence should be addressed to S. Nagarajan; s.nagarajan@meu.edu.et

Received 5 October 2022; Revised 29 October 2022; Accepted 24 November 2022; Published 15 February 2023

Academic Editor: Ramesh Balasubramanian

The aluminum metal matrix composites were broadly exploited in the applications of automotive, aerospace, and other defense with functionally graded materials-related application. Above applications definitely required excellent mechanical characteristics. Therefore, in this way, the major attempt was made on the nano-based composites with aluminum alloy utilization. In this research, aluminum alloy AA8011 and the ceramic-based reinforcement particles of nano boron carbide (B_4C) were selected for producing the metal matrix composites by the liquefying process or stir casting route. The weight percentage of nano boron carbide particles having 15 wt% was subjected to add into the aluminum alloy during the stir casting process. Then, processed nano boron carbide and AA8011 specimens were prepared to conduct tribological behaviors with various processing conditions like sliding velocity, setting wear temperature, and applied load by the tribometer setup. The scanning electron microscope was employed to examine the processed composites samples and worn-out surface samples. Finally, the multiobjective optimization was used to measure the individual performances of the tribological parameters by the gray relational technique.

1. Introduction

Aluminum-based metal matrix composites are well-admired materials to produce the enhanced composites material by the addition of exclusive strength and maximum modulus of elasticity. Owing to these processed aluminum-based metal matrix composites, it contains maximum wear resistance, lesser thermal expansion, and greater withstand of vibrating capability. The aluminum metal matrix compounds like to the top quality appearance even in the poor-based aluminum composites. These materials are come from bielement materials as well as to be matrix- and ceramic-based material or raw composites in the reinforcing elements [1–3].

In order to get the best material properties when combined with metal matrix composites, the various metals are grouped with the highest reinforced content. The irregular strengthened MMCs or aluminum metal matrix composites (AMMCs) possess lesser hardness and poorer wear resistances are the major factors that would not be reached the maximum attained performances in the tribological characteristics. In their low MMCs or AMMCs, it definitely enhances the mechanical properties when combine to the proper reinforcing particle especially in the nano-based

reinforcing particles and also selecting the process parameters or the processing technique. For that reason, these AMMCs are started in the widespread with aerospace, vehicle, and shipbuilding applications to boost their residential properties top quality in the metal matrix compounds than the unreinforced base material [4–6].

AMMCs disclose updated characteristics in the list below problems like wear resistance, specific mass ratio, abrasion, and rust resistance. Besides, additional buildup is utilized to improve the properties that are attained in the MMCs. For example, damping, electrical as well as thermal conductivity buildings in the textile-based applications as well as it plays a crucible role in the renovation of tribological performances in the numerous usages. From the current research studies, the metal matrix composites had optimum mechanical strength when it is reinforced with nanosized strengthening particles. When MMCs-based composites were being made, low ductility was substituted for good ductility, and this was enhanced simultaneously [7–9].

Additionally, nanosized reinforcements likewise enhance the effectiveness of the metal products as well as ductility structure. Among the various casting processes, the stir casting was the less expensive process and also enhances the mechanical properties from the processed aluminum metal matrix composites. Aluminum-based metal matrix composites generally strengthened by the various nanoceramic particles like silicon carbide, aluminum oxide, titanium oxide, tungsten carbide, and graphene- and boron-based carbides. These reinforcing materials are easily diffused into the any base aluminum alloys. Similarly, the agrowaste product was also prepared as the nanomaterials to produce the metal matrix composites. Some issues are happened during the casting between the base aluminum alloy and other agro-nanoparticles [10–13].

From the various nanoreinforcement particles, nano boron carbide particles are the most hardest particles, maximum stiffness, lesser compressibility, and also provide the better ballistic performance when utilizing with the appropriate aluminum alloys. Consequently, the reduced expense technique from various stir casting processes generated the metal matrix composites and also vortex was executed to develop the mixing in the uniform scattering by use of automated mechanical stirrer.

In this stir casting process, the main issues were wettability and also the melt. It is more called for to get over these concerns with blending of nanostrengthened fragments. Because of the better wettability of nanoparticles, uniform diffusion was generated in the matrix composites. The migration of load was easily moved from the matrix to the strengthened reinforcement in the matrix composite materials. Because of the better bonding structure, it was accumulated while doing so metal matrix composites. It leads to improving the upgraded system to achieve the exceptional mechanical-based characteristics in the nano-processed metal matrix composites [14–19].

From the above detailed reviews, it has been initiated that their metal matrix composites are enhancing the mechanical characteristics and improving the tribological performances. So, this research mainly aims to produce the aluminum-based metal matrix composites from the base material of AA8011 and superior characteristics of nano boron carbide particles and this alloy mainly utilized in the building materials, electrical sectors, and packaging of drugs and food. From the processed nanocomposites, tribological performances were accomplished by the appropriate processing conditions. Then, the tribological behaviors are analyzed by Taguchi-based technique to find the optimal processing parameters. Scanning electron microscope (SEM) analysis was used to measure the wear tracks and confirmation for the presence of nanoparticles during the stir casting process. Figure 1 shows the outline of the graphical abstract.

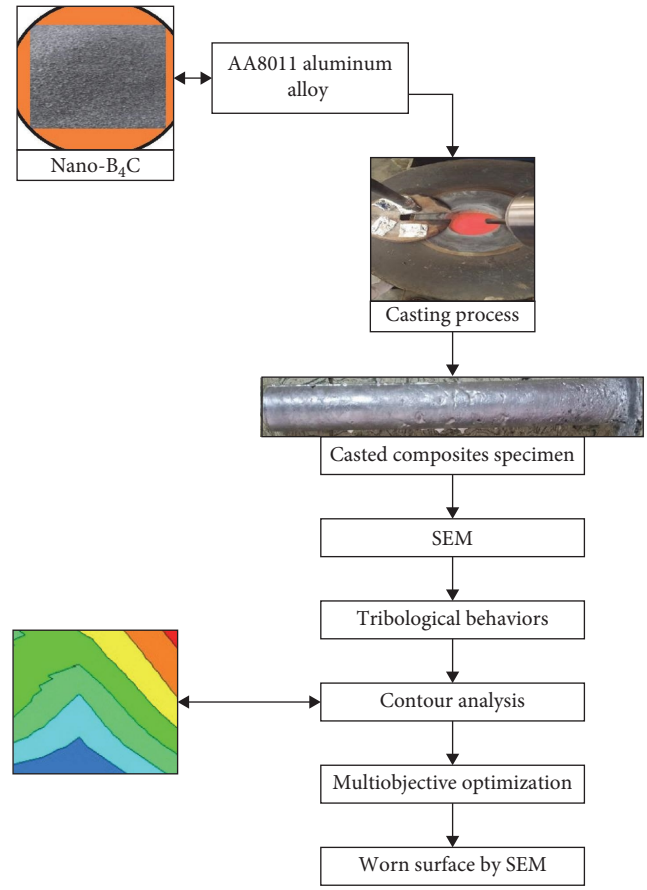

Figure 1: Experimental layout.

2. Base Material, Nanoparticle Reinforcements, and Preparation of Nano-Based Composites

The predominant aluminum alloy AA8011 was the working material. Due to this, alloy was extremely not hard and right material for space shuttle applications, best heat exchanger component, maximum deep drawing qualities, and other tanking purposes. It contains better features like workability, density, formability, ductility, corrosion resistance, and enhanced mechanical tensile strength. The chemical compositions of AA8011 aluminum alloy are 0.52 of Si, 0.28 of Mg, 0.13 of Cu, 0.028 of Cr, 0.74 of Fe, 0.46 of Mn, 0.084 of Zn, 0.016 of Ti, and balance of aluminum, respectively. In the combinational elements, this aluminum alloy AA8011 was specifically enhances in the aerospace component fabrication. Also, this material

Table 1: Tribological process parameters with Taguchi L9.

Wear samples order	Sliding velocity (m/s)	Setting wear temperature (°C)	Applied load (N)
1	2.25	30	25
2	2.25	40	35
3	2.25	50	45
4	3	30	35
5	3	40	45
6	3	50	25
7	3.75	30	45
8	3.75	40	25
9	3.75	50	35

was highly used in the maximum-related strength applications and weldments. Based on above situations, this research focused to select the AA8011 aluminum alloy that was the base material. The mechanical properties of AA8011 are 2,689 kg/m^3 of density, 110 MPa of tensile strength, 665°C of melting point, 65 of hardness, and 238 W/mk of thermal conductivity, respectively [20].

Based on the application, the respected base material chosen was the primary factors for every process. But, in this lightweight applications, lightweight metal AA8011 was the selected base material in this investigation. So, this selected base material was utilized as the matrix materials to compose the metal matrix composites with selected appropriate reinforcements. Therefore, in this investigation, proper reinforcements have special features that contain temperature resistance, stiffness, and strength. The processing technique was also important prospects to compose the better metal matrix composites. The specially made lightweight metal matrix composites were prepared by the quicker and easier process. In this way, stir casting process was most reasonable less expensive process over the other solidification techniques. Finally, the completed metastatic arrangements were made on the processed MMCs by the stir casting process. Considering the above issues, in this study, boron carbide with nanosized particles having the 25 μm sizes was selected as the reinforcement material.

Compared to other hardness material like boron nitride and diamond, boron carbide was superior hardened base abrasive material. This boron carbide generally contains superior abrasive characteristics, fabricating components in their specialized materials with less cost than the other reinforcements like aluminum oxide and silicon carbide. The boron carbide materials were highly utilized in the various applications like rocket propellants, welding applications, and defense-based components. The boron carbide also possesses lower thermal conductivity that results in lesser thermal resistance.

Processing technique is also an important factor to produce the aluminum metal matrix composites by the proper features. Therefore, in this investigation, liquid metallurgy-based stir casting process was utilized to compose AMMCs by the influence of aluminum alloy AA8011 and boron carbide nanoparticles. The B_4C with 15 wt% was mixed with the base alloy of AA8011, which was mixed together by the stir casting process with maintained process parameters like 800°C which was under the guidance of graphite crucible. Before adding of boron carbide into the aluminum alloy under the stir casting, reinforcement particles must be preheated at 300°C to eradicate the foreign particles than that the reinforcements were utilized to mixing together in the semi-liquid of AA8011 with proper maintaining parameters at 300 rpm of mechanical stirrer for 5–10 min and stirring speed at 100 m/s. Finally, the molten composites were poured into the mold to ready for the mechanical tests. Then, the solidified composites were attained in the mold which made up of cast iron to compose the cylindrical-based specimens. Next to mold, the required dimension of wear samples having the sizes of 10 and 30 mm of diameter and pin length was achieved to produce the wear performances. As per the condition of G-99, all the specimens were prepared. During the tribological experiments, sliding velocity, setting wear temperature, and applied load were the process parameters to conduct the investigations. The Taguchi L9 method was suitable to design the process parameters for tribological performances and is shown in Table 1. Figure 2 shows the SEM image of processed nanocomposites between B_4C/AA8011.

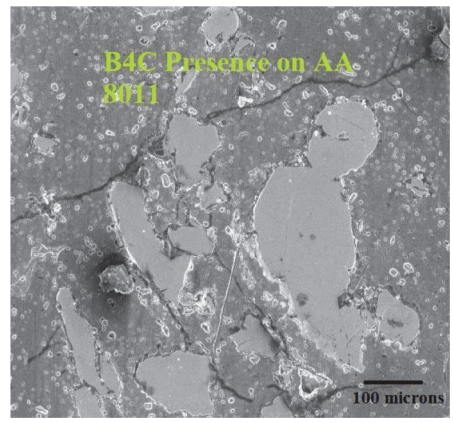

Figure 2: SEM micrographsfor stir-casted composites B_4C/AA8011.

As shown in Figure 2, the SEM reveals the presence of boron carbide nanoparticles on the AA8011 by the stir casting process with higher magnification. This image was clearly indicated the presence of boron carbide with homogeneous dispersion within the aluminum alloy AA8011. By adding the 15 wt%, B_4C was successfully accompanied into

Table 2: Wear rate and coefficient of friction on AA8011 and B_4C nanocomposites.

Wear samples order	Sliding velocity (m/s)	Setting wear temperature (°C)	Applied load (N)	Wear rate (mm^3/min)	Friction coefficient
1	2.25	30	25	2.451	0.159
2	2.25	40	35	3.684	0.651
3	2.25	50	45	2.985	0.416
4	3	30	35	2.485	0.162
5	3	40	45	3.124	0.528
6	3	50	25	3.951	0.591
7	3.75	30	45	3.012	0.492
8	3.75	40	25	4.005	0.752
9	3.75	50	35	4.415	0.786

the aluminum alloy with appropriated stir casting processing parameters. At the same time, the B_4C was well synthesized and better dispersion was attained by the liquefying process. Due to the maximum amount of boron carbide, it created the well-bonded structures against the aluminum alloy. The grain boundaries are also well presented and compose the better nanocomposites. Owing to improve the grain boundaries, it reduces the grain structure and the intermetallic particles are well bind together with well-suited optimal processing conditions.

3. Results and Discussion

3.1. Wear Rate and Friction Coefficient on Processed Nano-B_4C Composites. The pin on disk tribometer equipment was used to conduct the tribological behavior as per the ASTM of G-99. The working processing conditions of tribological performances were implemented by the following parameters like sliding velocity (2.25–3.75 m/s), setting wear temperature (30–50°C), and applied load (25–45 N), respectively.

The tribometer contains EN-32 that is made of spinning disk having the maximum hardness of 65 HRC which act as the counterweight against the testing sample pin by the influence of the abovementioned processing conditions. Other than the varying process, parameters sliding velocity, setting wear temperature, and applied load, sliding distance was constant for all the level of various process parameters. Before conducting the wear behavior, all the samples were polished as per the standards to improve the surface enhancement on the processed composites. The composites wear specimens were employed to produce the wear rate and coefficient of friction, respectively. As shown in Table 1, all the processing parameters were subjected to conduct the wear test for analyzing the tribological characteristics like wear rate and coefficient of friction. Table 2 shows the outcomes of wear rate and coefficient of friction.

3.2. Contour Interactions on the Various Tribological Process Parameters on Responses. Figure 3(a)–3(c) shows the contour experimentation between the various tribological process parameters within the effect of wear rate. Figure 3(a) shows the sliding velocity and wear temperature on the outcomes of wear rate, and it is revealed that the minimum wear rate was attained between the increasing of sliding velocity from 2.5 to 3.0 m/s and the combinations of wear temperature at less range of 30°C. The lesser wear rate was composed by the presence of boron carbide particles and it was against the sliding and temperature so that the wear rate also enhanced. Figure 3(b) shows the wear temperature and applied load on the processed composites to compose the wear rate, and it is understood that the enhanced wear resistance was highly attained between the combinations of lesser wear temperature and increasing applied load at 25–35 N. Figure 3(c) exhibits the wear performing process parameters like applied load and sliding velocity on the wear rate of the processed nanocomposites of AA8011 and B_4C, respectively, and it is implicit that the lesser wear was occurred between the lesser sliding velocity and medium of the applied load.

Figure 4(a)–4(c) exhibits the contour investigations involving the assorted tribological process parameters within the consequence of friction coefficient. Figure 4(a) shows the sliding velocity and wear temperature on the upshot of friction coefficient, and it is discovered that the minimum friction was generated between increasing of sliding velocity from 2.5 to 3.0 m/s and the combinations of wear temperature at less range of 30°C. The lesser friction was formed by the existence of maximum weight percentage of boron carbide particles and it was against the sliding and temperature that result in decreasing the friction. Figure 4(b) displays the wear temperature and applied load on the synthesized composites to produce the friction coefficient.

As shown in Figure 4(b), it is implicit that the superior friction coefficient was exceedingly accomplished between the arrangements of slighter wear temperature and rising applied load from 25 to 35 N. Figure 4(c) demonstrates the tribological performing process parameters like applied load and sliding velocity on the friction coefficient of the stir-casted nanocomposites of AA8011 and B_4C, respectively, and it is implied that the minor friction coefficient was take place between the lower and medium range of sliding velocity (2.25 and 3.0 m/s) and applied load (25 and 35 N). Figure 5 shows the individual responses of wear rate and friction coefficient by the nine various processing conditions.

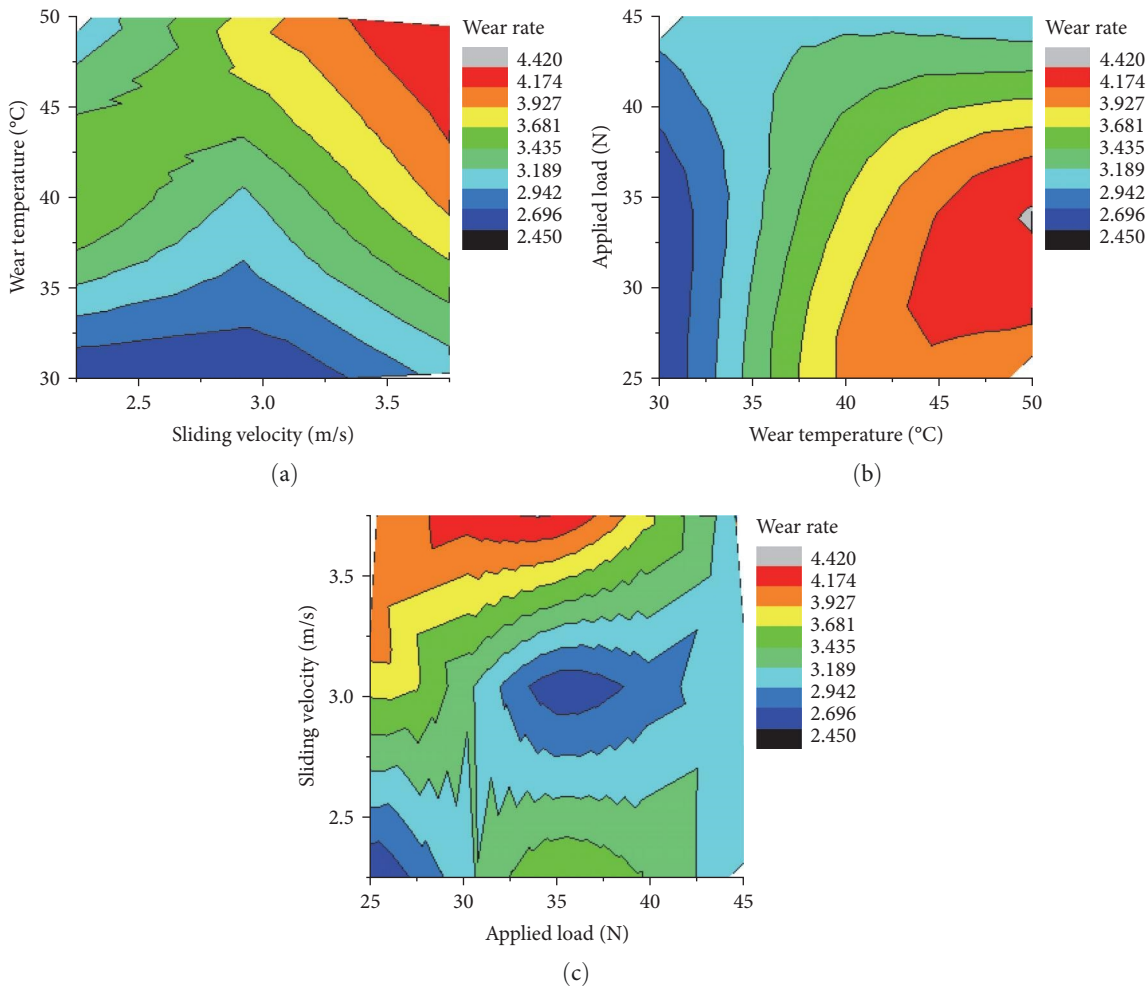

Figure 3: (a–c) Tribological process parameters on wear rate.

3.3. Multiobjective Optimization on the Tribological Responses by Gray Analysis. In this research, the wear rate and friction coefficient were successfully accomplished by the tribometer technique by the various influencing process parameters like sliding velocity, wear temperature, and applied load. Now those processing parameters required one appropriate technique to validate optimal parameters. Therefore, based on above mentioned issues are resolved by the gray relational analysis [21]. Among the various multiobjective techniques, gray relational analysis was most suited method to solve the difficult issues among the different implemented parameters for any processing. Now, this technique was utilized to confirm that the multiphase parameters were converted into the single objective. In this method, various steps like standardization, calculating the sequence, gray coefficient, and composite gray relational grade (GRG) and ranking method were utilized to produce the optimal process parameters. Table 3 shows the initialization of GRG with outcomes of wear rate and friction coefficient. As shown in Table 3, smaller the better option was implemented to discover the individual sequence of both the responses along with GRG. As shown in Table 3, 0 values were attained at the specimen of 1 and it was further established into the coefficient with gray to find the composite GRG and best ranking position. Table 4 shows the rank order and its coefficient of wear rate and friction coefficient responses. As shown in Table 4, better composites GRG and best rank were accumulated at the process parameters 2.25 m/s of sliding velocity, 30°C of setting temperature, and 25 N of applied load that compose the better wear rates and lesser friction. Also, the presence of boron carbide reduced the friction between the composite workpiece and counter disk of steel. Figure 6 exhibits the rank arrangements for mixed responses of wear rates and friction coefficient, and sample 1 accommodates rank 1.

3.4. Worn Surface Analysis of Processed Nano Boron Carbide and AA8011 Composites. Figures 7 and 8 show the micrograph of worn surface on the processed nanocomposites between the AA8011 and boron carbide, and belong to the worn surfaces of optimal parameters at 2.25 m/s of sliding velocity, 30°C of wear temperature and 25 N of applied load and poor parameters at 3.75 m/s of sliding velocity, 50°C of wear temperature, and 35 N of applied load, respectively. As shown in Figure 7, SEM analysis reveals that the wear track was slightly formed due to the maximum content of B_4C that was occupied to resist the wear which results in less wear

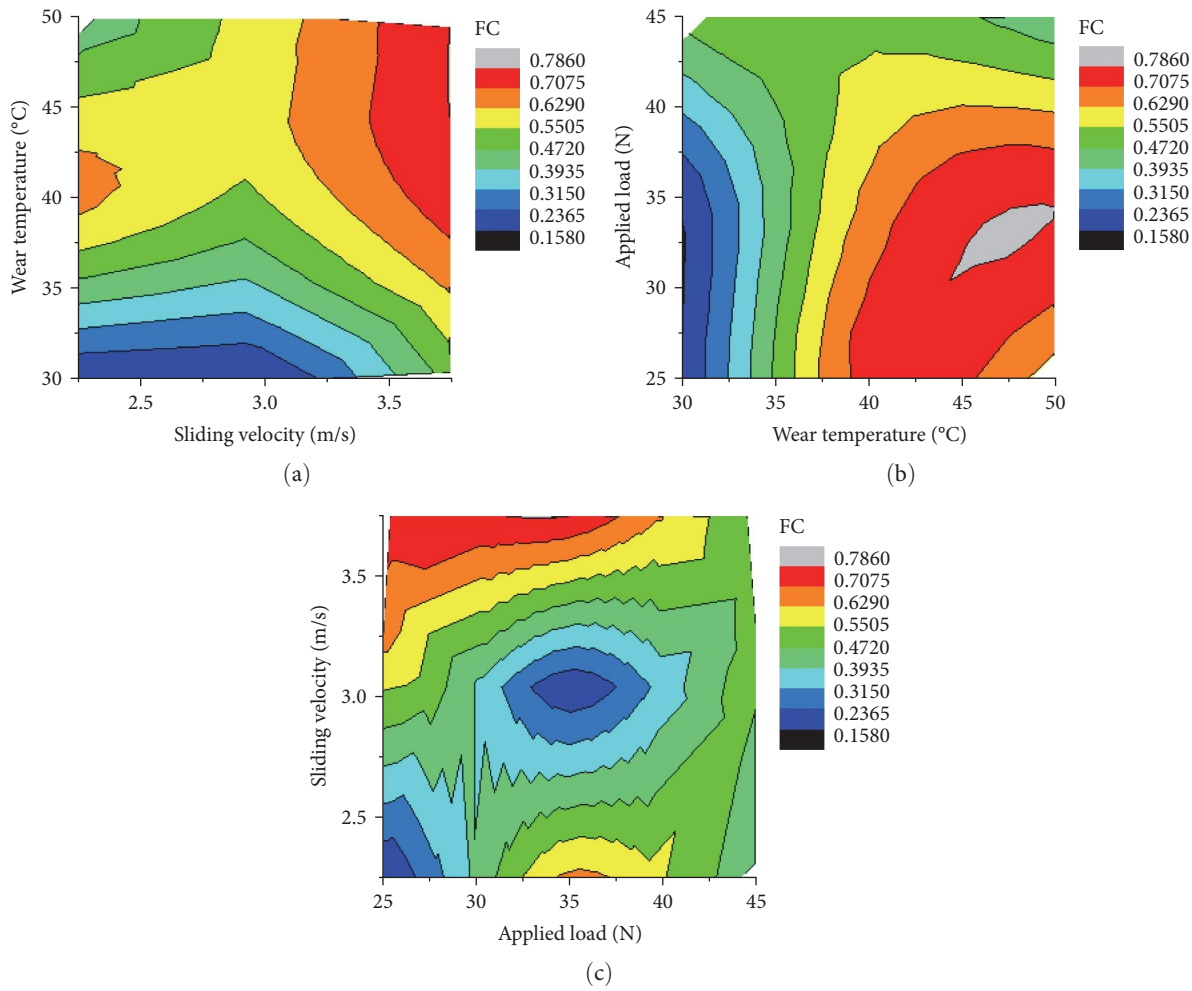

Figure 4: (a–c) Tribological process parameters on friction coefficient.

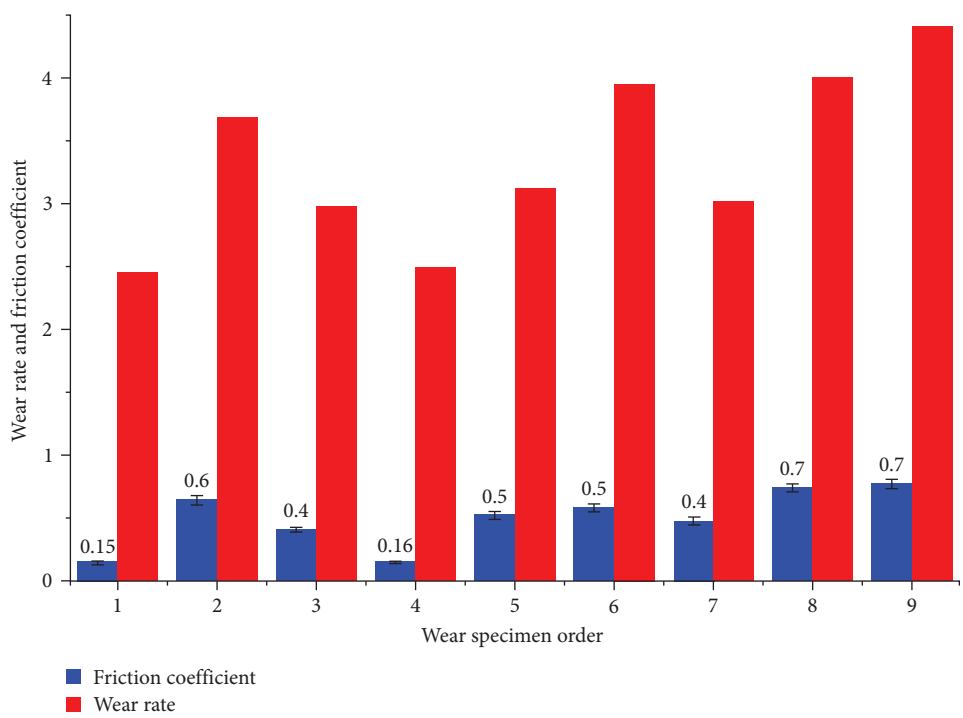

Figure 5: Wear rate and friction coefficient on various wear specimens.

Table 3: Standardization and sequence of GRG on processed composites.

Wear samples order	Wear rate (mm^3/min)	Friction coefficient	Standard GRG (WR)	Standard GRG (FC)	Sequence GRG (WR)	Sequence GRG (FC)
1	2.451	0.159	0.000	0.000	0.000	0.000
2	3.684	0.651	−0.628	−0.785	0.628	0.785
3	2.985	0.416	−0.272	−0.410	0.272	0.410
4	2.485	0.162	−0.017	−0.005	0.017	0.005
5	3.124	0.528	−0.343	−0.589	0.343	0.589
6	3.951	0.591	−0.764	−0.689	0.764	0.689
7	3.012	0.492	−0.286	−0.531	0.286	0.531
8	4.005	0.752	−0.791	−0.946	0.791	0.946
9	4.415	0.786	−1.000	−1.000	1.000	1.000

GRG, gray relational grade.

Table 4: Gray coefficient and rank position of wear rates and friction coefficient.

Wear samples order	Wear rate (mm^3/min)	Friction coefficient	Coefficient (WR)	Coefficient (FC)	Mixed GRG	GRG rank
1	2.451	0.159	1.000	1.000	1.000	1
2	3.684	0.651	0.443	0.389	0.416	6
3	2.985	0.416	0.648	0.550	0.599	3
4	2.485	0.162	0.967	0.991	0.979	2
5	3.124	0.528	0.593	0.459	0.526	5
6	3.951	0.591	0.396	0.421	0.408	7
7	3.012	0.492	0.636	0.485	0.561	4
8	4.005	0.752	0.387	0.346	0.367	8
9	4.415	0.786	0.333	0.333	0.333	9

GRG, gray relational grade.

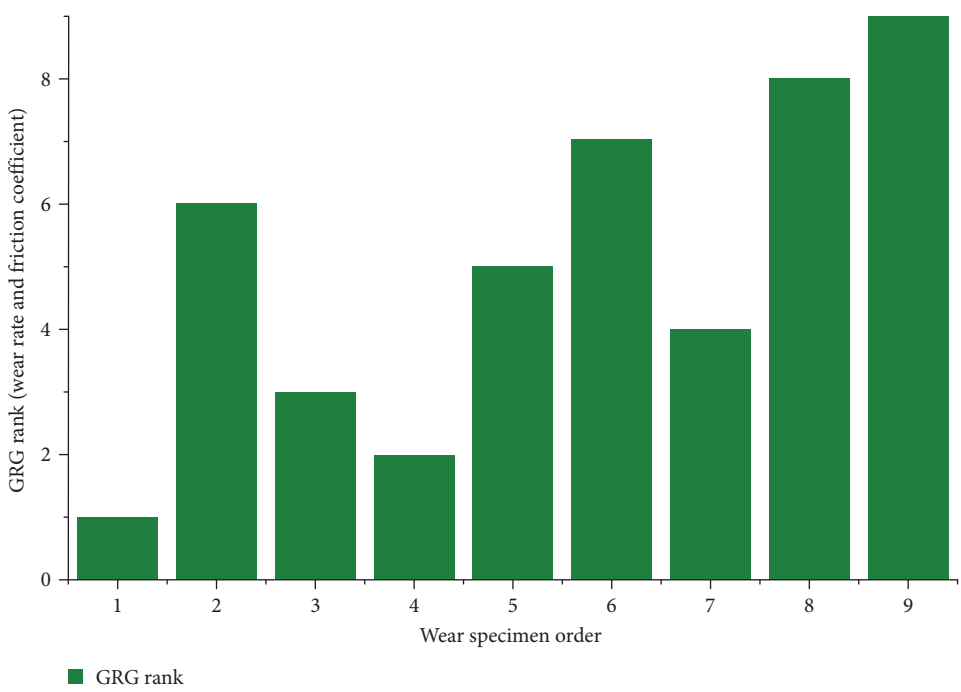

Figure 6: Gray relational grade rank for wear rates and friction coefficient.

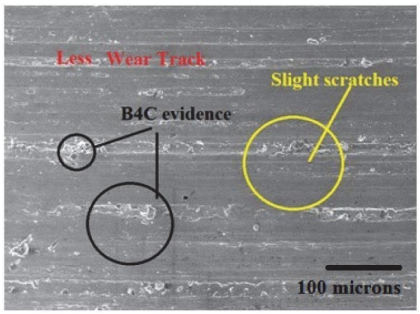

Figure 7: SEM worn surfaces on optimal parameters.

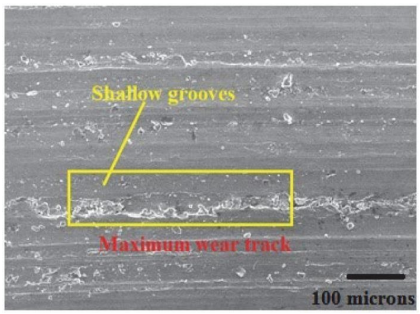

Figure 8: SEM worn surfaces on poorer parameters.

track that was formed. Process parameters were major reason to reduce the wear track due to less wear temperature along with less sliding velocity and low applied load. As shown in Figure 8, it was understood that the SEM analysis presents the maximum wear track that was generated by the maximum of sliding velocity and applied load. By utilizing maximum temperature, setting was initiated to improve the wear rate and coefficient of friction. At the same time, both processed composite specimens produced the better results due to the presence of boron carbide and this particles resist the sliding distance and maximum working load. The maximum weight percentage (15 wt%) was the major reason to enhance the better wear resistance and lesser coefficient of friction. It is revealed that the maximum frictional heat was generated between the specimen and counter disk, so that the heat was not increased on the specified composites by the presence of nano boron carbide particles [20–25]. The presence of nanosized boron carbide was a major aspect to improve their wear rates and similarly, the lesser setting temperature was another reason to reduce the wear tracks.

4. Conclusion

In this research, aluiminum alloy AA8011 and nano boron carbide particles were successfully synthesized by the liquefy stir casting process. During the casting process, appropriate setting conditions like mechanical stirrer speed, melting temperature, and preheating temperatures were accurately utilized to compose the better nanocomposites. The tribological behaviors like sliding velocity, setting wear temperature, and applied load were majorly influence to compose the fine wear rates and lesser friction coefficient during the process of nanocomposites. The multiobjective optimization technique of gray method effectively produced the optimal process parameters from the L9 Taguchi design. The maximum wear resistance and minimum coefficient of friction were composed at the parameters at 2.25 m/s of sliding velocity, 30°C of wear temperature, and 35 N of working load. Similarly, the SEM micrograph reveals that the presence of boron carbide on the AA8011 aluminum alloy showed the fine particles by the uniform arrangements during the stir casting process.

Data Availability

The data used to support the findings of this study are included within the article.

Conflicts of Interest

The authors declare that they have no conflicts of interest.

References

[1] A. E. A. Al-maamari, A. K. M. A. Iqbal, and D. M. Nuruzzaman, "Mechanical and tribological characterization of self-lubricating Mg–SiC–Gr hybrid metal matrix composite (MMC) fabricated via mechanical alloying," *Journal of Science: Advanced Materials and Devices*, vol. 5, no. 4, pp. 535–544, 2020.

[2] D. Bartkowski and G. Kinal, "Microstructure and wear resistance of Stellite-6/WC MMC coatings produced by laser cladding using Yb:YAG disk laser," *International Journal of Refractory Metals and Hard Materials*, vol. 58, pp. 157–164, 2016.

[3] O. B. Bembalge and S. K. Panigrahi, "Exploring a hybrid manufacturing process to develop high performance age hardenable ultrafine grained AA6063/SiC nano-composite sheets," *Journal of Manufacturing Processes*, vol. 70, pp. 508–517, 2021.

[4] S. Devaraj, R. Malkapuram, and B. Singaravel, "Performance analysis of micro textured cutting insert design parameters on machining of Al-MMC in turning process," *International Journal of Lightweight Materials and Manufacture*, vol. 4, no. 2, pp. 210–217, 2021.

[5] A. M. El-khatib, I. I. Bondouk, K. M. Omar, A. Hamdy, and M. El-khatib, "Impact of changing electrodes dimensions and different ACs on the characteristics of nano composites NZnO/MWCNTs prepared by the arc discharge method," *Surfaces and Interfaces*, vol. 29, Article ID 101736, 2022.

[6] V. Khalili, C. Sengstock, Y. Kalchev, J. Pfetzing-Micklich, and J. Frenzel, "Exploring MgO/HA ceramic nano-composites for biodegradable implants: exploring biological properties and micromechanics," *Surface and Coatings Technology*, vol. 445, Article ID 128730, 2022.

[7] S. Khoshsima, S. Mertdinç, A. Motallebzadeh, Z. Altıntaş, D. Ağaoğulları, and Ö. Balcı-Çağıran, "Enhanced hardness and wear resistance of Al-based hybrid MMCs by using of composite metal boride reinforcement particles," *Materials Chemistry and Physics*, vol. 288, Article ID 126377, 2022.

[8] L. Tharanikumar, B. Mohan, and G. Anbuchezhiyan, "Enhancing the microstructure and mechanical properties of Si_3N_4–BN strengthened Al–Zn–Mg alloy hybrid nano composites using vacuum assisted stir casting method," *Journal of Materials Research and Technology*, vol. 20, pp. 3646–3655, 2022.

[9] U. Müller, S. Prinz, S. Barth, and T. Bergs, "Simulation of friction between diamond and polycrystalline cubic boron nitride," *Procedia CIRP*, vol. 104, pp. 44–49, 2021.

[10] A. Naeimi, F. E. Ghadi, S. M. Saadatkhah, and M. Honarmand, "First and efficient bio-nano composite, SnO_2/Calcite based on Cypress leaves and eggshell wastes, for cytotoxic effects on HepG2 liver cancer cell lines and its antioxidant and antimicrobial activity," *Journal of Molecular Structure*, vol. 1259, Article ID 132690, 2022.

[11] K. Ramasubramanian, N. Arunachalam, and M. S. Ramachandra Rao, "Wear performance of nano-engineered boron doped graded layer CVD diamond coated cutting tool for machining of Al-SiC MMC," *Wear*, vol. 426-427, Part B, pp. 1536–1547, 2019.

[12] H. Shi, Z. Dou, Y. Meng, and T. Zhang, "Effects of reactants proportions on features of in-situ magnesiothermic self-propagating high temperature synthesized boron carbide powder," *Ceramics International*, vol. 48, no. 22, pp. 33400–33411, 2022.

[13] S. Sankara Raju, G. Srinivasa Rao, and C. Samantra, "Wear behavioral assessment of Al-CSAp-MMCs using grey-fuzzy approach," *Measurement*, vol. 140, pp. 254–268, 2019.

[14] J. C. Songara, J. N. Patel, and A. A. Mungray, "Preparation and characterization of PAA/GG-zeolite nano-composite hydrogel for agricultural applications," *Journal of the Indian Chemical Society*, vol. 99, no. 10, Article ID 100686, 2022.

[15] S. Thangaraj, G. M. Pradeep, M. S. Heaven Dani, S. Mayakannan, and A. Benham, "Experimental investigations on tensile and compressive properties of nano alumina and arecanut shell powder reinforced polypropylene hybrid composites," *Materials Today: Proceedings*, vol. 68, Part 6, pp. 2243–2248, 2022.

[16] T. Wang, X. Liu, S. Chen, J. Lei, and X. Song, "Study on microstructure and tribological properties of nano/micron TiC/TC4 composites fabricated by laser melting deposition," *Journal of Manufacturing Processes*, vol. 82, pp. 296–305, 2022.

[17] Y. Wang, Y.-D. Wu, and G.-H. Zhang, "Boronation reaction between molybdenum or tungsten powder and boron carbide in aluminium melt," *International Journal of Refractory Metals and Hard Materials*, vol. 105, Article ID 105813, 2022.

[18] H. Werheit, B. Herstell, W. Winkelbauer et al., "Electrical conductivity of boron carbide from ∼5 to ∼2100 K in the whole homogeneity range," *Solid State Sciences*, vol. 132, Article ID 106987, 2022.

[19] V. Zamora, F. J. Martínez-Vázquez, F. Guiberteau, and A. L. Ortiz, "Spark-plasma sintering of boron carbide–silicon carbide composites at 1400°C from B_4C + Si: densification and sintering/reaction mechanisms," *Journal of the European Ceramic Society*, vol. 42, no. 15, pp. 6876–6888, 2022.

[20] A. Aabid, M. A. Murtuza, S. A. Khan, and M. Baig, "Optimization of dry sliding wear behavior of aluminium-based hybrid MMC's using experimental and DOE methods," *Journal of Materials Research and Technology*, vol. 16, pp. 743–763, 2022.

[21] C. Chanakyan, S. Sivasankar, M. Meignanamoorthy, and S. V. Alagarsamy, "Parametric optimization of mechanical properties via FSW on AA5052 using Taguchi based grey relational analysis," *Incas Bulletin*, vol. 13, no. 2, pp. 21–30, 2021.

[22] W. Zhang, "A novel ceramic with low friction and wear toward tribological applications: boron carbide–silicon carbide," *Advances in Colloid and Interface Science*, vol. 301, Article ID 102604, 2022.

[23] F. Xiao, M.-X. Wu, Y.-X. Wang et al., "Effect of trace boron on grain refinement of commercially pure aluminum by Al–5Ti–1B," *Transactions of Nonferrous Metals Society of China*, vol. 32, no. 4, pp. 1061–1069, 2022.

[24] A. Sharma, S. Dixit, N. Baler, P. Agrawal, S. K. Makineni, and K. Chattopadhyay, "Impact of boron as an alloying addition on the microstructure, thermo-physical properties and creep resistance of a tungsten-free Co-base γ/γ' superalloy," *Materials Science and Engineering: A*, vol. 855, Article ID 143899, 2022.

[25] S. Bakkar, S. Thapliyal, N. Ku et al., "Controlling anisotropy of porous B_4C structures through magnetic field-assisted freeze-casting," *Ceramics International*, vol. 48, no. 5, pp. 6750–6757, 2022.

Hindawi
Journal of Nanomaterials
Volume 2023, Article ID 5723730, 15 pages
https://doi.org/10.1155/2023/5723730

Research Article

Study of Friction and Wear Behavior of Graphene-Reinforced AA7075 Nanocomposites by Machine Learning

I. S. N. V. R. Prasanth,[1] Prabahar Jeevanandam,[2] P. Selvaraju,[3] K. Sathish,[4] S. K. Hasane Ahammad,[5] P. Sujatha,[6] M. Kaarthik,[7] S. Mayakannan,[8] and Bashyam Sasikumar[9]

[1]*Department of Mechanical Engineering, Malla Reddy Engineering College, Hyderabad 500100, India*
[2]*Department of Mechanical Engineering, JCT College of Engineering and Technology, Pichanur, Coimbatore, Tamil Nadu, India*
[3]*Department of Mathematics, Rajalakshmi Institute of Technology, Chennai 600124, Tamil Nadu, India*
[4]*Department of Mechanical Engineering, Sri Eshwar College of Engineering, Coimbatore, Tamil Nadu, India*
[5]*Department of Electronics and Communication Engineering, Koneru Lakshmaiah Education Foundation, Guntur 522302, India*
[6]*Department of Information Technology, Vels Institute of Science, Technology and Advanced Studies, Pallavaram, Chennai 600117, Tamil Nadu, India*
[7]*Department of Civil Engineering, Coimbatore Institute of Technology, Coimbatore, Tamil Nadu, India*
[8]*Department of Mechanical Engineering, Vidyaa Vikas College of Engineering and Technology, Namakkal, Tiruchengode, Tamil Nadu, India*
[9]*Faculty of Mechanical and Production Engineering, Arba Minch University, Arba Minch, Ethiopia*

Correspondence should be addressed to Bashyam Sasikumar; bashyam.sasikumar@amu.edu.et

Received 21 September 2022; Revised 11 October 2022; Accepted 25 November 2022; Published 15 February 2023

Academic Editor: Muhammad P. Jahan

In this research, the friction and wear of AA7075 nanocomposites reinforced with graphene and graphite were studied. Graphene's inclusion dramatically enhanced the material's mechanical characteristics, friction, and wear resistance. AA7075 is strengthened with less graphene, and AA7075, reinforced with more graphite, exhibits similar wear and friction behavior. Wear rate and coefficient of friction predictions for AA7075-graphene nanocomposites were made using five machine learning (ML) regression models. ML simulations reveal that the wear and friction of AA7075-graphene composites are most sensitive to the proportion of graphene presence, the loadings, and the hardness.

1. Introduction

Due to their high quality, nanocomposites have found widespread use in a wide variety of technological applications. Weight-critical aerospace and automotive industries and tribological applications favor AA7075 nanocomposites over monolithic AA7075 [1, 2]. While AA7075 is highly stiff, strong, and corrosion resistant, it has poor tribological qualities and will seize in dry sliding or with inadequate lubrication. Nanocomposites of ceramics, graphene, graphite, and fiber-reinforced AA7075 have excellent mechanical and tribological properties [3]. Numerous studies have looked into the effects of incorporating ceramic particles into AA7075 composites to boost the materials' strength and tribological behavior. Powder metallurgy, centrifugal, stirring, and even traditional casting are just some of the many transformations applied to these nanocomposites [4]. The disadvantages of these composites include the difficulty in evenly dispersing the ceramic particles throughout the AA7075 matrix, increased brittleness, and decreased machinability. As a low-cost alternative with the potential to reduce seizing propensity, friction, and wear, AA7075-graphite composites have attracted a lot of interest. Casting, spray depositing, and powder metallurgy is common approaches to working with these nanocomposites. Therefore, the graphite particles embedded in AA7075-graphite nanocomposites improve the tribological performance of sliding

applications. Large graphite particles can decrease the mechanical properties of self-lubricating AA7075-graphite nanocomposites. Recent studies explain graphene-infused, self-lubricating AA7075-graphene nanocomposites that improve tribological and mechanical properties.

Graphene consists of sheets of single-atom carbon arranged in a honeycomb pattern [5]. Graphene is unlike other materials because of its unusual friction and wears features. Because of its atomically flat surfaces and ultrathin layers, graphene has applications at both the nano and microscales. Graphene lasts a long time since it has a high mechanical strength [6]. Using the nanoindentation method of atomic force microscopy, Arun et al. [7] determined that graphene is the most robust material yet quantified for monolayer graphene membranes. They found that the tensile strength of defect-free monolayer graphene was 131 GPa, whereas Young's modulus (E) was 1 MPa. Researchers [8] conducted their research and found that the bilayer has a tensile strength of 127 GPa, the trilayer has a tensile strength of 102 GPa, and Young's modulus of each is 1.05 and 0.99 GPa. Nanocomposites are composite materials that improve the mechanical and material properties produced by combining a matrix and reinforcing components, such as the matrix's toughness and flexibility and the reinforcement's strength and moduli. Unlike further carbon-based struts like graphite or else carbon nanotubes, graphene's plate structure makes its dispersion in the matrix phase easier. Graphene is an appealing choice for use as the reinforcing phase in self-lubricating nanocomposites because of its high mechanical capabilities, low cost, and good electrical, optical, and thermal properties.

Recent research [9, 10] has detailed the mechanical properties of graphene-reinforced AA7075 nanocomposites and the technologies used to make them. Graphene distributed throughout the metal matrix contributes to the nanocomposite's mechanical strength. The aggregation of particles may negatively affect the stability, which causes a nonuniform dispersion. Examples include the AA7075-graphene nanocomposites, which saw a 62% increase in tensile strength compared to the AA7075 base alloy when using graphene nanosheets as the reinforcing phase [11]. According to studies by Ul Haq and Anand [12], adding graphene at 3 and 5 wt% to an aluminum AA2124 matrix boosted the material's tensile strength by 20.4% and 21.6%, respectively, while also increasing the yield strength by 104% and 127.6%. Adding graphene nanoplatelets at a weight percent of 0.1–1 to an aluminum AA7068 matrix has been shown to boost the material's tensile strength, as reported by Ul Haq and Anand [13]. But others, such as Hasan et al. [14] and Patel et al. [15] found that adding graphene to AA7075 nanocomposites reduced the material's tensile strength.

Friction, wear, and lubrication are all aspects of tribology, which studies the relationship between moving and contacting surfaces and the forces acting upon them. The tribological behavior of AA7075-graphene nanocomposites has been the subject of several recent reports [16, 17]. The tribosurface of AA7075-graphene nanocomposites is coated with soft lubrication layers of graphene, making it suitable for sliding applications after a brief break-in period. A Gr-rich solid lubricating layer at the contact as more graphene smears out during further sliding. The lubrication layer isolates moving surfaces to prevent metal-on-metal interaction, similar to self-lubricating AA7075-graphite matrix composites, decreasing wear and friction. It predicts that multimaterial composites with graphene than graphite particles will have higher tribological performance [18]. It is because of the former's increased mechanical strength and hardness. Tribological behavior is of paramount importance in the design and synthesis of machine components involving sliding, rotating, or oscillating contacts since it is a system reaction rather than a material feature.

Understanding the behavior of AA7075-graphene nanocomposites is crucial for scheming effective systems for tribological approaches. It is an interesting process because the wear and friction performance of the two materials depends on variant material, mechanical, and tribological variables. One-sample trials and simple 2-parameter correlations have been the mainstays of research on AA7075-graphene nanocomposite wear behavior and friction. To perform this type of study, the coefficient of friction (COF) or wear resistance is plotted against a solitary factor, while all other experimental variables are held constant. It is often insufficient and inefficient to develop thorough knowledge when complicated tribological relationships are present simply. While the 2-parameter analysis has limitations, circumvent it by using a data-driven method that simultaneously considers numerous factors' impact across a larger domain.

It demonstrates that a fundamental obstacle to tribological research is the lack of calculations from the first rules of physics and chemistry. Data-driven AI and machine learning (ML) algorithms have allowed scientists to look at higher order correlations between several variables than was possible with the standard 2-parameter study. Complex ML models, such as the gradient boosting machine (GBM) and the artificial neural network (ANN), use elaborate approaches to understand the patterns in the dataset and produce accurate predictions. Friction and wear of AA7075-graphene nanocomposites were studied by Yang and Buehler [19] under different lubrication conditions, with the use of both separate and combined models. Statistical methods explain the friction and wear processes of AA7075-graphene nanocomposites. To better predict friction and wear and to identify trends in the tribological properties of these materials, we will employ experimental data to train ML models.

2. Mechanisms of Wear and Friction in AA7075-Graphene Nanocomposites

Tribology is concerned with the study of wear and friction because they are the most important causes of substantial corrosion and energy loss in dynamic arrangements. Friction and wear mechanisms in multiphase nanocomposites such as AA7075-graphene are challenging to characterize. Using AA7075-graphene nanocomposites as examples, the wear and friction mechanisms were seen and measured.

COF or μ is a standard metric for describing the resistance to motion between contacting surfaces. The following

equation, which factors in both the frictional forces (F_f) and the load (N) bearing capacity, can be used to determine the COF between two surfaces.

$$\mu = \frac{F_f}{N} = \frac{F_a + F_d}{N} = \frac{F_a}{N} + \frac{F_d}{N} = \mu_a + \mu_d \quad (1)$$

Adhesion between the sliding surfaces (Van der Walls, ionic, covalent, and metal bonds) contributes to COF [20]. Friction coefficient d fluctuates according to mechanical properties, including solidity, strength, and modulus, by the micro and macroscopic distortion of severities of the tribosurface. Friction's adhesion component is affected by the asperity contact area among the rubbing surfaces. After a short break-in period, a soft graphene tribofilm forms on the AA7075-graphene nanocomposites tribosurface. The actual severity contact area between nanocomposites and the counter face lessens as a stable solid-lubricating graphene coating forms. Due to the reduced metal-on-metal interaction and decreased asperity contact area, the sticky component of the COF falls considerably. Graphene's addition to an AA7075 matrix dramatically improves the material's hardness, tensile strength, and flexibility. Since steel is more rigid than most other counter face materials, friction's deformation or plowing component is declining.

Under varying loads, wear occurs when two surfaces gradually lose material due to sliding against one another. Inspecting the worn area can expose the primary wear processes for a specific substantial combination. Most AA7075 nanocomposites' wear in tribological applications falls into adhesive wear, abrasive wear, and delamination wear [21]. Adhesion between the sliding surfaces leads to wear known as adhesive wear. Displacement and surface fracture at the asperity layer cause the material to break apart and move between characters. As a result, AA7075 wears more slowly. Several tribological tests [22] have shown that adhesive wear is the dominant wear process for AA7075-Gr.

The operating situation and material attribute mainly determine the significant wear process. Wang et al. [23] state that the wear during sliding contact could range from insignificant to severe, depending on the average load. The transition between these two wear regimes results in drastically different wear behavior and happens at a critical load. In the same way, the sliding velocity also shows a shift in its wear pattern. A lower wear rate and the dominance of abrasion as the effective wear mechanism describe the mild wear regime. Surface smoothness and the presence of tiny grooves running slantways are telltale signs of abrasive wear on AA7075-graphene nanocomposites. The graphene coating continues to function and helps limit wear in light wear [24, 25]. The wear rate increases dramatically as the load or sliding speed increases, marking the shift from mild-to-severe wear (outside the range of acceptable values). Because of this, the lubricating coating is often irreparably harmed or loses its ability to prevent excessive wear [26]. Exfoliation wear necessitates poor mechanical characteristics due to inhomogeneous mingling of the reinforcing phase, displacement accumulation, and fracture at a subsurface layer. Delamination wear causes thin laminates to discard as waste due to the instability of crack propagation at the tribosurface's subsurface. Exfoliation, craters, and scratches are far less common on AA7075-graphene nanocomposites than on base AA7075, according to research by Li et al. [27] and Hossain et al. [28].

3. Variables Affecting Wear and Friction of AA7075-Graphene Composites

The wear and friction of AA7075-graphene nanocomposites are affected by tribological and material-specific factors. Here, it uses conventional analysis to discuss how these factors affect friction and wear.

3.1. Material Variables. Variables in materials include their makeup, microstructure, characteristics, and parameters related to the production method. Considerations such as industrial process, heat treatment, graphene weight, graphene type, thickness, matrix arrangement, and mechanical characteristics are all relevant when studying the friction and wear of AA7075.

3.1.1. Impact of the Heat Treatment and Manufacturing Method. According to theoretical studies, increasing the graphene content of AA7075 composites can significantly enhance the material's mechanical and tribological characteristics. These advancements are impossible to achieve without a uniform distribution of graphene in the AA7075 matrix and a robust interfacial connection between the two. That is why AA7075-graphene nanocomposites require careful attention during production and heat treatment. Defects in manufacturing include nanoparticle aggregation, pore formation, poor interfacial connection, carbide creation, and cracks in subsurface regions. Casting, severe deformations, additive manufacturing, and powder metallurgy are all standard techniques for making these nanocomposites. Production of AA7075-graphene nanocomposites has thus far relied most heavily on powder metallurgy. A filthy AA7075-graphene surface and oxidation of the AA7075 matrix are expected outcomes of this method due to the incorrect selection of process variables. There has been a shift away from casting AA7075-graphene nanocomposites in favor of powder metallurgy. This production method can be inexpensive but does not permit much management over the graphene's distribution in the AA7075 matrix. Casting procedures include high processing temperatures encouraging interfacial interactions between AA7075 and graphene. In addition, graphene nanoparticles are prone to segregation and accumulation due to the density mismatch between AA7075 and graphene. The weakness of these nanocomposites is due to porosity, which concerns the gravity casting method. All of these casting defects might reduce the quality of the casting in terms of mechanical and tribological characteristics. Microstructural flaws like crashes and breakages may occur during the production of AA7075-graphene composites using a robust plastic deformation strategy. The porosity and low flexibility of AA7075-graphene composites may make it challenging to create complex shapes using additive manufacturing techniques such as selective laser melting.

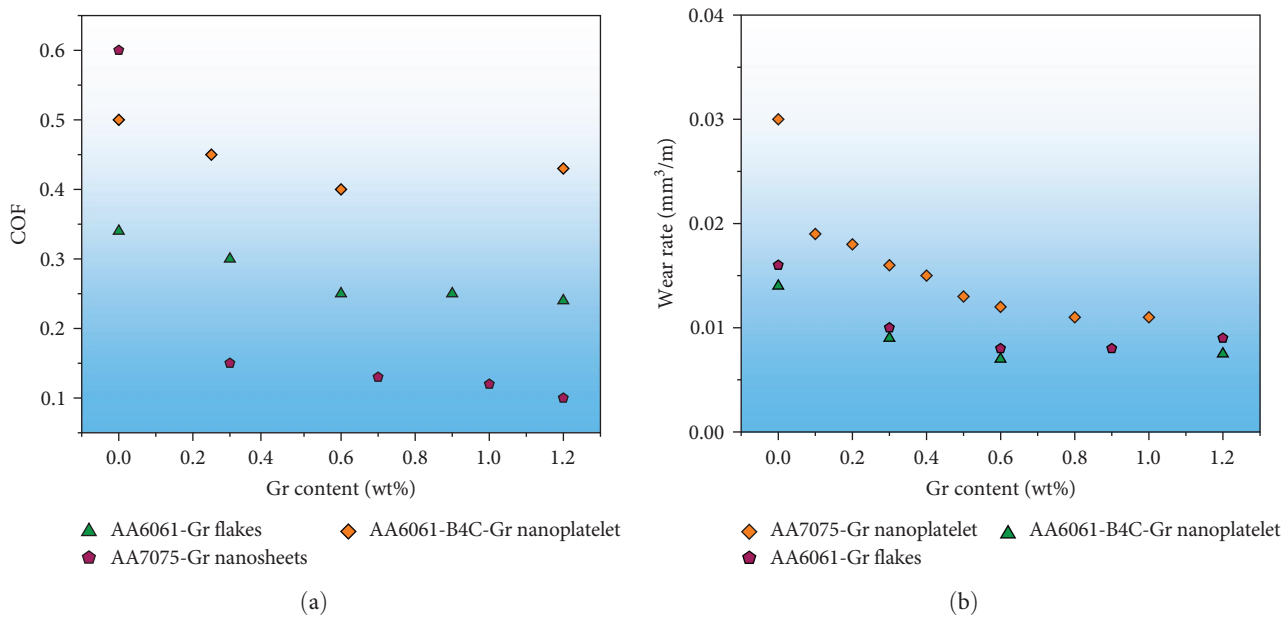

Figure 1: Impact of graphene wt% on (a) coefficient of friction and (b) wear rate.

AA7075-graphene composite's mechanical and surface qualities are very variable and dependent on the heat treatment methods and other factors.

3.1.2. Impact of Graphene Content. Graphene improves the tribological performance of composites by acting as a matrix material. Graphene, whether in a single sheet or several, acts as a solid lubricant when incorporated into a matrix for use in sliding mechanisms. The tribological characteristics of these nanocomposites modify by the method graphene changes their mechanical properties.

(1) Solid Lubricating Agent Graphene. Graphene addition to AA7075-graphene nanocomposites decreases COF and wear rate by improving the hardness and encouraging tribofilm formation.

Orowan reinforcement, load transmission, grain refining, and a mismatch in coefficient of thermal expansion (CTE) among graphene and the AA7075 make graphene-reinforced nanocomposites more challenging to work through. The addition of graphene decreases the wear rate because it improves hardness, which is inversely related to wear as calculated by the Archard equation. We can see in Figure 1(a) that the wear rate of AA7075-graphene nanocomposites steadily goes down as the graphene content increases. The wear rate reduces rapidly when the graphene content is lower, and then at a higher critical graphene content, the wear rate decreases more gradually. After the optimal graphene content attains, a slight wear rate acceleration obtains. It may be because AA7075-graphene becomes more brittle after reaching a specific graphene concentration in the matrix. This marginal improvement, however, pales in comparison to the substantial wear rate improvement that would result from reducing the graphene content.

When bulk graphene nanosheets disperse throughout the tribosurface through sliding wear, and create a graphene-rich tribofilm. By reducing the contact between the asperities of the contact surface and the maximum peak (R_p) and minimum valley (R_v) of the surface profile, a stable micro tribofilm can reduce wear. The lubricating properties of the tribofilm lessen the need for metal-on-metal contact, which in turn facilitates the friction heat produced by the sliding contact. Graphene addition consistently reduces the COF in AA7075-graphene nanocomposites, as seen by the COF against graphene content graphs (Figure 1(b)). Changes in COF are dramatic after even a little increase in graphene concentration from 0 wt%. A threshold graphene concentration got, after which additional surges in graphene content lead to a decrease in COF, but one less severe than before.

Using graphene (graphene nanoplatelets, oxide, microplatelets, flakes, monolayer Gr, rGO, and multilayer graphene) as the reinforcing phase reduces friction and wear, with the degree of reduction depending on the number of graphene layers and the kind of graphene utilized. It demonstrates that the frictional force decreases as the number of graphene layers increases. By allowing interlayer sliding, the frictional force lessens in multilayer Gr, graphene nanosheets, and graphene nanoparticles. Furthermore, Roccapriore et al. [29] have experimentally demonstrated that three or four-layer graphene is more resilient than monolayer graphene and resistant to sliding wear. The superior friction performance of AA7075-graphene composites over graphite nanocomposites can be substantially attributed to interlayer sliding between graphene nanosheets.

(2) Mechanical Properties of Graphene and Its Incorporation. The mechanical characteristics of AA7075 nanocomposites, such as hardness, strength, and Young's modulus, vary with reinforcing particle size. The mechanical properties of AA7075 diminish when big reinforcing particles or particle aggregation promote defects like pores and cracks. In Figure 2, graphene content is compared to tensile and hardness strengths for AA7075-graphene nanocomposites in Figure 1.

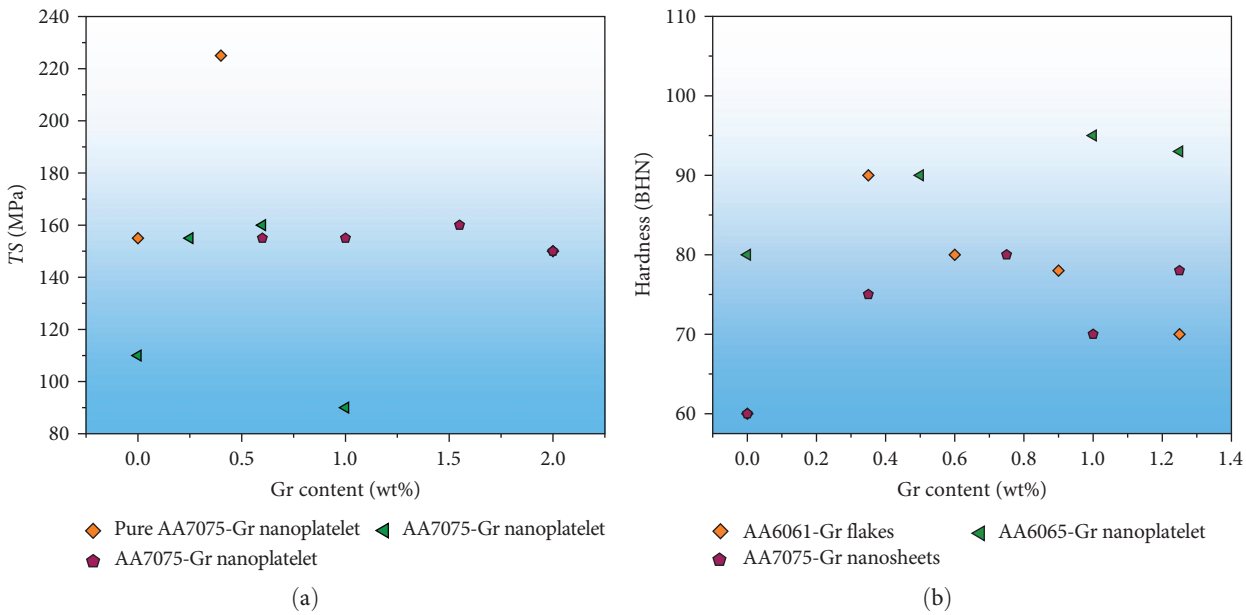

Figure 2: Impact of graphene content on (a) tensile strength and (b) hardness of AA7075-graphene nanocomposites.

As graphene adds, the material's tensile strength and hardness increase up to a certain point but then begin to decrease.

Mechanical qualities in AA7075-graphene nanocomposites improve by ensuring that graphene is evenly distributed and oriented throughout the composites. Researchers [30] found that the increased strength of composites can be attributed, in part, to the fact that the graphene nanoparticles (GNPs) are dispersed evenly throughout the AA7075 composites, allowing for efficient load transfer. They also discovered that mechanical behavior degraded and graphene shearing at the tribosurface increased while utilizing 1.2 wt% graphenes as the reinforcement. They reasoned that the GNPs could not usually diffuse across the matrix due to the increased weight percentage. Agglomeration expands porosity and cracks and degrades the structure, as seen by Zhao and Fang [31] when more than 1.2 wt% graphene adds. Furthermore, substantial flaws in AA7075-graphene nanocomposites are promoted by graphene agglomeration, leading to premature composite failure [32].

The higher strength of AA7075-graphene nanocomposites results from several different mechanisms, such as mismatch in CTE, load transmission, grain refining, and Orowan reinforcing [33]. The CTE mismatch enhances the interfacial prismatic punch of dislocations, increasing the composites' strength. High-aspect-ratio graphene reinforcements are the most effective at transmitting loads because they form strong bonds with the matrix. Increased interfacial contact between GNPs and the AA7075 matrix attain by their 2D structure and crumpled surface [34]. Hall–Petch connection [35] explains why grain refining makes a difference in strength. By introducing nanoparticles like GNPs, the Orowan bypass mechanism creates residual dislocation loops, which increase strength via repulsive back stress [36].

3.1.3. Impact of the Matrix Arrangement. The characteristics of the AA7075 utilized as the matrix affect the mechanical and tribological performance of AA7075-graphene composites. Strength, elasticity modulus, and hardness are only some of the mechanical qualities that improve upon by mixing pure AA7075 alloys with other alloying elements [37]. Each AA7075 alloy has distinct microstructural features that influence how much graphene disperses in the matrix, how strong the links are between the matrix and the reinforcing phase, and whether or not a chemical procedure is even possible. Properties like wear resistance and the critical load at which moderate to severe wearing occurs define by the AA7075 in AA7075-graphene nanocomposites (Figure 3(a)).

Average wear and COF under similar loading and testing circumstances for several types of unstrengthened AA7075 alloys and comparable graphene-reinforced (0.25–0.5 wt%) composite are displayed in Figure 3. Compared to their unreinforced counterparts, AA7075-graphene composites consistently showed lower friction and wear behavior (Figure 3(b)). Some alloys have a more noticeable discrepancy between COF and wear rate than others. Also, it is not always the case that reducing COF would slow down your wear rate or vice versa. Though reduced by adding 0.3% graphene to AA7075, the wear rate is slightly lower.

3.2. Tribological Variables. In this post, we will go over how various factors in tribological tests can impact the wear and friction performance of AA7075-graphene composites. Before conducting tribological testing, a few considerations are typical load, sliding distance, speed, and lubrication status.

3.2.1. Impact of Normal Load. According to Karathanasopoulos et al. [38], the average load is critical in determining when wear will progress from mild to severe. Average load's effect on AA7075-graphene and AA7075-graphene nanocomposites COF and wearing rate in Figure 4. More force results in better nano- and microscale asperity contact between the sliding surfaces. The tribosurface will plastically deform more when

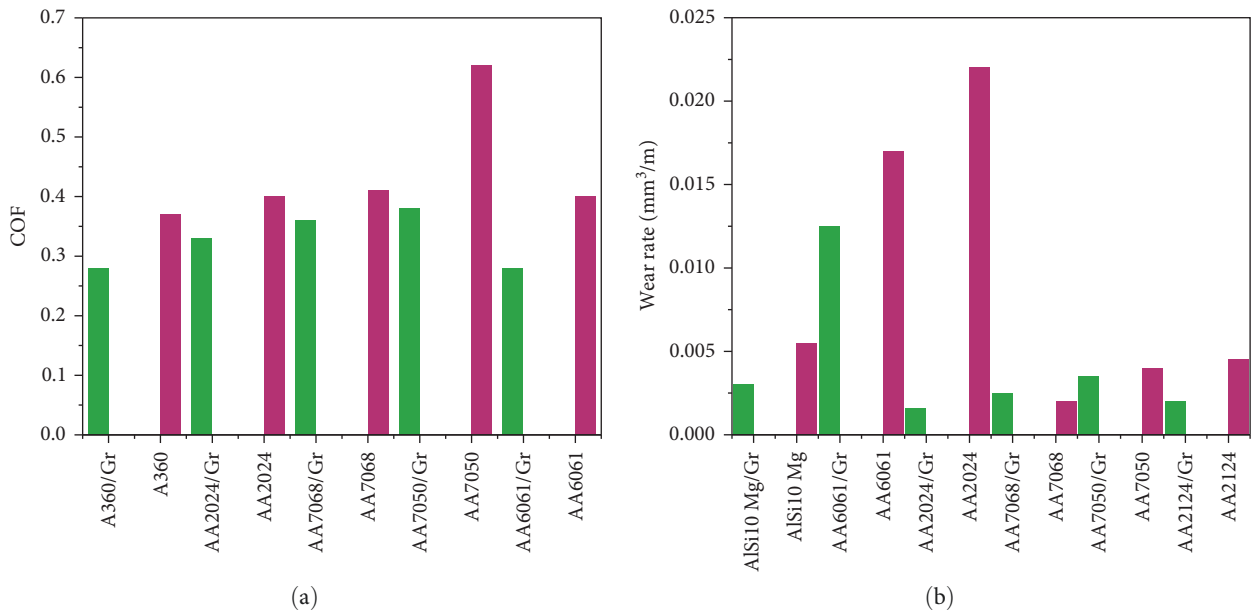

Figure 3: AA7075 base alloys and their corresponding AA7075-graphene nanocomposites with (a) coefficient of friction and (b) wear rate.

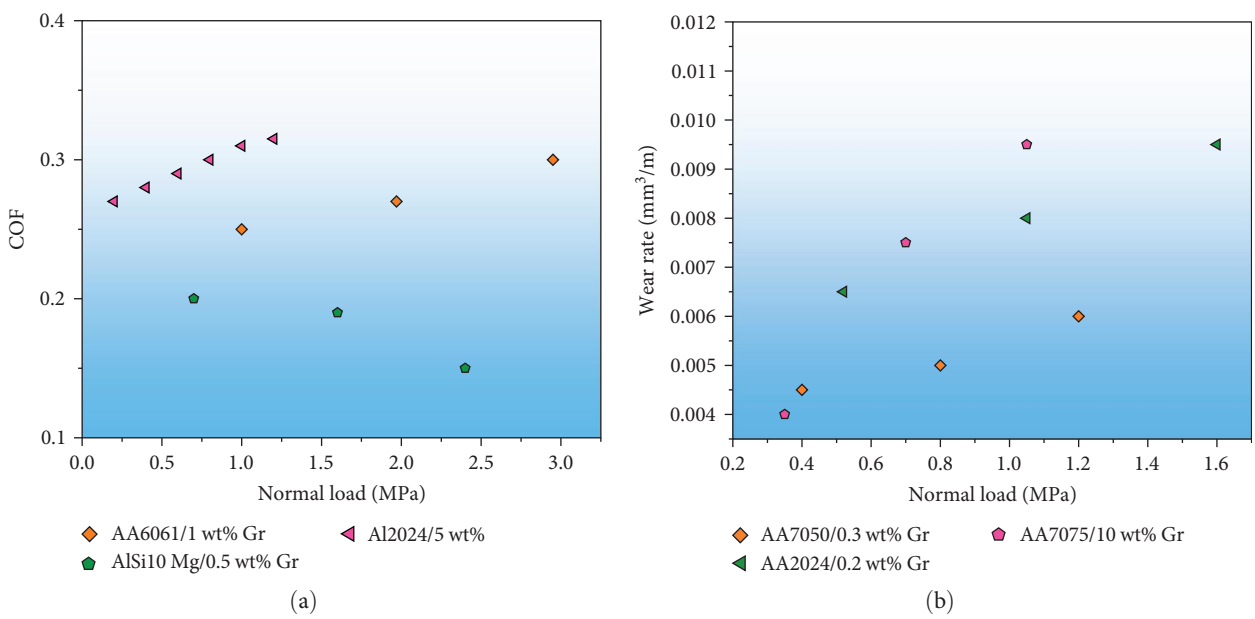

Figure 4: Impact of normal load on (a) coefficient of friction and (b) wear rate.

there are more asperities in connection. All of them contribute to a greater degree of resistance. The load dependence of wear and friction qualities may be more nuanced in AA7075-graphene nanocomposites because they are a two-stages self-lubricating material. Because the softer phase on the tribosurface might stretch out more with an increase in load. Since this is the case, AA7075-graphene nanocomposites have been shown in several studies to raise or reduce COF under normal load (Figure 4(b)).

Furthermore, it indicates that under constant loads, friction and wear were greater in AA7075-graphene composites with a higher weight percent of graphene than in those with a much lower weight percent of graphene (Figure 4). AA7075-graphene composites have advantageous mechanical properties. The graphene phase incorporated in the metal disperses via scraping the tribosurface. Repeated rubbing can cause the development of a stable Gr-rich coating, which, in comparison to the starting state, lowers the amount of wear and friction among the stressed surfaces. However, after a solid graphene covering has developed, friction and wear will likely rise under typical loading settings. When the graphene coating is unharmed, friction and wear reduce, allowing for mild wear at lower specific loads. When subjected to more significant stresses, the graphene-rich layer is frequently

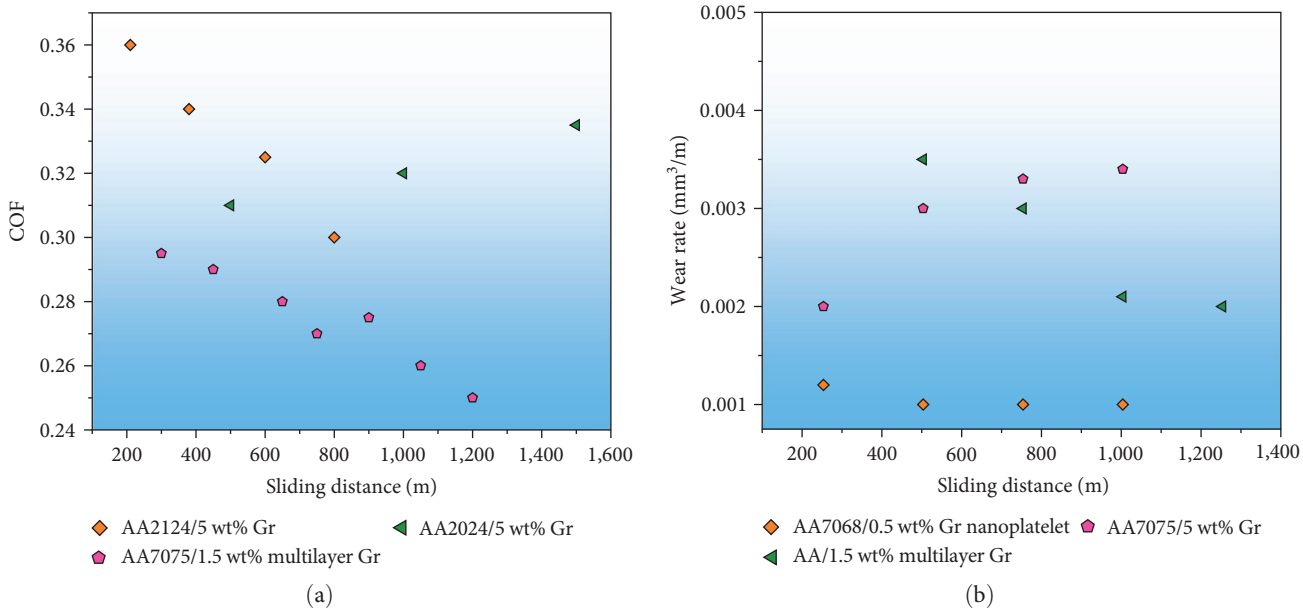

Figure 5: Comparison between sliding distance: (a) coefficient of friction and (b) wear rate.

damaged beyond repair or loses its ability to prevent the extreme wear that is otherwise detected. Researchers [39] found that the AA7075-graphene nanocomposite's wear mechanisms change from abrasive to delamination wear as the load increases. Surface roughness and shear strain were also higher in conjunction with high normal loads. Wear rate and COF for AA7075-graphene nanocomposites predicts with the help of an ANOVA.

3.2.2. Impact of Sliding Distance. Calculating the impact of the sliding distance of wear and friction is complicated due to the AA7075 matrix composites. The solid–fluid layer's production, load, and sliding properties may complicate the relationship. Figure 5 displays the correlation between sliding distance, wear rate, and COF for AA7075-graphene, and AA7075-graphite multimaterial composites. The COF and the rate of wear for AA7075-graphite nanocomposites both increased with sliding distance. These [40] result from long-term sliding due to microthermal softness triggered by interface heat and a diminished graphene coating on the tribosurface.

Constantly decreasing the COF and wear rate by sliding AA7075-graphene nanocomposites is a viable strategy. The complex graphene components that protrude from the surface of AA7075-graphene composites are the root of their wear resistance. This relationship links the wear rate and the sliding distance inversely. Stable graphene layers on the tribosurface further reduce the COF by allowing for a longer sliding distance with the same amount of effort. Sliding distance affects wear rate more than the COF, as shown by the ANOVA results for AA7075-graphene composites tribological data by Li et al. [41].

3.2.3. Impact of Sliding Speed. Frictional heat generates at a constant rate, and the tribosurface temperature rises in response to an increase in sliding velocity. This warming helps the matrix soften micro thermally. In addition, it facilitates the production of oxides and the dissolution of microstructure-associated precipitates, hence lowering flow stress. All of them contribute to the accelerated AA7075 nanocomposite wear rate. Figure 6 displays the correlation between sliding velocity and wear, and COF of AA7075-graphene and AA7075-graphite nanocomposites.

If the speed is low, the wear mechanism is relatively high; if it is high, the wear mechanism is quite severe. Low wear rates are reported in AA7075-graphene nanocomposites at low sliding speeds because of the fully functional graphene lubricating coatings. Wear rate briefly reduces with sliding speed [42] in the low-wear regime of AA7075-graphite nanocomposites. Wear increases for AA7075-graphene and AA7075-graphite nanocomposites as sliding speeds approach critical values. However, while having a more excellent reinforcing percentage, the wear rates found in AA7075-graphene nanocomposites were significantly lower.

In contrast, up to a certain sliding speed, the COF of AA7075-graphite and AA7075-graphene nanocomposites decreases. Increasing the sliding speed reduces the adhesive component of friction in addition to the lubricating provided by graphene or graphite-rich layers. Sliding contacts generate frictional heat, further reducing friction as speed increases. Even when sliding slowly, rises in strain rate raise flow hardness and strength [43]. COF and wear decrease when the contact area among mating surfaces diminishes.

4. Friction and Wear Behavior of AA7075-Graphene and AA7075-Graphite Composites

As indicated by a review of tribological performances from several studies, graphene as the reinforcing phase requires a substantially lower weight percentage than graphite to achieve the same COF and wear rate under similar loading conditions. When bigger graphite particles introduce into the AA7075

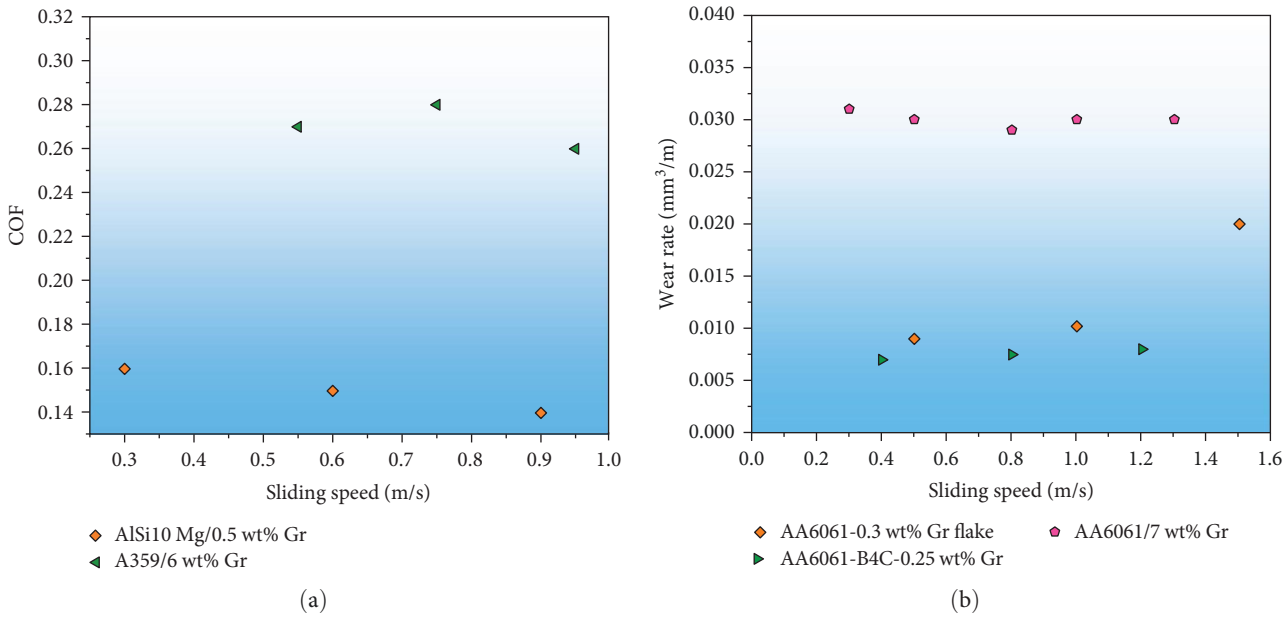

Figure 6: Comparison between sliding speed: (a) coefficient of friction and (b) wear rate.

matrix, the material's mechanical characteristics—hardness, flexibility, and strength—suffer severely. As a result of the AA7075 matrix, large graphite particles prefer to cluster together. Because of the previous factors, these composites may not be as effective as AA7075-graphene composites in terms of tribological performance. In contrast, smaller graphene nanoparticles scatter more uniformly in the AA7075 matrix. The addition of graphene nanoparticles to AA7075 composites significantly boosts their mechanical properties and, by extension, tribological performance. These hypotheses explain the superior performance of nanoparticle-reinforced AA7075-graphene composites in wear and friction tests.

It is intended to statistically evaluate the hypothesis that a much lower weight percent of graphene as the reinforcement in the AA7075 matrix can exhibit the same frictional behavior as a much bigger weight percent of graphite using the experimental results from the previous investigations. By employing the life cycle assessment function in IBM SPSS Statistics, we compared COF data for AA7075-graphite (10 wt%) and AA7075-graphene (0.5 wt%) under identical loading conditions to ascertain whether or not the COF values of the paired combinations is comparable. For AA7075-graphite composites, the mean and standard deviation of the COF were 0.1968 and 0.0862, while for AA7075-graphene composites, these values were 0.2047 and 0.0603. These numbers are representative of 33 datasets. According to the central limit formula, the sample size of the trial was sufficient to guarantee a normal approximation. In the linear component analysis, the p-value for the linear component was 0.77. Hence, the null hypothesis was not rejected (since a p-value less than 0.05 are considered essential). It can be concluded with 95% confidence interval that there is no significant difference in the mean COF value of the AA7075-graphene (5 wt%) and AA7075-graphite (10 wt%). The results suggest that the graphene reinforcement phase in the AA7075 matrix may offer the same features as a greater quantity of graphite in the AA7075 matrix under identical tribology settings.

5. Methods and Materials

This study provides the improved performance and refinement of the ML approach for calculating friction and wear. Data gathering, processing, model creation, and parameter optimization for various ML models are covered here.

5.1. Acquisition of Data and Input/Output Factors. The accuracy of ML predictions is highly dependent on the quality of the data employed to practice the models. Building ML models is done with a sizable, well-curated dataset from multiple sources, including various input–output correlations. Diversifying your data sources is advised, as over-reliance on information from a single source can reduce the models' generalization ability. It takes a lot of time and effort to set up a battery of tribological testing rigs and prepare samples of widely variable material characteristics that analyze to yield the required data. In order to develop reliable ML representations and have amassed tribological behavior data for Gr-enhanced AA7075 composites from the existing literature [20]. The developed ML models that can forecast COF and wear rate based on analyses of datasets, including 432 and 390 specimen data points, respectively. Tribological and material characteristics assess as predictors in the established regression models. Several variables consider, including graphene concentration, AA7075 concentration, SiC concentration, hardness, tensile strength, graphene type, graphene production process, heat treatment, flexibility, density, and many more. Consideration of sliding distance, load, velocity, counter face, and tribological testing technique. There were both categorical and numeric inputs; examples include graphene kind, production method, heat treatment, counter face, and tribotesting method.

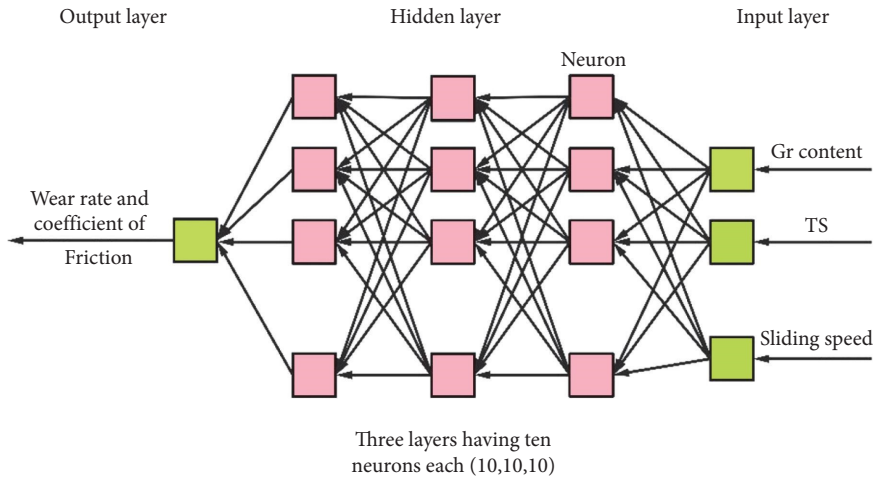

Figure 7: Multilayer perceptron structure of artificial neural network with various layers.

5.2. Data Preprocessing and Standardization. Data preparation includes tasks, including cleansing, repairing missing and odd values, randomizing, normalizing, and splitting the data into training and testing sets. While handling the share of data preprocessing and relying heavily on Python and its many available tools. Appropriate processes manually deal with missing and abnormal values in the datasets. We mixed up the data to prevent unintentional biases from entering the ML models. Getting the inputs into more consistent numerical values increases the adaptability of created system. Robust scaler, a tool for normalizing data and scaling its features to account for outliers, was used for this purpose. For the purpose of developing ML regression models, it is important to split the dataset into a training set and a testing set.

5.3. Machine Learning (ML) Models. If we have a set of input factors, supervised ML-trained regression models may be able to predict a result. To forecast the wear rate and friction of AA7075-graphene composites based on 15 materials and input parameters, developed five ML regression models (ANN, KNN, random forest (RF), support vector machine (SVM), and GBM). For ML analysis and model creation, Python and the sci-kit-learn library utilize. Our earlier studies [25–27] provide detailed coverage of the ML above models.

To make predictions, nonparametric KNN regression models use the training data points closest to the target value (neighbors). Forecasts can be made with KNN, an acronym for "k nearest neighbors," by looking at how similar instances are in a particular training set. Standard methods for tuning the KNN regression model include modifying the number of neighbors tested and the importance placed on the comparative distance among points. The KNN model's responsiveness to new data points may be influenced by overfitting or underfitting if n neighbors are kept relatively small.

To forecast outcomes, SVM regression models plot data on hyperplanes of increasingly finer granularity. Given that these hyperplanes exist in the high-dimension input data space, SVM can deal with complicated nonlinear relationships. Various kernel functions (such as the linear, polynomial, sigmoid kernel, radial basis function (RBF), etc.) utilize when structuring data on hyperplanes. Previous studies [1, 6] suggested that the RBF function worked better for tribological data. Two variables, the kernel coefficient (γ) and the regularization factor (C), determine how well an SVM model performs. When there are many input variables and only a few observations, SVM models nevertheless perform well.

Regression models based on ANNs are cutting-edge tools because of their ability to detect and incorporate nonlinear correlations into predictions. This model's learning strategy equates to the human brains. Many materials science and tribology areas have succeeded with ANN models. To bridge the gap between the input and output layers in an ANN model, multiple "neurons" or "intermodal units" are scattered throughout several "hidden" layers. It is a complex structure of layers and intermodal units that processes input into meaningful insights. In developing our ANN models, we explored the possibility of using multilayer perceptron (MLP), which process data in a feed-forward fashion. Figure 7 depicts an ANN's feed-forward MLP regressor design. In this research, three-tiered hidden layers use in the ANN regression models. Ten intermodal units (neurons) employ in each concealed layer. After extensive experiments, we determined that tan h and ReLU were the best activation functions for the ANN techniques used to forecast COF and wear rate.

The prediction model in GBM and RF models uses ensemble techniques based on decision trees. Regression models on decision trees for tribological data. The decision trees used in these models formulate in fundamentally different ways. While GBM uses a sequential approach, RF maintains unpredictability in data selection for creating decision trees. Bagging and boosting are the processes used by RF and GBM for this reason. Efficiency is augmented, and resilience is grown in RF models by avoiding overfitting, thanks to the bagging method. Increasing the number of features and depth of the decision trees in a model can improve its performance. Each tree in the boosting mechanism has its loss function (which can be arbitrarily differentiable) optimized to correct the errors of its predecessor. Since this is the case, GBM is an

Table 1: Coefficient of friction optimization models.

Type name	Chosen factors
Artificial neural network	Activation function: tan h, $\alpha = 0.013$, hidden layers = (10,10,10)
k-Nearest neighbor	Number of considered neighbors = 6, weights = "uniform"
Random forest	Maximum features = 5, n_estimators = 80
Support vector machine	Kernel = RBF, $\gamma = 0.09$, $C = 100$
Gradient boosting machine	Learning rate = 0.9, maximum-depth = 3, n_estimator = 150

RBF, radial basis function.

Table 2: Wear rate, optimum models.

Type name	Chosen factors
Artificial neural network	Activation function: tan h, $\alpha = 0.05$, hidden layers = (10,10,10)
k-Nearest neighbor	Number of considered neighbors = 4, weights = "uniform"
Random forest	Maximum features = 6, n_estimators = 30
Support vector machine	Kernel = RBF, $\gamma = 0.3$, $C = 100$
Gradient boosting machine	Maximum depth = 8, learning rate = 0.02, n_estimator = 150

RBF, radial basis function.

Table 3: Performance of coefficient of friction prediction models.

Machine learning model	ANN	KNN	RF	SVM	GBM
Mean absolute error	0.0342	0.0415	0.0252	0.0347	0.0225
Mean squared error	0.0038	0.0047	0.0014	0.0035	0.0013
Root mean squared error	0.0625	0.0695	0.0375	0.0593	0.0367
R^2 value	0.8943	0.8695	0.9637	0.9043	0.9642

GBM, gradient boosting machine; SVM, support vector machine.

excellent method for exploring complex causal relationships. It is necessary to optimize their maximum depth, learning value, and some boosting stages (n estimator).

5.4. Optimization of the Machine Learning Models. It is essential to carefully optimize the created ML models to maximize their prediction performance. In the previous paragraph, we covered the topic of the factors of many models that need optimum. The grid and cross-validation to fine-tune our prediction models' variables were used. These optimization techniques again to run the prediction algorithms with different values for each input parameter were employed. Tables 1 and 2 display the optimal optimization parameters for forecasting wear rate and COF. The complexity of an ANN depends on various factors. The activation function calculates the weightage amount of input variables for an ANN model. The best results were when attempting to forecast COF using an ANN model with three hidden layers and 10 neurons per layer, regularization variables $\alpha = 0.012$, and activation function tan h (Table 1).

Similarly, optimal settings for other models manipulate and improve their predictive abilities with concerning.

6. Result and Discussion

In this part, we report the data from our ML analyses and assess how well they perform using standard performance evaluation criteria. Also highlighted are the results of a data-driven investigation into the impact of various input variables on wear and friction in AA7075-graphene nanocomposites.

6.1. Result for COF Prediction. Several commonly employed statistical performance measures for gauging an ML regression model's performance; include the coefficient of determination (R^2), mean absolute error (MAE), mean square error (MSE), and root mean square error (RMSE). A regression model with an R^2 value between 0 and 1 and >0.9 indicates a very accurate prediction model. With $R^2 < 0$. The R^2 values for these five COF prediction models ranged from 0.8692 to 0.9643, and their error rates were low (Table 3). However, the GBM ($R^2 = 0.9642$) and RF ($R^2 = 0.9637$) models (both based on a decision tree) produced the best prediction results. It determined that the GBM and RF models' bagging and boosting processes worked well to deal with friction data containing categorical factors.

As regards accuracy in predicting COF, a GBM model with 150 boosting steps and a max deepness of two for separate regression performed the finest. Using the COF data, learning rates of 0.8 and above, together with other enhanced characteristics, were successful. Figure 8 shows how the COF measured in the lab compares to the COF predicted by the top GBM model. The anticipated and experimental COF values correlated highly well.

A set of 80 decision trees in the RF model, with four characteristics assessed at the optimal split, yielded the best R^2 value (0.9637), indicating the highest prediction performance (max features). The KNN based on distance functions was the simplest of the created models but also the least effective. The better predictive performance in the KNN model attains by assigning equal weight to a set of five

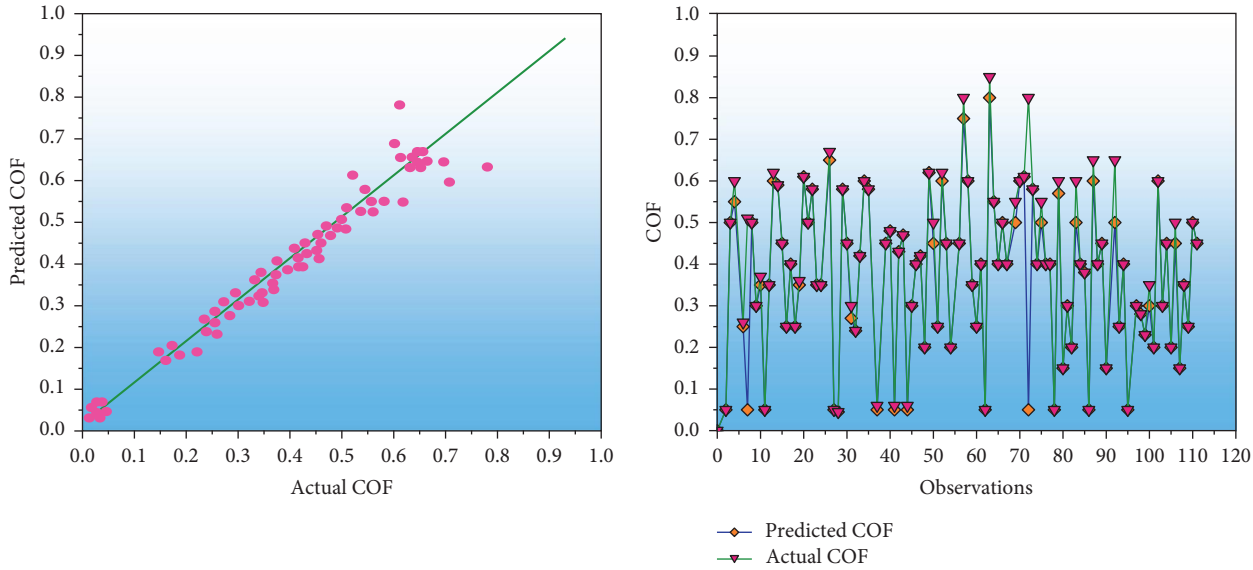

Figure 8: Evaluation of the gradient boosting machine regression model's prediction of coefficient of friction (COF) versus experimentally determined COF.

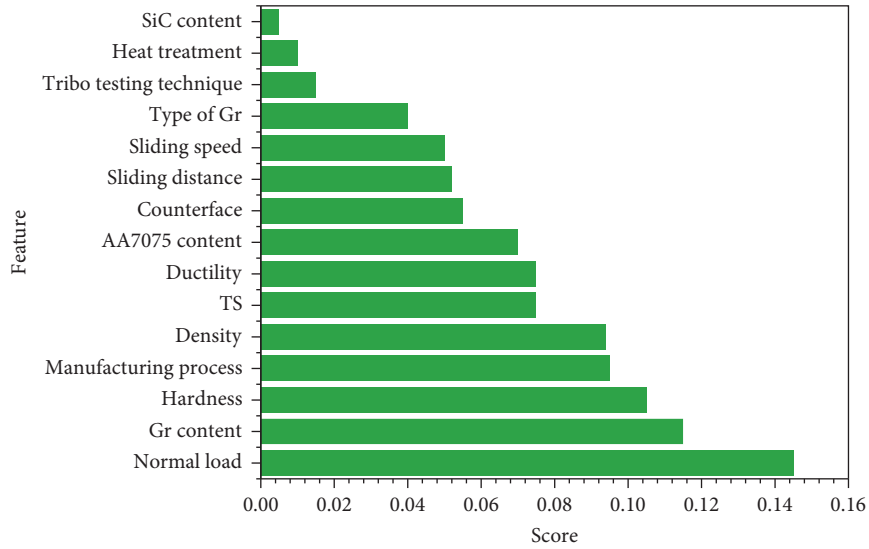

Figure 9: Predicting the coefficient of friction based on the relative relevance of input factors (feature importance).

neighboring data points used to construct a forecast for a novel data point. However, compared to other ML models, the model still had trouble dealing with the complicated COF dataset. The ANN model has an R^2 of 0.8943, indicating that it accurately predicted the COF with high confidence. The accuracy of the ANN model's predictions is satisfactory, with just modest error terms.

6.2. Impact of Input Parameters in the Forecasting of Coefficient of Friction. The significant feature of the RF model demonstrates forecasting the COF for AA7075-graphene nanocomposites. It shows that every input variable is crucial (Figure 9). If each factor on the feature importance analysis chart gives the same weight, the final score will be 1, as this is the minimum acceptable value. Individuals are more likely to contribute significantly to output prediction if their scores are higher, while individuals with lower scores are less likely to make any contribution. For the chosen input variables to affect the COF, they must all have non-zero values (Figure 9). The most important predictors of COF were graphene concentration, hardness, and load.

The graphene weight percentage is critical to further the self-lubricating effect and decrease friction, as described. For COF forecasting, the hardness of the material was also a significant factor. Research also demonstrated that COF forecasts for AA7075-graphene nanocomposites significantly impact the type of graphene employed.

6.3. Wear Rate Prediction. Table 4 displays the criteria used to evaluate the performance of ML models used to forecast wear rates for AA7075-graphene nanocomposites. R^2 values for the top-performing models were between 0.8902 and 0.9472. Among these were GBM, ANN, and RF. Furthermore, the KNN model based on distance functions incorrectly

Table 4: Performance of wear rate forecast models.

Machine learning	ANN	KNN	RF	SVM	GBM
Mean absolute error	0.0105	0.0143	0.0093	0.0131	0.0105
Mean squared error	0.0009	0.0027	0.0010	0.0012	0.0007
Root mean squared error	0.0273	0.0513	0.0321	0.0342	0.0246
R^2 value	0.9341	0.7357	0.9045	0.8902	0.9472

GBM, gradient boosting machine; SVM, support vector machine.

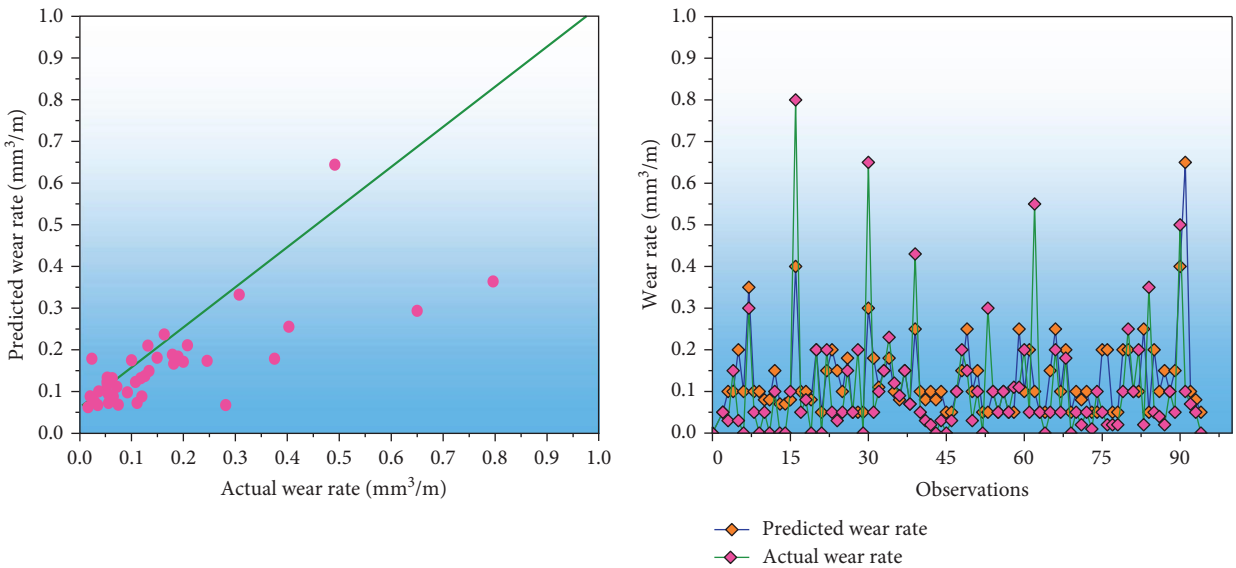

Figure 10: Analyzing the wear rate and contrasting it with experimental values.

estimated the wear rate because it oversimplified the complicated relationships in wear data. In spite of the complexity of the dataset involving wear rates, ANN performed admirably. The best overall prediction performance was achieved by the GBM model built on top of a decision tree. The typical could estimate the wear rate with a max accuracy of 94.69%. Despite definite factors in the wear rate, the GBM regression model's boosting method produced reliable outcomes.

Figure 10 compares the top GBM regression model's prediction and the observed (experimentally measured) wear rate. Results showed a strong relationship between predicted and measured wear rates. Similarly successful in predicting wear was RF, another decision tree-based model. The model executes successfully if the R^2 value is more than 0.9 and the error term values are modest. The ANN model performed admirably as a wear rate predictor with an R^2 of 0.9328 and exceptionally tiny MAE, RMSE, and MSE values. The ANN model with three hidden layers of 10 neurons each, the "real" activation function, and an intermediate regularization term ($\alpha = 0.05$) performed admirably with the complex wear rate data. Again, other models significantly outperformed the distance function-based KNN model when dealing with complex wear data.

6.4. Prediction Performance Comparison. For AA7075, AA7075-graphene composites, and AA7075-graphene composites, we evaluated machine language algorithms for COF and rate of wear prediction in dry conditions. The ML models trained with a decision tree (generalized decision tree, GBM, RF) consistently produce improved prediction ability for friction and wear rate when fed a categorical input. The AA7075-graphene and AA7075-graphite composite ML models showed statistically significant performance improvements over the ML algorithms for the AA7075 base alloys. Friction and wear parameters of composites made of AA7075 and graphite or graphene significantly impact the graphite and graphene self-lubricating action in the AA7075 matrix. Graphene and graphite percentages were significant in predicting wear and friction in studies of these composites. That's why our models made such precise forecasts. In the absence of lubrication, the COF and wear rate for AA7075 are susceptible to changes in material hardness and other tribological characteristics. The dataset reflected the complexity of the link between input and output variables and the degree to which they were unknown. As a result, the ML models were less effective than their graphene and graphite counterparts in AA7075.

6.5. Impact of the Input Parameters on Forecasting of Wear Rate. Wear on AA7075-graphene nanocomposites can be predicted using the RF model's feature significance attribute (Figure 11). All inputs with a score greater than zero affect the wear rate. We found that the concentration of Gr, its hardness, and the usual load best predict wear using feature

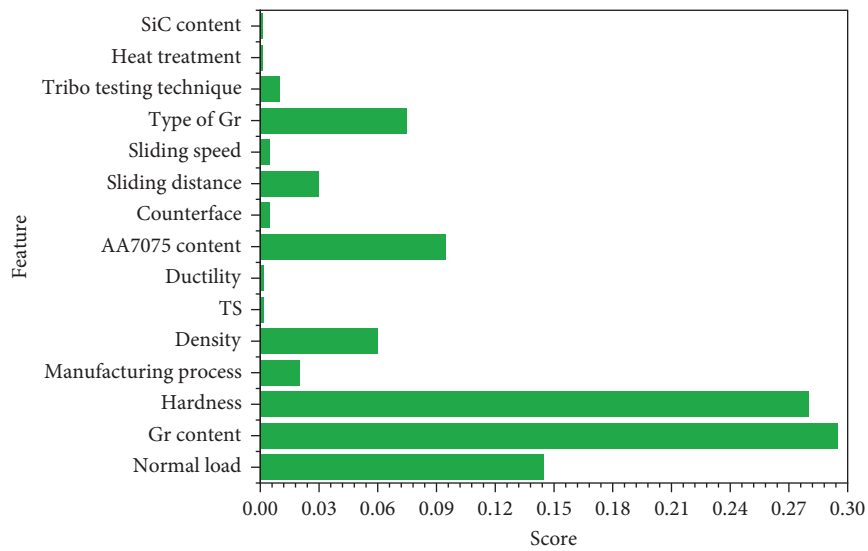

Figure 11: Significance of input parameters for forecasting the wear rate.

importance research. Graphene content is the most critical element in AA7075-graphene nanocomposites, with a direct correlation between increased mechanical characteristics and a self-lubricating effect. Since hardness was a brake on material loss during tribological interactions, it was an essential factor in wear prediction. Because surface hardness resists material removal rate more than bulk strength, that hardness substantially influences friction and wear more than TS. The standard load plays a crucial role in forming and maintaining the graphene coating on the tribosurface and controlling the transition from moderate-to-severe wear. Graphene type was more influential than COF in determining wear rate in AA7075-graphene nanocomposites. The type and amount of graphene layers and the self-lubricating action can influence the porosity, flexibility, hardness, strength, and connectivity of AA7075. Depending on its shape during tribological interactions, microcracking and brittle fracture can be induced in graphene. Wear in AA7075-graphene nanocomposites may be significantly impacted by all these factors.

The COF and wear rate of AA7075-graphene nanocomposites can be predicted with up to 96% accuracy using the ML models constructed. Without conducting any experiments, we can reliably predict COF and wear for various loading scenarios and material properties. Additionally, these algorithms can narrow in on the most crucial elements affecting wear and friction in AA7075-graphene nanocomposites by analyzing data from over 20 individual tests. To refine the AA7075-graphene nanocomposites synthesis procedure and identify optimal working conditions for actual use.

7. Conclusion

Self-lubricating AA7075-graphene nanocomposites had their graphene content analyzed to determine how the additive affected the materials' inherent qualities. We also performed a phenomenological study of wear and friction behavior in dry sliding contacts between these nanocomposites and AA7075-graphite nanocomposites to further understand the mechanisms. The ML models aim to help researchers determine the optimal conditions for future tribological testing of these composites in various settings.

(1) The addition of graphene to AA7075-graphene nanocomposites increased their hardness and tensile strength in several ways.

(2) The formation of a graphene-rich layer at the tri-surface is responsible for the decrease in wear rate and COF observed in the AA7075-graphene nanocomposites.

(3) Graphene concentrations in AA7075 composites analysis and results show that COF reductions are numerically similar at much lower graphene levels in the AA7075 composites as the reinforcing phase when tested under the same circumstances. Comparing wear rates across different nanocomposites found minimal variation.

(4) The models developed to anticipate wear and friction in AA7075-graphene nanocomposites performed exceptionally well. An ANN ($R^2 = 0.9341$, RMSE = 0.0273, MSE = 0.0009, and MAE = 0.0105) model providing the best forecasting for wear and GBM ($R^2 = 0.9472$, RMSE = 0.0246, MSE = 0.0007, and MAE = 0.0105) while the decision tree ($R^2 = 0.9642$, RMSE = 0.0367, MSE = 0.0013, and MAE = 0.0225) and RF ($R^2 = 0.9637$, RMSE = 0.0375, MSE = 0.0014, and MAE = 0.0252).

(5) Using ML, COF's most essential determinants were load, graphene content, and hardness. But the wear behavior of AA7075-graphene nanocomposites was most affected by graphene content, average load, and hardness.

Data Availability

All data supporting the findings of this study are included in this article.

Ethical Approval

All procedures performed in this study involving human participants were in accordance with the ethical standards of the institutional and/or national research committee and its later amendments or comparable ethical standards.

Conflicts of Interest

The authors declare that they have no conflicts of interest.

References

[1] M. S. Hasan, T. Wong, P. K. Rohatgi, and M. Nosonovsky, "Analysis of the friction and wear of graphene reinforced aluminum metal matrix composites using machine learning models," *Tribology International*, vol. 170, Article ID 107527, 2022.

[2] M. S. Hasan, A. Kordijazi, P. K. Rohatgi, and M. Nosonovsky, "Machine learning models of the transition from solid to liquid lubricated friction and wear in aluminum–graphite composites," *Tribology International*, vol. 165, Article ID 107326, 2022.

[3] V. Varadharajan, D. S. Senthilkumar, K. Senthilkumar et al., "Process modeling and toxicological evaluation of adsorption of tetracycline onto the magnetized cotton dust biochar," *Journal of Water Process Engineering*, vol. 49, Article ID 103046, 2022.

[4] P. Verma, P. Dhurvey, and V. P. Sundramurthy, "Structural behaviour of metakaolin geopolymer concrete wall-type abutments with connected wing walls," *Advances in Materials Science and Engineering*, vol. 2022, Article ID 6103595, 10 pages, 2022.

[5] W. T. Tysoe and N. D. Spencer, "Designing lubricants by artificial intelligence," *Tribology and Lubrication Technology*, vol. 76, no. 6, Article ID 78, 2020.

[6] M. Babič, D. Pršić, Z. Jurković et al., "A novel method for statistical pattern recognition using the network theory and a new hybrid system of machine learning," *Materiali in Tehnologije*, vol. 53, no. 1, pp. 95–100, 2019.

[7] V. Arun, R. Kannan, S. Ramesh et al., "Review on Li-ion battery vs Nickel metal hydride battery in EV," *Advances in Materials Science and Engineering*, vol. 2022, Article ID 7910072, 7 pages, 2022.

[8] M. S. Hasan, A. Kordijazi, P. K. Rohatgi, and M. Nosonovsky, "Triboinformatics approach for friction and wear prediction of Al-graphite composites using machine learning methods," *Journal of Tribology*, vol. 144, no. 1, Article ID 011701, 2022.

[9] A. G. Kamble, G. N. Kumar, K. V. P. Kumar, S. N. Karthik, P. B. Bagali, and A. Gajakosh, "Friction and wear performance of hot extruded AA7075/AIN/Gr hybrid composites," *Journal of The Institution of Engineers (India): Series D*, vol. 103, pp. 523–537, 2022.

[10] V. Gupta, B. Singh, and R. K. Mishra, "Tribological characteristics of AA7075 composites reinforced with rice husk ash and carbonized eggshells," *Proceedings of the Institution of Mechanical Engineers, Part L: Journal of Materials: Design and Applications*, vol. 235, no. 11, pp. 2600–2613, 2021.

[11] M. S. E. Bougoffa, M. N. B. bey, C. Benouali, T. Sayah, M. Fellah, and M. A. Samad, "Dry sliding friction and wear behavior of CuZn39Pb2 and AA7075 under industrial and laboratory conditions," *Journal of Bio- and Tribo-Corrosion*, vol. 7, Article ID 38, 2021.

[12] M. I. Ul Haq and A. Anand, "Friction and wear behavior of AA7075–Si_3N_4 composites under dry conditions: effect of sliding speed," *Silicon*, vol. 11, pp. 1047–1053, 2019.

[13] M. I. Ul Haq and A. Anand, "Dry sliding friction and wear behavior of AA7075–Si_3N_4 composite," *Silicon*, vol. 10, pp. 1819–1829, 2018.

[14] M. S. Hasan, A. Kordijazi, P. K. Rohatgi, and M. Nosonovsky, "Application of triboinformatics approach in tribological studies of aluminum alloys and aluminum–graphite metal matrix composites," in *Metal–Matrix Composites*, T. S. Srivatsan, P. K. Rohatgi, and S. Hunyadi Murph, Eds., The Minerals, Metals & Materials Series, pp. 41–51, Springer, Cham, 2022.

[15] S. K. Patel, J. Surve, J. Parmar, A. Natesan, and V. Katkar, "Graphene-based metasurface refractive index biosensor for hemoglobin detection: machine learning assisted optimization," *IEEE Transactions on NanoBioscience*, 2022.

[16] J. Chen, E. Xu, Y. Wei, M. Chen, T. Wei, and S. Zheng, "Graph clustering analyses of discontinuous molecular dynamics simulations: study of lysozyme adsorption on a graphene surface," *Langmuir*, vol. 38, no. 35, pp. 10817–10825, 2022.

[17] V. H. Ho, C. T. Nguyen, H. D. Nguyen, H. S. Oh, M. Shin, and S. Y. Kim, "Hydrogenated graphene with tunable poisson's ratio using machine learning: implication for wearable devices and strain sensors," *ACS Applied Nano Materials*, vol. 5, no. 8, pp. 10617–10627, 2022.

[18] S. Kumar, K. S. K. Singh, and K. K. Singh, "Data-driven modeling for predicting tribo-performance of graphene-incorporated glass–fabric reinforced epoxy composites using machine learning algorithms," *Polymer Composites*, vol. 43, no. 9, pp. 6599–6610, 2022.

[19] Z. Yang and M. J. Buehler, "High-throughput generation of 3D graphene metamaterials and property quantification using machine learning," *Small Methods*, vol. 6, no. 9, Article ID 2200537, 2022.

[20] F. Pashmforoush, "Mechanical properties prediction of various graphene reinforced nanocomposites using transfer learning-based deep neural network," *Proceedings of the Institution of Mechanical Engineers, Part E: Journal of Process Mechanical Engineering*, 2022.

[21] H. Sun, L.-Q. Tao, P. Wang, and T.-L. Ren, "A flexible graphene-based fabric ultrasound source for machine learning enhanced information encryption," *IEEE Electron Device Letters*, vol. 43, no. 9, pp. 1543–1546, 2022.

[22] K. S. K. Singh, S. Kumar, and K. K. Singh, "Computational data-driven based optimization of tribological performance of graphene filled glass fiber reinforced polymer composite using machine learning approach," *Materials Today: Proceedings*, vol. 66, Part 9, pp. 3838–3846, 2022.

[23] Z. Wang, S. Ye, H. Wang, Q. Huang, J. He, and S. Chang, "Graph representation-based machine learning framework for predicting electronic band structures of quantum-confined nanostructures," *Science China Materials*, vol. 65, pp. 3157–3170, 2022.

[24] N. Joshi, G. Pransu, and C. A. Conte-Junio, "Critical review and recent advances of 2D materials-based gas sensors for food spoilage detection," *Critical Reviews in Food Science and Nutrition*, 2022.

[25] G. Lu, Z. Zhang, T. Si, Y. Liu, and S. Chen, "Stability/instability of magnetorheological core sector structure for mechanical control braking system by the intelligent computer method," *Waves in Random and Complex Media*, 2022.

[26] J. Parmar, S. K. Patel, V. Katkar, and A. Natesan, "Graphene-based refractive index sensor using machine learning for detection of

mycobacterium tuberculosis bacteria," *IEEE Transactions on NanoBioscience*, vol. 22, no. 1, pp. 92–98, 2023.

[27] S. Li, N. Liu, M. Becton, X. Zeng, and X. Wang, "Mechanics prediction of 2D architectured cellular structures using transfer learning," *Journal of Micromechanics and Molecular Physics*, 2022.

[28] S. K. S. Hossain, S. S. Ali, S. Rushd, B. V. Ayodele, and C. K. Cheng, "Interaction effect of process parameters and Pd-electrocatalyst in formic acid electro-oxidation for fuel cell applications: implementing supervised machine learning algorithms," *International Journal of Energy Research*, vol. 46, no. 15, pp. 21583–21597, 2022.

[29] K. M. Roccapriore, O. Dyck, M. P. Oxley, M. Ziatdinov, and S. V. Kalinin, "Automated experiment in 4D-STEM: exploring emergent physics and structural behaviors," *ACS Nano*, vol. 16, no. 5, pp. 7605–7614, 2022.

[30] S. Zhang, S. Lu, P. Zhang et al., "Accelerated discovery of single-atom catalysts for nitrogen fixation via machine learning," *Energy & Environmental Materials*, vol. 6, no. 1, Article ID e12304, 2023.

[31] Z. Zhao and T. Fang, "A computational three-dimensional elasticity theory for bending and frequency analysis of the axisymmetric circular/annular plates via machine learning and discrete singular convolution integration methods," *Waves in Random and Complex Media*, 2021.

[32] F. Chen, J. Wang, Z. Guo, F. Jiang, R. Ouyang, and P. Ding, "Machine learning and structural design to optimize the flame retardancy of polymer nanocomposites with graphene oxide hydrogen bonded zinc hydroxystannate," *ACS Applied Materials & Interfaces*, vol. 13, no. 45, pp. 53425–53438, 2021.

[33] X. Liu, L. Zheng, C. Han et al., "Identifying the activity origin of a cobalt single-atom catalyst for hydrogen evolution using supervised learning," *Advanced Functional Materials*, vol. 31, no. 18, Article ID 2100547, 2021.

[34] B. A. Marquez, H. Morison, Z. Guo, M. Filipovich, P. R. Prucnal, and B. J. Shastri, "Graphene-based photonic synapse for multi wavelength neural networks," *MRS Advances*, vol. 5, pp. 1909–1917, 2020.

[35] M. Asmael, T. Nasir, Q. Zeeshan et al., "Prediction of properties of friction stir spot welded joints of AA7075-T651/Ti-6Al-4V alloy using machine learning algorithms," *Archives of Civil and Mechanical Engineering*, vol. 22, Article ID 94, 2022.

[36] A. Mishra and A. Vats, "Supervised machine learning classification algorithms for detection of fracture location in dissimilar friction stir welded joints," *Fratura ed Integrità Strutturale*, vol. 15, no. 58, pp. 242–253, 2021.

[37] H. Torbati-Sarraf, S. Niverty, R. Singh et al., "Machine-learning-based algorithms for automated image segmentation techniques of transmission X-ray microscopy (TXM)," *JOM*, vol. 73, pp. 2173–2184, 2021.

[38] N. Karathanasopoulos, K. S. Pandya, and D. Mohr, "Self-piercing riveting process: prediction of joint characteristics through finite element and neural network modeling," *Journal of Advanced Joining Processes*, vol. 3, Article ID 100040, 2021.

[39] F. Aydin, "The investigation of the effect of particle size on wear performance of AA7075/Al_2O_3 composites using statistical analysis and different machine learning methods," *Advanced Powder Technology*, vol. 32, no. 2, pp. 445–463, 2021.

[40] K. S. Pandya, C. C. Roth, and D. Mohr, "Strain rate and temperature dependent fracture of aluminum alloy 7075: experiments and neural network modeling," *International Journal of Plasticity*, vol. 135, Article ID 102788, 2020.

[41] G. Li, S. Datta, A. Chattopadhyay, N. Iyyer, and N. Phan, "An online–offline prognosis model for fatigue life prediction under biaxial cyclic loading with overloads," *Fatigue & Fracture of Engineering Materials & Structures*, vol. 42, no. 5, pp. 1175–1190, 2019.

[42] R. Chaturvedi, A. Sharma, K. Sharma, and M. Saraswat, "Tribological behaviour of multi-walled carbon nanotubes reinforced AA 7075 nano-composites," *Advances in Materials and Processing Technologies*, vol. 8, no. 4, pp. 4743–4755, 2022.

[43] M. I. Ul Haq and A. Anand, "Dry sliding friction and wear behaviour of hybrid AA7075/Si_3N_4/Gr self lubricating composites," *Materials Research Express*, vol. 5, no. 6, Article ID 066544, 2018.

Hindawi
Journal of Nanomaterials
Volume 2023, Article ID 9903119, 7 pages
https://doi.org/10.1155/2023/9903119

Review Article

Study on Water Absorption Characteristics, Various Chemical Treatments, and Applications of Biological Fiber-Reinforced Polymer Matrix Composites

Ramakrishnan Thirumalaisamy,[1] **S. Senthil Kumar**,[2] **Samson Jerold Samuel Chelladurai**,[3] **S. Gnanasekaran**,[4] **S. Sivananthan**,[5] **N. K. Geetha**,[6] **A. Ramesh**,[7] **and Gizachew Balcha Assefa**[8]

[1]*Department of Mechanical Engineering, Sri Eshwar College of Engineering, Coimbatore, Tamil Nadu, India*
[2]*Department of Mechanical Engineering, RMK College of Engineering and Technology, Puduvoyal 601206, India*
[3]*Department of Mechanical Engineering, Sri Krishna College of Engineering and Technology, Coimbatore, Tamil Nadu, India*
[4]*Department of Mechanical Engineering, Sri Shakthi Institute of Engineering and Technology, Chinniyampalayam, Coimbatore, Tamil Nadu, India*
[5]*Department of Mechanical Engineering, K.Ramakrishnan College of Engineering, Tiruchirappalli, Tamil Nadu, India*
[6]*Department of Mathematics, Dayananda Sagar College of Engineering, Bengaluru 560078, India*
[7]*Department of Mechanical Engineering, Chennai Institute of Technology, Malayambakkam, Tamil Nadu, India*
[8]*Department of Chemical Engineering, College of Biological and Chemical Engineering, Addis Ababa Science and Technology University, Addis Ababa, Ethiopia*

Correspondence should be addressed to Gizachew Balcha Assefa; gizachew.balcha@aastu.edu.et

Received 20 August 2022; Revised 20 September 2022; Accepted 13 December 2022; Published 1 February 2023

Academic Editor: Muhammad P. Jahan

This study presents an extensive survey of the many surface treatments that may be given to natural fibers for use in advanced composites. When put into reality, the primary disadvantages of working through biological fibers are the increased level of moisture intake that natural fibers possess as well as their low dimensional stability. The fundamental purpose of applying surface treatments to natural fibers is to optimize the bonding strength as well as the pressure transferability in composites made of biological natural fibers. Natural fiber-strengthened polymer composites (NFPC) have overall mechanical qualities that are strongly dependent on the morphological, aspect ratio, hydrophilic propensity, and high stiffness of the natural fibers that are employed in the composite. Cellulosic fibers are being studied for their effects both before and after being used as reinforcements for thermoset and thermoplastic polymers. Some of the chemicals utilized in treatments include alkalis, silane, acetyl, benzoylation, acrylation and polyamide grafting, maleated linking agents, ammonium nitrate, peroxide, phenoxy, stearic acid, potassium chalcopyrite, triazine, synthetic derivatives of fatty acids (oleoyl chloride), and fungi. After chemical treatment, composites made from organic fibers are stronger and more dimensionally stable than the untreated sample.

1. Introduction

Natural fibers can be used instead of man-made fibers in fiber-reinforced composites, which have led to more research and new business opportunities. Natural fibers are cheap, can be broken down by nature, and have a low density. Natural fiber composites are moisture-absorbent and incompatible with the matrix. As a result, biochemical behaviors are taken into consideration while trying to modify the fiber surface qualities. This article discusses the various chemical modifications that can be made to natural fibers for them to be used in natural fiber-reinforced composites. They include alkalis, silanes (acetylation and benzoylation), and other chemical treatments such as isocyanates and permanganates in their discussion. Fiber surface modification and fiber strength

both can be enhanced through chemical treatment targeted at enhancing adhesion between the superficiality of the fiber and the polymer matrices. Composite materials have enhanced mechanical characteristics and have lower water absorption rates than their predecessors. In this study, the chemical modification of the fiber, bonding characteristics, mechanical and water absorption behavior, and applications of various chemically treated natural fiber-reinforced composites have been studied.

2. The Effect of Chemical Modification on the Thermal and Mechanical Properties of Polymer Composite Materials with Banana Fibers

The purpose of this study is to investigate the heat transmission, tribological, and degrading behavior of banana fiber-reinforced polypropylene composites that have been treated with alkaline. Extrusion–injection molding processes were used to develop composites that contained BF at a ratio of 20% by weight-to-weight and had been treated with an aqueous solution of NaOH containing 5% by weight of the solvent's volume. Following the application of the chemical treatment, the composite demonstrates increases in its tensile strength of 3.8%, flexural strength of 5.17%, and impact strength of 11.50%, respectively. Fiber pull-out and fiber fracture are the primary causes of the nonsuccess of advanced composite material when subjected to ductile and impression loading, according to SEM inspection of evaluated specimens [1]. For the degradation studies, the samples were put in two different environments for 5 weeks: they were submerged in water or buried in the soil. The deterioration of composites was assessed in terms of both their weight and their mechanical characteristics of ductile, malleability, and withstands behavior. The composites that had been buried under soil showed the greatest amount of deterioration based on the mechanical behavior characterization [2]. The composite experienced a decrease in tensile strength of 7.69%, flexural strength of 12.06%, and impact strength of 3.27%. Due to their low weight, exceptional qualities, low production costs, and applicability for a variety of goods, organic fiber-reinforced polymer hybrids (NFPC) have become inescapably used in transportation practices. However, the most significant drawbacks associated with the utilization of these fibers are their low-dimensional space stability and excessive hydrophilicity. When it comes to figuring out the composite's physical behavior, the interfacial attachment between the reinforcement and the matrix is quite important. Various chemical treatments can be used to improve fiber–matrix adhesion, leading to composites with improved mechanical properties. Composites are being researched as a possible alternative to more conventional, high-density materials for use in transportation and aircraft. As a result, the plane's overall weight would be reduced and its performance enhanced. This page provides an in-depth introduction to biocomposites, discussing their many potential uses and the many chemical modifications that can be made to them [3].

3. Treatment Effects on the Moisture Intake Characteristics of NFRPC

A review was done on the effects that the treatment had on the water-absorbing capabilities of the natural fiber-reinforced polymer composites (NFRPC). It has been found that a variety of chemical treatments work well to minimize the hydrophilic nature of composites. One thing remains the same across the whole of the treatment, and that is the primary objective, which is to reduce the number of hydroxyl groups that are found in the fibers while concurrently raising the level of attachment between matrices and the fibers. The amount of moisture that the NFRPC could absorb was also significantly affected by its fiber composition and dimensions. Additionally, the polymer used in the manufacturing of NFRPC is significant, since several studies have discovered that PP-based hybrids have superior water absorption properties compared to PE-based composites. The extent to which the NFRPC's absorption capacity improves as a result of therapy is very sensitive to the kind of chemicals used. Treatment with sodium hydroxide had the worst effect on NFRPC's water absorption improvement among the chemicals examined. The treatment with acrylic acid, ethoxy, and potassium permanganate demonstrated a higher degree of effectiveness in increasing the water-absorption characteristics of the NFRPC. Chemical treatments such as sulfuric acid and hydrochloric acid are less effective at improving fiber-matrix interfacial adhesion and compatibility than peroxide preparation using benzoyl and dicumyl peroxides [4]. To lessen the amount of water that is absorbed by NFRPC, the majority of the research efforts have been directed toward developing a treatment that will lessen the amount of moisture that is absorbed by the fiber. It improves the adhesion that exists between the matrix and the fiber. According to Kakroodi et al. [5], NFRPC water absorption was linked to two key mechanisms. The first factor was the naturally occurring hygroscopic property of the natural fiber, which contributed to extending the improvement in the hydrophilic behavior of the composites. The second problem was that the structural inhomogeneity that existed between natural fibers reinforcement led to the creation of voids that were able to trap water at the interface. Because of this, it is expected that stronger adhesion and compatibility between the phases will minimize the likelihood of both mechanisms. When it comes to water absorption, the NFRPCs' interfacial adhesion, the type of fibers used to strengthen them, and the number of voids in those composites are all important factors that need to be taken into account, according to Pandian et al. Composites reinforced with various fiber types and matrices have varying degrees of water absorption, and the results of this investigation are summarized. Several distinct chemical processes were used to treat the fibers that were utilized as the reinforcing material. Sisal and bamboo were treated by Venkatesh et al. [6] by soaking them in a 10% NaOH solution for 24 hr at room temperature. After that, the natural fiber moisture content was removed by a hot air oven and then dried in the air for 24 hr each. According to the findings, the water absorption rate of polyester composites

produced from untreated fiber had a value of 19.6%, whereas the value of treated fiber's water absorption rate was 9.1%. Similar outcomes were discovered by Gupta and Srivastava [7] because sisal and jute filaments were submerged in a 5% NaOH solution and then dried in the oven at 70°C for 24 hr. When associated with composites made from unprocessed treatment fibers, the epoxy composites made from treated fibers demonstrated a water absorption rate that was 1.58% points lower than those made from untreated fibers (2.79% 6.09%). Epoxy composites reinforced with bagasse had a water absorption value of 8% after the fibers were treated with 1% alkali for 30 min and then submerged for 1 hr in 1% acrylic acid [8]. This is compared to 12% for untreated composites. Black sugar palmer was used to reinforce polypropylene composites by Zahari et al. [9], who observed that composites reinforced from vinyltrimethoxy silane-treated fiber exhibited somewhat reduced water absorption. This was the case when comparing treated fiber to a composite made from untreated fiber. The water absorption of a polypropylene composite that was reinforced with wood fiber and wheat husk and then subjected to a benzylation treatment was found to be much lower [10] than that of a composite that was manufactured from fiber that had not been treated. After being treated with pristine and NaOH, jute fiber was saturated with 5% by weight of both PP-maleic acetic anhydride and PE-maleic epichlorohydrin, and then it was dried at 80°C for 8 hr. A decrease in the amount of water that the composites absorbed after being implanted with PP-maleic acetic anhydride and PE-maleic epichlorohydrin was seen as a consequence of this change. In comparison to composites based on PE, PP-based composites showed a much lower water absorption rate [11]. In addition to the fibers being pretreated, the NFRPC being post-treated demonstrated significant improvement in water behavior. Post-treatment of a coir-reinforced polypropylene composite by Ali et al. [12] was carried out at a temperature of 70°C for 4 hr using a solution in which phenylhydrazine was saturated in ethanol. According to the findings, 0.18% water absorption of the composite after treatment was less than that of the composite before treatment (0.32%).

4. Different Treatments for Natural Fibers

The increasing demand of renewable materials, there are many industries using these eco-friendly materials. Biocomposites have seen a renaissance in the previous two decades as a material for a wide variety of goods, even those in the transportation, packing, sports, and construction sectors [13]. The hydrophilicity of these filaments must be diminished through the use of surface treatments that also enhance their characteristics and interfacial interaction with polymer matrices. Chemical, physical, and biological procedures are the three broad classifications that best describe these approaches. Chemical techniques involve the utilization of chemical reagents to bring about the desired decrease in the hydrophilic propensity of the filaments and, consequently, an improvement in their interaction with the matrix. They also enhance efficient interaction with the matrix by exposing more aromatic rings on the fiber surface. The chemical makeup of the fibers is not drastically altered by the physical approaches, but the altered superficial and structural properties of the fibers do distress the interfacial adhesion by matrices [14]. In comparison to chemical approaches, they are less complicated and produce fewer side effects. To alter the characteristics of the fiber's exterior, biological techniques employ organisms such as fungi, enzymes, and bacteria. These techniques are neither harmful to the environment like chemical procedures nor energy-consuming like physical ones [15].

4.1. Physical Treatments. To appreciate how lignocellulosic fiber may be used in high-performance industrial applications, it is crucial to recognize how the features of the cell wall segments rely on the properties of the fiber. With this information, you will be able to grasp the potential applications of lignocellulosic fiber. Hydrophobicity is typically lacking in natural fibers, which result in poor chemical resistance, weak mechanical properties, and a porous structure. Because of these properties, natural fibers can only be used for so many technical tasks. The hydrophilicity of textile products also restricts their usability, particularly in the transportation and packaging industries [16]. The various treatments that are used in the creation of NFRPCs are another key aspect that virtually influences the characteristics and interfacial behavior of the NFRPCs. Before natural fibers undergo any chemical processing, they go through many different physical processes first. Corona discharge, plasma, ultraviolet light, fiber beating, and heat are all examples of such treatments. The use of a corona discharge as a method for activating surface oxidation is probably the most exciting of all of the available options. This treatment modifies the interfacial tension of the cellulose filaments, which increases the fibers' compatibility with the hydrophobic matrix [17].

The use of plasma treatment has proven to be a successful method for removing pollution and dust particles from the fibers, which has resulted in an enhanced surface for the fibers. For the processing to go smoothly, the type of gas, the pressing factor, and the concentration all need to be properly managed. In recent years, ultraviolet (UV) light has gained popularity as a novel method for cleaning the exterior of plant fibers of any accumulated dust. Some aspects of UV therapy, such as the stream and the type of gas used, cannot be regulated. To oxidize the fibers' surfaces, the strands are placed in a special chamber before the treatment begins. Also, the UV treatment increases the polarization on the surface of the fibers. This makes the fibers easier to wet, which makes the NFRPCs stronger [18].

4.2. Chemical Treatments. Natural fibers-fillers are becoming increasingly popular as a component of composite materials due to their low cost and abundant availability. Natural fibers have several uses that are limited by their difficulty to cling to surfaces and their propensity to get mineralized. Natural fibers cannot be used in composites until they undergo a treatment that at the very least enhance their surface properties. Biochemical (alkaline, silane, acetylation, etc.), physical (corona, plasma), and biological therapies are all examples (enzymes). However, the benefits of each treatment, taking

into consideration energy consumption and effluent formation, should be evaluated in greater depth [16]. To suggest a more sustainable treatment in the treatment section in the manufacturing of natural fibers–polymer composites, this study conducted a literature review to compare the mechanical properties, energy consumption, and created pollutants of chemical methods (NaOH, silane, acetylation, and maleated connection) (gate-to-gate). During this review study, it was demonstrated that maleated interactions are a more environmentally friendly method because it does not require any particular form of energy during the primary treatment, it does not produce any effluent, and it consistently enhances the mechanical property performance of composites [19].

5. Natural Fiber-Reinforced Polymer Uses

The strict rules imposed on the environment and the search for more sustainable materials have pushed researchers in the direction of developing environmentally friendly materials. Exceptional NFPCs are needed in today's economy, particularly in the automotive and civil infrastructure sectors. Natural fiber reinforcement is a great option for polymer composites since it is inexpensive to produce, has superior thermal and acoustic qualities, and is processed in an eco-friendly manner. NPCs have a promising prospect in load-bearing applications due to the great qualities that they possess. As a significant portion of the natural materials and their respective polymer mixes have not been investigated, there appears to be a massive amount of untapped potential. Exploration of the many native species that can be used to make natural fibers is also something that should be done. The study of hybrid polymer composites as well as the synergistic effect of a variety of natural fibers is something that could be pursued in further research in the future. To broaden the range of applications for NFPCs, it is necessary to find solutions to the problems of temperature stability and moisture absorption. An important step forward in polymer composites research will be taken as a result of this paper [20].

5.1. Natural Fibers in Car Structural Applications. Natural fibers are becoming increasingly popular in the car industry, thanks to both the global trend toward lighter materials and the tightening of environmental regulations. Although there are a wide variety of natural fibers available, only a select handful of them are utilized in the production of vehicle components. Throughout the entirety of the European automobile industry's history, NFPCs have been deployed. The most recent piece of law that was established by the European Union mandates that by the end of year 2006, 80% of an automobile must be either recyclable or reusable, and by 2015, that number should be increased to 85% [21]. The growing popularity of eco-friendly automobiles has stoked interest in studying natural fiber composites (NFPCs). It is normal practice in the German auto industry to use natural fiber composites based on polyester and polypropylene when producing car parts [22].

Natural fiber composites are used almost exclusively for side panels, the rear package compartment, seat covers, and various other parts connected to dampening and insulation, among other uses. Al-Qureshi [23] was the one who conceived and carried out the design and fabrication of the banana-reinforced polymer composite. He concluded that the connection between the fiber matrixes was very strong and that there were no signs of delamination or delamination anywhere in the structure. The mechanical properties of the aforementioned element were improved thanks to the utilization of a hybrid composite that was constructed out of kenaf and glass fiber-reinforced epoxy as framed structures in automobile bumper beams [20]. As a result of the discovery that the composite possessed a greater elasticity and compressive than the standard material utilized in automotive bumper beams, the door was opened for the composite material to be utilized as engineered structures in some bumper sticker beams. Jute fibers were used as an alternative to glass fibers in the frontal hood of a vehicle to evaluate their impact on a variety of factors, including the environment, society, technology, and the economy. Except for the technical aspects, the performance that jute fibers deliver for these structural purposes is superior to that of glass fibers [22, 24, 25]. Pineapple and cassava flours were mixed into the biopolymers PLA and PBS to see how much of a contribution they made to the total emissions of volatile organic compounds (VOCs). Pineapple, cassava/PLA, and PBS-based composites were shown to significantly reduce smell emissions, and this characteristic is particularly beneficial in automobile interior components. the mechanical characteristics of hybrid composites consisting of abaca, jute, and fiberglass were investigated in all three cases [26]. The maximum fiber volume percent was set to 0.4 for all three composites. According to the findings of the research conducted, the tensile strength of the hybrid composite was significantly different from that of other composites. According to the authors, abaca-based composites have greater impact and flexural strengths than jute and hybrid composites. The authors correspondingly determined that hybrid composites are good replacements [27]. In addition, when there is a demand for higher impact strength, the usage of a composite made from abaca can be an option. The scientists also indicated that abaca and cotton fibers can be employed as reinforcements in polymeric composites, which can then be used to produce vehicle components like mudguards and engine covers. The compression molding technique is used to create a composite made of sisal and urea-formaldehyde. The authors researched to determine how fiber loading affected the mechanical properties of the material [28]. The study found that composites produced with 30% sisal fiber had the highest flexural strength and 50% had the highest impact strength. How many jute layers affect the mechanical qualities of a compression-molded jute/epoxy composite? The number of fiber layers affects a material's mechanical properties [29]. According to the findings of the study, composites consisting of five sheets of fiber had superior mechanical capabilities. According to the findings of the study, NFPCs offer significant benefits in a variety of structural applications within the Indian Railway industry. NFPCs are used in the construction of berths, dividers, floor and ceiling panels, and modular toilets in the railway sector. If low power consumption, low weight, low inertia, and low track wear are among the desired

outcomes, then natural fibers should be employed in railway construction. The authors also mentioned that agave fiber is another viable contender for these purposes and that it may be used in those ways [30, 31].

The efforts that DaimlerChrysler has made toward sustainability have prepared the path for technology transfer programs in South America, the Philippines, and South Africa that entail the use of environmentally friendly materials. Bio-based automotive supply chains will begin with farmers and conclude at car distributors as the organization emphasized the use of renewable sources rather than traditional fossil fuels to promote international sustainability. NFPCs are currently being utilized in the production of a variety of different components by virtually all of the major car manufacturers [13].

5.2. Natural Fiber Applications in Building. Natural fiber and polymer matrix biocomposite materials are a class of man-made composites with a wide range of uses. More and more people are using these materials because they are easy to design with, have good properties, and look good. However, the interaction at the fiber–matrix interface determines the biocomposite's application. This document summarizes the most recent published studies on the fiber–matrix interface. A quick introduction to biocomposite materials is given. The alteration of natural fibers and its impact on fiber–matrix interfacial adhesion and characteristics are the primary topic of this review. The impact of chemical modification on fiber structure and fiber–matrix interfacial adhesion mechanism is also explored [32]. When used as the primary component in biocomposite construction materials, natural fibers that have been reclaimed from annual agricultural waste have the potential to confer many distinct benefits. Fibers like hay as well as other nonwood fibers have the lowest price when compared to certain other natural fibers that may be found on the market for industrial use. Densification of agro-fibers, building plans for specific uses, and production methods are all included in this research. The composite material was made by combining natural fibers with three different types of biopolymers. A polyamide, a thermoplastic, and an elastic thermosetting polymer were all present among these biopolymers. This allowed for varying final designs and geometries but necessitated modifying fabrication methods accordingly. Mechanical qualities and an assessment of their impact on the environment were investigated to provide evidence that the newly produced items had practical applications [33]. The natural fiber composites, also known as NFCs, in which polymeric resins serve as the matrix components are the primary subject of this chapter. At least one key component of NFCs has a renewable biological origin, making them biodegradable. The fundamentals of NFC materials, including reinforcements preforms, matrix polymers, composite production procedures, characterization, and quality assurance, are described in this article. Since NFC materials made from renewable resources can be used to make low-cost structural parts and sustainable and environmental alternatives to traditional structural materials in the automotive and construction industries, microbially structural composites are also being looked at for use in the construction and automotive industries [22]. To evaluate the acoustic absorption capabilities of a set of 21 elastic material high-frequency resonant construction (HFRC) prototypes, the impedance tube method was applied. Natural and synthetic fiber polymeric components, including polyamide, lignocellulose, keratin, and alginate biopolymer, were recovered from postconsumer and end-of-life industrial wastes to generate the nanocomposite blends. The discussion focuses on two significant environmental pollution issues, namely urban sound and waste fibers, as well as how these wastes can be converted into construction materials. The end goal is a two-pronged solution that has positive effects on the environment, the economy, and society. Creating high-end, nontoxic solutions for acoustical structures help to facilitate the removal of valuable fiber components from landfills [34, 35]. Although urban vibration is a major contributor to pollutants in industrialized metropolitan areas, the focus of this work is on the sound-absorbing qualities of HFRCs. The results showed the modest absorption at mid-frequencies (500 Hz to 2.4 kHz) and considerable absorption at higher frequencies (2.4–6.5 kHz). Low-density prototypes with small filler-matrix interfacial gaps and natural fibers with hierarchical intraparticle microstructure achieved 0.79 peak sound absorption. These novel reduced materials from wastes provide an environmentally friendly alternative to standard commercial synthetic products for improving indoor quality by reducing noise, especially in dense urban areas [36].

6. Conclusion

Numerous researchers have been inspired to develop innovative materials as a result of the deteriorating state of the atmosphere, rising concerns about the state of the environment, and the requirement for increased levels of innovation.

(1) Researchers from all around the world are efficiently responding to worries about the environment by moving their focus toward materials that are biodegradable and sustainable. Since this is the case, NFRPCs are rapidly replacing other materials in a wide variety of industrial settings.

(2) An uptick in inquiries on NFRPCs inspired this study of natural fibers, their production, chemical processing, and many applications. Chemical treatments were examined in depth as a means of improving surface qualities such as hydrophobic nature and adherence among fibers and polymeric materials.

(3) The choice of natural fibers is determined by factors such as their availability, weight, and cost, as well as their mechanical qualities. The degree to which the fibers adhere to one another is the primary factor that determines the material characteristics of NFRPCs. The pretreatment of the fibers can result in an improvement in this characteristic.

(4) It is possible to use alkali treatment because it is regarded as the method that is the most successful for all NFRPCs. Other treatments, such as those

consisting of alkali and silane, can also be employed in conjunction. Significant improvements in the fibers' mechanical characteristics are brought about as a result of both the increased chemical concentration and the lengthened soaking time. New developments in NFRPCs can be seen as a promising material for numerous applications in the future.

(5) The interfacial connection of natural fibers with the matrix continues to be the most important issue in terms of inclusive performance. In all of the chemical treatments that have been researched, the alkali treatment stands out as the most straightforward, time-honored, and successful method for treating many types of fibers. This treatment, which can be carried out on virtually every type of natural fiber, can improve the interfacial bond of the fibers. The phenomena of biodegradation or the possible igniting of NFRPCs is just somewhat new. As a result, researchers should also examine how NFRPCs decompose.

(6) Biodegradation and deterioration time must be accurately accounted for to make an informed decision. It is likely that in the not-too-distant future, similar NFRPCs will achieve total biodegradability and mechanical qualities that are comparable to those of composites reinforced with synthetic fibers.

(7) Improvements in NFRPC composite materials are projected to focus on mass production, as well as their application in the large-scale market, soon. Furthermore, the incorporation of nanocellulose (possibly nanoclay) into NFRPC can improve a variety of beneficial qualities, and finally, the investigation of NFRPC tribological properties should be one of the primary topics of focus in larger prospective studies.

Data Availability

The data used to support the findings of this study are included within the article.

Conflicts of Interest

The authors declare that they have no conflicts of interest.

References

[1] U. K. Komal, V. Verma, T. Ashwani, N. Verma, and I. Singh, "Effect of chemical treatment on thermal, mechanical and degradation behavior of banana fiber reinforced polymer composites," *Journal of Natural Fibers*, vol. 17, no. 7, pp. 1026–1038, 2020.

[2] N. Karthi, K. Kumaresan, S. Sathish, S. Gokulkumar, L. Prabhu, and N. Vigneshkumar, "An overview: natural fiber reinforced hybrid composites, chemical treatments and application areas," *Materials Today: Proceedings*, vol. 27, Part 3, pp. 2828–2834, 2020.

[3] M. Y. Khalid, R. Imran, Z. U. Arif et al., "Developments in chemical treatments, manufacturing techniques and potential applications of natural-fibers-based biodegradable composites," *Coatings*, vol. 11, no. 3, Article ID 293, 2021.

[4] J. Abd Halip, L. S. Hua, Z. Ashaari, P. M. Tahir, L. W. Chen, and M. K. A. Uyup, "Effect of treatment on water absorption behavior of natural fiber-reinforced polymer composites," in *Mechanical and Physical Testing of Biocomposites, Fibre-Reinforced Composites and Hybrid Composites*, M. Jawaid, M. Thariq, and N. Saba, Eds., *In Woodhead Publishing Series in Composites Science and Engineering*, pp. 141–156, Woodhead Publishing, 2019.

[5] A. R. Kakroodi, Y. Kazemi, and D. Rodrigue, "Mechanical, rheological, morphological and water absorption properties of maleated polyethylene/hemp composites: effect of ground tire rubber addition," *Composites Part B: Engineering*, vol. 51, pp. 337–344, 2013.

[6] R. Prasanna Venkatesh, K. Ramanathan, and V. Srinivasa Raman, "Tensile, flexual, impact and water absorption properties of natural fibre reinforced polyester hybrid composites," *Fibres and Textiles in Eastern Europe*, vol. 24, pp. 90–94, 2016.

[7] M. K. Gupta and R. K. Srivastava, "Mechanical, thermal and water absorption properties of hybrid sisal/jute fibre reinforced polymer composite," *Indian Journal of Engineering & Materials Sciences*, vol. 23, pp. 231–238, 2016.

[8] V. Mittal and S. Sinha, "Effect of chemical treatment on the mechanical and water absorption properties of bagasse fiber-reinforced epoxy composites," *Journal of Polymer Engineering*, vol. 35, no. 6, pp. 545–550, 2015.

[9] W. Z. W. Zahari, R. N. R. L. Badri, H. Ardyananta, D. Kurniawan, and F. M. Nor, "Mechanical properties and water absorption behavior of polypropylene/ijuk fiber composite by using silane treatment," *Procedia Manufacturing*, vol. 2, pp. 573–578, 2015.

[10] P. Upadhyaya, M. Garg, V. Kumar, and A. K. Nema, "The effect of water absorption on mechanical properties of wood flour/wheat husk polypropylene hybrid composites," *Materials Sciences and Applications*, vol. 3, no. 5, pp. 317–325, 2012.

[11] O. Baykus, A. Mutlu, and M. Doğan, "The effect of pre-impregnation with maleated coupling agents on mechanical and water absorption properties of jute fabric reinforced polypropylene and polyethylene biocomposites," *Journal of Composite Materials*, vol. 50, no. 2, pp. 257–267, 2016.

[12] M. E. Ali, Z. Sultana, M. S. Uddin, S. A. Mamun, M. M. Haque, and M. Hasan, "Effect of hydrazine post-treatment on natural fibre reinforced polymer composites," *Materials Research Innovations*, vol. 17, no. sup2, pp. s19–s26, 2013.

[13] T. Ramakrishnan, M. D. Mohan Gift, S. Chitradevi et al., "Study of numerous resins used in polymer matrix composite materials," *Advances in Materials Science and Engineering*, vol. 2022, Article ID 1088926, 8 pages, 2022.

[14] S. E. Samaei, H. A. Mahabadi, S. M. Mousavi, A. Khavanin, M. Faridan, and E. Taban, "The influence of alkaline treatment on acoustical, morphological, tensile and thermal properties of Kenaf natural fibers," *Journal of Industrial Textiles*, vol. 51, no. 5_suppl, pp. 8601S–8625S, 2022.

[15] P. Madhu, M. R. Sanjay, P. Senthamaraikannan et al., "Effect of various chemical treatments of *Prosopis juliflora* fibers as composite reinforcement: physicochemical, thermal, mechanical, and morphological properties," *Journal of Natural Fibers*, vol. 17, no. 6, pp. 833–844, 2020.

[16] R. Thirumalaisamy and S. P. Subramani, "Investigation of physico-mechanical and moisture absorption characteristics of raw and alkali treated new *Agave angustifolia* marginata (AAM) fiber," *Materials Science*, vol. 24, no. 1, pp. 53–58, 2018.

[17] M. Prithiviraj and R. Muralikannan, "Investigation of optimal alkali-treated *Perotis indica* plant fibers on physical, chemical, and morphological properties," *Journal of Natural Fibers*, vol. 19, no. 7, pp. 2730–2743, 2022.

[18] K. Raja, P. Senthilkumar, G. Nallakumarasamy, and T. Natarajan, "Effect of eco-friendly chemical treatment on the properties of *Sesbania rostrata* fiber," *Journal of Natural Fibers*, vol. 18, no. 12, pp. 2241–2253, 2021.

[19] H.-C. Nguyen, K.-H. Lin, S.-L. Ho, C.-M. Chiang, and C.-M. Yang, "Enhancing the abiotic stress tolerance of plants: from chemical treatment to biotechnological approaches," *Physiologia Plantarum*, vol. 164, no. 4, pp. 452–466, 2018.

[20] R. Kumar, M. I. Ul Haq, A. Raina, and A. Anand, "Industrial applications of natural fiber-reinforced polymer composites—challenges and opportunities," *International Journal of Sustainable Engineering*, vol. 12, no. 3, pp. 212–220, 2019.

[21] M. S. Fogorasi and I. Barbu, "The potential of natural fibres for automotive sector—review," *IOP Conference Series: Materials Science and Engineering*, vol. 252, Article ID 012044, 2017.

[22] Y. K. Kim and V. Chalivendra, "Natural fibre composites (NFCs) for construction and automotive industries," in *Handbook of Natural Fibres*, pp. 469–498, Woodhead Publishing, 2020.

[23] H. A. Al-Qureshi, "The use of banana fibre reinforced composites for the development of a truck body," in *Second International Wood and Natural Fibre Composites Symposium*, pp. 1–8, Kassel/Germany, 1999.

[24] D. Verma and I. Senal, "Natural fiber-reinforced polymer composites: feasibility study for sustainable automotive industries," in *Biomass, Biopolymer-Based Materials, and Bioenergy*, pp. 103–122, Woodhead Publishing, 2019.

[25] N. M. Nurazzi, M. R. M. Asyraf, S. Fatimah Athiyah et al., "A review on mechanical performance of hybrid natural fiber polymer composites for structural applications," *Polymers*, vol. 13, no. 13, Article ID 2170, 2021.

[26] D. P. Ferreira, J. Cruz, and R. Fangueiro, "Surface modification of natural fibers in polymer composites," in *Green Composites for Automotive Applications*, pp. 3–41, Woodhead Publishing, 2019.

[27] N. Ramli, N. Mazlan, Y. Ando et al., "Natural fiber for green technology in automotive industry: a brief review," *IOP Conference Series: Materials Science and Engineering*, vol. 368, Article ID 012012, 2018.

[28] T. Khan, M. T. B. Hameed Sultan, and A. H. Ariffin, "The challenges of natural fiber in manufacturing, material selection, and technology application: a review," *Journal of Reinforced Plastics and Composites*, vol. 37, no. 11, pp. 770–779, 2018.

[29] O. T. Adesina, T. Jamiru, E. R. Sadiku, O. F. Ogunbiyi, and L. W. Beneke, "Mechanical evaluation of hybrid natural fiber-reinforced polymeric composites for automotive bumper beam: a review," *The International Journal of Advanced Manufacturing Technology*, vol. 103, pp. 1781–1797, 2019.

[30] K. N. Keya, N. A. Kona, F. A. Koly, K. M. Maraz, M. N. Islam, and R. A. Khan, "Natural fiber reinforced polymer composites: history, types, advantages, and applications," *Materials Engineering Research*, vol. 1, no. 2, pp. 69–85, 2019.

[31] T. Ramakrishnan, S. Senthil Kumar, S. J. S. Chelladurai et al., "Effect of moisture content on mechanical properties of AAM natural fiber-reinforced isophthalic polyester composites," *Advances in Materials Science and Engineering*, vol. 2022, Article ID 3533143, 10 pages, 2022.

[32] S. O. Amiandamhen, M. Meincken, and L. Tyhoda, "Natural fiber modification and its influence on fiber-matrix interfacial properties in biocomposite materials," *Fibers and Polymers*, vol. 21, pp. 677–689, 2020.

[33] H. Dahy, "Biocomposite materials based on annual natural fibres and biopolymers–design, fabrication and customized applications in architecture," *Construction and Building Materials*, vol. 147, pp. 212–220, 2017.

[34] K.-T. Lau, P.-Y. Hung, M.-H. Zhu, and D. Hui, "Properties of natural fibre composites for structural engineering applications," *Composites Part B: Engineering*, vol. 136, pp. 222–233, 2018.

[35] S. Alsubari, M. Y. M. Zuhri, S. M. Sapuan, M. R. Ishak, R. A. Ilyas, and M. R. M. Asyraf, "Potential of natural fiber reinforced polymer composites in sandwich structures: a review on its mechanical properties," *Polymers*, vol. 13, no. 3, Article ID 423, 2021.

[36] C. A. Echeverria, F. Pahlevani, W. Handoko, C. Jiang, C. Doolan, and V. Sahajwalla, "Engineered hybrid fibre reinforced composites for sound absorption building applications," *Resources, Conservation and Recycling*, vol. 143, pp. 1–14, 2019.

Hindawi
Journal of Nanomaterials
Volume 2022, Article ID 1033216, 9 pages
https://doi.org/10.1155/2022/1033216

Research Article

Analysis of Spectroscopic, Morphological Characterization and Interaction of Dye Molecules for the Surface Modification of TiB_2 Nanoparticles

S. Mayakannan,[1] R. Rathinam,[2] Rajasekaran Saminathan,[3] R. Deepalakshmi,[4] Mahesh Gopal,[5] J. Justin Maria Hillary,[6] S. Nanthakumar,[7] V. Y. Ganvir,[8] and Pallavi Singh[9]

[1]*Department of Mechanical Engineering, Vidyaa Vikas College of Engineering and Technology, Tiruchengode, Namakkal, Tamilnadu, India*
[2]*Department of Chemistry, Sri Eshwar College of Engineering, Coimbatore, 641202 Tamilnadu, India*
[3]*Mechanical Engineering, College of Engineering, Jazan University, Jazan city, Jazan, Saudi Arabia*
[4]*Computer Applications, Department of Inter-Disciplinary Studies, The Tamil Nadu Dr. Ambedkar Law University, Chennai, Tamilnadu, India*
[5]*Department of Mechanical Engineering, Wollega University, P.O. Box. 395 Nekemte, Ethiopia*
[6]*Department of Mechatronics Engineering, Sri Krishna College of Engineering and Technology, Coimbatore, Tamilnadu, India*
[7]*Department of Mechanical Engineering, PSG Institute of Technology and Applied Research Neelambur, Coimbatore, 641062 Tamilnadu, India*
[8]*Department of Applied Physics, Yeshwantrao Chavan College of Engineering, Nagpur, India*
[9]*Department of Biotechnology, Graphic Era Deemed to be University, Dehradun, Uttarakhand, India*

Correspondence should be addressed to Mahesh Gopal; doctorgmahesh@gmail.com

Received 4 September 2022; Accepted 30 September 2022; Published 15 October 2022

Academic Editor: Ridwan Yahaya

Nanoparticles of titanium diboride (TiB_2) coated with a conductive polymer and subjected to an oxidizing agent was carried out in this research. TiB_2 nanoparticles coated with polypyrrole (PPy) were studied using XRD and TEM techniques. Nitrogen adsorption and desorption properties of nanoparticles are covered with modified polypyrrole to understand better the surface zone, structural features, and pore geometries of the nanoparticles. The water-based hazardous anionic Congo red (CR) dye was removed using polypyrrole-coated titanium diboride (PPy@TiB_2) nanoparticles. Numerous cutting-edge experimental techniques, including FTIR, FE-SEM, EDXS, and element mapping analysis, were used to confirm the CR color's adhesion to the PPy@TiB_2 nanoadsorbent study. While conducting batch experiments, coated TiB_2 nanoadsorbents with polypyrrole enhanced the adsorption behaviour. One of the factors evaluated in the adsorption tests was pH; another was contact time, and a third was dose. At pH = 4, 98.75% of Congo red dye was detached using 60 mg of PPy-coated TiB_2 nanoadsorbent. Several sorption-desorption cycles were performed on this nanoadsorbent to determine its reusability. An excellent adsorption capacity for water treatment is reported in PPy-coated TiB2 nanoadsorbent.

1. Introduction

Every continent has a textile industry, and this sector contributes significantly to global economic growth [1]. Due to the coloring, printing, and washing processes carried without the appropriate pretreatment measures, textile wastewater is increasingly dyed. There are various concentrations of colored components in textile wastewater, which contribute

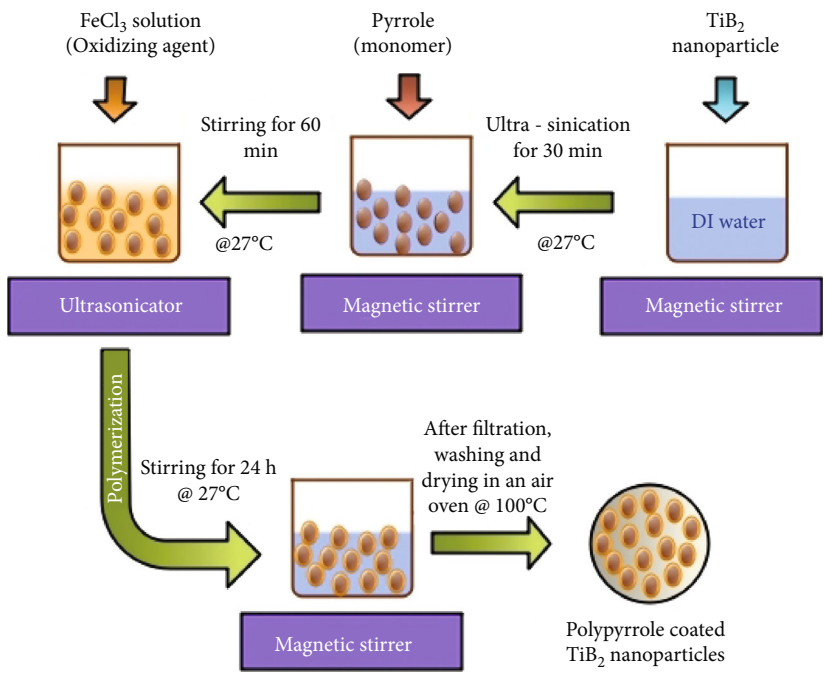

Figure 1: Diagram for the production of PPy@TiB_2.

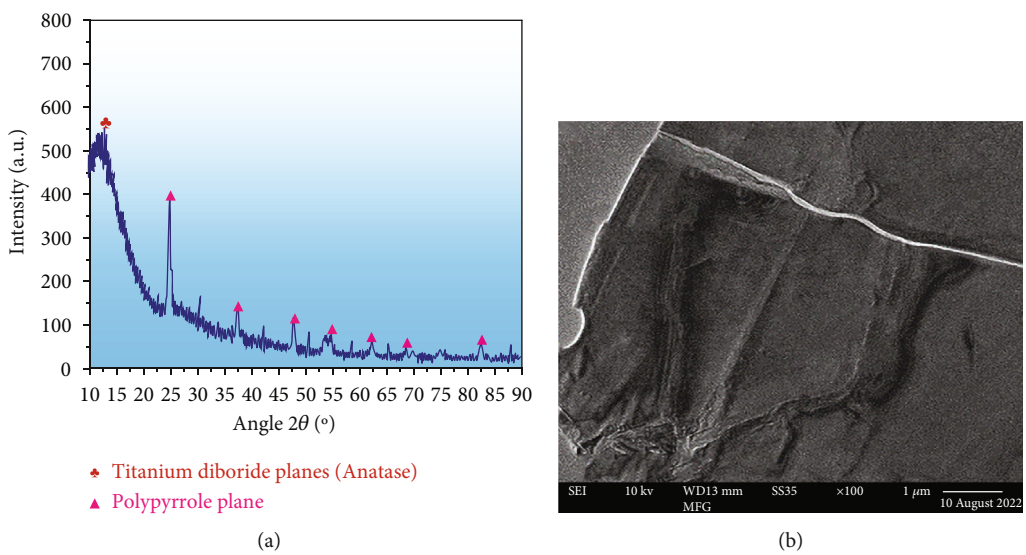

(a) (b)

Figure 2: (a) XRD and (b)TEM analysis of PPy@TiB_2.

to its pollution [2]. Therefore, textile effluent is clean since it has a high concentration of pigment molecules. Due to CR's ability to convert to benzidine, the anionic synthetic diazo dye is carcinogenic. Because of its aromatic structure, CR dye is both physiochemically and thermally stable [3]. CR's color changes depending on the pH, turning red at a pH of less than 5. Toxic to humans and animals, industrial effluent contains significant levels of COD and BOD, suspended particles and colloids, salts, and some other hard materials [4]. To deal with textile wastewater treatment issues, energy, water, and chemicals are required. There are numerous advantages to adsorption over other water treatment methods that are investigated as a viable option [5].

Various adsorbent forms are tried, including polar and nonpolar adsorbents. High surface-area adsorbent materials have effectively extracted different dye compounds from textile effluent. Various essential uses for nanomaterials have also been demonstrated [6–8]. Nanoparticles of titanium diboride (TiB_2) were employed in multiple material science applications: high-performance solar cells and photocatalytic devices using TiB_2-based nanotubes or nanoflowers, TiB_2 nanoparticles, and a PVDF membrane covered with a TiB_2 layer amplified for photocatalytic wastewater purification [9–11]. A polymer matrix alters the material's properties, such as combining polypropylene, polypyrrole, polyamide, or polylactic acid. Environmental scientists have

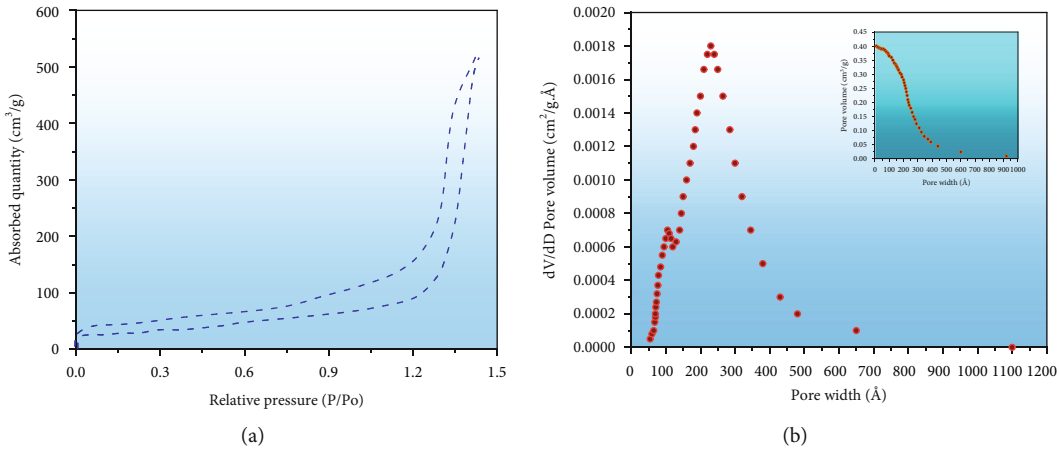

Figure 3: (a) Isotherm of N-adsorbed and desorbed of PPy@TiB_2 and (b) grain size dispersal plot and comparison of pore width and volume plot.

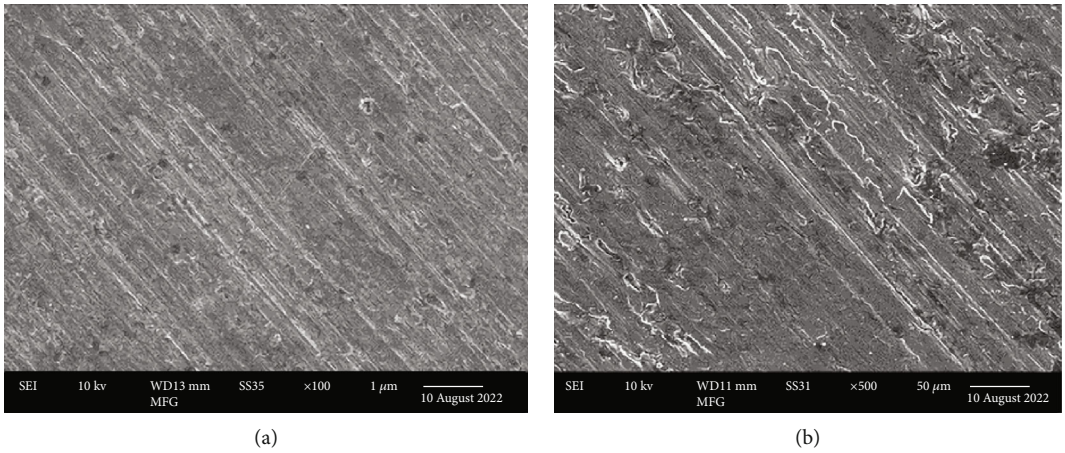

Figure 4: FESEM images of various magnifications of (a) PPy@TiB_2 and (b) CR-adsorbed PPy@TiB_2.

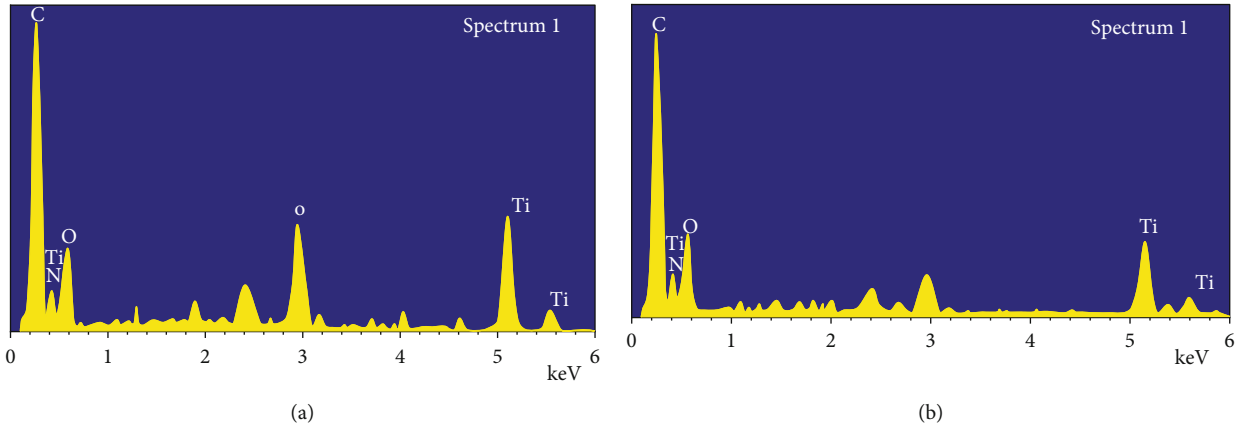

Figure 5: Energy dispersive X-ray analysis of (a) PPy@TiB_2 and (b) Congo red-adsorbed PPy@TiB_2.

been considering polymeric nanoadsorbents based on polypyrrole for several years.

The polymer has many properties that make it an ideal solution for water pollution problems [12]. Scientists have found that polypyrrole-based nanocomposites effectively clean the environment of heavy metal ions and radioactive pollutants, pigments, chemical compounds, and pesticides. Recent studies highlight photovoltaic efficiency, optical features, degradation capacity of photocatalytic materials, physical characteristics, and electric characteristics [13–15]. The

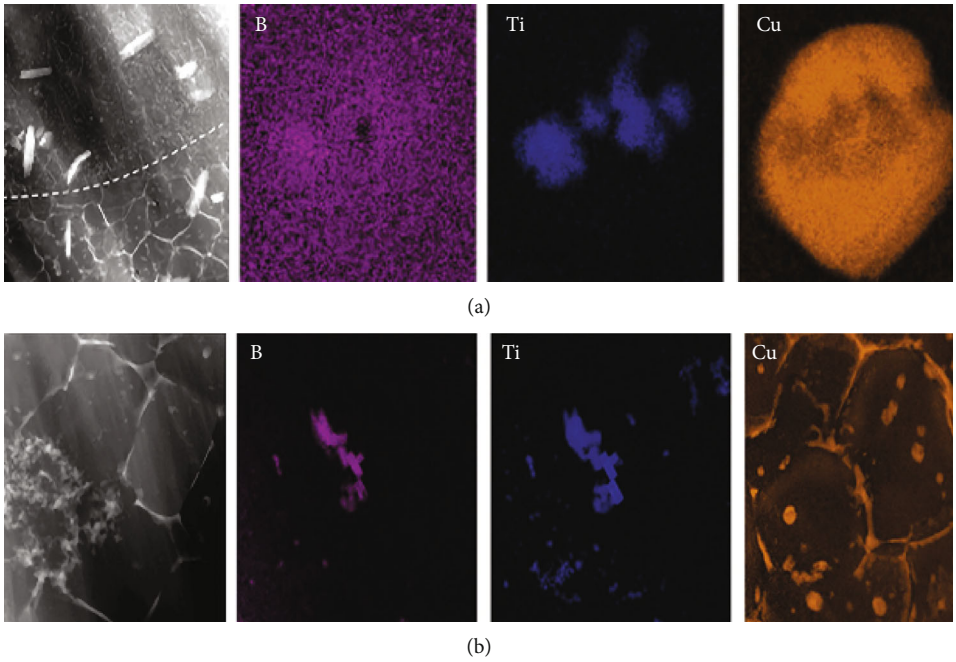

Figure 6: (a) PPy@TiB_2 and (b) process after Congo red-adsorbed PPy@TiB_2 elemental mapping analysis.

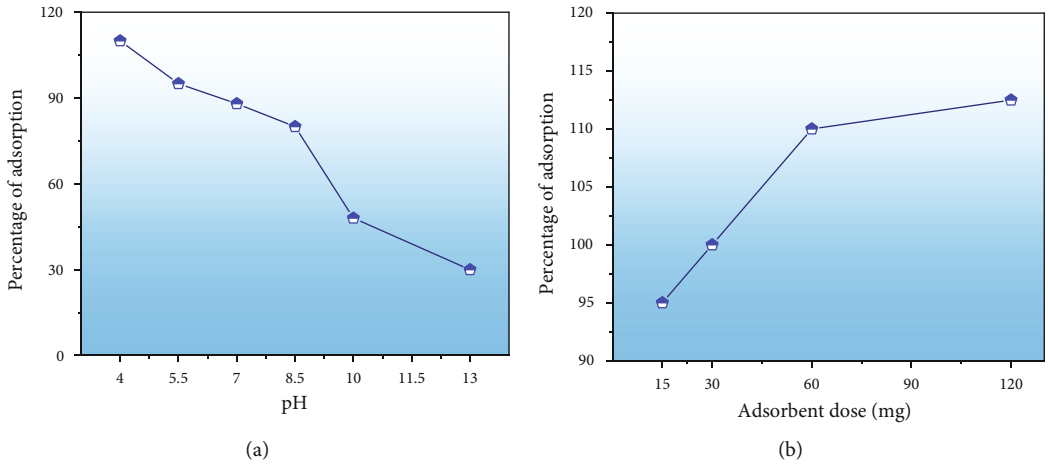

Figure 7: (a) Impact of pH and (b) impact of adsorbent dosage.

chemical polymerization production of polypyrrole-coated titanium diboride (PPy@TiB_2) has positively affected the environment. In the adsorption investigation, several traits and parameters were analyzed. Scientists have used the produced PPy@TiB_2 nanomaterial for wastewater dye removal due to its excellent performance and ease of reusing [16].

2. Experimentation

2.1. Methods and Materials. In the presence of a PPy monomer, a chemical polymerization approach is used to create a PPy@TiB_2 nanoadsorbent. There were 2 mL of pyrrole monomer and 30 minutes of ultrasonication at 27°C to prepare TiB_2 nanoparticles. The pyrrole monomer was allowed to adsorb on the TiB_2 nanoparticles' surfaces by swirling the dispersion for 60 minutes at 27°C [17, 18]. Iron was added to the TiB_2 dispersion as an oxidizing agent to polymerize the pyrrole on the nanoparticles' surfaces. The mixture was stirred for an additional 24 hours at 27°C using an electric stirrer. A four-hour oven drying at 100°C removed the contaminants and unreacted oxidants after cleaning the PPy@TiB_2 nanoadsorbent with deionized water and acetone after polymerization. An illustration of TiB_2 nanoparticles coated with polypyrrole is indicated in Figure 1.

2.2. Characterization. PPy@TiB_2 nanoadsorbent including TEM, HR-TEM, and fast Fourier transform (FFT) were synthesized. TESCAN FE-SEM, elemental mapping, and EDX analyze the PPy@TiB_2 nanoadsorbent earlier and the subsequent adsorption. X-ray diffraction measurements were determined using Cu Kα radiation with a 10° to 90° (2Θ) wavelength range [19]. The nitrogen adsorption technique

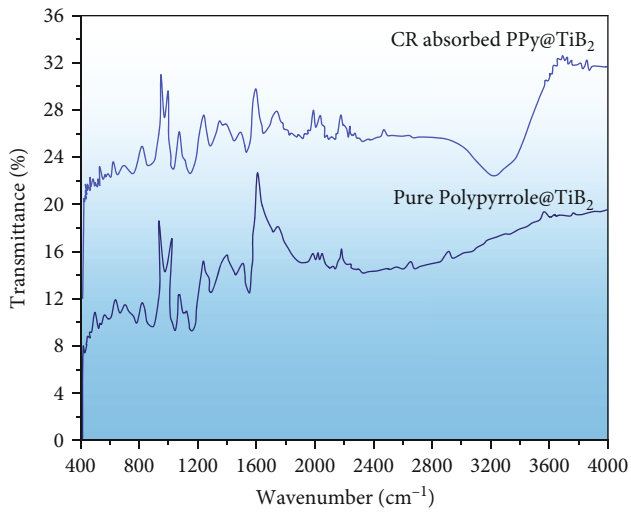

Figure 8: Image of attenuated total reflection-Fourier transform infrared spectroscopy.

measures pore size distributions and particular surface area. Using an FTIR spectrometer, it was necessary to conduct pre- and postadsorption studies on the nanoadsorbent, nano-PPy@TiB_2 [20].

2.3. Adsorption Studies. When removing Congo red (CR), batch experiments were carried out to test how the as-synthesized PPy@TiB_2 nanoadsorbent performed. The nanoadsorbent PPy@TiB_2 nanoadsorbent was studied to assess the effects of pH (acidity), contact time, and dosage on adsorption performance [21]. A pH experiment was conducted to check the PPy@TiB_2 nanoadsorbent-adsorbed CR at various pH levels (4 to 13). Adsorbent doses of 60 mg and 10 ppm of CR were used to test the adsorption performance. The synthetic nanoadsorbent was evaluated at various doses (15, 30, 60, and 120 mg) in a 10 ppm CR dye concentration to determine the effect of the dose [22]. Color concentrations were measured using a UV-V spectrophotometer during the batch adsorption trials. The formula used to calculate the percentage of CR dye that is eradicated is as follows [23, 24]:

$$\text{Percentage of Removal} = \frac{C_i - C_f}{C_i} \times 100 \quad (1)$$

C_i starting concentration of Congo red color
C_f CR dye's ending concentration

3. Results and Discussions

3.1. Properties of PPy@TiB_2 Nanoparticles. Investigation of PPy@TiB_2 nanocrystalline adsorbent structure was done using XRD. As-synthesized PPy@TiB_2 is indicated in Figure 2(a). Results showed that TiB_2 nanoparticles in composite form with PPy polymer were anatase crystalline. There were no visible phases other than TiB_2 in Figure 2(a), which verify the XRD pattern of its different stages (rutile and brookite). It discovered that PPy@TiB_2 nanocomposite reduced the crystalline phase of TiB_2 and PPy's amorphous nature by interacting with TiB_2. XRD data suggest that the surface morphology of TiB_2 nanoparticles with conducting polymer PPy was successful, as demonstrated by these results [25, 26]. Furthermore, TEM and HR-TEM analysis strongly support these findings.

Yet, Figure 2(b) shows the TEM patterns of the synthesized PPy@TiB_2. The TEM image of the synthesized PPy@-TiB_2 showed that only the TiB_2 facet had PPy polymer deposited on it, regardless of the other aspect [27]. A patch of unilluminated PPy polymer showed TiB_2 nanoparticles scattered everywhere, while PPy polymer granules with TiB_2 nanoparticles interacted tightly. TiB_2's high contrast made it distinct from PPy, which has lower contrast (Figure 2(b)). This nanoadsorbent formed using TiB_2 in the TEM image inset clearly showed the crystalline structure of the TiB_2 [28]. High resolution-TEM and FFT confirm that TiB_2 nanocomposite PPy@TiB_2 nanocomposite had an anatase crystalline phase as shown in supplemental Figures 3(a) and 3(b).

The surface, structural characteristics, and pore geometries of the PPy@TiB_2 nanospecific adsorbent were determined by the isotherm of nitrogen attachment shown in Figure 3(a). It reveals that saturation is observed at higher pressures, with a gradual increase in adsorption up to roughly 0.70 relative pressure (P/Po) [29]. Because of this, mesoporous adsorbents have a unique isotherm. The average pore diameters of the nanoadsorbent with 62.27 m_2/g surface area are 245.307 Å for adsorption and 216.698 Å for desorption using the nitrogen adsorption-desorption isotherm and the BJH technique [30]. In Figure 3(b), the average BET pore sizes for adsorption and desorption were 232.0041 Å and 247.2938 Å, respectively. According to IUPAC guidelines, mesoporous materials have pore diameters between 20 and 500 nm. Thus, the PPy@TiB_2 nanoadsorbent favours the mesoporous character of the material because of its pore sizes. Desorption is showed to be possible in Figure 3(a), where the desorption sum pore volume (0.385022 cm^3/gram) is greater than the adsorption sum pore volume (0.361217 cm^3/gram) at P/Po = 0.982. It shows that reversible desorption is conceivable. The regeneration results confirmed this tendency even more conclusively. A mesopore capillary condensation is present in the isotherm, in accordance with IUPAC's classifications of physisorption isotherm/hysteresis loops [31].

These images were taken at three different magnification levels and show the material's granular structure. As the magnification increased, the brightness decreased, indicating that the brightest particles were on the surface while the dullest particles were discovered deep within the layer (Figures 4(a) and 4(b)). It appeared like the character was uniform and smooth. Nanoparticles prepared before CR adsorption became more dispersed and bulkier in their microstructures.

Additionally, the components in the adsorbed PPy@TiB_2 were found out by FESEM-EDX analysis. As depicted in Figure 5, pure and CR-adsorbed PPy@TiB_2 samples have different elemental compositions. In the EDX spectra, carbon, oxygen, nitrogen, and titanium (Ti) are all visible (Figure 5(a)). Because of their relative atomic weights of

Table 1: Assignment of FTIR peaks in the pure and Congo red-adsorbed PPy@TiB_2.

FTIR peaks of PPy@TiB_2 (wavenumber cm^{-1})	Peaks role	FTIR peaks of Congo red-adsorped PPy@TiB_2 (wavenumber cm^{-1})	Peaks role
1537.64	Carbon-carbon pyrrole bond stretching vibration	1521.56	Carbon-carbon pyrrole bond stretching vibration
1447.79	Conjugated C-N band for stretching	1436.68	Conjugated C-N band for stretching
1291.17	A band of conjugated deformation in the plane of C-H	1272.28	A band of conjugated deformation in the plane of C-H
1142.18	Conjugated carbon-nitrogen stretching vibrations	1136.32	Conjugated carbon-nitrogen stretching vibrations
1034.13	Nitrogen-hydrogen in the planar deformation band	1025.04	Nitrogen-hydrogen in the planar deformation band
992.25, 882.29, 780.08	Deformations of the pyrrole ring G-H in and out of the plane	988.32, 860.58, 754.42	Deformations of the pyrrole ring G-H in and out of the plane
664.89	Characteristic peak of TiB_2	649.33	Characteristic peak of TiB_2
478.71	Stretching mode for the titanium-boride bond	477.51	Stretching mode for the titanium-boride bond

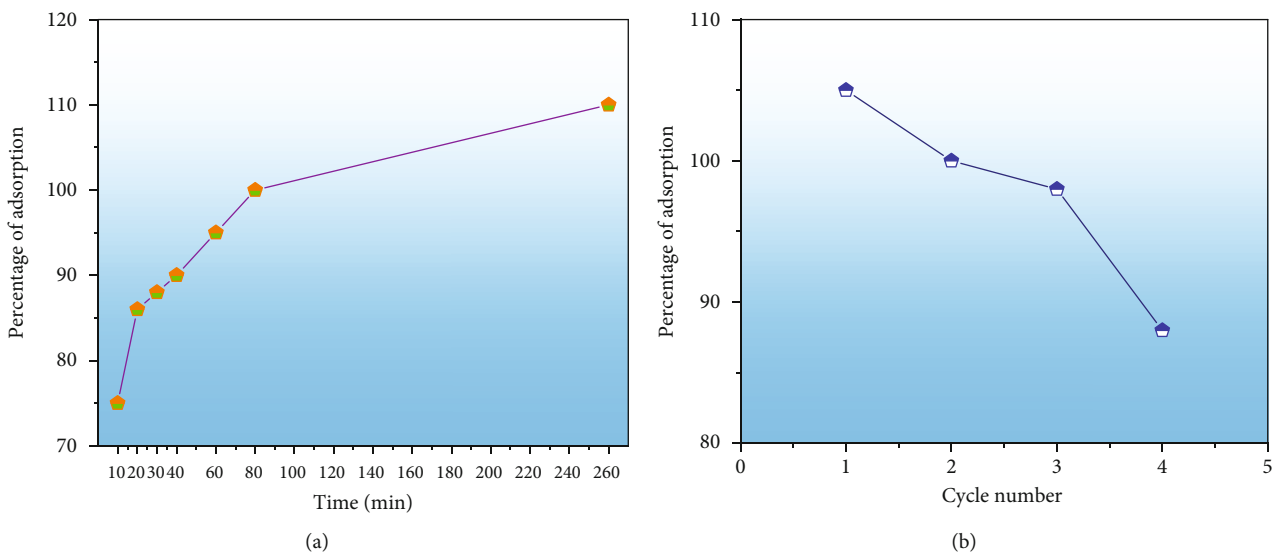

Figure 9: (a) Impact of contact duration and (b) regeneration capabilities of PPy@TiB_2 for Congo red dye adsorption.

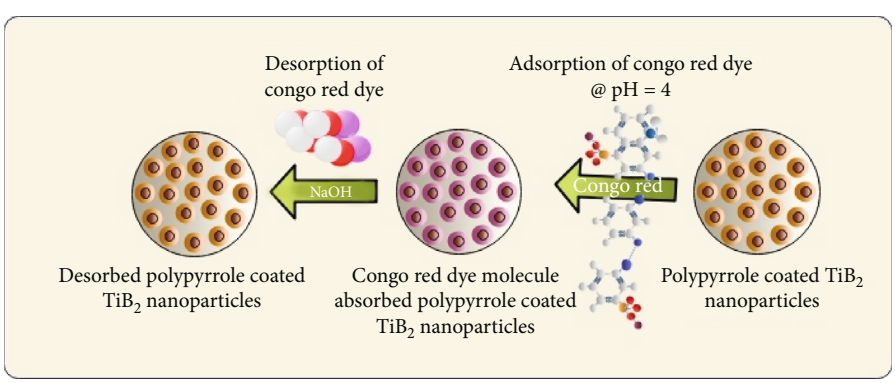

Figure 10: Diagram for adsorbed and desorbed mechanism of Congo red dye molecule on PPy@TiB_2.

50.75 and 28.21%, C and O atoms may have an effect on PPy@TiB_2's adsorption to CR dye molecules. In Figure 5(b), Na, C, and O atoms with high atomic masses indicate as evidence that CR molecules adsorb onto PPy@-TiB_2. Elements in PPy@TiB_2 and CR-adsorbed PPy@TiB_2 were studied further by an elemental mapping experiment [32, 33]. Before and after CR dye adsorption on PPy@TiB_2, the elemental mapping is indicated in Figure 6. In the PPy@-TiB_2 nanoadsorbent, carbon, oxygen, nitrogen, and titanium were all evenly distributed. C, O, and Na distributions were validated by exposing the nanoadsorbent PPy@TiB_2 nanoadsorbent to CR molecules [32, 33].

3.2. Behaviour of Adsorption

3.2.1. Impact of pH. When the aqueous phase's pH alters, it alters both the binding sites and ionization processes in this experiment [34, 35]. Figure 7(a) illustrates the percentage of Congo red adsorption by PPy@TiB_2 at different pH values (4.0, 5.5, 7, 8.5, 10.0, and 13.0). The starting pH level of 4.0 (98.75%) had the highest adsorption rate, which decreased as the pH increased. Positively charged PPy@TiB_2 surface was inhibited by electrostatic contact with negatively charged CR (due to the presence of two $-SO_3$ groups) [36]. Both Congo red and PPy@TiB_2 became negatively charged as the pH increased and the adsorption percentage reduced [37].

3.2.2. Effect of Adsorbent Dose. The amount of PPy@TiB_2 used had a beneficial impact on the adsorption percentage (Figure 7(b)). The percentage of adsorption rate was increased to obtain the equilibrium state of maximum adsorption [38]. Adsorption on the PPy@TiB_2 surface increases when the dose increases as the number of adsorption sites increases. The optimum PPy@TiB_2 amount attains to be 0.05 gm due to this study.

The AT-FTIR spectrum of pure PPy@TiB_2 and that of CR-adsorbed PPy@TiB_2 is indicated in Figure 8. Band assignments and wavenumbers are shown in Table 1 for the two samples, including the pure TiB_2 and TiB_2+CR-adsorbed PPy@TiB_2 FTIR bands. Most peaks experienced a minor shift to the lower wavenumbers after CR dye adsorbs on PPy@TiB_2 [39]. Therefore, these shifting peak values make it clear that the CR dye was successfully adsorbing onto PPy@TiB_2.

3.2.3. Effect of Adsorption Time. In adsorption experiments, adsorption time is critical. CR adsorption is illustrated in various time intervals in Figure 9(a). During the first 30 minutes of the investigation, the percentage of CR slowly adsorbing into the PPy@TiB_2 grew dramatically, reaching a maximum (110%) after 260 minutes. CR adsorption was stable, indicating that it attains the equilibrium phase. For the nanoadsorbent PPy@TiB_2 nanoadsorbent, 260 minutes show the optimal duration for carbon dioxide adsorption. When PPy@TiB_2 is adsorbed, the diffusion process is evidenced by the gradual rise in the adsorbed percentage [40].

3.2.4. Regeneration Study. The exhausted adsorbent (Congo red-adsorbed PPy@TiB_2) was evaluated on how well it can revitalize in a regeneration study [41]. It is shown in Figure 9(b) that NaOH was used as a desorbing agent for four cycles. This PPy@TiB_2 nevertheless showed outstanding regeneration efficacy with an adsorption decrease from 98.75 to 97% in Figure 9(b). PPy@TiB_2 proves to be a valuable and economical material for removing CR. The reproducibility of PPy@TiB_2 for eliminating CR from textile wastewater was established.

3.2.5. Adsorption Mechanism. The dynamic, active sites on the PPy@TiB_2 surface allowed CR to adsorb on it. A schematic diagram of CR dye molecule adsorption and desorption onto PPy@TiB_2 nanoadsorbent is indicated in Figure 10. Chemical polymerization was employed to synthesize nanocomposite using TiB_2 nanoparticles. Dispersed TiB_2 nanoparticles were used to adsorb the Polypyrrole monomer. Then, the pyrrole-adsorbed TiB_2 dispersal is treated with the $FeCl_3$ solution as an oxidizing agent. Finally, CR adsorption was determined using the polymerized PPy@TiB_2 nanoadsorbent. Carbo-oxygen-nitrogen-titanium elements make up its surface. Adsorption of textile wastewater is made more accessible with the final polymer form's increased surface area and chemical functionality. This positive charge is created by protonating the PPy@TiB_2 surface functional groups at pH = 4. This positive charge is used to interact with CR's negative $-SO_3$ groups. Due to the negative CR's electrostatic attraction to the TiB_2 surface, the adsorption is reduced as pH rises, whereas deprotonation caused a decrease in surface charge density.

4. Conclusion

Chemical polymerization with pyrrole (monomer) and ferric chloride successfully converted tiny titanium diboride nanoparticles (oxidizing agent). Polypyrrole originates on the surface of TiB_2 nanocomposites. PPy@TiB_2 nanoparticles were formed, and CR molecules could adhere to them, according to spectroscopic, structural, and morphological studies. It discovered that pH = 4260 minutes of contact hours, 60 mg of adsorbent, and a Congo red dye concentration of 10 ppm were the ideal adsorption conditions. After four cycles, a nanoadsorbent could maintain 90% of the CR color. The outcomes show that polypyrrole-coated titanium oxide nanoparticles are an effective treatment option for colored wastewater containing dye.

Data Availability

All authors confirmed that all necessary data are available in the manuscript.

Conflicts of Interest

The authors declare that they have no conflicts of interest.

References

[1] U. Sudhakara and J. Srinivasb, "Mechanical characteristics and corrosion behavior of friction stir AA5251-AA6063 butt

welds," *Materials Today: Proceedings*, vol. 15, pp. 132–137, 2019.

[2] Rajesh and P. Kaushik, "Micro structural behavior analysis of friction stir processed Al alloy AA6063/SIC," *The International Journal of Mechanical Engineering and Technology*, vol. 8, no. 11, pp. 991–998, 2017, [Online]. Available: https://www.scopus.com/inward/record.uri?eid=2-s2.0-85036561589&partnerID=40&md5=9100d82d683bd81f02d51a289c90ec1e.

[3] T. Teker, T. Kuṛsun, and T. Kurşun, "Weldability of AA6063 alloys by using keyhole gas tungsten arc welding technique," *Kovove Materialy-Metallic Materials*, vol. 52, no. 4, pp. 237–242, 2021.

[4] I. Sabry, A. M. El-Kassas, A.-H. I. Mourad, D. T. Thekkuden, and J. A. Qudeiri, "Friction stir welding of T-joints: experimental and statistical analysis," *Journal of Manufacturing and Materials Processing*, vol. 3, no. 2, 2019.

[5] R. Ramamoorthi, K. P. Yuvaraj, C. Gokul, S. J. Eashwar, N. Arunkumar, and S. A. T. Dheen, "An investigation of the impact of axial force on friction stir-welded AA5086/AA6063 on microstructure and mechanical properties butt joints," *Materials Today: Proceedings*, vol. 37, Part 2, pp. 3159–3163, 2021.

[6] Z. Ahmadi, M. Zakeri, M. Farvizi, A. Habibi-Yangjeh, S. Asadzadeh-Khaneghah, and M. Shahedi Asl, "Synergistic influence of SiC and C3N4 reinforcements on the characteristics of ZrB2-based composites," *Journal of Asian Ceramic Societies*, vol. 9, no. 1, pp. 53–62, 2021.

[7] N. Kaushik, S. Singhal, P. G. Rajesh, and B. N. Tripathi, "Experimental investigations of friction stir welded AA6063 aluminum matrix composite," *Journal of Mechanical Engineering Science*, vol. 12, no. 4, pp. 4127–4140, 2018.

[8] A. Sharma and D. B. Karunakar, "Effect of SiC and TiC addition on microstructural and mechanical characteristics of microwave sintered ZrB_2 based hybrid composites," *Ceramics International*, vol. 47, no. 18, pp. 26455–26464, 2021.

[9] S. A. A. Alem, R. Latifi, S. Angizi et al., "Development of metal matrix composites and nanocomposites via double-pressing double-sintering (DPDS) method," *Materials Today Communications*, vol. 25, p. 101245, 2020.

[10] S. A. Delbari, J. Lee, M. Sheikhlou et al., "Effect of iron nanoparticles on spark plasma sinterability of ZrB2-based ceramics," *Journal of the Australian Ceramic Society*, vol. 58, no. 4, pp. 1117–1128, 2022.

[11] E. S. Motailo, L. A. Lisyanskii, S. V. Vikhman, and D. D. Nesmelov, "Physical and mechanical properties of composite ceramics in the ZrB2–SiC–MoSi2 system," *Glass Physics and Chemistry*, vol. 47, no. 6, pp. 646–652, 2021.

[12] M. Shahedi Asl, Y. Azizian-Kalandaragh, Z. Ahmadi, A. Sabahi Namini, and A. Motallebzadeh, "Spark plasma sintering of ZrB2-based composites co-reinforced with SiC whiskers and pulverized carbon fibers," *International Journal of Refractory Metals and Hard Materials*, vol. 83, article 104989, 2019.

[13] T. Chen, W. Lu, Y. Fu, T. Chen, and W. Li, "Synthesis and characterization of chrom-free Zr-Ti-Ni pale green coating on AA6063 aluminium alloy," *Advanced Materials Research*, vol. 1053, pp. 414–420, 2014.

[14] V. A. Shcherbakov, A. N. Gryadunov, Y. N. Barinov, and O. I. Botvina, "Synthesis and properties of composites based on zirconium and chromium borides," *Russian Journal of Non-Ferrous Metals*, vol. 60, no. 2, pp. 179–185, 2019.

[15] B. Mohammadzadeh, S. Jung, T. H. Lee et al., "Characterization and FEA evaluation of a ZrB_2-SiC ceramic containing TaC for beam-column joint application," *Ceramics International*, vol. 47, no. 8, pp. 11438–11450, 2021.

[16] A. D. Sytchenko, S. B. Kabildina, and P. V. Kiryukhantsev-Korneev, "Effect of nitrogen concentration in a gas mixture on the structure and properties of Zr–B–(N) coatings obtained by the HIPIMS methods," *Russian Journal of Non-Ferrous Metals*, vol. 62, no. 6, pp. 785–793, 2021.

[17] S. Cheneke and D. Benny Karunakar, "The effect of solution treatment on aging behavior and mechanical properties of AA2024-TiB2 composite synthesized by semi-solid casting," *SN Applied Sciences*, vol. 1, no. 11, pp. 1–17, 2019.

[18] S. C. Lemessa and D. B. Karunakar, "Characterization and mechanical properties of 2024/Y2O3 composite developed by stir rheocasting," *Lecture Notes in Mechanical Engineering.*, vol. 1, pp. 439–453, 2020.

[19] S. Cheneke and D. B. Karunakar, "Microstructure characterization and evaluation of mechanical properties of stir rheocast AA2024/TiB2 composite," *Journal of Composite Materials*, vol. 54, no. 7, pp. 981–997, 2020.

[20] Y. R. Wang, C. J. Jin, and J. I. Song, "Mechanical characteristics of Al2O3, TiO2 and Al2O3-40.wt%TiO2 thermal coating on AISI 1045 matrix by nano-indentation test," *8th Asian-Australasian Conference on Composite Materials 2012, ACCM 2012 - Composites: Enabling Tomorrow's Industry Today,*, vol. 1, pp. , 2012639–645, 2012, [Online]. Available: https://www.scopus.com/inward/record.uri?eid=2-s2.0-84892991822&partnerID=40&md5=acf24a5e41c4f2209d799b3f515de0cd.

[21] C. Badini, P. Fino, M. Musso, and P. Dinardo, "Thermal fatigue behaviour of a 2014/Al_2O_3-SiO_2 (Saffil® fibers) composite processed by squeeze casting," *Materials Chemistry and Physics*, vol. 64, no. 3, pp. 247–255, 2000.

[22] O.-G. Lademo, O. S. Hopperstad, and M. Langseth, "An evaluation of yield criteria and flow rules for aluminium alloys," *International Journal of Plasticity*, vol. 15, no. 2, pp. 191–208, 1999.

[23] J. Feng, X. Du, Y. Sun, K. Zhao, Z. Shi, and M. Liu, "Effect of La–O–S complex inoculant on microstructure and mechanical characteristics of ductile iron," *Journal of Materials Science*, vol. 57, no. 8, pp. 5288–5297, 2022.

[24] S. Dharani Kumar and S. Sendhil Kumar, "Investigation of mechanical behavior of friction stir welded joints of AA6063 with AA5083 aluminum alloys," *Mechanics and Mechanical Engineering*, vol. 23, no. 1, pp. 59–63, 2019.

[25] T. S. Mahmoud, "Effect of friction stir processing on electrical conductivity and corrosion resistance of AA6063-T6 Al alloy," *Proceedings of the Institution of Mechanical Engineers, Part C: Journal of Mechanical Engineering Science*, vol. 222, no. 7, pp. 1117–1123, 2008.

[26] M. Abu-Okail, N. A. Alsaleh, W. M. Farouk et al., "Effect of dispersion of alumina nanoparticles and graphene nanoplatelets on microstructural and mechanical characteristics of hybrid carbon/glass fibers reinforced polymer composite," *Journal of Materials Research and Technology*, vol. 14, pp. 2624–2637, 2021.

[27] T. Kannan, B. Arulmurugan, L. Feroz Ali, and L. Rajeshkumar, "Performance analysis of AA3103 and AA6063 dissimilar weld joints by friction stir welding," *Songklanakarin Journal of Science & Technology*, vol. 44, no. 2, pp. 316–322, 2022, https://www.scopus.com/inward/record.uri?eid=2-s2.0-

8 5 1 3 2 8 9 7 8 7 2 & p a r t n e r I D = 4 0 & m d 5 = 28f9d950f7503bca3caec366bfa43639.

[28] T.-Y. Chen, W. Lu, W.-F. Li, and Y.-Q. Fu, "Synthesis of chrome-free coloring conversion coating on AA6063 aluminium alloy and its electrochemical properties," *Cailiao Gongcheng/Journal Materials Engineering*, vol. 43, no. 12, pp. 52–57, 2015.

[29] F. O. Edoziuno, A. A. Adediran, B. U. Odoni, O. G. Utu, and A. Olayanju, "Physico-chemical and morphological evaluation of palm kernel shell particulate reinforced aluminium matrix composites," *Materials Today: Proceedings*, vol. 38, pp. 652–657, 2021.

[30] O. S. I. Fayomi, O. P. Gbenebor, M. Abdulwahab, C. A. Bolu, and A. P. I. Popoola, "Structural modification, strengthening mechanism and electrochemical assessment of the enhanced conditioned AA6063-type Al-mg-Si alloy," *Journal of New Materials for Electrochemical Systems*, vol. 16, no. 1, pp. 59–64, 2013.

[31] D. Özyürek, T. Tunçay, and H. Kaya, "The effects of t5 and t6 heat treatments on wear behaviour of aa6063 alloy," *High Temperature Materials and Processes*, vol. 33, no. 3, pp. 231–237, 2014.

[32] G. N. Kumar, V. M. Reddy, Y. V. M. Reddy, and K. H. Reddy, "Study of abrasive wear behavior of AA 6063/TICP In-situ composites," *International Journal of Mechanical Engineering and Technology*, vol. 8, no. 5, pp. 42–52, 2017, [Online]. Available: https://www.scopus.com/inward/record.uri?eid=2-s2.0-8 5 0 1 9 5 5 0 6 2 6 & p a r t n e r I D = 4 0 & m d 5 = 0627f78d6d5367e54b06132b8dfa5740.

[33] P. Sureshkumar and V. C. Uvaraja, "Effect of ceramic and metallic reinforcement on mechanical, corrosion, and tribological behavior of aluminum composite by adopting design of experiment through Taguchi technique," *Journal of Tribology*, vol. 140, no. 5, 2018.

[34] N. Kaushik and S. Singhal, "Experimental investigations on microstructural and mechanical behavior of friction stir welded aluminum matrix composite," *International Journal of Engineering*, vol. 32, no. 1, pp. 162–170, 2019.

[35] O. S. I. Fayomi, I. G. Akande, A. P. I. Popoola, and H. Molifi, "Potentiodynamic polarization studies of cefadroxil and dicloxacillin drugs on the corrosion susceptibility of aluminium AA6063 in 0.5 M nitric acid," *Journal of Materials Research and Technology*, vol. 8, no. 3, pp. 3088–3096, 2019.

[36] T. Chen, W. Lu, W. Li, and Y. Fu, "Preparation and performace of a black-grey coating on AA6063 aluminium alloy," *Journal of Chinese Society for Corrosion and protection*, vol. 35, no. 2, pp. 177–182, 2015.

[37] T. Chen, Y. Fu, W. Lu, T. Chen, and W. Li, "Synthesis and characterization of chrom-free dark coating on AA6063 aluminium alloy with K2ZrF6," *Advanced Materials Research*, vol. 1053, pp. 421–428, 2014.

[38] S. Arnuri and S. N. Gurugubelli, "The effect of T8 heat treatment on wear behaviour and microstructure of 6063 aluminium alloy deformed by Cryo and RT ECAP," *Minerals, Metals and Materials Series*, pp. 1727–1741, 2021.

[39] A. Sabahi Namini, S. A. Delbari, M. Shahedi Asl, Q. V. Le, and M. Shokouhimehr, "Characterization of reactive spark plasma sintered (Zr,Ti)B2-ZrC-SiC composites," *Journal of the Taiwan Institute of Chemical Engineers*, vol. 119, pp. 187–195, 2021.

[40] E. R. Ferkhatly, A. V. Kovalska, and Y. I. Bogomol, "Microstructure and micromechanical properties of directionally crystallized composites of the B4C–(TixZr1 – x)B2 system," *Journal of Superhard Materials*, vol. 44, no. 2, pp. 111–116, 2022.

[41] V. A. Shcherbakov, A. N. Gryadunov, and M. I. Alymov, "Microstructural features of SHS-pressing ZrB2-B4C and TiB2-B4C composites," *Letters on Materials*, vol. 9, no. 1, pp. 11–16, 2019.

Hindawi
Journal of Nanomaterials
Volume 2022, Article ID 2302131, 12 pages
https://doi.org/10.1155/2022/2302131

Research Article

Study on Properties of Epoxy Composites Modified by Functional Graphite Oxide and Polyurethane

Yansong Kang,[1] Zenghui Feng,[1] Xinhua Jiang,[1] Lanxuan Liu,[1] Jiafa Tao,[2] Xiwang Huang,[1] Weiwei Wang,[1] and Xiangding Xiao[1]

[1]*Wuhan Research Institute of Materials Protection, Wuhan 430000, China*
[2]*CRRC Yangtze Co., Ltd, Wuhan 430000, China*

Correspondence should be addressed to Xiangding Xiao; 15040140333@xs.hnit.edu.cn

Received 26 July 2022; Accepted 23 August 2022; Published 15 September 2022

Academic Editor: Ridwan Yahaya

To improve the performance of the epoxy resin, isophorone diisocyanate (IPDI)-modified graphene oxide (GO) nanosheets were used, and the modified graphene oxide (iGO) was grafted with epoxy resin using polyurethane (PU) chain segments as a bridge to prepare epoxy composites. The iGO was characterized by Fourier transform infrared spectroscopy (FT-IR), X-ray photoelectron spectroscopy (XPS), X-ray diffraction analysis (XRD), and transmission electron microscopy (TEM), and the results showed that IPDI increased the layer spacing of iGO from 0.79 nm to 1.06 nm by grafting with hydroxyl and carboxyl groups on the surface of GO nanosheets, which improved the degree of exfoliation of iGO. Tensile testing, dynamic thermomechanical analysis (DMA), and scanning electron microscopy (SEM) were used to figure out the thermomechanical properties of the modified epoxy composites. The results show that the tensile strength and elongation at break of the as-prepared 0.5% iGO-PU/EP composites are 0.2 and 6.3 times higher than those of pure EP, respectively, and that the glass transition temperature was raised by about 2°C, with a significant increase in crosslinking.

1. Introduction

Epoxy resin (EP) is a widely used thermosetting material with low shrinkage on curing, high adhesion to the substrate surface, high mechanical strength, and excellent flame retardancy, corrosion resistance, and electrical resistance for a variety of applications. However, the disadvantages of low toughness and poor resistance to crack extension of epoxy resins [1, 2] limit their application in the fields of high impact strength and high fracture strength. For this reason, a lot of research has been done on toughening epoxy resins, some of which focused on introducing rubber phases into epoxy resins to compensate for the deficiencies of their own materials.

Polyurethane (PU) is an industrially important synthetic elastomer with excellent flexibility and elasticity, as well as high tensile strength, abrasion resistance, tear resistance, and solvent resistance. PU/EP systems have been previously reported and are commonly used in coating preparation and structural modification [3, 4] to mitigate the brittleness problems of epoxy systems. Wang and Chen [5, 6] synthesized three PUs (hydroxyl, amine, and anhydride) with different functionalized end groups to toughen bisphenol epoxy resin (DGEBA)/4,4-diaminodiphenyl sulfone (DDS) systems. Studies have shown that PU/EP with different molecular weights and contents can form homogeneous or multiphase [7, 8]. Polyurethane chains can be physically entangled and chemically bonded to the epoxy network to form grafted interpenetrating polymer network structures, forming interpenetrating polymer networks (IPN). However, the use of elastomer toughening also has unavoidable drawbacks; in general, the addition of elastomers or tougheners to polymers leads to a severe decrease in tensile strength, modulus of elasticity, and flexural strength [9]. To improve their mechanical properties, the addition of fillers and pigments to epoxy coatings is a very effective modification method [10, 11]. In the past few years, many researchers have been interested in nanomaterials when making composite materials.

Graphene oxide (GO) is a nanomaterial with an ultra-high specific surface area, a unique structure (SP2 hybridized two-dimensional single molecule film), and excellent thermal properties and is an effective choice for reinforcing polymer composites [12–14]. Reports from the past show that GO and functionalized GO nanosheets can improve the mechanical properties of epoxy coatings [15–18]. The surface of GO contains carbonyl, carboxyl, and hydroxyl groups, and the oxygen-containing groups of GO can be used for chemical modification. GO can be incorporated into polymers as covalent bonds by modification, but the large number of oxygen-containing groups leads to the incompatibility of GO with most non-polar solvents, which makes it difficult to disperse in organic polymers. Due to van der Waals forces, GO nanosheets are highly susceptible to aggregation in an epoxy resin matrix, which easily leads to thermal and mechanical degradation of the resin [19, 20]. Many researchers are now modifying the surface of GO nanosheets to solve the problem of difficult GO dispersion. Guo et al. [21] showed that GO nanosheets can be easily dispersed in organic polymers by grafting onto the surface of GO containing 2,4,6-trichloro-1,3,5-triazine (TCT) and the functionalization of GO by TCT-DETA can significantly improve the dispersibility and compatibility of GO, and the tensile and flexural strengths of GO-TCT-DETA/epoxy composites are higher than those of epoxy resin. The tensile and flexural strengths of GO-TCT-DETA/epoxy composites were increased by 40.79% and 48.56%, respectively, compared to epoxy resin. Yao et al. [22] achieved uniform dispersion of GO nanosheets in epoxy resin by chemical functionalization of GO with 4-nitrophenyl diazonium salt. When the content of modified graphene nanosheets was 0.8 wt%, the tensile strength and elongation at break of epoxy nanocomposites were increased by more than 30% and 50%, respectively. When the content of modified graphene nanosheets was 5 wt%, the thermal conductivity of the epoxy nanocomposites was increased to 0.56 W/m K, which was about 2.5 times that of pure epoxy resin.

PU was used as a second phase to toughen the epoxy resin and to disperse GO by grafting functionalized GO with PU to achieve the purpose of dispersing GO while improving the strength of the material. Based on this idea, this thesis carried out a study on the chemical grafting of GO into epoxy resins via PU. Graphene oxide was covalently modified with isophorone diisocyanate (IPDI) and reacted with polyol to form a graphene oxide-urethane (iGO-PU) prepolymer. The iGO-PU prepolymer was grafted to modify the epoxy resins, and the modified products were analyzed for their properties.

2. Experimental

2.1. Main Raw Materials. Graphene oxide (GO) is provided by Wuhan Low Dimensional Materials Research Institute Co., Ltd.; isophorone diisocyanate (IPDI) is purchased from BASF; polytetrahydrofuran ether (PTMG1000) is purchased from Taicang Company of Sinochem; bisphenol A diglycidyl ether epoxy resin (J-51) is purchased from Shanghai Junjiang New Materials sales Co., Ltd.; and diethylene methylene diamine curing agent (MH-222) is purchased from Changsha Xindehang Chemical Co., Ltd. Dibutyltin dilaurate (DBTDL) was purchased from Shanghai Aladdin biochemical Technology Co., Ltd., and N,N-dimethylacetamide (DMAC) and acetone are analytically pure.

2.2. Surface Modification of GO. Disperse 2 g GO in 200 mL DMAC, ultrasonically disperse for 2 hours, then transfer to a three-necked flask, add 18 g IPDI, add 2 drops of DBTDL, gradually heat up to 90°C in an oil bath, and stir under reflux for 20 hours under a nitrogen atmosphere. The product was suction filtered, washed with acetone, and dried in vacuo to obtain the final product, iGO.

2.3. iGO-PU Prepolymer Synthesis. In a three-necked flask equipped with IPDI, 2 drops of DBTDL were added, and iGO of different contents was added to PTMG1000 for mechanical grinding for 2 h and added dropwise to the flask, keeping the reaction temperature below 50°C. After the addition, the temperature was raised to 80°C and the reaction was allowed to react for 2 h to obtain modified graphene oxide-polyurethane prepolymers (iGO-PU) with different content.

Continue to prepare graphene oxide/polyurethane prepolymer (GO/PU) and pure polyurethane prepolymer (PU) according to the above method.

2.4. Preparation and Application of iGO-PU/EP Composites. Fill several three-necked flasks with 60 g of each type of prepolymer, then add 240 g of epoxy resin (J51), heat to 70°C, and thoroughly stir the reaction. The specific mix is shown in Table 1. Curing agent MH-222 (the ratio of epoxy resin content to curing agent is 3:1) was added, and curing at room temperature for 12 hours and at 80°C for 4 hours was performed to obtain composite samples. The preparation process of the composite material is shown in Figure 1, and the schematic diagram of the sample synthesis reaction is shown in Figure 2.

2.5. Testing and Characterization

2.5.1. Characterization of iGO Nanosheets. The infrared spectra of GO and iGO were obtained using the Nexus Fourier transform infrared spectrometer (FT-IR).

The diffraction spectra of GO and iGO were obtained using the D8 advance X-ray diffractometer (XRD).

The elements and energy levels of GO and iGO were obtained using the ESCALAB 250Xi X-ray photoelectron spectrometer (XPS).

The shapes of GO and iGO were obtained using the JEM-1400 Plus 120KV transmission electron microscope (TEM).

2.5.2. Composite Characterization. The polymer composite membrane is made of a polytetrafluoroethylene plate, and the dry film thickness is 0.5 mm ±0.05 mm. The mechanical properties of the composites were analyzed by dynamic thermomechanical analysis (DMA) and tensile test.

Using an Instron 5967 tensile testing machine, the room temperature tensile test was carried out at the strain rate of 5 mm/min.

Table 1: Preparation schemes for epoxy resins and different composites.

Sample	J51 (wt%)	PU (wt%)	GO (wt%)	iGO (wt%)
EP	100	0	0	0
0.5% iGO/EP	99.5	0	0	0.5
PU/EP	80	20	0	0
0.5% GO/PU/EP	80	19.5	0.5	0
0.1% iGO-PU/EP	80	19.9	0	0.1
0.5% iGO-PU/EP	80	19.5	0	0.5
1.0% iGO-PU/EP	80	19.0	0	1.0

Using a DMA Q800 dynamic thermomechanical analyzer, the storage moduli, loss factors, and glass transition temperatures of different composites were obtained at a temperature range of 25°C to 150°C, a frequency of 1 Hz, and a heating rate of 5°C/min.

The fracture morphology of the composites was obtained using the JSM-6510 scanning electron microscope (SEM).

3. Results and Discussion

3.1. Characterization of Graphene Nanosheets

3.1.1. FT-IR Analysis. The characteristic peaks of the FT-IR spectra of GO and iGO nanosheets are shown in Figure 3. The characteristic peaks of GO at 3334 cm^{-1}, 1731 cm^{-1}, 1619 cm^{-1}, 1234 cm^{-1}, and 1062 cm^{-1} correspond to the stretching vibrations of O-H, C=O (carboxyl), O=C-O, C-O, and C-O-C (alkoxy), respectively. The peak of iGO near 2946 cm^{-1} is attributed to a large number of C-H bonds in the alicyclic group of IPDI, and the carboxyl peak of 1731 cm^{-1} almost disappears because part of IPDI reacts with carboxyl to form substituted amide derivatives. The peak at 1626 cm^{-1} is amide carbonyl stretching (so-called amide I vibratory stretching). The new peaks at 1556 cm^{-1} may come from amides or carbamates, corresponding to the coupling of C-N stretching vibration and N-H deformed vibration (the so-called amide II vibration) [23]. The new peaks at 3340 cm^{-1} (overlapping with O-H), 750 cm^{-1}, and 1240 cm^{-1} are related to the stretching vibration, bending vibration, and C-O stretching vibration of N-H, respectively [24]. IPDI reacts with carboxyl (-COOH) and hydroxyl (-OH) on the surface of GO to form amides and carbamates, indicating that IPDI has been successfully grafted onto the surface of GO.

3.1.2. XRD Analysis. Figure 4 shows the XRD patterns of GO and iGO nanosheets. GO shows a strong characteristic diffraction peak (001) at 11.14 [25]. The diffraction angle of iGO (001) was shifted to a lower angle ($2\theta = 8.36^{\circ}$) by the surface modification of GO by IPDI. The interplanar spacing (d) of iGO nanoplatelets was increased from 0.79 nm to 1.06 nm. The results show that IPDI molecules are embedded between the GO sheets, resulting in an increase in the interlayer spacing of GO, and IPDI has been successfully grafted onto the edges and surfaces of GO nanosheets. In addition, compared with the sharp peaks of GO, the diffraction peak shape of iGO is obviously broadened and the diffraction intensity is reduced, which indicates that the successful grafting of IPDI destroys the original structure of the grains, makes the crystals more disordered, and further increases the distance between the lamellae, reducing the possibility of reunion.

3.1.3. XPS Analysis. The elemental composition of GO and iGO is analyzed by XPS. Figures 5(a) and 5(b) are XPS full spectra of GO and iGO, respectively. In the full spectrum of GO, ~284.1 eV and ~533.1 eV correspond to the characteristic peaks of C1s and O1s, respectively. The XPS spectrum of iGO increases the characteristic peak of N1s (~399.1 eV), which shows that the sample contains N elements. Table 2 shows the contents of carbon, oxygen, and nitrogen. It can be seen that after IPDI modification of GO, the oxygen atom content of iGO decreased from 33.67% to 17.19%, while the N atom content increased to 7.55%, indicating the introduction of N-containing groups after modification. These results show that there is a chemical reaction between GO and IPDI.

The C1s peaks of GO and iGO are shown in Figures 5(c) and 5(d). The C1s spectrum of GO is mainly composed of C=C (284.3 eV), C-C (284.8 eV), C-O (286.5 eV), C=O (carbonyl 287.0 eV), and O-C=O (carboxyl 288.5 eV). After modification, although there are the same oxygen-containing groups in the C1s of iGO, the intensity of the C-O peak becomes weaker. In addition, the C-N peak in ~286.1 eV coincides with the C-O peak to form a wide peak [26, 27], which is lower than the single peak of 0.4 eV of C-O in GO, which further indicates that some oxygen-containing groups in GO react with IPDI and form other chemical bonds. The intensity of O-C=O (288.2 eV) and C=O (287.0 eV) in the C1s peak of iGO is still very strong, which is due to the formation of NH-COO- and -NH-C=O groups. The peak intensity of the C1s spectrum of GO at a lower binding energy (~284.7 eV) is larger than that at a higher binding energy (~286.8 eV), while the opposite is true for iGO, which indicates the SP2 structure of some C atoms in iGO is destroyed to form SP3 hybrids. This shifts the GO further towards "disordering," increasing the distance between the sheets and reducing the likelihood of agglomeration. This corroborates with the results mentioned in XRD.

Figures 5(e) and 5(f) show the O1s scanning spectra of GO and iGO, respectively, and 532.6 eV and 531.0 eV are the peaks of C-O and C=O, respectively. Similar to the results of the C1s spectrum, the atomic percentage of O in the form of C=O increased from 0.03% to 27.5% due to the modification of iGO. On the one hand, it is because of the presence of unreacted -NCO groups, and on the other hand, the carboxyl groups on the graphene oxide nanosheets are consumed.

The high-resolution N1s spectrum of (g) iGO in Figure 5 shows two peaks at 399.4 eV and 400.1 eV, corresponding to -CONH and -NCO [28, 29], respectively, indicating the formation of a covalent bond between GO and IPDI.

3.1.4. TEM Analysis. The flake morphologies of GO and iGO were observed by transmission electron microscopy (TEM). It was found that the two kinds of particles had flat flake structures and no obvious agglomeration (Figure 6). In the

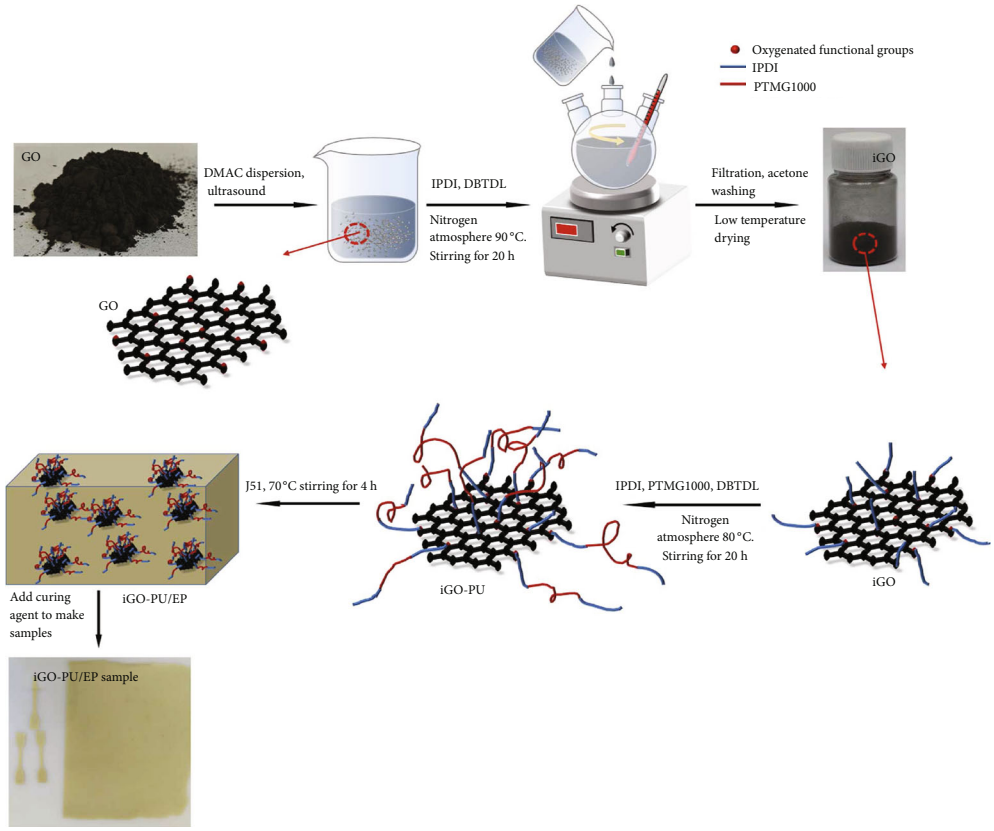

Figure 1: Schematic diagram of sample preparation.

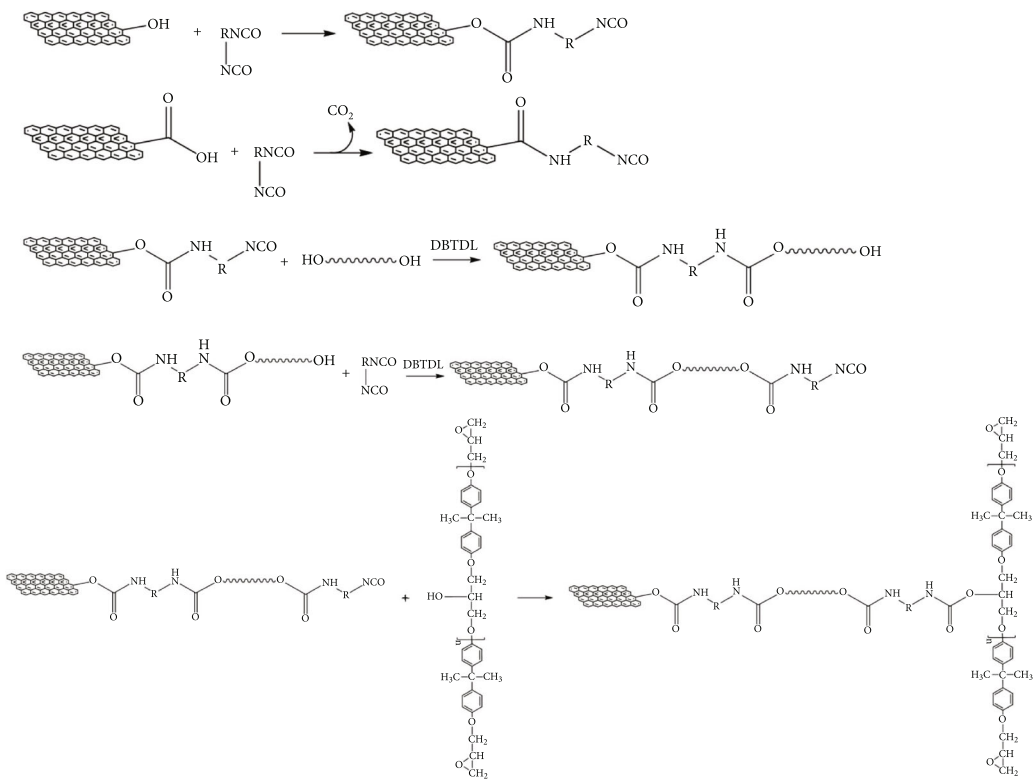

Figure 2: Schematic diagram of the sample synthesis reaction.

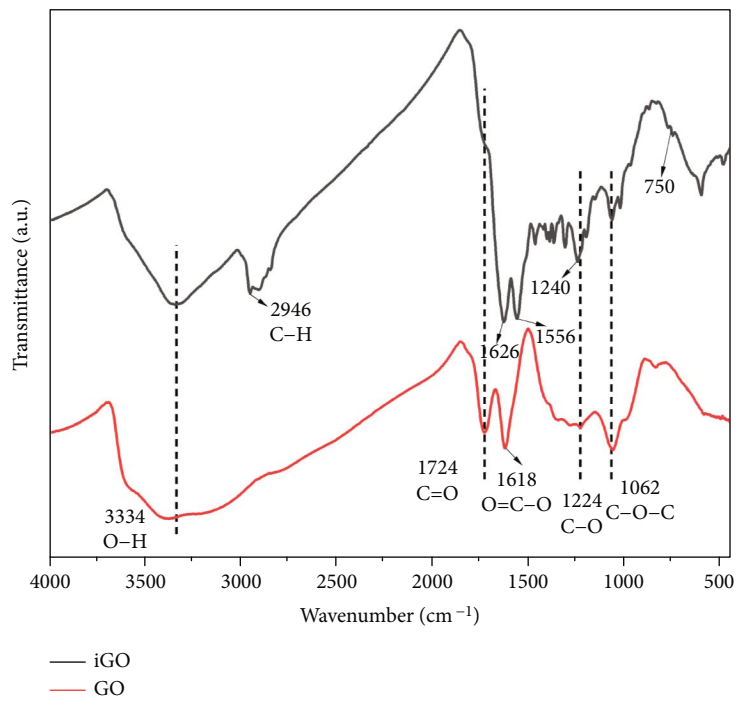

Figure 3: Infrared spectra of GO and iGO.

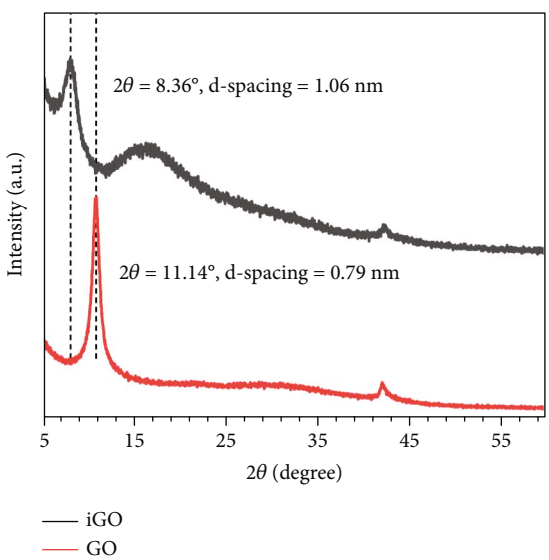

Figure 4: XRD patterns of GO and iGO.

process of modification, the morphology of GO changed clearly, and some worm-like particles appeared on its surface (Figure 6(b)), which was due to the grafting of IPDI onto the surface of GO. The iGO nanosheets show small size and many folds. It can be seen that part of IPDI is grafted between iGO layers, which increases the distance between layers and improves the dispersion of iGO in polar organic solvents [30].

3.1.5. iGO Dispersion and Stability Analysis. Figure 7 depicts the dispersion of iGO and GO in DMAC at 25°C. The left picture shows the sample of 0.1giGO (a) and GO (b) after ultrasonic dispersion for 30 min in 10 ml DMAC, and the picture on the right shows the sample after standing for 40 min. There was no obvious change in iGO after standing for 40 min, but GO had already settled. The dispersion stability of iGO in organic solvents was significantly improved. This is attributed to the functionalization of the hydroxyl groups on the iGO surface after modification, which reduces the density of hydrogen bond donor groups. The effect of van der Waals forces is weakened due to the increase in the interlayer spacing, and the organic solvent can pass through the layers of the GO sheet and break these hydrogen bonds [31].

Figure 8 shows the dispersion of the iGO-PU and GO/PU prepolymers at 25°C. The left picture shows the dispersion of 0.5% iGO-PU (a) and 0.5% GO/PU (b) at the beginning of the experiment, and the right picture shows the dispersion after standing for 10 days. It can be seen that after standing for 10 days, the iGO-PU hardly settles. This is attributed to the increased spacing after iGO nanosheets, which makes it easier to disperse, and after grafting -NCO groups, iGO will react with PTMG1000 containing -OH groups, increasing the steric hindrance, making it not difficult settle in the matrix. This shows good stability in PU prepolymer.

3.2. Composite Characterization

3.2.1. DMA Analysis. The DMA analysis results are shown in Figures 9(a)–9(d), including the temperature change from 30°C to 160°C, storage modulus ($E0$), and dissipation factor ($\tan\delta$). Table 3 presents the DMA data for neat epoxy and other composites. It can be seen that the storage modulus of PU/EP, 0.5%GO/PU/EP, and 0.5%iGO-PU/EP is lower than that of pure epoxy resin at 30°C because PU contains long-chain macromolecular ether bonds, reducing the strength of

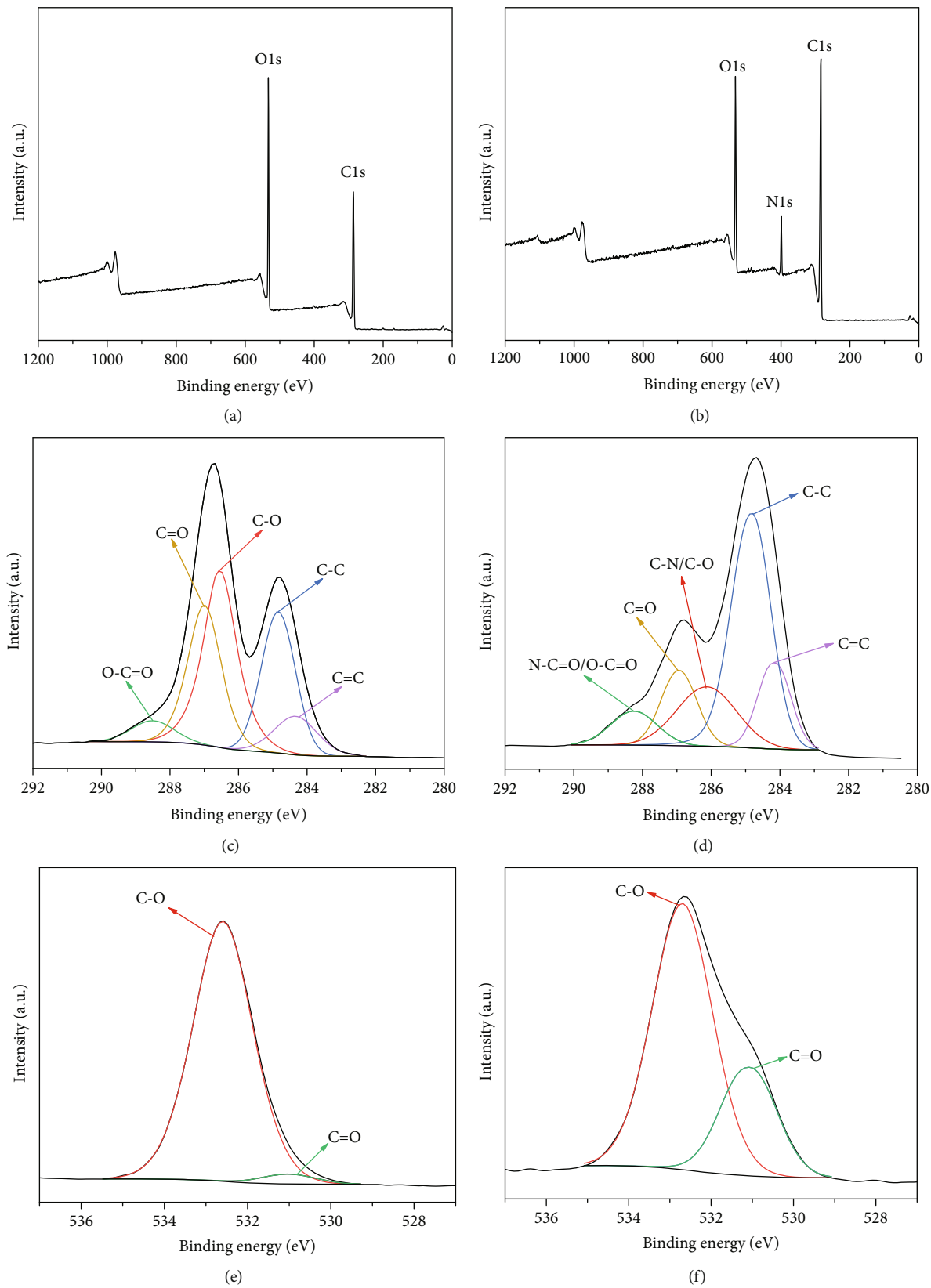

Figure 5: Continued.

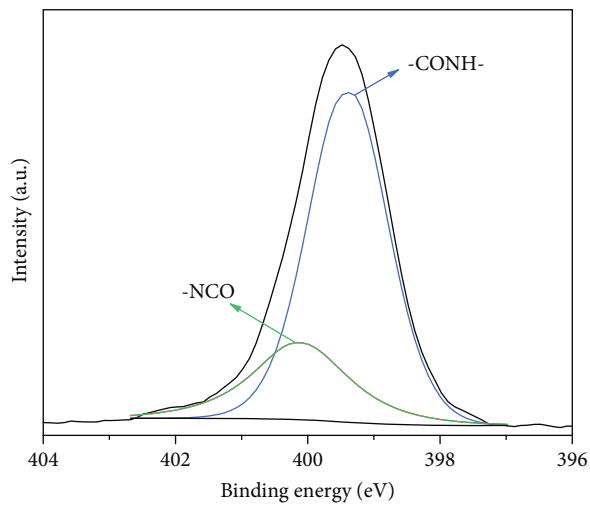

(g)

Figure 5: (a) XPS spectrum of GO, (b) XPS spectrum of iGO, (c) C1s high-resolution spectrum of GO, (d) C1s high-resolution spectrum of iGO, (e) O1s high-resolution spectrum of GO, (f) O1s high-resolution spectrum of iGO, and (g) N1s high-resolution spectrum of iGO.

Table 2: XPS atomic percentage of carbon, oxygen, and nitrogen.

Sample	C (at%)	O(at%)	N (at%)
GO	66.33	33.67	0
iGO	68.28	17.19	7.55

the composite material. By adding iGO, the storage modulus of PU/EP was increased by 65%. The good dispersion of iGO in the PU and the interaction with the PU interface limit the segment motion around the iGO sheet in the PU to a certain extent. The storage modulus of the GO-added composite material is slightly higher than that of PU/EP, and the GO nanosheets can strengthen the composite material to a certain extent. There is limited improvement in the mechanical properties of composites [32].

The T_g value is the maximum peak value of the tanδ and temperature curve. T_g measures the crosslinking degree and heat resistance of epoxy composites, and the storage modulus above T_g can also reflect the crosslinking degree of epoxy composites. The higher the storage modulus, the greater the crosslinking degree. The crosslink density v is calculated by [33, 34]:

$$v = \frac{E_r}{3RT_r} \tag{1}$$

where T_r is the temperature above T_g, E_r is the storage modulus corresponding to Tr obtained from the DMA data, and R is the actual gas constant. The obtained results are listed in Table 3.

The T_g of pure EP was 71.05°C. The T_g of EP decreased slightly with the addition of iGO, and the crosslink density reached its maximum, while the addition of PU caused the T_g to decrease by about 10°C and the crosslink density to also decrease significantly. The addition of 0.5% GO to PU/EP increased T_g by about 2°C, while the addition of 0.5% iGO increased the T_g of PU/EP by about 11°C, and even the crosslink density and T_g values exceeded those of pure EP. This further indicates that the addition of iGO induces an increase in the crosslinking density, which is due to the sufficient crosslinking of the iGO nanosheets with the epoxy resin through the PU linker chain and the restricted movement of the epoxy resin segment and the PU macromolecular chain, which delays the glass transformation.

By adding different amounts of iGO to PU/EP, it can be found that when the amount of iGO is less than 0.5%wt, with the increase of iGO content, $E0$, T_g, and crosslinking density all increase. However, when 1.0%wt iGO was added, the $E0$, T_g, and crosslinking density decreased. This may be due to the fact that the excess iGO could not be completely grafted to PU during the preparation process, and the "free" iGO will form a large number of defects in the matrix. In addition, a large amount of iGO dispersed in the material may coat the curing agent and affect the crosslinking and curing of the material, thereby affecting the thermodynamic properties of the material [32].

3.2.2. Tensile Test Analysis. Tensile tests were performed to investigate the mechanical properties of the composites. Figure 10(a) shows the tensile curves of different types of composites, and the specific values are listed in Table 4.

It can be seen that the elongation at break of pure epoxy resin is the lowest, and the tensile strength and elongation at break of iGO-EP are improved to a certain extent. Adding iGO will improve the strength of epoxy resin to a certain extent.

After PU is added to EP, an obvious yield point appears, and the elongation at break increases from 3.25% to 10.37%, which means that the epoxy resin changes from brittleness to toughness, and the isocyanate-terminated PU can cross the hydroxyl group of the oxygen resin. The movement of the soft segment (long-chain macromolecular alcohol) in PU can greatly improve the elongation at break of epoxy resin. Generally speaking, the tensile strength, elastic modulus, and

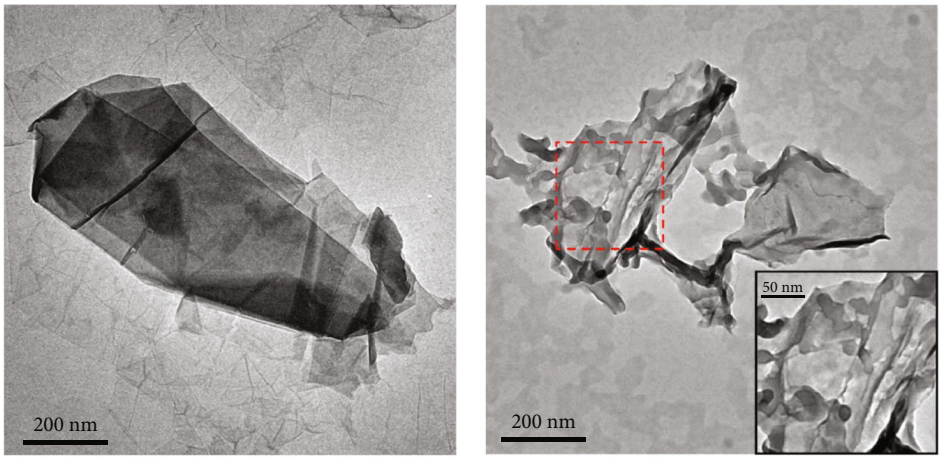

(a) (b)

Figure 6: TEM images of (a) GO and (b) iGO.

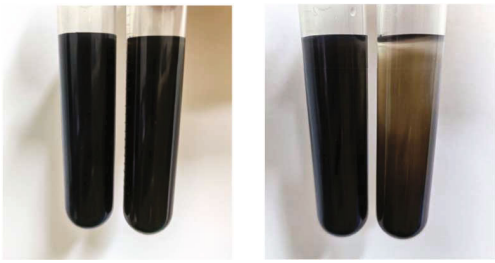

(a) (b) (a) (b)

Figure 7: Dispersion of iGO and GO in DMAC.

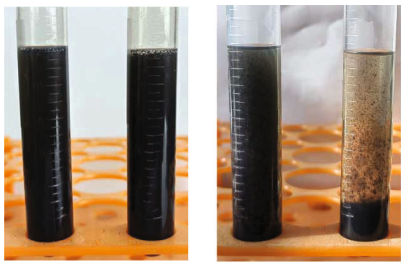

(a) (b) (a) (b)

Figure 8: Dispersion of iGO-PU and GO/PU prepolymers.

flexural strength of the material will be significantly reduced by adding elastomers or toughening agents to the polymer [9].

The tensile strength of 0.5% iGO-PU/EP composites was 48.46 MPa, and the elongation at break was 20.57%, which were significantly higher than the other samples. Compared with the pure EP composites, the tensile strength and elongation at break were 0.2 and 6.3 times higher, respectively, with significantly improved mechanical properties. This was attributed to the enhanced dispersion of iGO nanosheets in the epoxy matrix composites through PU grafting, which increased the contact area between the nanosheets and the polymer base, thus improving the transfer of stress from the epoxy matrix composites to the iGO nanosheets [35] and increasing the toughness of the material.

The tensile strength of 0.5% GO/PU/EP composites was improved compared with PU/EP, and the elongation at break was only 12.92%, which was close to that of PU/EP. The addition of GO did not further improve the elongation at break of the material, which was due to the poor dispersion of GO in the system, and the stress suffered was not uniformly dispersed, which led to the crack extension.

Next, the effect of iGO content on the composites was investigated. Figure 10(b) shows the tensile curves of iGO-PU/EP composites with different contents. It can be seen that at iGO content less than 0.5 wt%, the tensile strength and elongation at break gradually increase with increasing iGO content, and the mechanical properties of the material are improved. This changed when the iGO content was increased to 1.0 wt%, and the elongation at break decreased and was close to that of PU/EP composites without iGO addition, while the tensile strength increased and the yield point shifted to the left. It indicates that the high filling amount of iGO increases the number of defects and dislocations inside the composites and improves the stiffness of the material, which tends to lead to stress concentration and a large number of microcracks, and reduces the elongation at break of the material [36].

3.2.3. SEM Analysis. The pure EP fracture has a relatively smooth, oriented fracture pattern surface (Figure 11(a)), implying that crack propagation is unhindered. These characteristics are typical of brittle thermoset polymers [37].

The fracture surface of PU/EP composites should be relatively rough, resembling a channel-like structure and producing some microcracks with a rough and irregular fracture surface [38], implying that crack propagation requires a relatively high fracture energy.

The fracture of the 0.5% GP/PU/EP composites revealed a structural trend of crack deflection (Figure 11(c)), as well as many fine particles in the fracture, which may be related to graphene agglomeration, and agglomerated non-reticulated GO nanosheets are more likely to lead to crack sprouting and extension, reducing the toughening effect on the composites [39].

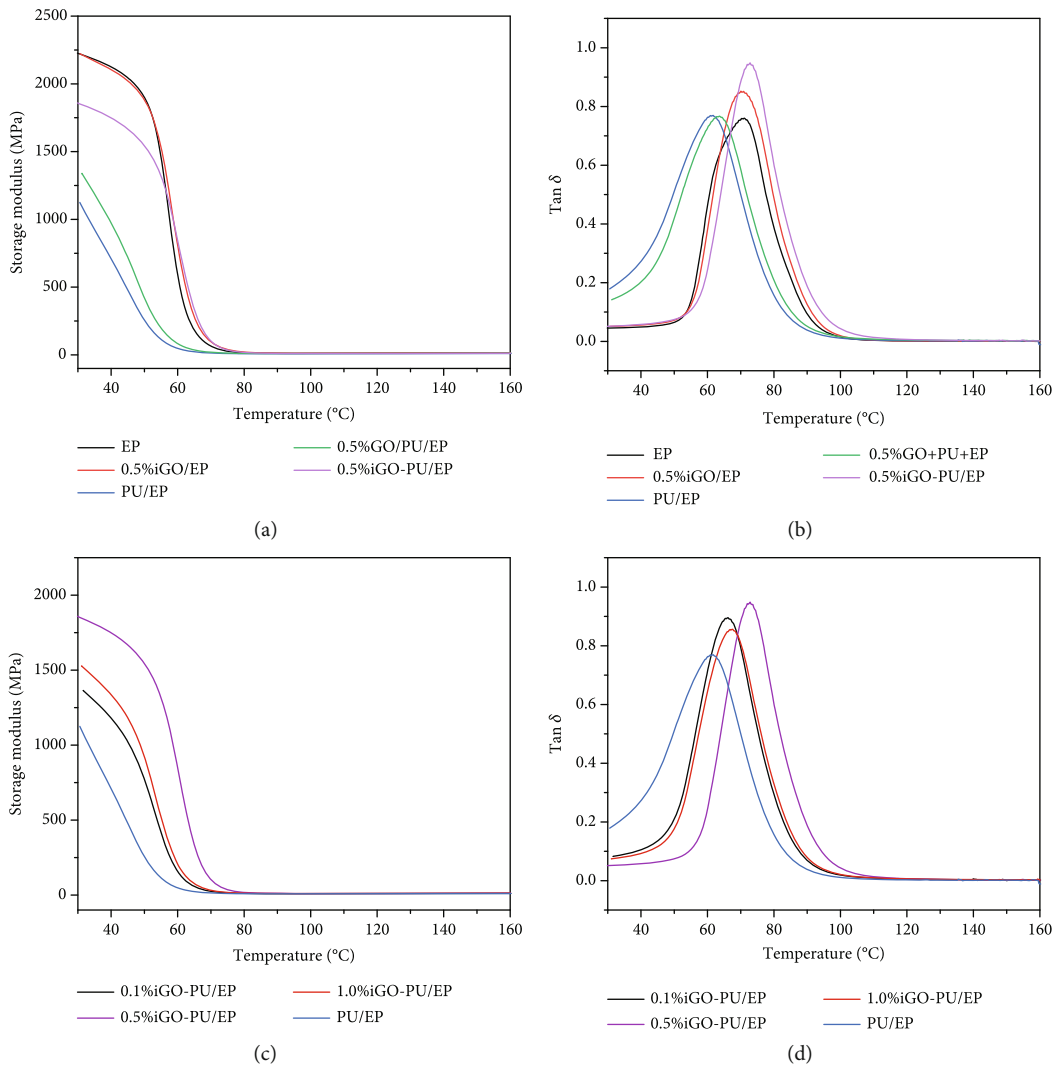

Figure 9: The curves of storage modulus (a) and tanδ with temperature (b) for pure epoxy resin and different composites, and the curves of storage modulus (c) and tanδ with temperature (d) for composites with different iGO contents.

Table 3: Storage modulus, glass transition temperature, and crosslink density of pure epoxy resin and different composites.

Sample	Storage modulus $E0$ (30°C, MPa)	Glass transition temperature T_g (°C)	Crosslinking density ν (mol/m^3)
EP	2212	71.05	3749.33
0.5%iGO/EP	2217	70.91	5399.27
PU/EP	1125	61.48	1236.29
0.5%GO/PU/EP	1339	63.59	1663.80
0.1%iGO-PU/EP	1364	66.23	1871.86
0.5%iGO-PU/EP	1857	72.82	5015.67
1.0%iGO-PU/EP	1528	67.6	2199.92

The fractures of 0.5% iGO-PU/EP composites show a high number of crack deflections in the form of grooves and vortex-like structures (Figure 11(d)), indicating that a greater degree of matrix deformation occurs, consuming a large amount of fracture energy and resulting in a more pronounced toughness enhancement [40]. The 0.5% iGO-PU/EP composites show much higher toughness than other materials, similar to the movement of dislocations through the crystals. Cracks in the material also have linear tension, and crack extension is hindered when encountering iGO nanosheets. Continuing to increase the stress, the cracks will bend around, resulting in an increase in fracture energy. In addition, since rigid particles do not produce large deformation, interfacial debonding between the matrix and rigid particles occurs under tensile stress, forming cavities, while the presence of greater compressive stress in rigid particles leads to premature yielding in

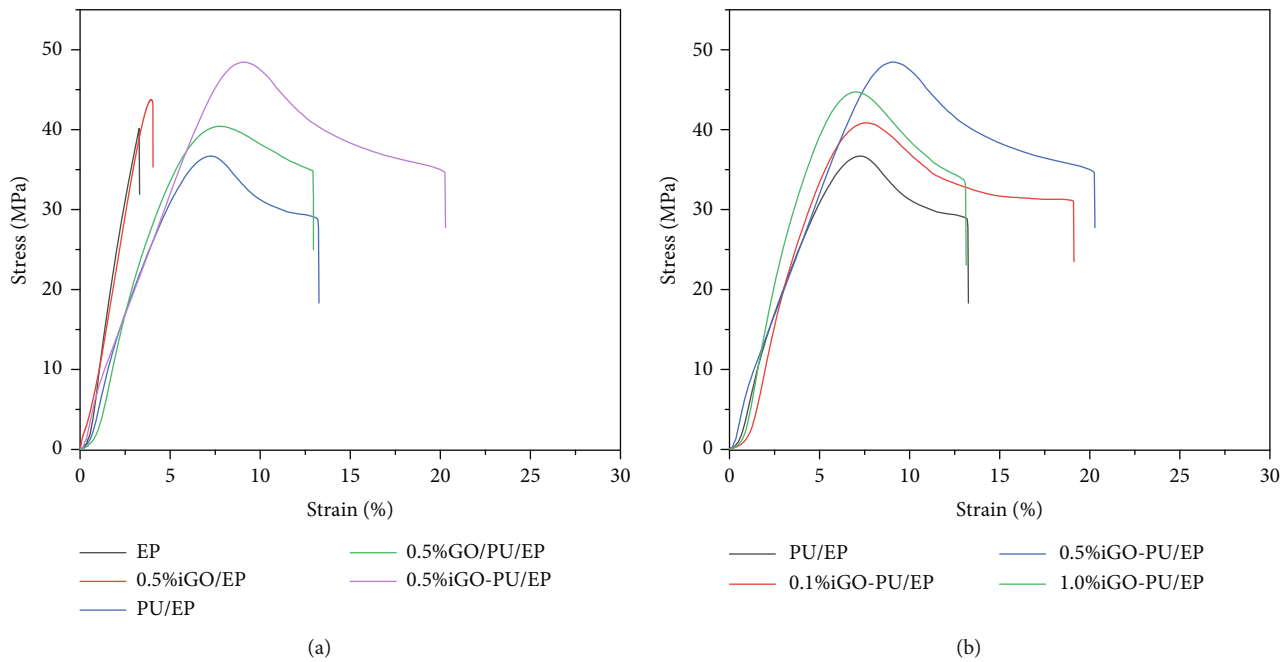

Figure 10: Tensile curves of different types of composites (a) and composites with different iGO contents (b).

Table 4: Elongation at break, tensile strength, and fracture energy of pure epoxy resin and different composites.

Sample	Elongation at break (%)	Tensile strength (MPa)	Fracture energy (J/m^2)
EP	3.28	40.13	61.51
0.5%iGO/EP	4.04	43.70	91.84
PU/EP	13.20	36.70	348.12
0.5% GO/PU/EP	12.93	40.41	381.32
0.1% iGO-PU/EP	19.10	40.84	566.72
0.5% iGO-PU/EP	20.57	48.46	701.07
1.0% iGO-PU/EP	13.10	44.69	419.28
iGO- PU/EP	26.51	40.18	247.77

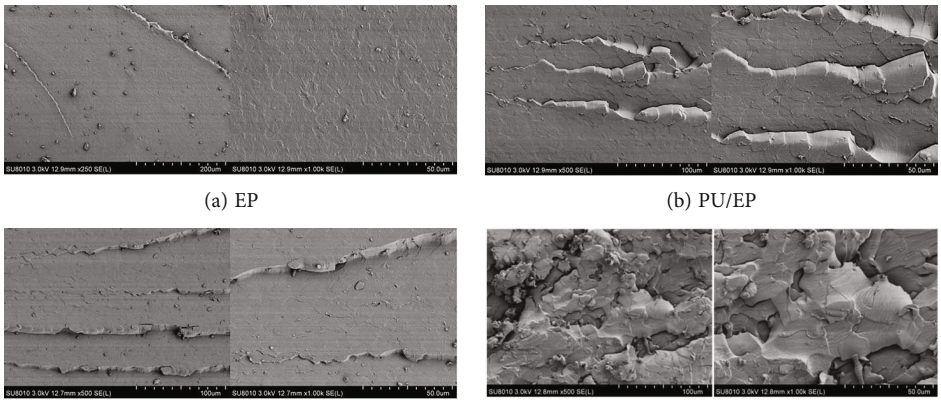

(a) EP (b) PU/EP

(c) 0.5%GO/PU/EP (d) 0.5%iGO-PU/EP

Figure 11: Fracture topography of pure epoxy resin and different composites.

localized regions. Concentrated stresses produce yielding and interfacial debonding, both of which require more energy consumption to achieve the purpose of strengthening and toughening [41].

4. Conclusions

In this work, functionalized graphene oxide (iGO) was prepared by modifying GO nanosheets with IPDI and grafting iGO with polyurethane PU. The results showed that the layer spacing of iGO increased from 0.79 nm to 1.06 nm, and the functionalized modification significantly improved the dispersion of GO in organic solvents, which could be stably dispersed in the prepolymer for more than 10 days. The synthesized iGO-PU prepolymer was then added to epoxy resin (EP) to produce iGO-PU/EP high-tough composites. This structure of rigid lamellae grafted with flexible chain segments can improve the strength while increasing the flexibility of the epoxy resin. The results showed that the tensile strength and elongation at break of 0.5% iGO-PU/EP composites were 0.2 and 6.3 times higher than those of pure EP, respectively, and the glass transition temperature was also increased by about 2°C. This was due to the good dispersion uniformity of iGO and the high crosslinking density, which increases the contact area between the nanosheets and the polymer matrix, improves the stress transfer from the epoxy-based composite to the iGO nanosheets, and increases the toughness of the material.

In this paper, the synthesis and grafting of iGO provide a new idea to prevent the agglomeration of nano-fillers in polymers, while the toughening of epoxy resin by grafting graphene oxide with elastomer overcomes some drawbacks (significant decrease in heat resistance and strength) of pure elastomer toughening. It has been shown that iGO-PU/EP composites could be used in special fields that need high toughness and high impact strength.

Data Availability

All data and information recorded or analyzed throughout this study are included in this paper.

Conflicts of Interest

The authors declare that they have no conflicts of interest.

References

[1] B. Wetzel, P. Rosso, F. Haupert, and K. J. E. Friedrich, "Epoxy nanocomposites-fracture and toughening mechanisms," *Engineering fracture mechanics*, vol. 73, no. 16, pp. 2375–2398, 2006.

[2] P. Rosso and L. J. M. Ye, "Epoxy/silica nanocomposites: nanoparticle-induced cure kinetics and microstructure," *Macromolecular rapid communications*, vol. 28, no. 1, pp. 121–126, 2007.

[3] C. B. Qu, T. Wu, G. W. Huang et al., "Improving cryogenic mechanical properties of carbon fiber reinforced composites based on epoxy resin toughened by hydroxyl-terminated polyurethane," *Composites Part B: Engineering*, vol. 210, article 108569, 2021.

[4] T. Wu, Y. Liu, N. Li, G. W. Huang, C. B. Qu, and H. M. Xiao, "Cryogenic mechanical properties of epoxy resin toughened by hydroxyl- terminated polyurethane," *Polymer Testing*, vol. 74, pp. 45–56, 2019.

[5] H. H. Wang and J. C. Chen, "Modification and compatibility of epoxy resin with hydroxyl-terminated or amine-terminated polyurethanes," *Polymer Engineering & Science*, vol. 35, no. 18, pp. 1468–1475, 1995.

[6] H. H. Wang and J. C. Chen, "Toughening of epoxy resin by functional-terminated polyurethanes and/or semicrystalline polymer powders," *Journal of applied polymer science*, vol. 82, no. 12, pp. 2903–2912, 2001.

[7] Y. C. Chern, K. H. Hsieh, and J. S. Hsu, "Interpenetrating polymer networks of polyurethane cross-linked epoxy and polyurethanes," *Journal of materials science*, vol. 32, no. 13, pp. 3503–3509, 1997.

[8] D. S. Kim, K. Cho, J. H. An, and C. E. Park, "Toughening mechanisms of modified unsaturated polyester with novel liquid polyurethane rubber," *Journal of materials science*, vol. 29, no. 7, pp. 1854–1866, 1994.

[9] H. N. Tien, N. T. Hien, E. S. Oh et al., "Synthesis of a highly conductive and large surface area graphene oxide hydrogel and its use in a supercapacitor," *Journal of Materials Chemistry A*, vol. 1, no. 2, pp. 208–211, 2013.

[10] B. Ramezanzadeh, A. Ahmadi, and M. J. C. S. Mahdavian, "Enhancement of the corrosion protection performance and cathodic delamination resistance of epoxy coating through treatment of steel substrate by a novel nanometric sol-gel based silane composite film filled with functionalized graphene oxide nanosheets," *Corrosion Science*, vol. 109, pp. 182–205, 2016.

[11] A. Javidparvar, B. Ramezanzadeh, and E. J. P. Ghasemi, "Effects of surface morphology and treatment of iron oxide nanoparticles on the mechanical properties of an epoxy coating," *Progress in organic coatings*, vol. 90, pp. 10–20, 2016.

[12] J. Shen, M. Shi, H. Ma et al., "Synthesis of hydrophilic and organophilic chemically modified graphene oxide sheets," *Journal of colloid and interface science*, vol. 352, no. 2, pp. 366–370, 2010.

[13] Z. Li, R. J. Young, R. Wang et al., "The role of functional groups on graphene oxide in epoxy nanocomposites," *Polymer*, vol. 54, no. 21, pp. 5821–5829, 2013.

[14] L. Lei, J. Shan, J. Hu, X. Liu, J. Zhao, and Z. J. C. S. Tong, "Co-curing effect of imidazole grafting graphene oxide synthesized by one-pot method to reinforce epoxy nanocomposites," *Composites Science and Technology*, vol. 128, pp. 161–168, 2016.

[15] N. D. Alexopoulos, Z. Paragkamian, P. Poulin, and S. K. Kourkoulis, "Fracture related mechanical properties of low and high graphene reinforcement of epoxy nanocomposites," *Composites Science and Technology*, vol. 150, pp. 194–204, 2017.

[16] P. Gogoi, R. Boruah, and S. K. Dolui, "Jatropha curcas oil based alkyd/epoxy/graphene oxide (GO) bionanocomposites: Effect of GO on curing, mechanical and thermal properties," *Progress in Organic Coatings*, vol. 84, pp. 128–135, 2015.

[17] P. A. Okafor, J. Singh-Beemat, and J. O. Iroh, "Thermomechanical and corrosion inhibition properties of graphene/epoxy ester- siloxane-urea hybrid polymer nanocomposites," *Progress in Organic Coatings*, vol. 88, pp. 237–244, 2015.

[18] A. K. Pathak, M. Borah, A. Gupta, T. Yokozeki, and S. R. Dhakate, "Improved mechanical properties of carbon fiber/

graphene oxide-epoxy hybrid composites," *Composites Science and Technology*, vol. 135, pp. 28–38, 2016.

[19] B. Shen, W. Zhai, M. Tao, D. Lu, and W. Zheng, "Chemical functionalization of graphene oxide toward the tailoring of the interface in polymer composites," *Composites Science and Technology*, vol. 77, pp. 87–94, 2013.

[20] S. Y. Lee, M. H. Chong, M. Park, H. Y. Kim, and S. J. Park, "Effect of chemically reduced graphene oxide on epoxy nanocomposites for flexural behaviors," *Carbon letters*, vol. 15, no. 1, pp. 67–70, 2014.

[21] S. Guo, L. Ma, G. Song et al., "Covalent grafting of triazine derivatives onto graphene oxide for preparation of epoxy composites with improved interfacial and mechanical properties," *Journal of Materials Science*, vol. 53, no. 24, pp. 16318–16330, 2018.

[22] H. Yao, S. A. Hawkins, and H. J. Sue, "Preparation of epoxy nanocomposites containing well-dispersed graphene nanosheets," *Composites Science and Technology*, vol. 146, pp. 161–168, 2017.

[23] H. Günzler and H.-U. Gremlich, *IR-Spektroskopie: Eine Einführung*, John Wiley & Sons, 2012.

[24] B. Di Credico, M. Levi, and S. Turri, "An efficient method for the output of new self-repairing materials through a reactive isocyanate encapsulation," *European Polymer Journal*, vol. 49, no. 9, pp. 2467–2476, 2013.

[25] P. Song, Z. Cao, Y. Cai, L. Zhao, Z. Fang, and S. Fu, "Fabrication of exfoliated graphene-based polypropylene nanocomposites with enhanced mechanical and thermal properties," *Polymer*, vol. 52, no. 18, pp. 4001–4010, 2011.

[26] P. Lin, L. Meng, Y. Huang, L. Liu, and D. Fan, "Simultaneously functionalization and reduction of graphene oxide containing isocyanate groups," *Applied Surface Science*, vol. 324, pp. 784–790, 2015.

[27] J.-J. Bai, G.-S. Hu, J.-T. Zhang et al., "Preparation and rheology of isocyanate functionalized graphene oxide/thermoplastic polyurethane elastomer nanocomposites," *Journal of Macromolecular Science, Part B*, vol. 58, no. 3, pp. 425–441, 2019.

[28] Y. Xue, J. Liu, H. Chen et al., "Nitrogen-doped graphene foams as metal-free counter electrodes in high-performance dye-sensitized solar cells," *Angewandte Chemie International Edition*, vol. 51, no. 48, pp. 12124–12127, 2012.

[29] J. Che, Y. Xiao, X. Wang, A. Pan, W. Yuan, and X. Wu, "Grafting polymerization of polyacetal onto nano-silica surface via bridging isocyanate," *Surface and Coatings Technology*, vol. 201, no. 8, pp. 4578–4584, 2007.

[30] J. Shen, M. Zhang, G. Liu, K. Guan, and W. Jin, "Size effects of graphene oxide on mixed matrix membranes for CO2 separation," *AICHE Journal*, vol. 62, no. 8, pp. 2843–2852, 2016.

[31] S. Stankovich, R. D. Piner, S. T. Nguyen, and R. S. Ruoff, "Synthesis and exfoliation of isocyanate-treated graphene oxide nanoplatelets," *Carbon*, vol. 44, no. 15, pp. 3342–3347, 2006.

[32] S. Chhetri, P. Samanta, N. C. Murmu, S. K. Srivastava, and T. Kuila, "Effect of dodecyal amine functionalized graphene on the mechanical and thermal properties of epoxy-based composites," *Polymer Engineering & Science*, vol. 56, no. 11, pp. 1221–1228, 2016.

[33] M. Lotfi, A. Azizi, H. Yari, and M. Ganjaee Sari, "Aminosilane-co-graphene oxide/epoxy nanocomposite coating: an approach towards toughness and viscoelastic properties enhancement," *Progress in Organic Coatings*, vol. 151, p. 106050, 2021.

[34] J. S. Jayan, A. Saritha, B. D. S. Deeraj, and K. Joseph, "Triblock copolymer grafted graphene oxide as nanofiller for toughening of epoxy resin," *Materials Chemistry and Physics*, vol. 248, p. 122930, 2020.

[35] X. Wang, W. Xing, P. Zhang, L. Song, H. Yang, and Y. Hu, "Covalent functionalization of graphene with organosilane and its use as a reinforcement in epoxy composites," *Composites science and technology*, vol. 72, no. 6, pp. 737–743, 2012.

[36] M. Sahu and A. M. Raichur, "Toughening of high performance tetrafunctional epoxy with poly(allyl amine) grafted graphene oxide," *Composites Part B: Engineering*, vol. 168, pp. 15–24, 2019.

[37] H. Kulkarni, P. Tambe, and G. Joshi, "High concentration exfoliation of graphene in ethyl alcohol using block copolymer surfactant and its influence on properties of epoxy nanocomposites," *Fullerenes, Nanotubes and Carbon Nanostructures*, vol. 25, no. 4, pp. 241–249, 2017.

[38] L. Pan, J. Ban, S. Lu et al., "Improving thermal and mechanical properties of epoxy composites by using functionalized graphene," *RSC Advances*, vol. 5, no. 74, pp. 60596–60607, 2015.

[39] B. Qi, Z. Yuan, S. Lu et al., "Mechanical and thermal properties of epoxy composites containing graphene oxide and liquid crystalline epoxy," *Fibers and Polymers*, vol. 15, no. 2, pp. 326–333, 2014.

[40] M. Naeem, H. C. Kuan, A. Michelmore et al., "A new method for preparation of functionalized graphene and its epoxy nanocomposites," *Composites Part B: Engineering*, vol. 196, article 108096, 2020.

[41] M. Rubinstein and R. H. Colby, *Polymer physics*, vol. 23, Oxford university press, New York, 2003.

Hindawi
Journal of Nanomaterials
Volume 2022, Article ID 4031059, 7 pages
https://doi.org/10.1155/2022/4031059

Review Article

Recent Developments in Stimuli Responsive Smart Materials and Applications: An Overview

T. Ramakrishnan,[1] S. Senthil Kumar,[2] Samson Jerold Samuel Chelladurai,[3] S. Gnanasekaran,[4] S. Sivananthan,[5] N. K. Geetha,[6] Ramesh Arthanari,[7] and Gizachew Balcha Assefa[8]

[1]*Department of Mechanical Engineering, Sri Eshwar College of Engineering, Coimbatore, Tamil Nadu, India*
[2]*Department of Mechanical Engineering, RMK College of Engineering and Technology, Puduvoyal, 601206, India*
[3]*Department of Mechanical Engineering, Sri Krishna College of Engineering and Technology, Coimbatore, Tamil Nadu, India*
[4]*Department of Mechanical Engineering, Sri Shakthi Institute of Engineering and Technology, Chinniyampalayam, Coimbatore, Tamil Nadu, India*
[5]*Department of Mechanical Engineering, K.Ramakrishnan College of Engineering, Tiruchirapalli, Tamil Nadu, India*
[6]*Department of Mathematics, Dayananda Sagar College of Engineering, Bangalore 560078, India*
[7]*Department of Mechanical Engineering, Chennai Institute of Technology, Tamil Nadu, India*
[8]*Department of Chemical Engineering, College of Biological and Chemical Engineering, Addis Ababa Science and Technology University, Addis Ababa, Ethiopia*

Correspondence should be addressed to T. Ramakrishnan; ramakrishnankct@gmail.com,
Samson Jerold Samuel Chelladurai; samsonjeroldsamuel@skcet.ac.in, and Gizachew Balcha Assefa; gizachew.balcha@aastu.edu.et

Received 15 August 2022; Accepted 6 September 2022; Published 14 September 2022

Academic Editor: Muhammad P. Jahan

The term "smart materials" can be used to refer a wide variety of different kinds of substances. One capacity that is shared by all of them is the capability to radically alter one or more aspects while operating inside carefully controlled conditions. The age of intelligent materials is arrived, and we are living in it right now. An older definition of smart material described it as a substance that responds swiftly to the environment in which it is located. It has been argued that the word "smart material" now refers to any substance that is capable of detecting, transmitting, or processing a stimulus in order to produce a beneficial effect. This idea has been put forward as a possible expansion of the original meaning of the term. The purpose of this research is to define and categorize different types of intelligent materials. Uses of smart materials are being contemplated in a wide variety of domains, spanning from the realm of technology to that of the modern environment.

1. Introduction

The term "smart materials" is difficult to describe in a manner that is free of ambiguity; however, these are typically conceived of as materials that respond to an outside physical or chemical stimuli in a controlled manner in order to carry out a task that has already been specified. Nevertheless, this definition is far too broad because virtually every material responds or reacts in some way to the kinds of stimuli described, and there is unquestionably a thin line that separates "smart" materials from other types of materials. Perhaps it is more helpful to think of the responding, also known as "smart behaviour," which occurs when a substance senses some stimulation from its surroundings and reacts in a way that is helpful, reliable, and reproducible. This type of response takes place when a material sensory perception some positive reinforcement from its environment [1, 2].

This report analyzes recent advancements in three subfields of smart manufacturing techniques: self-healing (SH) components, sensors and communication equipment and

sensing skins, and shape-changing materials. Self-healing materials are discussed first, followed by sensing and actuation materials and sensing skins, and finally shape-changing materials [3]. This study offers a comprehensive introduction to multifunction intelligent bio-based composites as well as the applications that can be developed using them. Natural resources of biopolymers such as cellulose, microbial cellulose, chitosan, collagen, cornstarch, polycaprolactone, and polylactic acid are introduced, and the active behaviors of these raw materials in terms of electrical and ionic working characteristics are discussed. The analysis also takes into consideration polymer matrices and gels as potential options. Recent years have seen a rediscovery of cellulose's potential as an active material, specifically in the form of electroactive paper (EAPap). This chapter describes the manufacturing and actuation basis of EAPap, as well as its three subareas, which may be broken down into capacitive EAPap, composite EAPap, along with their respective applications. In order to increase the usefulness of biopolymers even further, heterostructures of inorganic functional elements are being introduced by integrating graphene, carbon nanotubes, titanium dioxide, and tin oxide with biopolymers. These metal nanoparticles are also being included. Their dynamic responses in response to electrical or pH stimulation are also depicted here. Because natural polymers are bioactive, biodegradable, and capable of extensive chemical modification, there are many electrohydraulic implementations of multipurpose smart biopolymer composites that are possible. Some examples of these applications include biomaterials robotic systems, reconfigurable lens structures, and artificial muscles [4–6].

2. Two-Dimensional Smart Membrane Advancement

Artificial smart membranes based on the biosystems have garnered growing attention in the sectors of separation process, desalination, nanofiltration, healthcare, and environmental remediation due to their ability to govern mass transport and molecular conversion. Trade-off limits in polymeric membranes severely limit the implementation of intelligent membranes with porous structure and manipulability. In recent years, two-dimensional (2D) materials have inspired the development of 2D metal alloys smart membranes (2DSMs) capable of intelligent control under varied inputs [7, 8]. It is possible to create 2DSMs with numerous functional groups to vary their characteristics and produce adjustable interlayer spacings under varied external circumstances by modifying them through chemical modification. Using 2D materials as a foundation, we examine current developments in artificial smart membranes. 2DSMs are first described in terms of their conceptual design and practical implementation strategies. That is followed by the introduction and classification of the 2DSMs that have been produced and categorized by the sort of responsive stimuli that they respond to. Then there are the 2DSMs that have unique capabilities such as separation process, pressure transducers, blue energy generation, photoelectrochemical sensors, and biomimetic devices for harvesting energy from the blue. Finally, 2DSM development ideas and problems are examined [9].

2.1. Smart, Active, Biodegradable Food Packaging Materials. An overview of the advancements in food-safe recyclable smart, dynamic, and smart packaging by highlighting the problems and limits of each. The use of aromatic plants and plant extracts in the creation of food packaging that is both intelligent and active has been a great success. For intelligent and active packaging, anthocyanins (particularly) play a crucial role in signaling changes in food properties or enhancing shelf life. Research into smart biodegradable packaging, which differs significantly from its two predecessors that is a developing and promising field, has gained momentum in recent years. Improved regulated release of bioactive substances in active packaging, reduction of reliance on pH change, and development of ways to protect film integrity are all needed in intelligent packaging [10].

2.2. Green Materials for Bioanalysis Sample Preparation. It is difficult to analyze biological samples because of their complexity as well as the decreased level of target analytes. Therefore, a variety of bioanalytical sample treatment strategies have been presented, with a focus on microextraction methodologies. Using microextraction and smart materials in combination delivers ecologically friendly sample treatment options with better selectivity, sensitivity, and reuse. In addition to antibodies and antigens, other types of smart solid materials comprise aptamers, nanostructured polymeric materials, metal organic frameworks, and materials with restricted access. In contrast, bio-based fluids, biomolecules solvents, ion exchange, and polar aprotic solvents are among the smart liquid materials employed in bioanalysis sample preparation. A sustainable analytical chemistry approach has been used to analyze the synthesis and use of smart materials [11].

There will be a growing impact on human health and well-being from the development of materials and gadgets during the next decade. Smart materials are not any exception. Smart materials are the foundation for many new scientific innovations due to their unique characteristics of neural stimulation and autonomous activity. Smart materials, which include electromechanical polymers and shape-memory materials, have revolutionized the design process and broadened their range of applications. In robotics, for example, the transition from rigid-bodied robots to soft robots made of flexible materials has been swift. Bioengineering and mechanical engineering will need to work together to create new kinds of robots that can grow and alter shape and function as their physical and chemical environments change. Smart materials may also be used to create artificial systems that work in concert with biological species, blurring the line between the two. Innovative medical applications, such as physiological monitoring, minimally invasive surgery and medication administration, as well as human–computer interface and rehabilitation, rely on smart materials in addition to more traditional fields like environmental sensors and actuators. It is possible that future intelligent materials will be even more useful to humans due to

their increased functionality, controllability, and biocompatibility [12–16].

2.3. Smart Material Manufacture in Additive Manufacturing Utilizing IoT for Industry 4.0. There is a major impact of Industry 4.0 on mass customization and personalization. There is no way to mass produce the 3D printed work using additive manufacturing (AM) technology, despite the fact that they can produce personalized items. A further drawback is their incapacity to carry out production operations for large-sized products. Therefore, the industries are reluctant to use AM methods for commercial manufacturing. Research-based investigation intends to increase AM processes' dependability as well as mass 3D print advanced materials for businesses across the world by using Industry 4.0 technology. Industry 4.0 technologies are examined, and the advantages of using information technology (IT) in AM operations are examined. This is followed by an examination of IoT-integrated additive manufacturing processes and their impact on industry and material producers [17–19]. The documentation, on the other hand, is limited to theoretical work alone. Because AM automation is still a new idea, there is not much research material to work with. A reduction in manufacturing waste and a higher level of customer satisfaction may be expected when IoT is used in AM. As a result of AM's role in product invention and development, improvements are needed to make the technology more user-friendly [20].

3. Types, Qualities, and Applications of Smart Materials

The immediate development of smart materials for use in fields such as self-sustaining wireless communication, self-tuned vibrating energy recovery devices, seismic applications, and other similar fields is a necessity at this point in time. These kinds of advanced materials have the ability to be used in the construction of smart buildings and smart materials. Piezoelectric materials, polymer materials alloys, electrorheological fluid, and magnetorheological fluid are examples of smart materials that respond to external stimuli. Smart materials form a diverse group of materials that may be utilized for vibration control. There is a considerable degree of parallelism that can be drawn between biological systems and intelligent materials [21–23]. For example, piezoelectric hydrophones that show a resemblance as that of ears with which fish sense piezoelectric material, substances that can cause with an amalgamation of electromechanical coupling, shape-memory materials with the potential to recollect the original shape, techno fluids with deceitful viscosity strength, and so on are some examples. This potential drew the attention of researchers and gave them the opportunity to consider and incorporate a wide variety of additional technologies into compact, multifunctional packages. Their end goal is to develop more advanced and sophisticated materials and to revolutionize the field of smart materials research. In the beginning of this review, a concise synopsis of the previously described stimulus-responsive smart materials is discussed, and then, after that, a detailed explanation of some of the biomaterials is presented [24].

4. Smart Facade Material Selection Based on Sustainable Development Goals

Structures take up huge quantities of energy and damage the surrounding environment in a variety of different ways. The building's facade is a component of the building's architecture that has the potential to significantly contribute to the reduction of energy consumption and the amelioration of the building's adverse impacts on the surrounding environment. There have only been a relatively small number of research done on the aforementioned topics, despite the fact that the use of intelligent materials on the facades of buildings can significantly aid in accomplishing the aims indicated. In addition, the investigations that have been done so far have only looked at a small number of intelligent materials all at once. As a result, the purpose of this investigation is to carry out a more comprehensive analysis, locate and rank the smart materials that would work best for building facades in Shiraz, Iran in accordance with the Sustainable Development Goals (SDGs) [25–28]. The Friedman experiment and Analytical Hierarchical Analysis (AHP), both available through the software packages SPSS and Expert Choice, were utilized in the process of analyzing the data. According to the findings that were obtained, "Photovoltaic materials," "Thermochromic materials," and "Photostrictive materials" were the most effective options for implementation onto the facade of a structure. The findings that were collected from this research can assist the construction sector in moving toward a more sustainable future [29].

5. Smart Hybrid Nickel–Titanium Materials for the Auto Industry

Intelligent hybrid materials are increasingly being employed in a wide range of sectors because of their smart properties. Innovative composite membranes change their properties in a controlled way in response to an external stimulus. Pressure, pH, temperature, as well as electric and magnetic forces, may all be detected by smart materials. Combining NiTi alloys in a certain ratio results in a "smart material," which has the properties of a smart alloy [30–33]. The biomedical, aerospace, automotive, and electrical and electronic sectors can all benefit from the usage of NiTi alloys. However, the automobile industry, which is the focus of this chapter, employs them the most. Suspension systems, fender systems, wing mirrors, windscreen wipers, door knobs and safety lock units, turbines, controllers, and batteries modules may all utilize smart materials in automotive vehicles. Furthermore, NiTi may be employed in other smart materials, such as shape-memory alloys, for the automotive sector. Additionally, magnetostrictive, piezoelectric, and intelligent polymeric materials are all examples of smart materials. Smart-hybrid materials and NiTi advanced materials in the automobile sector are the focus of this section [34].

6. Cardiovascular Smart Materials

The field of "Smart materials," which are rising in popularity and have a great deal of promise for use in a variety of medical contexts, includes the category of "shape memory alloys." These materials are very well-suited for use in the design of implants due to the fact that they are capable of undergoing deformation while still maintaining their initial shape following the removal of any external stimulus. This article focuses on the use of magnetization superalloys (FSMA) and piezoelectric material materials in the design of cardiovascular devices, particularly those that are most likely to be appropriate for young heart patients. In the presence of a magnetic field, certain materials undergo morphological transformations. Materials that have a crystal structure that is unlike any other are now under consideration for use in the creation of stents and coronary applications. This study reveals how stents constructed of FSMA may be magnetically triggered and finds uses for them in peripheral and arterial heart illnesses. As a result, this work replaces the present technology used for stents [35].

7. Advanced Textile Materials

A trending area of discussion in engineering is the development of intelligent textiles through the application of novel materials. These materials include functionalized nanoparticles injected into the fiber matrix as well as unique or modified polymers that are employed in the creation of smart filaments, yarns, and textiles. Because of the variety of capabilities that a fabric substrate is capable of acquiring and the ways in which it may interact with its wearer, "smart textiles" have emerged as a material category that is both significant and innovative in the textile industry [36, 37]. Due to the contemporary significance of the topic, the purpose of this review is to present, in a condensed form, the basic aspects of a smart textile, as well as its categories, various applications, and highlight the primary materials used in the preparation of intelligent textiles. In addition, the scientific contributions that we made on this subject were taken into consideration [38].

8. Smart Materials for Aqueous Contamination

The amount of freshwater accessible is gradually decreasing as the population is rising exponentially. The major source of environmental contamination is the generation of a considerable volume of wastewater each year. The problem of water contamination compelled researchers to devise new and more effective methods of purifying water quickly and cheaply. It is clear that the adsorption technique has had a significant impact in the treatment of wastewater. Smart adsorbent materials, such as light, temperature, pH, and other environmental cues, have recently provided a new avenue for cleaning coolants in industrial settings. It is becoming increasingly common for scientists throughout the world to focus on producing smart adsorbents capable of extracting contaminants such as hazardous metals, textile dyes, and other organic substances from wastewater. In addition to their great selectivity, these smart adsorbents demonstrate effective regeneration without the use of a separate solvent for the regenerating process. New carbon-based materials for wastewater treatment are examined in this review paper for their features and performance efficiency. Here, sensory perceptions carbon-based materials with their binding efficiencies are described, detailed discussion on discrimination, self-healing, self-cleaning features, limits, and the potential for future study [39].

The fire prevention and safety are of fundamental importance in modern civilization, yet they have been a global problem. Massive deaths and irreversible property losses are caused by frequent fire catastrophes, which have a severe influence on the worldwide ecosystem. Intelligent active fire protection substances and detectors that combine classic passive flame-retardant tactics with extreme fire-alarm response have recently been an emerging issue. However, an analytical and comparative analysis of these fire-warning systems is still lacking. Passive flame-retardants, standard-active detectors, and next-generation smart sensors are all included in this review, as well as thermal properties of combustible materials. There is a thorough evaluation of smart warning materials' concept generation, synthesis, characterizations, and production methods. Later, the effectiveness and applications of various fire-alarm sensor systems, such as resistance-type, phase/shape-change, thermoelectric response and color-change observation were evaluated and compared. Finally, some of the most pressing issues linked with active fire-protection materials/sensors are discussed, followed by a look at the future [40].

9. Fluorescent Smart Materials: A Detailed Survey

Increasing attention has been paid to the development of microbially fluorescence-smart materials and associated multifunctional applications in recent years. It is possible to create a large variety of useful products from cellulose, one of the world's most widely available and inexpensive basic materials. This article outlines the process of turning cellulose into luminous smart materials by chemical modification [41]. It also discusses the fabrication of fluorescent materials into films and fibers as well as carbon dots and hydrogels that can be used in a variety of sensing applications, including bioimaging of toxic metals and anions as well as pH and bioimaging of common organic solvents, as well as for fluorescence printing and coating and anti-counterfeiting applications. To conclude, the ligno-luminescence sensors are discussed in terms of forthcoming research, problems, and potential solutions. Chemical engineers, biochemists, and chemists interested in developing ligno-fluorescent materials for a wide range of applications may benefit greatly from this review [42].

10. Sustainable Materials

Advances in green technology have made it more feasible to utilize ecologically friendly materials in building. It is possible to reduce the embodied energy and maximize the usage of renewable resources by using recycled industrial waste.

The success of green construction projects depends on the use of cutting-edge technology. Many green building solutions with heat dissipation, wastewater systems and energy efficiency are included in this study. Also included is a solar powered cooling system [43, 44]. BIM and ontology are utilized in green building to coordinate multidisciplinary operations. The SWRL and OWL models were based on the Jess logic program and were coupled to increase building efficiency. Materials derived from industrial waste that are environmentally friendly contribute to a reduction in the amount of carbon dioxide emitted into the atmosphere. Activators are used to enhance the material's strength, workability, and density. There are several external elements that influence how smart materials work. Structural faults may be detected using the Electrical Impedance (EMI) method, which uses smart materials. It is possible in smart homes to utilize technology to regulate energy use. Examples of smart materials utilized in smart, sustainable urbanization include polymeric metals, fiber optics, piezoresistive, magnetoreheological fluids, and electrorheological fluids. Construction costs were lowered because to the IoT's (IoT) technology ability to collect construction data. In order to help India accomplish its long-term sustainability goals, the study will make recommendations on the best procedures and materials to use in the country [45].

11. Machinability of Smart Materials

Even if in the future the power source of automobiles changes from an internal combustion engine to an electric motor, transmissions are still necessary for the development of maximum speed, quietness, and fuel economy. This is true even if the future power source of automobiles is an electric motor. After the hot forging process, the machinability of the material that will be used in vehicle transmissions is being improved through the application of a heat treatment procedure that we are researching. In the past, following hot forging, the material's latent heat would simply be vented into the surrounding air. By cooling the material after hot forging, we were able to successfully regulate the heat that was stored within the forged material, which allowed us to successfully impart machinability onto the material.

12. An Overview of Smart Composite Materials

Over the past decade, attention in intelligent (smart or responsive) materials, especially composites, has grown. In sensing and actuation, the ability to manipulate multimaterial characteristics using external inputs is intriguing. Smart composite materials may be developed (and applied) to multiple length scales, from huge structural components to wearable technological gadgets [46]. This section includes chapters on synthesis processes for smart composites, key components connected to the single architecture or technology, and application domains based on stimulus they react to. Each smart composite material's difficulties and potential are also discussed [47]. Keeping food safe from spoilage, infection, or waste is a major concern whether it is stored, transported, or sold throughout the world. In order to address these issues, different packaging substances are being created. Antimicrobials and antioxidants are being included into active packaging materials in an effort to improve the shelf life of food [48]. Food quality, ripeness, and safety may be monitored in real time using smart packaging materials. Photoluminescent or photocatalytic materials are being used to create these photoactivated food packaging. Sensors based on photoluminescence can be used to detect changes in food packaging's environment, such as harmful gases, cleanliness, and the presence of certain bacteria. Devices based on photocatalysis can be utilized for color indicators, microbial inhibition, and gas removal. Photosensitive polymers in intelligent and proactive food packaging are the subject of this review, which highlights the most recent findings [49, 50]. Prepared materials for food packaging are examined, as are the principles of operation and uses of photoactivated materials, along with the possible benefits and drawbacks of each. The information given might lead to greater study into the development and deployment of revolutionary intelligent and proactive food containers in the food sector [51].

13. Conclusion

The technology behind smart materials is a very diverse topic of study:

(i) Beginning with the study of scientific fields such as physics and chemistry, as well as mechanics and electronics, computing, and electronics, it then moves on to include applied sciences and engineering fields such as aeronautics and mechanical engineering

(ii) Even while research into smart materials is advancing at a rapid pace, the use of advanced materials in engineering systems appears to be developing at a glacial pace

(iii) In the current environment, the utilization of intelligent materials and structures is among the most promising technological developments in terms of lifespan efficiency and increased dependability

(iv) The ultimate goals of study in this subject are to understand and regulate the chemical and morphology of any new materials. Doing so is vital to the manufacture of high-quality smart materials and is one of the discipline's ultimate objectives

Data Availability

The data used to support the findings of this study are included within the article.

Conflicts of Interest

The authors declare that there are no conflicts of interest regarding the publication of this paper.

References

[1] M. Su and Y. Song, "Printable smart materials and devices: strategies and applications," *Chemical Reviews*, vol. 122, no. 5, pp. 5144–5164, 2022.

[2] P. Yang, F. Zhu, Z. Zhang, Y. Cheng, Z. Wang, and Y. Li, "Stimuli-responsive polydopamine-based smart materials," *Chemical Society Reviews*, vol. 50, no. 14, pp. 8319–8343, 2021.

[3] J. Gardan, "Smart materials in additive manufacturing: state of the art and trends," *Virtual and Physical Prototyping*, vol. 14, pp. 1–18, 2019.

[4] Y. Yang, J.-j. Tian, L. Wang, Z. Chen, and P. Shouzhi, "D-π-a type carbazole and triphenylamine derivatives with different π-conjugated units: tunable aggregation-induced emission (AIE) and mechanofluorochromic properties," *Journal of Photochemistry and Photobiology A: Chemistry*, vol. 429, p. 113905, 2022.

[5] G.-P. Li, H.-F. Xie, P.-F. Hao et al., "Size effect of arylenediimide π-conjugate systems on the photoresponsive behaviors in Eu 3+ -based coordination polymers," *Inorganic Chemistry*, vol. 61, no. 17, pp. 6403–6410, 2022.

[6] L. Mérai, Á. Deák, I. Dékány, and L. Janovák, "Fundamentals and utilization of solid/ liquid phase boundary interactions on functional surfaces," *Advances in Colloid and Interface Science*, vol. 303, p. 102657, 2022.

[7] F. Shengjie, X. Feng, N. Zhou, S. Zhang, X. Liu, and X. Defang, "Mechano-responsive D-A luminogen based on bisarylic methanone derivative with brightly tricolored mechanochromic luminescence," *Journal of Luminescence*, vol. 247, p. 118802, 2022.

[8] S. Ghosh, S. Ghosh, N. Baildya, and K. Ghosh, "Dehydroabietylamine-decorated imino-phenols: supramolecular gelation and gel phase selective detection of Fe 3+ , Cu 2+ and Hg 2+ ions under different experimental conditions," *New Journal of Chemistry*, vol. 46, no. 18, pp. 8817–8826, 2022.

[9] X. Ai, Y.-H. Li, Y.-W. Li, T. Gao, and K.-G. Zhou, "Recent progress on the smart membranes based on two-dimensional materials," *Chinese Chemical Letters*, vol. 33, no. 6, pp. 2832–2844, 2022.

[10] U. Amin, M. K. I. Khan, A. A. Maan et al., "Biodegradable active, intelligent, and smart packaging materials for food applications," *Food Packaging and Shelf Life*, vol. 33, article 100903, 2022.

[11] S. Armenta, F. A. Esteve-Turrillas, S. Garrigues, and M. de la Guardia, "Smart materials for sample preparation in bioanalysis: a green overview," *Sustainable Chemistry and Pharmacy*, vol. 21, article 100411, 2021.

[12] A. Abramov, S. Bonardd, C. Saldías, and D. D. Díaz, "Visible-light-triggered degradation of pH-responsive micelles based onortho-Hydroxy cinnamates," *ChemPhotoChem*, vol. 6, no. 5, 2022.

[13] J. Zhang, L. Jiayu, W. Wang, X. Zhang, H. Lan, and S. Xiao, "Pyran-based derivative: non-conventional organogel and tricolored high- contrast mechanochromism," *Tetrahedron Letters*, vol. 100, p. 153888, 2022.

[14] M. Bartoli, D. Torsello, E. Piatti et al., "pressure-responsive conductive poly(vinyl alcohol) composites containing waste cotton fibers biochar," *Micromachines*, vol. 13, no. 1, p. 125, 2022.

[15] G. Picci, M. T. Mulvee, C. Caltagirone et al., "Anion-responsive fluorescent supramolecular gels," *Molecules*, vol. 27, no. 4, p. 1257, 2022.

[16] M. H. El-Newehy, H. Y. Kim, T. A. Khattab, and M. E. El-Naggar, "Production of photoluminescent transparent poly(methyl methacrylate) for smart windows," *Luminescence*, vol. 37, no. 1, pp. 97–107, 2021.

[17] L. Li, R. Sun, and R. Zheng, "Tunable morphology and functionality of multicomponent self-assembly: a review," *Materials & Design*, vol. 197, article 109209, 2021.

[18] A. M. Genaev, G. E. Salnikov, and Y. Konstantin, "Unusual temperature-sensitive protonation behaviour of 4-(dimethylamino)pyridine," *Organic & Biomolecular Chemistry*, vol. 19, no. 4, pp. 866–872, 2021.

[19] H. Shaghaleh, X. X. Shifa Wang, L. Guo, and F. Dong, "Innovative two-phase air plasma activation approach for green and efficient functionalization of nanofibrillated cellulose surfaces from wheat straw," *Journal of Cleaner Production*, vol. 297, p. 126664, 2021.

[20] R. Ashima, A. Haleem, S. Bahl, M. Javaid, S. Kumar Mahla, and S. Singh, "Automation and manufacturing of smart materials in additive manufacturing technologies using Internet of Things towards the adoption of industry 4.0," *Mater. Today Proc.*, vol. 45, pp. 5081–5088, 2021.

[21] C. Liang, M. Li, and Y. Chen, "Amphiphilic diazapyrenes with multiple stimuli-responsive properties," *ACS Applied Materials & Interfaces*, vol. 13, no. 17, pp. 20698–20707, 2021.

[22] M. Mrinalini, M. Naresh, S. Prasanthkumar, and L. Giribabu, "Porphyrin-based supramolecular assemblies and their applications in NLO and PDT," *Journal of Porphyrins and Phthalocyanines*, vol. 25, pp. 382–395, 2021.

[23] L. Li, R. Sun, R. Zheng, and Y. Huang, "Anions-responsive supramolecular gels: a review," *Materials & Design*, vol. 205, article 109759, 2021.

[24] S. Bahl, H. Nagar, I. Singh, and S. Sehgal, "Smart materials types, properties and applications: a review," *Mater. Today Proc.*, vol. 28, pp. 1302–1306, 2020.

[25] J. Sun, F. Wang, H. Zhang, and K. Liu, "Azobenzene-based photomechanical biomaterials," *Advanced NanoBiomed Research*, vol. 1, no. 9, p. 2100020, 2021.

[26] S. Amukarimi and M. Mozafari, "4D bioprinting of tissues and organs," *Bioprinting*, vol. 23, p. e00161, 2021.

[27] D. Guo, Z. Kang, Y. Wang, and M. Li, "Design of multi-material soft pneumatic modules," *Smart Materials and Structures*, vol. 30, no. 9, p. 095006, 2021.

[28] V. Gokul, D. Devadiga, and T. N. Ahipa, "Pyridine based mechanochromic compounds: an overview," *Dyes and Pigments*, vol. 195, article 109692, 2021.

[29] A. Balali and A. Valipour, "Identification and selection of building façade's smart materials according to sustainable development goals," *Sustainable Materials and Technologies*, vol. 26, article e00213, 2020.

[30] Y. Mochizuki, H. Imai, and Y. Oaki, "A layered polydiacetylene containing hydrogen-bonding 4,4′-bipyridyl guests: reversible color changes with a wide-range temperature response," *ChemPlusChem*, vol. 86, no. 12, p. 1546, 2021.

[31] Y. Ru, Z. Shi, J. Zhang et al., "Recent progress of photochromic materials towards photocontrollable devices," *Materials Chemistry Frontiers*, vol. 5, no. 21, pp. 7737–7758, 2021.

[32] A. Eremin, "Effects of photoswitching in complex partially ordered systems," *Liquid Crystals Reviews*, vol. 8, no. 1, pp. 29–43, 2021.

[33] R. Diana, U. Caruso, and B. Panunzi, "Stimuli-responsive zinc (II) coordination polymers: a novel platform for supramolecular chromic smart tools," *Polymers*, vol. 13, no. 21, p. 3712, 2021.

[34] A. Behera, A. K. Sahoo, and S. S. Mohapatra, "14 - Nickel-titanium smart hybrid materials for automotive industry," in *Micro and Nano Technologies*, S. Thomas, Ed., pp. 271–295, Elsevier, 2022.

[35] M. Bhatia and S. Bhatia, "Smart materials for cardiovascular devices," *Mater. Today Proc.*, vol. 53, pp. 307–309, 2022.

[36] P. Frangville, S. Kumar, M. Gelbcke, K. Van Hecke, and F. Meyer, "Stimuli responsive materials supported by orthogonal hydrogen and halogen bonding or I···alkene interaction," *Molecules*, vol. 26, no. 24, p. 7586, 2021.

[37] T. A. Khattab, M. E. El-Naggar, M. S. Abdelrahman, and A. Aldalbahi, "Mohammad Rafe Hatshan, facile development of photochromic cellulose acetate transparent nanocomposite film immobilized with lanthanide-doped pigment: ultraviolet blocking, superhydrophobic, and antimicrobial activity," *Luminescence*, vol. 36, no. 2, pp. 543–555, 2020.

[38] C. R. S. de Oliveira, A. H. da Silva Júnior, A. P. S. Immich, and J. Fiates, "Use of advanced materials in smart textile manufacturing," *Materials Letters*, vol. 316, article 132047, 2022.

[39] V. Gadore and M. Ahmaruzzaman, "Smart materials for remediation of aqueous environmental contaminants," *Journal of Environmental Chemical Engineering*, vol. 9, no. 6, article 106486, 2021.

[40] L.-Y. Lv, C. F. Cao, Y. X. Qu et al., "Smart fire-warning materials and sensors: design principle, performances, and applications," *Materials Science & Engineering R: Reports*, vol. 150, article 100690, 2022.

[41] H. Holman, M. N. Kavarana, and T. K. Rajab, "Smart materials in cardiovascular implants: shape memory alloys and shape memory polymers," *Artificial Organs*, vol. 45, no. 5, pp. 454–463, 2020.

[42] H. Nawaz, X. Zhang, S. Chen, T. You, and F. Xu, "Recent studies on cellulose-based fluorescent smart materials and their applications: a comprehensive review," *Carbohydrate Polymers*, vol. 267, article 118135, 2021.

[43] M. E. Sánchez-Vergara, C. Rios, O. Jiménez-Sandoval, and R. Salcedo, "A comparative study of the semiconductor behavior of organic thin films: TCNQ-doped cobalt phthalocyanine and cobalt octaethylporphyrin," *Molecules*, vol. 25, no. 24, p. 5800, 2020.

[44] W. Han, S. Wang, X. Rui, Y. Dong, and H. Choi, "Core/shell magnetite/copolymer composite nanoparticles enabling highly stable magnetorheological response," *International Journal of Mechanical System Dynamics*, vol. 2, no. 2, pp. 155–164, 2022.

[45] M. Patil, S. Boraste, and P. Minde, "A comprehensive review on emerging trends in smart green building technologies and sustainable materials," *Mater. Today Proc.*, vol. 65, pp. 1813–1822, 2022.

[46] K. Aravinth, T. Ramakrishnan, V. D. Tamilarasan, and K. Veeramanikandan, "A Brief Review on Plant Fibres Composites: Extraction, Chemical Treatment and Fibre Orientation," *Materials Today: Proceedings*, vol. 62, pp. 2005–2009, 2022.

[47] E. Pellicer, *Smart Composite Materials: An Introduction*, D. B. T.-E. M. C. Brabazon, Ed., Elsevier, Oxford, 2021.

[48] A. Yadav, S. Trivedi, V. Haridas, J. B. Essner, G. A. Baker, and S. Pandey, "Effect of ionic liquid on the fluorescence of an intramolecular exciplex forming probe," *Photochemical & Photobiological Sciences*, vol. 19, no. 2, pp. 251–260, 2020.

[49] T. Ramakrishnan, M. Gift, S. Chitradevi et al., "Study of numerous resins used in polymer matrix composite materials," *Advances in Materials Science and Engineering*, vol. 2022, Article ID 1088926, 8 pages, 2022.

[50] T. Ramakrishnan, S. Senthil Kumar, S. J. Samuel Chelladurai et al., "Effect of moisture content on mechanical properties of AAM natural fiber-reinforced Isophthalic polyester composites," *Advances in Materials Science and Engineering*, vol. 2022, Article ID 3533143, 10 pages, 2022.

[51] H. Xu, L. Chen, D. Julian McClements et al., "Progress in the development of photoactivated materials for smart and active food packaging: photoluminescence and photocatalysis approaches," *Chemical Engineering Journal*, vol. 432, article 134301, 2022.

Hindawi
Journal of Nanomaterials
Volume 2022, Article ID 8729258, 10 pages
https://doi.org/10.1155/2022/8729258

Review Article

Synthesis and Food Applications of Resistant Starch-Based Nanoparticles

Fakhar Islam,[1] Muhammad Noman,[1] Muhammad Afzaal,[1] Farhan Saeed,[1] Shabana Ahmad,[1] Muhammad Waqas Zubair,[1] Syeda Mahvish Zahra,[2] Muzzamal Hussain,[1] Huda Ateeq,[1] and Chinaza Godswill Awuchi[3]

[1]*Department of Food Sciences, Government College University, Faisalabad, Pakistan*
[2]*Department of Environmental Design, Health and Nutritional Sciences, Allama Iqbal Open University, Islamabad, Pakistan*
[3]*School of Natural and Applied Sciences, Kampala International University, Box 20000 Kansanga, Kampala, Uganda*

Correspondence should be addressed to Chinaza Godswill Awuchi; awuchichinaza@gmail.com

Received 5 August 2022; Accepted 25 August 2022; Published 14 September 2022

Academic Editor: Ramesh Balasubramanian

Starch is recognized biopolymer because it is abundant in nature. Dietary starches are major energy source for various human civilizations, and it is obvious that they may also contribute to health in very particular ways. Resistant starch has got a lot of interest because of its possible health advantages (similar to soluble fibre) as well as its functional qualities. Resistant starch improves blood cholesterol levels, microbial flora, gastrointestinal tract function, the glycemic index, and helps with diabetes management. Aside from the significant health advantages of starch, there is an additional benefit that it has a smaller effect on food sensory characteristics than usual sources of fibre, such as grains, bran, or fruits. Moreover, when boiled, many starches form weak-bodied and unpleasant gels, which are influenced negatively by temperature, humidity, and storage duration. The present review article highlights resistant starch as a functional food, starch extraction method, preparation of starch nanoparticles, and nano- and microencapsulation of probiotics in detail.

1. Introduction

Starch is a well biopolymer that is prevalent in environment. It has piqued the curiosity of experts all around the world since it is biodegradable, renewable, and environmentally benign, and it has been extensively researched for usage in the pharmacological, food, and cosmetics sectors [1]. Starch is a chemical found in plants that is used to store glucose. It is made up of two different polymers: amylopectin, a branching molecule, and amylose, a linear molecule. Starch is a primary storage of carbohydrate and, after cellulose, the 2nd most prevalent polymer. In tubers (sweet potato and potato), immature fruits (mango and banana), unripe seeds of legume plants or cereal, and various other storage organs of plants, starch can be found in the type of granules. Starchy foods have long been utilized by humans and their predecessors. Over 50% of daily energy consumption for people in agricultural societies and about 25% of people in westernized civilization comes from starch, which is a key component of the majority of plant-derived meals and feeds as well as many industrial raw materials [2]. Up to 25% of the calories in a typical human diet come from starch, which may be converted to glucose by a group of enzymes called amylases and amylos glucosidases. Although starch is widely utilized in the food industry, it is insoluble in water at ambient temperature. In addition, a lot of starches when boiled form weak-bodied and unfavourable gels due to the adverse effects of temperature, relative humidity, and storage duration (retrogradation mechanism) [3]. Since native starches lack the qualities necessary to ensure the quality of finished food items, the food sector has been for a long period to enhance the physicochemical characteristics of starches. Because starch is broken down quickly in the human intestine, blood glucose rises quickly as well. This can cause chronic disorders such inflammation, oxidative stress, and impaired

insulin sensitivity [5]. New technology and ingredients are being used more often as a result of growing customer demand for high-quality food items. Health issues (such as cholesterol, obesity, and cancer), variations in demographic characteristics, the desire for convenience, modifications to distribution networks, and pricing are some of the variables that have an impact on changes in consumer demand. These developments have led to a sharp rise in demand in new items, notably those that are convenience-oriented and produced utilizing cutting-edge technology, with high pressures [6].

2. Resistant Starch

A portion of starch known as resistant starch (RS) avoids breakdown of food with in intestine and moves intact through to the large intestine. After that, bacteria in the gastrointestinal tract ferment RS to create short-chain fatty acids (SCFAs). It was Englyst who first used the phrase "resistant starch" in 1982 [7]. The absence of leftover starch constituents seen in human wastes has led to the assumption that starch is totally absorbed by the human's body. However, scientists have shown via in vitro tests that amylase does not hydrolyze all components of starch. Additionally, parts that are not digested are known as resistant starch (RS), which is a particular component of the starch molecule that resists enzymatic degradation, reaches the intestine, and almost completely enters the colon. In recent times, undigested parts have become a popular delicacy all around the world [8]. The potential health advantages and practical qualities of resistant starch have drawn a lot of interest. As a portion of starch that is robust to pancreatic-amylase breakdown, resistant starch travels from the intestine to the large intestine wherever it serves as a prebiotic for the gastrointestinal bacteria [9]. Both normal and abnormal patients have benefited from resistant starch's positive benefits on fatty acid (FA) digestion, inflammation mitigation, and glycemic management [10]. SCFAs which are produced by the digestion process of resistant starch in the colon can control glucose homeostasis, protect colorectal cancer by red meat, promote postprandial lipid oxidation, and boost feelings of satiety [11]. Scientists have categorized resistant starch into four groups based on its structural traits, chemical modifications, the effects of cooking, or associations with lipids (RS1, RS2, RS3, and RS4). Each kind must be taken into account separately because to the variety in content, structure, and effects caused by different processing procedures. When RS enters the colon, it is fermented by bacteria in the gastrointestinal, mostly making the SCFAs acetate, propionate, and butyrate [12]. Although butyrate has been specifically recognized for improving health and is the short-chain fatty acids that is most elevated by RS ingestion, propionate and acetate can also have effects on wellbeing. Butyrate has a significant impact on gut health in humans, minimizing risk factors for colorectal cancer, decreasing inflammation, and enhancing gastrointestinal barrier activity [13]. Table 1 shows the physiological benefits of resistant starch.

2.1. Resistant Starch as a Functional Food. Starch is categorized into four kinds based on the pace and degree of in vitro digestion (see Table 2). The first 2 categories are highly digestible starch (HDS, or the quantity of starch that is quickly digested and assimilated by enzymes in less than 20 minutes in vitro method) and slowly digestible starch (SDS, which could be entirely metabolized yet not as quickly from 20 minutes to 120 minutes) [18]. People are becoming more interested in functional food as their living conditions rise. Dietary fibre, as an incredibly significant raw dietary ingredient, has piqued the interest of nutrition and medical experts. Every country in the world has specific guidelines for daily fibre consumption. As a novel form of food additives, RS has the physiological role of dietary fibre as well as other benefits that dietary fibre does not have. Its fundamental properties are comparable to normal starch, and when added to food, it affects the flavour, texture, and sensory assessment. RS's structure, production process, deuterium action mechanism, and health qualities have all been widely explored to date. Furthermore, a large amount of RS is employed as a dietary component in the food sector [19]. Many RS products are also on the market. Given the specific functional features and physiological advantages of RS, manufacturing and managing RS are simple, especially given the RS's low water retention capacity [20]. RS functions similarly to dietary fibre. Colloidal RS4 nanoparticles derived from acid hydrolysis and cross-linking are appropriate for developing a fibre-rich beverage [21]. To guarantee that RS meets the functional needs of the beverage sector, the natural sources, mixed flavour, white colour, good viscosity ability and rheological qualities, and weak water-retaining capacity were identified [22]. RS is used as a texture modifier in a variety of baked goods, providing bread crumbs a desirable brittleness and softness [23]. According to Jain and Anal, the produced stability employing protein hydrolysates was improved with the inclusion of RS [24]. RS significantly increases emulsion emulsifying ability and slows oxidation process of lipid in food items. This deduction is supported by the published study [25]. Because of its enhanced viscosity, tiny particle size, high sticking temperature, and weak water-retaining capabilities, RS may also be employed as a thickening ingredient in soups and dairy products. Additionally, RS utilized as feed additives is a substitute to in-feed antibiotic, which can boost protein and energy utilization to raise animal development rate [26]. Owing to the physical boundaries generated by protein matrices and cell walls, RS1 is unavailable to enzymes for digestion. When contrasted to other varieties, it is less resistant to digestion. (1) RS2 is starches that are resistant to digestion owing to their crystalline form. (ii) RS3 is a retrograded starch generated after cooking and cooling starchy meals (e.g., pasta and potatoes). Amylopectin's long, branching chains create double helices that gastrointestinal enzymes cannot catalyze the hydrolysis. (iii) RS4 is cross-linked, etherized, or esterified starch. Because of its tiny particle size, pale colour, excellent extrusion, mixed flavour, film-developing capabilities, high gelatinization temperature, low calorific significance (1.6-2.8 kilo calories per grams), and low water interaction ability, RS has great

Table 1: Resistant starch's physiological benefits. Source: Grabitske et al. [14], Nugent [7], Sharma et al. [15], Brouns et al. [16], and Scholz-Ahrens et al. [17].

Physiological consequences	Preventive function
Micronutrient absorption has improved	Increased calcium uptake, osteoporosis
Regulation of glycemic as well as insulinemic actions	Diabetes
Enhanced satiety and decreased energy intake	Obesity
Better bowel role	Inflammatory bowel disease, colorectal cancer, ulcerative colitis, constipation, and diverticulitis, are all possibilities
Protagonist of prebiotics and culture	Healthy colon

Table 2: Different types of resistant starch, the origins of such starches, and how they resist digestion in the intestine. Source: Sharma et al. [15], Lunn and Buttriss [8], Sajilata et al. [33], Rahman et al. [34], and Nugent [7].

Sources of food	Description	Lowered resistance by	Starch types	Small intestine digestion
Seeds and grains, whole or partially milled, pasta, and legumes	It is physically entrapped in a nondigestible matrix, making it unavailable for digestion in small intestine digestion	Chewing, grinding	RS1	Slow pace; limited degree If appropriately milled, it is completely digested
High amylose starches, raw potatoes, certain legumes, and green bananas	Type-B crystalline resistant granules that have not been gelatinized, slowly breakdown by alpha amylase	Cooking and food processing	RS2	Small degree; very slower rate freshly prepared food is completely digested
Bread, cooked, and chilled potatoes, corn flakes, and foodstuffs that have been subjected to a lengthy and/or repeated wet heat treatment	When starch-comprising foodstuffs are cooked and chilled, retrograded starch is produced	Conditions of processing	RS3	Slowly; to a limited extent digestion that can be reversed: reheating increases digestibility
Drinks and foodstuffs containing modified starches are high in fibre (certain cakes and breads)	A few chemically altered resistant starches and dietary components that have undergone industrial processing	In vitro digestibility is less susceptible	RS4	Can withstand hydrolysis as a consequence of a chemical change

prospective as a functional component [27, 28]). Because of these qualities, RS has been effectively included into a wide range of foods, including baked goods, pasta, and dairy products, [29, 30]. RS has also been used to microencapsulate probiotics in dairy products [31] in an endeavour to boost viability, as well as fish oil to minimize oxidation as well as odour [32].

3. Starch Nanoparticles

Because of its significant specific surface area and quantum size impact, nanoparticles have been one of the effective and interesting in recent times. Due to their biodegradability, biodegradable nanoparticles are extensively employed in biotechnology, medicine, food, and other sectors [35]. SNPs have several features that make them appropriate for use as bioactive components in meals, including better water dispersibility, high specific surface area, small size, low toxicity, low immunogenicity, and high biocompatibility [4]. Furthermore, resistant starch nanoparticles have the benefit of being resistant to breakdown by digestible enzymes in the upper gastrointestinal tract (like amylase). As a consequence, RS nanoparticles have the ability to be used as prebiotics, colon-specific delivery methods, and bioactive elements [36]. Because of their mechanical qualities and renewable form, these starch nanoparticles have been extensively employed in food packaging [37, 38], plastic fillers, treatment and diagnosis of heart diseases, and medication administration [39, 40]. Figure 1 shows the preparation methods of starch nanoparticles and their applications.

3.1. SNP Preparation Method. Starch nanoparticles are resistant to enzymatic hydrolysis owing to their compact shapes and significant level of crystallinity. As a result, they are a novel type of RS that may be used as a functional component in meals and other goods. RS nanoparticles offer certain significant benefits as functional components in meals as compared to regular resistant starch, including their tiny size, high surface-to-volume ratio, strong adsorption characteristics, and superior water dispersibility [41]. RS nanoparticles might be used as amylase inhibitors and medication delivery vehicles, in addition to their intrinsic prebiotic properties comparable to soluble dietary fibres. As a result, the creation of RS microparticles has gained increasing interest.

3.2. Emulsion. Through the interaction of two phases—an aqueous phase comprising the soluble polymers and an

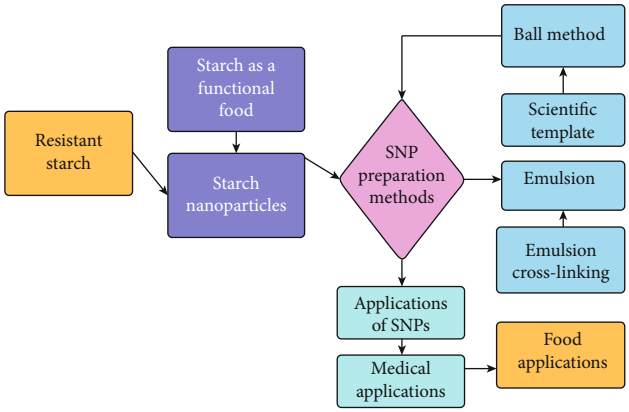

Figure 1: The starched nanoparticle preparation methods and their applications.

organic solvent which is completely or partially miscible in water—an emulsion is created. The two stages are then vigorously stirred together using an ultrasonic homogenization, such as microfluidization or mechanical homogenizer, to create an emulsion. To sustain the emulsion, a surfactant must be present. The agitation-induced droplets serve as nanoreactors to cause the regulated crystallization of starch within the shape of nanoparticles [42]. Emulsifiers reduce the surface pressures between the two nonmiscible fluids, minimizing the repulsive force between the two fluids and so reducing the adhesion between constituents of the same fluid, which is the concept on which the process of emulsion is developed [43].

3.3. Emulsion Cross-Linking. It has been claimed that SNPs were created using an emulsion cross-linking process. In this method, an aqueous layer containing cross-linking reagents is combined with another liquid containing dissolved starch. The combination is then introduced into an organic or oily phase, while emulsifiers are still present. Small nanoparticles are produced by a cross-linking process within the liquid droplets of this W/O emulsion. The particles produced by this emulsion cross-linking method are, however, rather big and on the microscopic scale [44].

3.4. Scientific Template. This technique is particularly useful for manufacturing porous or hollow particles. Until recently, hollow nanoparticles (HNPs) were created by producing a void space within a solid precursor using a range of physical and chemical approaches like nozzle reactor techniques, phase separation, emulsion polymerization, and sacrificial template method [37, 45]. The hard templating approach is one of the simplest and most widely used methods [46]. This method usually entails covering a substance that will serve as a prototype with a composite matrix, in this example starch, and then gradually removing the template component unless a hollow particle are formed [47].

3.5. Ball Method. Ball milling is one of the most dependable methods for producing nanomaterials without the use of additives or the need for a subsequent step of dehydration to retrieve the nanoparticles. The ball milling method has been studied over time for the nanoreduction of various polymeric substances, especially starch [4], cellulose [26], and protein-based polymers [48] for *Appl. Sci.* 2021, *11*, 4547 9 of 26 different applications. This procedure can be carried out either wet (with solvents) or dry (without solvents). Milling happens as a result of mechanical action between the crushing medium, like balls of varying sizes, and the powdered material. Typically, the grinding balls and the container are constructed of the same exceptionally hard substance (corundum, stainless steel, and zirconia). The rotational movement of the bowl, as in a planetary ball mill, provides mechanical energy to the system. Wet ball milling is also regarded a green chemical technique because it does not need high temperatures (conserving energy) and uses little solvents [49]. Acid hydrolysis is a mechanism that may be classified into three stages depending on the activity rates involved: slow, rapid, and extremely slow. SNPs are commonly produced by a sequence of stages utilizing the acid enzymatic hydrolysis: (i) the starch is blended by the acid; (ii) this solution is heated for a fixed period of time while being persistently stirred; (iii) the consequential suspension is rinsed with distilled water with consecutive centrifugation until neutralisation is attained; and (iv) the suspension is kept in the fridge for a set duration of time [50].

4. Applications of SNPs

4.1. Medical Applications. Cancer treatment is one of the key medicinal uses for SNPs that are possible. In a recent research, Alp et al. [51] showed the benefits of encapsulating anticancer drugs in polymeric nanomaterials for increasing the drug's solubilization, delaying the onset of cytotoxicity, and guarding against fast systemic metabolism. The researchers tested the encapsulated medication on MCF-7 breast carcinoma cells to gauge its efficacy. The evidence showed that encapsulating CG-1521 in SNPs increased anti-MCF-7 cell functional effectiveness and recommended that additional hormone-dependent malignancies could benefit from this encapsulation method [51]. Additionally, Yang et al. [52] conducted in vitro studies using synthetic, antibiotic-loaded SNPs. They used MTT tests to compare normal hepatic cells (AML12) versus liver hepatocellular lines (HepG2), and the results showed that SNPs had remarkable bioactivity for both types of cells. Moreover, due to direct engagement with carcinoma cells, the free-drug showed stronger antitumor behaviour than nanoparticles attached to Hepg2, even while loaded SNPs demonstrated a slower drug discharge. But at the other side, researchers also showed that for the various antibiotic doses investigated, AML12 cells had a greater vitality than Hepg2 [52]. SNPs have been shown to be effective as medication delivery methods by Wang et al. [53]. Rats were used in the investigations, and serum specimens were taken for examination. The drug or drug-loaded SNPs, in addition to the drug topically on the resistant starch, were administered orally. The average values discovered for the particle

residence time did not differ considerably from those of the unprocessed paclitaxel. It was determined that the method used to prepare SNPs had a significant impact on the bioactivity of paclitaxel and that using SNPs had a greater impact than loading the medication directly onto starch. As a result, creating SNPs is a successful way to boost paclitaxel's bioactivity [53]. Some investigators also conducted studies to assess the performance of SNPs packed with pharmaceuticals to confirm their usefulness as carriers of drugs within a very broad clinical application range. A histopathological research on the skin of rat was carried out by El-Naggar et al. [54] to determine if the manufacturing was accepted without producing irritant symptoms. Rodents' skin was covered with a gel containing the medication diclofenac sodium that was incorporated with cross-linked SNPs, and the outcomes were matched to a control group in which the rodents' skin was not coated. Last but not least, the study showed that the drug-loaded SNPs had no negative effects on the rodents' skin, making them an excellent treatment option for rheumatoid illnesses and also other chronic inflammation conditions [54].

4.2. Food Applications. Ahmaad et al. [1] have investigated the discharge of catechin from SNPs for food uses in order to maintain the qualities of the beneficial chemical during simulating intestinal and stomach environments. The SNPs aided maintain catechin's bioactive characteristics during in vitro digestion pathway by shielding it from the harsh stomach environment [1]. Ahmad et al. [55] also conducted in vitro tests on the probiotic loaded SNPs' survival. Utilizing both simulating gastric juice and synthetic intestine liquid, the investigation was conducted under simulated gastrointestinal as well as processing circumstances. Although it was demonstrated that the nanoparticles were quite tiny to incorporate the probiotics within them, they were nonetheless directly discharged into the simulated gastrointestinal solutions, which led to cell damage owing to the severe climates of such environments, leading to the conclusion that SNPs are not excellent probiotic delivery systems [56]. Various food simulators, a few of which were designed to imitate high hydrophilic meals and many others and highly lipophilic meals, were utilized to examine curcumin outflow patterns in a current research by Nieto-Suaza et al. [57]. The investigators came to the conclusion that lowering the polarity of the SNPs might limit the emitted curcumin, which was preferred in lipophilic compounds [57]. The in vitro emission of SNPs coated with polyphenol in simulating intestinal and stomach fluids was also studied by Liu et al. [52]. This research demonstrated continuous polyphenol release patterns from SNPs and demonstrated that SNPs might be intriguing and effective nanocarriers for protecting bioactive substances from harsh conditions and controlling their release [58].

4.2.1. Water Chestnut Starch. Nontraditional food sources have received a great deal of notice in recent years since they are employed as bioactive components in innovative food creation and food formulations. Water chestnut (*Trapa natans* L.), a member of the Trapaceae family, is an aquatic warm-season crop that floats on the surface of lakes and ponds. It is an aqueous angiospermic plant that thrives in fresh water wet areas, lakes, ponds, swamps, and slow portions of rivers and freshwater or brackish estuaries. According to Hummel and Kiviat [59], water chestnut harvesting area worldwide is 603,076 hectares, with a total production of 2327495 tonnes [60]. Water chestnut is frequently referred to as "Singhara" in Pakistan. The water chestnut kernel contains vital minerals, proteins, and carbs. Dried water chestnut weighs about 100 g protein (10.8 percent), moisture (7.3 percent), fibre (6.4 percent), fat (1.85 percent), iron (3.8 mg), ash (8.5 percent), calcium (102.8 mg), and phosphorus (325 mg) are the other macronutrients [55]. In terms of dry weight, the water chestnut's starch content ranged from 85 to 97.4% [62].

5. Probiotic

The word "probiotic" is Greek in origin and translates to "for life." For "life," we mean any element or creature that helps the host maintain good health. Probiotics were defined by the WHO and FAO as "live microorganisms that, when provided in suitable proportions, impart a health benefit on the host" in 2002. Probiotic bacteria have been shown to have a number of positive effects, including (a) improving food products' nutritional value, (b) regulating and lowering serum cholesterol, (c) strengthening the immunological system, (d) trying to prevent gut infectious diseases as well as reducing antibiotic-associated diarrhoea, (e) lowering symptoms of lactose intolerance, (f) lowering the risk of colorectal cancer, and (g) enhancing the breakdown of gliadin versus celiac in gluten-containing foods that are dependent [63]. Individuals are interested in ingesting goods that include probiotics because of these capabilities. Products containing probiotics standout among the goods with health claims that have been created and promoted in the media in recent years [64]. Due to these delivery systems' negative health implications, marketing campaigns attempting to produce innovative functional food items have been launched. Probiotics can be found in a variety of commercially available delivery modalities, including food items (such as dairy, processed meat, vegetables, juices, and cereal-based products), dietary supplements (tablet, liquid, pill, and in powder form), and medications. Over time, the meaning of the term "probiotic" has evolved and become more inclusive. Although most researchers agree with the definition given by FAO and WHO, additional definitions have recently been introduced to the probiotic vocabulary, including "paraprobiotics" (probiotic inactivated cells) and "postbiotics" (probiotics' beneficial metabolites). Therefore, research has demonstrated that *Lactobacillus* species are common in the atmosphere and found in a variety of surfaces, like water, soil, and plants, as well as decayed cells (either intact or cell extracts/ruptured cells). Additionally, *Lactobacillus* spp. are naturally occurring commensal occupants of the female vaginal tract, GIT, and oral cavity [65]. *Lactobacillus rhamnosus* GG (LGG) (ATCC 53103) is a probiotic now being utilized in methodological approaches for cancer treatment [66]. The name of the species is derived from LGG's biochemical

property of *rhamnose* metabolism and fermentation, which is used to distinguish this species of *Lactobacillus*. A variety of techniques, PFGE characterization of *L. rhamnosus* GG, comprising species-specific PCR, phage type, proteome characterization with the utilization of 2D-DIGE, and culture techniques (by means of MRS growth agar medium), are used to identify *Lactobacillus* spp. Some *L. rhamnosus* strains have positive impacts on the body that called them as probiotics. In particular, LGG can successfully adhere to the gastrointestinal mucosa and survive stomach acidity and bile salts. The power of the bacteria to create antistress proteins, which increase its capacity for survival in intestinal movement after oral ingestion, results in its ability to tolerate acidity of stomach and bile salts [66]. Exopolysaccharides with high galactose residue content and particular sticky pili on the bacterial wall both promote adhesion to the intestinal membrane. The activation and production of various cytokines, including IL-12, IFN-, IL-10, IL-6, TNF-, and IL-1, as well as a specific protein, p40, secreted by *L. rhamnosus* GG cells that can lessen the inflammatory process and programmed cell death of intestinal epithelium, account for the impact on the immune response. In a later section of the paper, it will be discussed how other apoptosis inhibition pathways are connected to the control of cyclooxygenase-2 (COX-2). As a result, LGG is well understood and is renowned for a variety of anti-inflammation actions. Therefore, therapy with LGG may lower the incidence of colon cancer in animal models by regulating the gastrointestinal microbiota and downregulating proinflammation chemicals. First discovered in a healthy adult's faecal sample in the late 1980s, LGG has now had its whole genome sequence thoroughly described and registered. In specific, a study recognized LGG-specific islands comprising genes that code for 3 secreted LPXTG-like pilins (spaCBA) but a pilin-specific sortase infamously involved in the pathways of adhesion to the intestine-epithelium through contrast of the genomic sequences of *Lactobacillus* species include LGG. It satisfies the probiotic selection criteria, which include strong in vitro adhesion, survival through the GIT (bile and gastric acid), and propensity to make colonies with excellent intestinal persistence. Additionally, the cellular metabolites may have a substantial negative influence on human health [67].

6. Encapsulation of Probiotic

Encapsulation may be thought of as a technique for putting components into capsules before putting them into a system. Probiotics can be packaged as powder formulations to protect living microorganisms, increase their stability, and provide advantages for targeted distribution [68]. Encapsulated materials can be created by packing bioactive compounds such as enzymes, antioxidants, polyphenols, and micronutrients into wall substances. Encapsulation technique is referred to as microencapsulation (from 3 to 800 m) or nanoencapsulation depending on the particle size (from 10 to 1000 nm). By protecting bioactive chemicals from harmful surroundings and delivering them directly to the target location, nano-/microencapsulation can increase their bioavailability [69]. Encapsulation is frequently utilized in a number of food and nutritional purposes to deliver food components just where they are needed [41]. Functional ingredients are shielded from harsh process parameters during food security by being encapsulated, which also improves food safety by better hindering microbial growth and increase sensory quality by covering up unpleasant flavours (such as the bitterness of polyphenols) [12]). The bioavailability of bioactive compounds during human digestion can be increased by encapsulating bioactive substances. The encapsulation increases the bioactive ingredients' water solubility, safeguards them from adverse circumstances in a specific area of the digestive tract (such as the stomach), and emits them in a targeted area (such as the intestine) for improved human absorption [70, 71]. For instance, amylose inclusion structures enhanced the in vivo efficacy of genistein (a type of isoflavones) in a rat model [70].

7. Microencapsulation

The technique of microencapsulation involves packing tiny amounts of solid, liquid, or gas (active core) into a secondary substance (encapsulant) to create a capsule (microcapsules have a size range between 1 and 1000 nm, while nanocapsules are in the submicron range). The encapsulation of essential oils, colorings, flavours, sweeteners, and microbes is just a few examples of the many uses for microencapsulation in the pharmacological, agricultural, medical, and food sectors. In the food sector, microencapsulated substances may shield essential molecules from the impacts of the environment (heat, oxygen, moisture, and light). The creation of probiotic encapsulates uses a variety of microencapsulation processes.

7.1. Emulsion Technique. A liquid is dispersed into another immiscible liquid to create an emulsion. Probiotic cells are encapsulated when they are added to the dispersion liquid [13]. The connection and association between the phases of discontinuity and continuity are the foundation of this approach. To be more precise, the procedure entails dispersing the cells in a little amount of a suspension of a polymer based on water (dispersed stage). It is then added to a sizable amount of oil and organic stage (continuous phase) and mechanically homogenized with the help of a surfactant, and a water-in-oil emulsion is created as a result. Gel beads inside the oil phase are produced as the water-soluble biopolymer becomes insolubilized and are collected by centrifugal or filtration. According to the properties of the supporting material being employed, the insolubilization method differs [72]. It can be started by chilling the emulsion or adding a cross-linking substance to it [73].

7.2. Extrusion Technique. Probiotic cells are injected into hydrocolloid components like carrageenan and alginate resulting in their physical encapsulation [74]. It is a common and well-known method that entails pushing a solution having the cells through nozzles or other small holes while using the proper droplet-generating equipment [13]. A biopolymer solution is initially combined with the bacterial culture to make a suspension [75, 76]. The finished liquid is

extruded under high pressure through a nozzle, and the resulting droplets are collected in a bath of gelling liquid (most frequently a CaCl2 solution). The cells are confined in a grid in three dimensions created by because of the polymer's ionic cross-linking, and gel beads are generated as a result [75]. The size of the generated microspheres is influenced by a number of variables, including the viscous and fluid velocity of the polymer solutions, its concentration and temperature, the orifice's diameter, and its drop altitude or distances from the cross-linking solution.

7.3. Spray Drying (SD). One of the most common methods of microencapsulation is spray drying (SD). The mixture of heat and mass transfer from the air to the atomized droplets and back is its fundamental idea [37]. Probiotics are emulsified or dispersed in an aqueous solution of a carrier components in the process. The liquid combination is then atomized through a nozzle or spinning wheel and evaporated by making contact with hot air or gas [75–77]. The carrier acts as a defensive agent against abrasive elements during storage and transit through the digestive tract while encasing the cells (Huang et al. 2016). Using a cyclone or bag filter, the dry particles are removed from humid air and gathered [76, 77]. Probiotic properties (growth phase and probiotic strain), dryer qualities (drying time and temperature type of atomization), feed character traits (carrier material and its intensity and particular conditions applied: oxidative, mechanical, or osmotic), operational conditions (feed rate and drying temperature), and storage conditions are the main variables that can impact the method's efficiency [76].

7.4. Freeze Drying (FD). For heat-sensitive constituents, such bacterial cells, freeze drying (FD), also described as lyophilization or cryodesiccation, is the most common drying technique. It depends on water freezing and then sublimating under vacuum from the solid/frozen state into the gas state [76, 77]. Probiotics are negatively impacted by FD because it alters the structure of sensitive cell proteins and the condition of cell membrane lipids [78]. To solve this issue, it has been suggested using probiotics combined with cryoprotectants like as polymers, sugars (trehalose, lactose, maltodextrin mannose, and fructose), honey, milk, polyols (sorbitol), and amino acids (monosodium glutamate) [79]. Different cultures have varying degrees of cryoprotection [80]. Additionally, according to reports, some probiotic strains have great viability after freeze drying because of specific variations in the strains' properties, such as surface area, cell wall, and membrane composition [80]. The immobilized cell technique is also a potential solution for viability problems [81].

8. Conclusion and Future Perspectives

Starch-based nanoparticles have generated a lot of attention recently because of their tiny size, excellent biocompatibility, environmental friendliness, and prospective uses in meals, drug delivery systems, and biodegradable edible films. RS can be used as an enzyme-responsive carrier because it can be enzymatically degraded into glucose in vivo, unlike non-starch polysaccharides. Higher adsorption properties, water dispersibility, small size, and high surface-to-volume ratio are only a few of the major benefits that RS nanoparticles offer as functional food components and can be prepared by using extrusion, cross-linking, ball milling method, and scientific template methods. The solubility of the nanosized starch particles, as well as their bioaccessibility and bioavailability in vitro or in vivo, is significantly increased by their ultrafine structure and large surface area. The use of derivatives of starch nanoparticles as drug delivery platforms is gaining popularity recently because of their biocompatibility, enhanced mechanical and absorption characteristics, and flexibility in functional qualities. Similar pharmacological and physiological functions are also carried out by resistant starches, such as endorsing the development of a healthy gut flora, improving mineral absorption, lowering the risk of colon cancer, and reducing the levels of blood sugars etc. However, further research is still required to determine efficient ways to increase the RS content in various types of starchy foods and to clarify the effects of increasing RS levels on food quality (such as appearance, texture, and mouthfeel). Furthermore, research is also needed to determine the gastrointestinal destiny of various RS nanoparticle types in the human body.

Data Availability

Any additional data is available on request, although all the relevant data has been provided here.

Conflicts of Interest

All authors have affirmed zero conflict of interest.

Acknowledgments

The authors are thankful to the Government College University, Faisalabad, and Kampala International University, Kampala, for the provision of the facilities used for this study.

References

[1] M. Ahmad, P. Mudgil, A. Gani, F. Hamed, F. A. Masoodi, and S. Maqsood, "Nano-encapsulation of catechin in starch nanoparticles: characterization, release behavior and bioactivity retention during simulated in-vitro digestion," *Food Chemistry*, vol. 270, pp. 95–104, 2019.

[2] Z. Ma and J. I. Boye, "Research advances on structural characterization of resistant starch and its structure-physiological function relationship: a review," *Critical Reviews in Food Science and Nutrition*, vol. 58, no. 7, pp. 1059–1083, 2018.

[3] P. H. Campelo, A. S. Sant'ana, and M. T. Clerici, "Starch nanoparticles: production methods, structure, and properties for food applications," *Current Opinion in Food Science*, vol. 33, pp. 136–140, 2020.

[4] L. Dai, C. Li, J. Zhang, and F. Cheng, "Preparation and characterization of starch nanocrystals combining ball milling with acid hydrolysis," *Carbohydrate Polymers*, vol. 180, no. 122–127, pp. 122–127, 2018.

[5] C. Egbuna, V. K. Parmar, J. Jeevanandam et al., "Toxicity of Nanoparticles in Biomedical Application: Nanotoxicology," *Journal of Toxicology*, vol. 2021, Article ID 9954443, 21 pages, 2021.

[6] E. Fuentes-Zaragoza, M. J. Riquelme-Navarrete, E. Sánchez-Zapata, and J. A. Pérez-Álvarez, "Resistant starch as functional ingredient: a review," *Food Research International*, vol. 43, no. 4, pp. 931–942, 2010.

[7] A. P. Nugent, "Health properties of resistant starch," *British Nutrition Foundation, Nutrition Bulletin*, vol. 30, no. 1, pp. 27–54, 2005.

[8] J. Lunn and J. L. Buttriss, "Carbohydrates and dietary fibre," *Nutrition Bulletin*, vol. 32, no. 1, pp. 21–64, 2007.

[9] A. Salehi-Abargouei, R. Ghiasvand, and M. Hariri, "Prebiotics, prosynbiotics and synbiotics: can they reduce plasma oxidative stress parameters? A systematic review," *Probiotics and antimicrobial proteins*, vol. 9, no. 1, pp. 1–11, 2017.

[10] K. L. Johnston, E. L. Thomas, J. D. Bell, G. S. Frost, and M. D. Robertson, "Resistant starch improves insulin sensitivity in metabolic syndrome," *Diabetic Medicine*, vol. 27, no. 4, pp. 391–397, 2010.

[11] X. Si, P. Strappe, C. Blanchard, and Z. Zhou, "Enhanced anti-obesity effects of complex of resistant starch and chitosan in high fat diet fed rats," *Carbohydrate Polymers*, vol. 157, no. 10, pp. 834–841, 2017.

[12] K. E. Bach Knudsen, H. N. Lærke, M. S. Hedemann et al., "Impact of diet-modulated butyrate production on intestinal barrier function and inflammation," *Nutrients*, vol. 10, no. 10, p. 1499, 2018.

[13] A. Geirnaert, M. Calatayud, C. Grootaert et al., "Butyrate-producing bacteria supplemented *in vitro* to Crohn 's disease patient microbiota increased butyrate production and enhanced intestinal epithelial barrier integrity," *Scientific reports*, vol. 7, no. 1, pp. 11450–11454, 2017.

[14] H. A. Grabitske and J. L. Slavin, "Low-digestible carbohydrates in practice," *Journal of the American Dietetic Association*, vol. 108, no. 10, pp. 1677–1681, 2008.

[15] A. Sharma, B. S. Yadav, and Ritika, "Resistant starch: physiological roles and food applications," *Food Reviews International*, vol. 24, no. 2, pp. 193–234, 2008.

[16] F. Brouns, B. Kettlitz, and E. Arrigoni, "Resistant starch and "the butyrate revolution"," *Trends in Food Science & Technology*, vol. 13, no. 8, pp. 251–261, 2002.

[17] K. E. Scholz-Ahrens, P. Ade, B. Marten et al., "Prebiotics, probiotics, and synbiotics affect mineral absorption, bone mineral content, and bone structure," *Journal of Nutrition*, vol. 137, no. 3, pp. 838S–846S, 2007.

[18] F. Jiang, C. Du, W. Jiang, L. Wang, and S. K. Du, "The preparation, formation, fermentability, and applications of resistant starch," *International Journal of Biological Macromolecules*, vol. 150, pp. 1155–1161, 2020.

[19] A. Homayouni, A. Amini, A. K. Keshtiban, A. M. Mortazavian, K. Esazadeh, and S. Pourmoradian, "Resistant starch in food industry: a changing outlook for consumer and producer," *Resistant starch in food industry: A changing outlook for consumer and producer, Starch-Stärke*, vol. 66, no. 1-2, pp. 102–114, 2014.

[20] B. A. Ashwar, A. Gani, A. Shah, I. A. Wani, and F. A. Masoodi, "Preparation, health as benefits and applications of resistant starch-a review," *Starch-Stärke*, vol. 68, no. 3–4, pp. 287–301, 2016.

[21] O. Jeong and M. Shin, "Preparation and stability of resistant starch nanoparticles, using acid hydrolysis and cross-linking of waxy rice starch," *Food Chemistry*, vol. 256, pp. 77–84, 2018.

[22] K. Kapusniak and E. Nebesny, "Enzyme-resistant dextrins from potato starch for potential application in the beverage industry," *Carbohydrate polymers*, vol. 172, no. 172, pp. 152–158, 2017.

[23] S. Djurle, A. A. M. Andersson, and R. Andersson, "Effects of baking on dietary fibre, with emphasis on β-glucan and resistant starch, in barley breads," *Journal of Cereal Science*, vol. 79, pp. 449–455, 2018.

[24] S. Jain and A. K. Anal, "Preparation of eggshell membrane protein hydrolysates and culled banana resistant starch-based emulsions and evaluation of their stability and behavior in simulated gastrointestinal fluids," *Food Research International*, vol. 103, pp. 234–242, 2018.

[25] T. A. Nasrin and A. K. Anal, "Enhanced oxidative stability of fish oil by encapsulating in culled banana resistant starch-soy protein isolate based microcapsules in functional bakery products," *Journal of Food Science and Technology*, vol. 52, no. 8, pp. 5120–5128, 2015.

[26] S. Deng, R. Huang, M. Zhou, F. Chen, and Q. Fu, "Hydrophobic cellulose films with excellent strength and toughness via ball milling activated acylation of microfibrillated cellulose," *Carbohydrate Polymers*, vol. 154, no. 129–138, pp. 129–138, 2016.

[27] L. Shen, M. J. Keenan, R. J. Martin et al., "Dietary resistant starch increases hypothalamic POMC expression in rats," *Obesity*, vol. 17, no. 1, pp. 40–45, 2009.

[28] H. Twinomuhwezi, C. G. Awuchi, and R. Mihigo, "Comparative study of the proximate composition and functional properties of composite flours of amaranth, rice, millet, and soybean," *American Journal of Food Science and Nutrition*, vol. 6, no. 1, pp. 6–19, 2020.

[29] N. Aravind, M. Sissons, C. M. Fellows, J. Blazek, and E. P. Gilbert, "Optimisation of resistant starch II and III levels in durum wheat pasta to reduce *in vitro* digestibility while maintaining processing and sensory characteristics," *Food Chemistry*, vol. 136, no. 2, pp. 1100–1109, 2013.

[30] E. L. Almeida, Y. K. Chang, and C. J. Steel, "Dietary fibre sources in bread: Influence on technological quality," *LWT-Food Science and Technology*, vol. 50, no. 2, pp. 545–553, 2013.

[31] T. F. Vandamme, G. K. Gbassi, T. L. Nguyen, and X. Li, "Microencapsulation of probiotics," in *In Encapsulation and Controlled Release Technologies in Food Systems*, J. M. Lakkis, Ed., Wiley, New York, 2016.

[32] C. G. Awuchi, C. N. Chukwu, A. O. Iyiola et al., "Bioactive Compounds and Therapeutics from Fish: Revisiting Their Suitability in Functional Foods to Enhance Human Well-being," *BioMed Research International*, vol. 2022, Article ID 3661866, 18 pages, 2022.

[33] M. G. Sajilata, R. S. Singhal, and P. R. Kulkarni, "Resistant starch – a review," *Comprehensive Reviews in Food Science and Food Safety*, vol. 5, no. 1, pp. 1–17, 2006.

[34] S. Rahman, A. Bird, A. Regina, Z. Li, J. P. Ral, and S. McMaugh, "Resistant starch in cereals: exploiting genetic engineering and genetic variation," *Journal of Cereal Science*, vol. 46, no. 3, pp. 251–260, 2007.

[35] I. J. Joye and D. J. McClements, "Production of nanoparticles by anti-solvent precipitation for use in food systems," *Trends in Food Science & Technology*, vol. 34, no. 2, pp. 109–123, 2013.

[36] N. Sivapragasam, P. Thavarajah, J. B. Ohm, and K. Margaret, "Novel starch based nano scale enteric coatings from soybean meal for colon- specific delivery," *Carbohydrate Polymers*, vol. 111, pp. 273–279, 2014.

[37] C. G. Awuchi, S. Morya, T. A. Dendegh, O. D. R. Okpala, and M. Korzeniowska, "Nanoencapsulation of food bioactive constituents and its associated processes: a revisit," *Bioresource Technology Reports*, vol. 19, no. 101088, p. 101088, 2022.

[38] L. Dai, C. Qiu, L. Xiong, and Q. J. Sun, "Characterisation of corn starch-based films reinforced with taro starch nanoparticles," *Food Chemistry*, vol. 174, pp. 82–88, 2015.

[39] M. A. Dar, A. Ingle, and M. Rai, "Enhanced antimicrobial activity of silver nanoparticles synthesized by Cryphonectria sp. evaluated singly and in combination with antibiotics," *Nanomedicine: Nanotechnology, Biology and Medicine*, vol. 9, no. 1, pp. 105–110, 2013.

[40] S. Muthukrishnan, S. Bhakya, T. Senthil Kumar, and M. V. Rao, "Biosynthesis, characterization and antibacterial effect of plant-mediated silver nanoparticles using Ceropegia thwaitesii an endemic species," *Industrial Crops and Products*, vol. 63, pp. 119–124, 2015.

[41] D. J. McClements and Y. Li, "Structured emulsion-based delivery systems: controlling the digestion and release of lipophilic food components," *Advances in Colloid and Interface Science*, vol. 159, no. 2, pp. 213–228, 2010.

[42] S. F. Chin, A. Azman, and S. C. Pang, "Size controlled synthesis of starch nanoparticles by a microemulsion method," *Journal of Nanomaterials*, vol. 2014, Article ID 763736, 7 pages, 2014.

[43] F. Islam, F. Saeed, M. Afzaal, M. Hussain, A. Ikram, and M. A. Khalid, "Food grade nanoemulsions: promising delivery systems for functional ingredients," *Journal of Food Science and Technology*, vol. 2022, pp. 1–11, 2022.

[44] Y.-Y. Fang, L.-J. Wang, D. Li et al., "Preparation of crosslinked starch microspheres and their drug loading and releasing properties," *Carbohydrate Polymers*, vol. 74, no. 3, pp. 379–384, 2008.

[45] S. D. Steichen, M. Caldorera-Moore, and N. A. Peppas, "A review of current nanoparticle and targeting moieties for the delivery of cancer therapeutics," *European Journal of Pharmaceutical Sciences*, vol. 48, no. 3, pp. 416–427, 2013.

[46] J. Hu, M. Chen, X. Fang, and L. Wu, "Fabrication and application of inorganic hollow spheres," *Chemical Society Reviews*, vol. 40, no. 11, pp. 5472–5491, 2011.

[47] T. Nakashima and N. Kimizuka, "Interfacial synthesis of hollow TiO2 microspheres in ionic liquids," *Journal of the American Chemical Society*, vol. 125, no. 21, pp. 6386-6387, 2003.

[48] K. Ramadhan and T. J. Foster, "Effects of ball milling on the structural, thermal, and rheological properties of oat bran protein flour," *Journal of Food Engineering*, vol. 229, pp. 50–56, 2018.

[49] L. Protesescu, S. Yakunin, O. Nazarenko, D. N. Dirin, and M. V. Kovalenko, "Low-cost synthesis of highly luminescent colloidal Lead halide perovskite nanocrystals by wet ball milling," *ACS applied nano materials*, vol. 1, no. 3, pp. 1300–1308, 2018.

[50] D. C. Aldao, E. Šárka, P. Ulbrich, and E. Menšíková, "Starch nanoparticles—two ways of their preparation," *Czech Journal of Food Sciences*, vol. 36, no. 2, pp. 133–138, 2018.

[51] E. Alp, F. Damkaci, E. Guven, and M. Tenniswood, "Starch nanoparticles for delivery of the histone deacetylase inhibitor CG-1521 in breast cancer treatment," *International Journal of Nanomedicine*, vol. 14, pp. 1335–1346, 2019.

[52] J. Yang, F. Li, M. Li et al., "Fabrication and characterization of hollow starch nanoparticles by gelation process for drug delivery application," *Carbohydrate Polymers*, vol. 173, pp. 223–232, 2017.

[53] L. Wang, X. Zhao, F. Yang et al., "Loading paclitaxel into porous starch in the form of nanoparticles to improve its dissolution and bioavailability," *International Journal of Biological Macromolecules*, vol. 138, pp. 207–214, 2019.

[54] M. E. El-Naggar, M. H. El-Rafie, M. A. El-Sheikh, G. S. El-Feky, and A. Hebeish, "Synthesis, characterization, release kinetics and toxicity profile of drug- loaded starch nanoparticles," *International Journal of Biological Macromolecules*, vol. 81, pp. 718–729, 2015.

[55] M. Ahmad, P. Mudgil, A. Gani, F. Hamed, F. A. Masoodi, and S. Maqsood, "Nano encapsulation of catechin in starch nanoparticles: characterization; release behavior and bioactivity retention during in-vitro digestion," *Food Chemistry*, vol. 270, pp. 95–104, 2019.

[56] M. Ahmad and A. Gani, "Ultrasonicated resveratrol loaded starch nanocapsules: characterization, bioactivity and release behaviour under in-vitro digestion," *Carbohydrate Polymers*, vol. 251, article 117111, 2021.

[57] L. Nieto-Suaza, L. Acevedo-Guevara, L. T. Sánchez, M. I. Pinzón, and C. C. Villa, "Characterization of Aloe vera-banana starch composite films reinforced with curcumin-loaded starch nanoparticles," *Food Structure*, vol. 22, article 100131, 2019.

[58] C. Liu, S. Ge, J. Yang et al., "Adsorption mechanism of polyphenols onto starch nanoparticles and enhanced antioxidant activity under adverse conditions," *Journal of Functional Foods*, vol. 26, pp. 632–644, 2016.

[59] M. Hummel and E. Kiviat, "Review of world literature on water chestnut with implications for management in North America," *Journal - Aquatic Plant Management Society*, vol. 42, pp. 17–28, 2004.

[60] Food and Agriculture Organization, 2017, http://www.fao.org/faostat/en/#data/QC/visualize (Accessed May 1, 2019).

[61] P. Adkar, A. Dongare, S. Ambavade, and V. H. Bhaskar, "*Trapa bispinosa* Roxb.: a review on nutritional and pharmacological aspects," *Advances in Pharmacological Sciences*, vol. 2014, Article ID 959830, 13 pages, 2014.

[62] A. Gani, S. S. Haq, F. A. Masoodi, A. A. Broadway, and A. Gani, "Physico-chemical, morphological and pasting properties of starches extracted from water chestnuts (Trapa natans) from three lakes of Kashmir, India," *Brazilian Archives of Biology and Technology*, vol. 53, no. 3, pp. 731–740, 2010.

[63] F. Zendeboodi, N. Khorshidian, A. M. Mortazavian, and A. G. da Cruz, "Probiotic: conceptualization from a new approach," *Current Opinion in Food Science*, vol. 32, pp. 103–123, 2020.

[64] K. Tsilingiri and M. Rescigno, "Postbiotics: what else?," *Beneficial Microbes*, vol. 4, no. 1, pp. 101–107, 2013.

[65] S. Coudeyras, H. Marchandin, C. Fajon, and C. Forestier, "Taxonomic and strain-specific identification of the probiotic strain Lactobacillus rhamnosus 35 within the Lactobacillus casei group," *Applied and Environmental Microbiology*, vol. 74, no. 9, pp. 2679–2689, 2008.

[66] G. L. Banna, F. Torino, F. Marletta et al., "*Lactobacillus rhamnosus* GG: an overview to explore the rationale of its use in cancer," *Frontiers in Pharmacology*, vol. 8, p. 603, 2017.

[67] M. D. Lena, G. M. Quero, E. Santovito, J. Verran, M. D. Angelis, and V. Fusco, "A selective medium for isolation and

accurate enumeration of Lactobacillus casei-group members in probiotic milks and dairy products," *International Dairy Journal*, vol. 47, pp. 27–36, 2015.

[68] K. S. Yoha, S. Nida, S. Dutta, J. A. Moses, and C. Anandharamakrishnan, "Targeted delivery of probiotics: perspectives on research and commercialization," *Probiotics and Antimicrobial Proteins*, vol. 14, pp. 15–48, 2021.

[69] P. M. Reque and A. Brandelli, "Encapsulation of probiotics and nutraceuticals: Applications in functional food industry," *Trends in Food Science & Technology*, vol. 114, pp. 1–10, 2021.

[70] R. Cohen, B. Schwartz, I. Peri, and E. Shimoni, "Improving bioavailability and stability of genistein by complexation with high-amylose corn starch," *Journal of Agricultural and Food Chemistry*, vol. 59, no. 14, pp. 7932–7938, 2011.

[71] C. G. Awuchi, M. Akram, I. C. Owuamanam, C. C. Ogueke, C. G. Awuchi, and H. Twinomhwezi, "Nanotechnological application of peptide- and protein-based therapeutics," in *Applications of Nanotechnology in Drug Discovery and Delivery*, C. Egbuna, M. A. Gaman, and J. Jeevanandam, Eds., pp. 205–238, Elsevier, Netherlands, 2022.

[72] T. Heidebach, P. Först, and U. Kulozik, "Microencapsulation of probiotic cells for food applications," *Critical Reviews in Food Science and Nutrition*, vol. 52, no. 4, pp. 291–311, 2012.

[73] S. Rathore, P. M. Desai, C. V. Liew, L. W. Chan, and P. W. S. Heng, "Microencapsulation of microbial cells," *Journal of Food Engineering*, vol. 116, no. 2, pp. 369–381, 2013.

[74] J. Burgain, C. Gaiani, M. Linder, and J. Scher, "Encapsulation of probiotic living cells: From laboratory scale to industrial applications," *Journal of Food Engineering*, vol. 104, no. 4, pp. 467–483, 2011.

[75] L. M. Sagis, "Theoretical Modeling of Mechanical Behavior and Release Properties of Microcapsules," in *In Microencapsulation and Microspheres for Food Applications*, pp. 207–232, Academic Press, 2015.

[76] V. Manojlović, V. A. Nedović, K. Kailasapathy, and N. J. Zuidam, "Encapsulation of probiotics for use in food products," in *In Encapsulation technologies for active food ingredients and food processing*, pp. 269–302, Springer, New York, NY, 2010.

[77] Z. Fang and B. Bhandari, "Spray drying, freeze drying and related processes for food ingredient and nutraceutical encapsulation," in *Encapsulation technologies and delivery systems for food ingredients and nutraceuticals*, pp. 73–109, Woodhead Publishing, 2012.

[78] A. Nag and S. Das, "Improving ambient temperature stability of probiotics with stress adaptation and fluidized bed drying," *Journal of Functional Foods*, vol. 5, no. 1, pp. 170–177, 2013.

[79] D. Dianawati, V. Mishra, and N. P. Shah, "Survival of microencapsulated probiotic bacteria after processing and during storage: a review," *Critical Reviews in Food Science and Nutrition*, vol. 56, no. 10, pp. 1685–1716, 2016.

[80] P. Capela, T. K. C. Hay, and N. P. Shah, "Effect of cryoprotectants, prebiotics and microencapsulation on survival of probiotic organisms in yoghurt and freeze-dried yoghurt," *Food Research International*, vol. 39, no. 2, pp. 203–211, 2006.

[81] D. Dimitrellou, P. Kandylis, T. Petrović et al., "Survival of spray dried microencapsulated *Lactobacillus casei* ATCC 393 in simulated gastrointestinal conditions and fermented milk," *LWT-Food Science and Technology*, vol. 71, pp. 169–174, 2016.